TECHNISCHE UNIVERSITÄT
ILMENAU

Doctoral Thesis

Applications of Compressive Sensing to Direction of Arrival Estimation

Mohamed Ibrahim

Dissertation zur Erlangung des akademischen Grades Doktor-Ingenieur (Dr.-Ing.)

Anfertigung im: Fachgebiet Elektronische Messtechnik & Signal Verarbeitung
Institut für Informationstechnik
Fakultät für Elektrotechnik und Informationstechnik

Gutachter: Univ.-Prof. Dr.-Ing. Giovanni Del Galdo
Prof. Dr.-Ing. João Paulo Carvalho Lustosa da Costa
Prof. Dr. Ahmed El-Sayed El-Mahdy

Vorgelegt am: 02.07.2018
Verteidigt am: 28.11.2018

urn:nbn:de:gbv:ilm1-2018000490

Abstract

Direction of Arrival (DOA) estimation of plane waves impinging on an array of sensors is one of the most important tasks in array signal processing, which have attracted tremendous research interest over the past several decades. The estimated DOAs are used in various applications like localization of transmitting sources, massive MIMO and 5G Networks, tracking and surveillance in radar, and many others. The major objective in DOA estimation is to develop approaches that allow to reduce the hardware complexity in terms of receiver costs and power consumption while providing a desired level of estimation accuracy and robustness in the presence of multiple sources and/or multiple paths.

Compressive sensing (CS) is a novel sampling methodology merging signal acquisition and compression. It allows for sampling a signal with a rate below the conventional Nyquist bound. In essence, it has been shown that signals can be acquired at sub-Nyquist sampling rates without loss of information provided they possess a sufficiently sparse representation in some domain and that the measurement strategy is suitably chosen. CS has been recently applied to DOA estimation, leveraging the fact that a superposition of planar wavefronts corresponds to a sparse angular power spectrum.

This dissertation investigates the application of compressive sensing to the DOA estimation problem with the goal to reduce the hardware complexity and/or achieve a high resolution and a high level of robustness. Many CS-based DOA estimation algorithms have been proposed in recent years showing tremendous advantages with respect to the complexity of the numerical solution while being insensitive to source correlation and allowing arbitrary array geometries. Moreover, CS has also been suggested to be applied in the spatial domain with the main goal to reduce the complexity of the measurement process by using fewer RF chains and storing less measured data without the loss of any significant information.

In the first part of the work, we investigate the model mismatch problem for CS based DOA estimation algorithms off the grid. To apply the CS framework a very common approach is to construct a finite dictionary by sampling the angular domain with a predefined sampling grid. Therefore, the target locations are almost surely not located exactly on a subset of these grid points. This leads to a model mismatch which deteriorates the performance of the estimators. We take an analytical approach to investigate the effect of such grid offsets on the recovered spectra showing that each off-grid source can be well approximated by the two neighboring points on the grid. We propose a simple and efficient scheme to estimate the grid offset for a single source or multiple well-separated sources. We also discuss a numerical procedure for the joint estimation of the grid offsets of closer sources.

In the second part of the thesis, we study the design of compressive antenna arrays for DOA estimation that aim to provide a larger aperture with a reduced hardware complexity and allowing reconfigurability, by a linear combination of the antenna outputs to a lower number of receiver channels. We present a basic receiver architecture of such a compressive array and introduce a generic system model that includes different options for the hardware implementation. We then discuss the design of the analog combining network that performs the receiver channel reduction. Our numerical simulations demonstrate the superiority of the proposed optimized compressive arrays compared to the sparse arrays of the same complexity and to compressive arrays with randomly chosen combining kernels.

Finally, we consider two other applications of the sparse recovery and compressive arrays. The first application is CS based time delay estimation and the other one is compressive channel sounding. We show that the proposed approaches for sparse recovery off the grid and compressive arrays show significant improvements in the considered applications compared to conventional methods.

Zusammenfassung

Die Schätzung der Einfallsrichtungen (Directions of Arrival/DOA) mehrerer ebener Wellenfronten mit Hilfe eines Antennen-Arrays ist eine der prominentesten Fragestellungen im Gebiet der Array-Signalverarbeitung. Das nach wie vor starke Forschungsinteresse in dieser Richtung konzentriert sich vor allem auf die Reduktion des Hardware-Aufwands, im Sinne der Komplexität und des Energieverbrauchs der Empfänger, bei einem vorgegebenen Grad an Genauigkeit und Robustheit gegen Mehrwegeausbreitung.

Diese Dissertation beschäftigt sich mit der Anwendung von Compressive Sensing (CS) auf das Gebiet der DOA-Schätzung mit dem Ziel, hiermit die Komplexität der Empfängerhardware zu reduzieren und gleichzeitig eine hohe Richtungsauflösung und Robustheit zu erreichen. CS wurde bereits auf das DOA-Problem angewandt unter der Ausnutzung der Tatsache, dass eine Superposition ebener Wellenfronten mit einer winkelabhängigen Leistungsdichte korrespondiert, die über den Winkel betrachtet sparse ist. Basierend auf der Idee wurden CS-basierte Algorithmen zur DOA-Schätzung vorgeschlagen, die sich durch eine geringe Rechenkomplexität, Robustheit gegenüber Quellenkorrelation und Flexibilität bezüglich der Wahl der Array-Geometrie auszeichnen. Die Anwendung von CS führt darüber hinaus zu einer erheblichen Reduktion der Hardware-Komplexität, da weniger Empfangskanäle benötigt werden und eine geringere Datenmenge zu verarbeiten und zu speichern ist, ohne dabei wesentliche Informationen zu verlieren.

Im ersten Teil der Arbeit wird das Problem des Modellfehlers bei der CS-basierten DOA-Schätzung mit gitterbehafteten Verfahren untersucht. Ein häufig verwendeter Ansatz um das CS-Framework auf das DOA-Problem anzuwenden ist es, den kontinuierlichen Winkel-Parameter zu diskretisieren und damit ein Dictionary endlicher Größe zu bilden. Da die tatsächlichen Winkel fast sicher nicht auf diesem Gitter liegen werden, entsteht dabei ein unvermeidlicher Modellfehler, der sich auf die Schätzalgorithmen auswirkt.

In der Arbeit wird ein analytischer Ansatz gewählt, um den Effekt der Gitterfehler auf die rekonstruierten Spektra zu untersuchen. Es wird gezeigt, dass sich die Messung einer Quelle aus beliebiger Richtung sehr gut durch die erwarteten Antworten ihrer beiden Nachbarn auf dem Gitter annähern lässt. Darauf basierend wird ein einfaches und effizientes Verfahren vorgeschlagen, den Gitterversatz zu schätzen. Dieser Ansatz ist anwendbar auf einzelne Quellen oder mehrere, räumlich gut separierte Quellen. Für den Fall mehrerer dicht benachbarter Quellen wird ein numerischer Ansatz zur gemeinsamen Schätzung des Gitterversatzes diskutiert.

Im zweiten Teil der Arbeit untersuchen wir das Design kompressiver Antennenarrays für die DOA-Schätzung. Die Kompression im Sinne von Linearkombinationen der Antennensignale, erlaubt es, Arrays mit großer Apertur zu entwerfen, die nur wenige Empfangskanäle benötigen und sich rekonfigurieren lassen. In der Arbeit wird eine einfache Empfangsarchitektur vorgeschlagen und ein allgemeines Systemmodell diskutiert, welches verschiedene Optionen der tatsächlichen Hardware-Realisierung dieser Linearkombinationen zulässt. Im Anschluss wird das Design der Gewichte des analogen Kombinations-Netzwerks untersucht. Numerische Simulationen zeigen die Überlegenheit der vorgeschlagenen kompressiven Antennen-Arrays im Vergleich mit dünn besetzten Arrays der gleichen Komplexität sowie kompressiver Arrays mit zufällig gewählten Gewichten.

Schließlich werden zwei weitere Anwendungen der vorgeschlagenen Ansätze diskutiert: CS-basierte Verzögerungsschätzung und kompressives Channel Sounding. Es wird demonstriert, dass die in beiden Gebieten durch die Anwendung der vorgeschlagenen Ansätze erhebliche Verbesserungen erzielt werden können.

Acknowledgments

My years as a Ph.D. student at Ilmenau University have been one of the most defining moments of my life, during which I grew intellectually and professionally. I would like to thank many who have contributed in more than one way to this journey.

First and foremost, I would like to express my deepest appreciation and sincerest gratitude to my advisor and my mentor, Dr. Florian Römer for his continuous support. I am deeply indebted to him for his enthusiasm, immense knowledge, and kindness that have greatly influenced me in my Ph.D. years. A superb researcher and mentor, he taught me how to accumulate my research skills, tapped into my full potential, as well as build up my confidence step by step in the course of researching. He was always available to help work out the problems whenever I was stuck. I truly take pride in working with him. Without him, this work would have never been possible.

I feel so grateful for Prof. Giovanni Del Galdo, who has led me to this EMS family at the Ilmenau University of Technology since 2013. He has provided me tremendous help. I owe many thanks to him for his encouragement, patience, and guidance. I have learned greatly from his remarkable knowledge both academically and personally.

I also thank Prof. João Paulo C. Lustosa da Costa and Prof. Ahmed El-Mahdy for reviewing my thesis. Their valuable comments and discussions helped me achieve the final version of this thesis.

I would also like to thank all friends, professors and colleagues at the EMS group for the friendly environment during my stay. It has been a great pleasure working with you all. I did learn from you a lot.

I have been fortunate to have many friends outside the university, who have helped me and made my life more enjoyable.

On a more personal note, I wish to dedicate this thesis to my family for their endless and continuous encouragement throughout my life and my studies. My mother, my wife and my daughter, I can not thank you enough for your selfless love and unconditional support, patience, and perseverance over the years. No matter where I am and what I am doing, you are the love of my life for eternity. To you, I dedicate this work.

Contents

Chapter 1

Introduction

The introduction of mobile and wireless communication systems in the late 20th century has radically changed the life of human beings. In a few years time, the wireless communications industry has grown to become one of the largest in the world. The markets show significant growth, and the volumes are high. According to the Ericsson mobility report 2017 [14], the estimated amount of subscribers in 2017 is 7.8 billion, while the expected amount of subscribers for 2023 is 9.1 billion. Moreover, the total mobile data traffic is expected to increase to almost seven times. In addition to the more traditional services such as speech, texting, and video, wireless communication systems can also provide other services to improve the quality of life, including health care, home automation, emergency services and many others.

Since the early days of wireless communication, the simple single antenna has been used to transmit and receive wireless signals. In order to improve the effectiveness of a wireless communication system, an array of antennas can be used to transmit and receive. An antenna array consists of a set of antennas that are located at different points in space with reference to a common reference point. These sensors listen to the incoming signals and provide a means of sampling these signals in space. Compared to single sensor systems, array systems have some crucial advantages. A significant advantage is signal enhancement over noise by appropriate processing of the received signals. Moreover, it allows spatial selection of where to transmit power. This boosts the range of the communication link by focusing the power toward a certain user rather than radiating energy in all directions. Spatial selection also enables frequency reuse, which means that the same frequency can be used by multiple nodes by spatially discriminating between them [15]. Similarly, sensor arrays can be used to monitor the position of a source by tracking its signature as it moves in space.

The sensor array data is then processed to extract useful information. This corresponds to either the content of the signal itself as often found in communications or some parameters related to the recorded data. Array signal processing is used in several application areas such as radar, sonar, wireless communications, radio astronomy, seismology, acoustics, and medical imaging [16,17]. Early contributions to this field have been made mostly in the context of wireless communications and radar systems in the first half of the 20th century. In the second half of the 20th century, the tremendous progress of digital processing hardware led to numerous new developments and applications [18].

A typical objective of array signal processing is to estimate the direction-of-arrival (DOA) of an incoming signal. Through the collection of received time samples and by processing of spatial signals, detection of multiple incoming sources and estimation of their DOAs can be realized [19]. The estimated DOAs are used in various applications like localization of transmitting sources, for direction finding [20,21], massive MIMO and 5G Networks [21,22], channel sounding and modeling [23–26], tracking and surveillance in radar [27], and many others. The major objective in DOA estimation is to develop approaches that allow minimizing the hardware complexity in terms of receiver costs and power consumption while providing a desired level of estimation accuracy and robustness in the presence of multiple sources and/or multiple paths.

Research on DOA estimation using array processing has largely focused on uniform arrays (e.g., linear and circular) [28] for which many efficient parameter estimation algorithms have been developed. The main goal is to locate closely spaced signals in angle, in the presence of high-variance noise and a low number of snapshots. To perform well, all such algorithms require to fulfill certain conditions on the sampling of the wavefront of the incident waves in the spatial domain. Namely, the distance between adjacent sensors should be less than or equal to half a wavelength of the impinging planar wavefronts; otherwise it leads to grating lobes (sidelobes) in the spatial correlation function which correspond to ambiguities in the array manifold. At the same time, to achieve DOA estimation with a high resolution, the receiving arrays should have a relatively large aperture. This implies that arrays with a large number of antennas are needed to obtain a high resolution, which is not always feasible.

It was shown in [29] that if the field is modeled as a superposition of a few planar wave-fronts, the DOA estimation problem can be expressed as a sparse recovery problem and the Compressed Sensing (CS) framework can be applied. Compressive Sensing (CS) [30–32] is a novel paradigm in sampling theory that provides an analytical framework for the sampling of signals below the Shannon-Nyquist sampling rate. In essence, it has been shown that signals can be acquired at sub-Nyquist sampling rates without loss of

information provided they possess a sufficiently sparse representation in some domain and that the measurement strategy is suitably chosen. In particular, guarantees for recovering the signal from a certain number of linear measurements have been derived which have also led to insights on how to determine applicable measurement designs. Recently, compressive sensing has been widely studied and applied to various fields, such as imaging [33, 34], magnetic resonance imaging [35, 36], video processing [37, 38], radar [39–41], analog-to-information conversion [42], sensor networks [43, 44], array processing [45], communications [46, 47], astronomy [48, 49] and biology [50].

Many powerful CS-based DOA estimation algorithms have been proposed in recent years showing tremendous advantages with respect to the hardware complexity of the receiving arrays and the complexity of the numerical solution while being insensitive to source correlation and allowing arbitrary array geometries. However, they all face a common problem. Although the model is sparse in a continuous angular domain, to apply the CS framework we need to construct a finite dictionary by sampling this domain with a predefined sampling grid i.e., the angle space is divided into a large number of grids where the source directions of interest are assumed to exactly lie on some of the grids. However, the target locations in practice are almost surely not located exactly on a subset of these grid points. This leads to a model mismatch that results in the degradation of the performance.

Compressed sensing has also been suggested to be applied in the spatial domain (e.g., array processing and radar) with the main goal to reduce the complexity of the measurement process by using fewer RF chains and storing less measured data without the loss of any significant information. In particular, the CS paradigm can be applied in the spatial domain by employing N antenna elements that are combined using an analog combining network to obtain a smaller number of $M < N$ receiver channels. Since only M channels need to be sampled and digitized, the hardware complexity remains comparably low (e.g., consuming less energy and storing less data) while a larger aperture is covered which yields a better selectivity than a traditional, Nyquist ($\lambda/2$) spaced M-channel antenna array.

The objective of this dissertation is threefold. Firstly, CS based DOA estimation methods exploring sparsity will be studied with the main goal to lift the off-grid model mismatch. We study the problem analytically and propose an efficient CS based DOA estimation technique that works with off-grid sources. Secondly, we propose a compressive array for DOA estimation with a lower hardware complexity and an optimized design for the compressive network. Thirdly, we consider two other applications of the sparse recovery and compressive arrays. The first application is CS based time delay

estimation and the other one is compressive channel sounding. We show that the proposed approaches for sparse recovery off the grid and compressive arrays show significant improvements in the considered applications compared to conventional methods.

Overview and Contributions

The work in this thesis is organized as follows:

Chapter 2 provides the theoretical background for the main topics covered in this thesis namely, compressed sensing (CS) and direction of arrival (DOA) estimation. It starts with a review of the CS theory and its fundamentals, with the aim of providing a summarized, yet a standalone background to this thesis. The fundamentals of DOA estimation are then presented where first the array design essentials are reviewed and then parameter estimation techniques are discussed and summarized. While no novel material is presented in this chapter, its role is essential in agreeing on the notation and concepts addressed in the rest of this work.

Chapter 3 deals with the problem of applying CS techniques to DOA estimation off the grid. We take an analytical approach to investigate the effect of recovering the spectrum of sources not lying on the grid. Unlike earlier works that have provided a quantitative analysis of the approximation error, we examine the specific shape of the resulting spectrum. We show that for one off-grid source the recovered spectrum is not sparse but it can be well approximated by the closest two dictionary atoms on the grid and their coefficients can be exploited to estimate the grid offset. We then extend our model to consider multiple sources. In the second part of the chapter, a full polarimetric CS based DOA estimator (also off the grid) is proposed. Almost all CS based DOA estimation techniques consider a non-polarimetric model which can lead to entirely useless estimation results. We show that our polarimetric CS based model can estimate both the DOA and the polarization state of each individual path with very high accuracy. The results shown in this chapter have been published in [1–3].

Chapter 4 discusses the design and the performance of compressive arrays employing linear combinations in the analog domain by means of a network of power splitters, phase shifters, and power combiners. We present a basic receiver architecture of such a compressive array and introduce a generic system model that includes different options for the hardware implementation. Importantly, the model reflects the implications for the noise sources. Based on the generic system model we then discuss the design of the combining matrix, with the goal to obtain an array that is suitable for DOA estimation (i.e., minimum variance of DOA estimates and robustness in terms of low side lobe levels

or low probability of false detections). We propose two design approaches. The first is based on the spatial correlation function which is a low-complexity scheme that in certain cases even admits a closed-form solution. The second is based on the minimization of the Cramér-Rao Bound (CRB). We show by numerical simulations that both of the proposed design approaches have a significant performance improvement compared to the state of the art, namely an array with a randomly chosen combining matrix and a sparse array with optimized sensor positions. The results proposed in this chapter are published in [4–9].

Chapter 5 extends the ideas from the previous chapters applying them to time delay estimation (TDE) and synchronization. We first treat the special case of estimating the delay of a signal with a known pulse shape from a noisy superposition of several delayed copies. The main contribution of the first part of the chapter is an optimization based design for the measurement kernels of the CS based TDE architectures. We demonstrate numerically that the proposed optimized CS kernels outperform a randomly chosen one in terms of the delay estimation accuracy. In the second part of the chapter, we turn our attention to synchronization of the TDE network. We proposed a CS based reference broadcast synchronization where the reference signal is an opportunistic signal already in the system (e.g., FM or TV signals). We show that using CS, the correlation can be calculated in the compressed domain, yet achieving a correlation characteristics comparable to the high bandwidth correlation obtained with opportunistic signals. The ideas discussed in this chapter have been published in [10–12].

Chapter 6 exploits the application of CS to the double-directional channel sounder in the spatial domain that includes joint DOA/DOD estimation. Extending the ideas of compressive arrays discussed in Chapter 4, a compressive spatial channel sounder is proposed and evaluated based on real scenarios showing superior advantages in terms of time, hardware complexity and resolution. In particular, the proposed approach reduces the total number of switching periods, which implies a reduced channel acquisition time and thus an improved Doppler bandwidth. On the other hand, the compressive approach reduces the number of RF chains, which is a very relevant advantage in terms of the overall receiver complexity, the amount of data to be processed in the digital domain (e.g., FPGA), power consumption, as well as RF hardware calibration. Alternatively, for the same measurement time and/or hardware complexity, one can increase the number of array elements to cover a larger aperture and so achieving better performance in terms of resolution. The ideas presented in this chapter are published in [13].

Chapter 7 concludes the work presented and summarizes the main contributions of this thesis providing directions for future work.

Chapter 2

Background

This chapter overviews some background of the two main topics related to the research contributions presented in this thesis: Compressive Sensing (CS) and Direction of Arrival (DOA) estimation. In Section 2.1, the CS theory is first reviewed where the underlying principles are presented and the main concepts are explained. Afterwards, we turn our attention to the DOA estimation problem using antenna arrays in Section 2.2. We start by deriving the array signal model and then the main parameter estimation techniques used for DOA estimation are discussed and compared. Due to the large volume of existing literature, the chapter here is only directly related to the current thesis and is by no means a complete treatment of all past work.

2.1 Compressive Sensing

We live in an analog world. Most natural phenomena are the representation of variations in physical quantities in any given time. These parameters include electricity, temperature, light, sound and pressure among others. With the invention of transistors and microprocessors around 1950, the digital revolution started and it was reported in 2014 that more than 99% of the world's technologically stored information is in digital format [51]. Digital technology allows information to be copied and replicated precisely. It is due to digital technology that our society is now so defined by computers, smartphones, internet access, and cell phone communication. The Digital Revolution, in fact, marks the beginning of a new age: the Information Age [52].

To go from analog to digital, we rely on two main principles: sampling and quantization. This conversion is achieved via an Analog-to-Digital Converter (ADC), which is an electronics component present in any digital device that processes an analog input signal. The ADC converts an analog signal to a discrete time signal and a discrete

amplitude signal. Through sampling, the ADC transforms the continuous signal with an infinite number of possible values to a finite number of samples. Furthermore, the ADC must quantize the input signal, meaning that every sample must be represented by a value from a finite set of possible values [53].

Sampling theorems provide conditions required for lossless conversion between the continuous and the discrete-time worlds for digital signal processing. For many years, signal processing has been relying on the well-known Nyquist/Shannon sampling theorem [54, 55], stating that the sampling rate must be at least twice as high as the highest frequency to avoid losing information while capturing the signal.

Such strategy faces difficulties in the acquisition of wideband signals where the required sampling rates exceed the limits of state-of-art commercial ADC systems. The hardware implementation of devices to obtain such high resolution (in image acquisition for example) requires very complex designs with very high costs. Moreover, it might not be possible to store all the data because of limited storage, or the data amount might be too large to be processed so that it becomes necessary to apply compression methods to get rid of the redundant information and keep the minimum information required for almost perfect reconstruction [56]. This means that very complex ADC devices are deployed to acquire samples of the signal and then compression techniques are applied to dump most of these samples since only a few of them are significant for recovery.

In [57] the authors show that it is possible to lower the necessary sampling rate and still attain a desired level of information if the information rate is much lower than the actual signal dimensionality. For example, an image of a million pixels has a million degrees of freedom. However, a typical image is very sparse or compressible over the wavelet basis, namely, very likely only a small fraction of wavelet coefficients, say, one hundred thousand out of a million wavelet coefficients, are significant in recovering the original images, while the rest of wavelet coefficients are discarded in many compression algorithms.

In the last decade, a new theory of compressive sensing (CS), also known under the terminology of compressed sensing or compressive sampling, has considerably drawn the attention of researchers. It builds a fundamentally novel approach to data acquisition and compression which overcomes drawbacks of the traditional method. In his famous paper [30], Donoho posed the ultimate goal of merging compression and sampling. Instead of acquiring all the signal data to through it away afterwards, it was suggested to directly measure the part that will not end up being thrown away. This was the fundamental idea for which the field of compressive sensing has emerged. In 2006, Donoho, Candès, Romberg and Tao [30–32] conducted a series of in-depth research based on the

discovery that a signal may still be recovered even though the number of data is deemed insufficient by Shannon's criterion, and built the theory of compressive sensing. Instead of acquiring this large number of samples and then compressing them, obtain only these few non-zero coefficients directly. In other words, compress the data while sampled.

Recently, compressive sensing has been widely studied and applied to various fields, such as imaging [33, 34], magnetic resonance imaging [35, 36], video processing [37, 38], radar [39–41], analog-to-information conversion [42], sensor networks [43, 44], array processing [45], communications [46, 47], astronomy [48, 49] and biology [50].

In this section, we will display the main theoretical results of the compressive sensing paradigm together with the main underlying principles. We start in Section 2.1.1 by briefly describing the traditional sampling approach. Afterwards, we discuss the three main principles underlying the CS theory: sparsity in Section 2.1.2, incoherent measurements in Section 2.1.3 and sparsity based non-linear recovery in Section 2.1.4.

2.1.1 Conventional Sampling

Figure 2.1 shows the process of conventional Nyquist-Rate sampling. A source emits a signal $\boldsymbol{x} \in \mathbb{C}^{N\times 1}$ which is an N dimensional complex signal. In the noiseless case, N linear measurements $\boldsymbol{y} \in \mathbb{C}^{N\times 1}$ are taken using an $N \times N$ measurement ensemble $\boldsymbol{\Phi}$, i.e.,

$$\boldsymbol{y} = \boldsymbol{\Phi} \cdot \boldsymbol{x}. \tag{2.1}$$

Afterwards, the obtained signal $\boldsymbol{y}$ can be analyzed and processed digitally where traditional compression techniques (e.g., JPEG [58]) can be applied to get rid of the redundancy and keep only the $M < N$ significant coefficients sufficient for the signal's recovery.

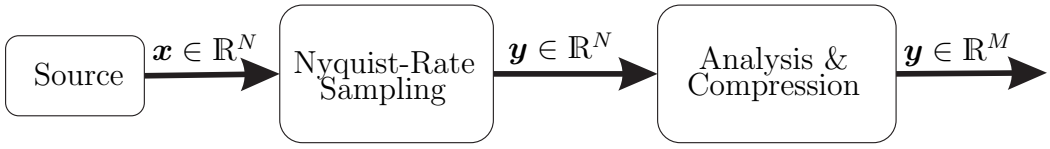

Figure 2.1: Conventional Nyquist-Rate Sampling

Conventional Nyquist-Rate sampling suggests that N linearly independent measurements are required for the exact recovery of an arbitrary signal $\boldsymbol{x}$. The matrix $\boldsymbol{\Phi}$ should be a square matrix that has a full rank, i.e., its columns are linearly independent and span an N dimensional subspace. Therefore, it can be used to represent all possible signals in $\mathbb{C}^N$ and each signal has one unique representation. In such a case, if $\boldsymbol{y}$ and

$\boldsymbol{\Phi}$ are given and $\boldsymbol{\Phi}$ has full rank, $\boldsymbol{x}$ can be obtained by solving the system of linear equations, which is equivalent to multiplying $\boldsymbol{y}$ with the inverse of $\boldsymbol{\Phi}$ denoted $\boldsymbol{\Phi}^{-1}$.

If $M < N$ measurements are taken, the problem becomes underdetermined and the measurement cannot be uniquely inverted. This is where the CS theory comes into play suggesting the possibility to solve such an ill-posed, underdetermined problem promising to reconstruct a signal accurately and efficiently from a set of a few non-adaptive linear measurements $M \ll N$. Figure 2.2 shows the CS scheme. The compressed signal $\boldsymbol{y} \in \mathbb{R}^M$ can be directly acquired from the signal of interest $\boldsymbol{x} \in \mathbb{R}^N$ via an $M \times N$ compressive measurement ensemble $\boldsymbol{\Phi}$. To get back the original signal $\boldsymbol{x}$ from the compressed signal $\boldsymbol{y}$, non-linear recovery techniques are employed.

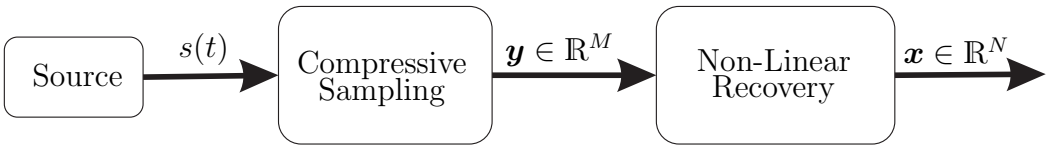

Figure 2.2: Compressive Sensing Architecture

In this sense, the CS theory counts on three key elements: sparsity (Section 2.1.2), incoherent measurements (Section 2.1.3) and non-linear recovery (Section 2.1.4). Sparsity screens out the signal of interest, while incoherence restricts the sensing schema. Specifically, a large but sparse signal $s(t)$ is encoded by a relatively small number of incoherent linear measurements $\boldsymbol{y} \in \mathbb{R}^M$. Using non-linear recovery algorithms, the original signal can be reconstructed from the encoded sample by finding the sparsest signal from the solution set of an underdetermined linear system. Each of these principles is comprised of a dense, rapidly evolving literature of which only the fundamentals are reviewed in the following sections of this chapter as a basic background for this thesis.

2.1.2 Sparsity

Sparsity is the signal structure behind many compression algorithms that employ transform coding and is the most famous signal structure used in CS.

Definition 1. *The ℓ_p-norm of a vector signal $\boldsymbol{x}$ is defined as*

$$\|\boldsymbol{x}\|_p = \left(\sum_{n=1}^{N} \|x_n\|^p \right)^{(1/p)} \text{ for } p \geq 1. \tag{2.2}$$

At times a quasinorm such as ℓ_0 is also used, which cannot be used in the above

formula, but which corresponds only to counting all the non-zero entries in the vector $\boldsymbol{x}$.

Definition 2. *A signal $\boldsymbol{x} \in \mathbb{C}^{N\times 1}$ is said to be K-sparse for some $K \in \mathbb{N}$, if at most K of its entries are non-zero, i.e., if $\|\boldsymbol{x}\|_0 \leq K$.*

The use of sparsity as a model for signal processing dates back to Donoho and Johnstone's initial works in the early 1990s [59], where wavelet-sparse signals and images were denoised by assuming that the noiseless version of the signal is sparse. Since then, many mathematicians, applied mathematicians, and statisticians have employed sparse signal models for applications that include signal enhancement and super resolution, signal deconvolution, and signal denoising [60].

Sparse representations are the core tenet of compression algorithms based on transform coding. In transform coding, a sparse signal $\boldsymbol{x}$ is compressed by obtaining its sparse representation $\boldsymbol{s}$ in a suitable basis $\boldsymbol{\Psi}$ and encoding the values and locations of its nonzero coefficients. Transform coding is the foundation of most commercial compression algorithms; examples include the JPEG image compression algorithm, which uses the discrete cosine transform [58], and the JPEG2000 algorithm, which uses the discrete wavelet transform [61].

While transform coding algorithms are able to encode sparse signals without distortion, the signals that we observe in nature are not exactly sparse, but rather compressible.

Definition 3. *For a signal $\boldsymbol{x} \in \mathbb{C}^{N\times 1}$, some $K \in \mathbb{N}$ and some $p \geq 1$, we define the K-term approximation error of $\boldsymbol{x}$ with respect to the p-norm as*

$$\sigma_K(\boldsymbol{x})_p := \min_{\hat{\boldsymbol{x}}\in\boldsymbol{\Sigma}_K} \|\boldsymbol{x} - \hat{\boldsymbol{x}}\|_p, \tag{2.3}$$

where $\boldsymbol{\Sigma}$ denotes the set of all K-sparse vectors $\in \mathbb{C}^{N\times 1}$.

A signal is called compressible if there exists a good K-term approximation $\boldsymbol{x}_K$ with a fast decaying approximation error σ_K for some $p \geq 1$, i.e., most of its energy is concentrated around no more than K entries.

While a widely accepted standard, the sample-then-compress ideology behind transform coding compression suffers from three inherent inefficiencies: First, we must start with a potentially large number of samples N even if the ultimate desired K is small. Second, the encoder must compute all of the N transform coefficients $\boldsymbol{s}$, even though it will discard all but K of them. Third, the encoder faces the overhead of encoding the locations of the large coefficients.

One would think intuitively to acquire just a few linear measurements proportional to the signal sparsity K. This is indeed correct, but the difficulty is determining in which lower dimensional subspace such a signal lies [62]. That is, we may know that the signal has a few non-zero coordinates, but we do not know which coordinates those are. It is thus clear that we may not reconstruct such signals using a simple linear operator, and that the recovery requires more sophisticated techniques.

2.1.3 Incoherent Measurements

Assume now that $\boldsymbol{x}$ is sparse in a domain $\boldsymbol{\Psi}$, where $\boldsymbol{\Psi}$ is an $N \times N$ basis matrix. This means that $\boldsymbol{x}$ has only K non-zero elements with $K \ll N$. If the positions of the non-zero coefficients of $\boldsymbol{x}$ were known in advance, we could reconstruct it from exactly K linear measurements, i,e, each row of $\boldsymbol{\Phi}$ can be set to zero everywhere but at the position of a non-zero entry of $\boldsymbol{x}$.

This is exactly where the theory of CS comes into play. It introduces measurement and reconstruction strategies so that $M \ll N$ linear measurements are sufficient for exact reconstruction of K-sparse signals where $K \leq M$. The CS measurement process can be described as a linear projection of the signal vector into a set of carefully chosen projection vectors that gathers all (or most of) the information contained in the signal. Each measurement of a signal should give some global information. With incoherent measurements, every measurement gives a little bit of information that adds up to give the whole information content of the signal of interest [63].

The measurement matrix $\boldsymbol{\Phi}$ is then a "fat" matrix with much fewer rows than columns, and the system(2.1) is massively underdetermined with infinitely many solutions. The matrix does not constitute an isometry for all input vectors $\boldsymbol{x}$. However, near-isometry is possible if only a subset of input vectors is allowed, which is the case when assuming only sparse signals.

Definition 4. *A matrix $\boldsymbol{\Phi} \in \mathbb{C}^{M \times N}$ is said to satisfy the restricted isometric property (RIP) of order $K \in \mathbb{N}$, if there exists a constant $0 \leq \delta < 1$ such that*

$$(1 - \delta_K)\|\boldsymbol{x}\|_2^2 \leq \|\boldsymbol{\Phi} \cdot \boldsymbol{x}\|_2^2 \leq (1 + \delta_K)\|\boldsymbol{x}\|_2^2 \tag{2.4}$$

holds for every K-sparse $\boldsymbol{x} \in \boldsymbol{\Sigma}_K$.

The smallest such constant is denoted by σ_K, and is called the restricted isometric constant (RIC) of $\boldsymbol{\Phi}$. If the RIC of a matrix $\boldsymbol{\Phi}$ is small (i.e., as close to 0 as possible), the restriction of $\boldsymbol{\Phi}$ to any subset of K columns behaves analogously like an isometry.

This theorem is very important because it means that if a matrix $\mathbf{\Phi}$ can be found that satisfies the RIP of order $2K$, it will approximately preserve the distance between any pair of K-sparse input vectors with respect to some constant σ_K.

It is important to mention that testing this property for a generic sensing matrix requires the computation of the singular values of all its $\binom{N}{K}$-column submatrices, and is non-deterministic polynomial-time (NP)-hard [64], which makes it practically not feasible to design an appropriate measurement matrix based only on this criteria.

Another method to assess the information-preserving properties of sensing matrices is the coherence (also mutual coherence) which can be defined as follows [65]

Definition 5. *The coherence of a matrix $\mathbf{\Phi}$, $\mu(\mathbf{\Phi})$, is the largest inner product between any columns $\boldsymbol{\phi}_i, \boldsymbol{\phi}_j$ of $\mathbf{\Phi}$:*

$$\mu(\mathbf{\Phi}) = \max_{1 \leq i < j \leq N} \frac{\left| \boldsymbol{\phi}_i^{\mathrm{H}} \cdot \boldsymbol{\phi}_j \right|}{\|\boldsymbol{\phi}_i\|_2 \cdot \|\boldsymbol{\phi}_j\|_2}. \tag{2.5}$$

In fact, it is possible to relate the RIP property and the coherence [66], but they can give different insights about the measurement ensemble. Coherence is essentially an index of linear dependence between the columns of $\mathbf{\Phi}$ and should be made as small as possible as to guarantee the recoverability of sparse vectors. Contrarily to the RIP, coherence, however, has the benefit of being computable on any instance of $\mathbf{\Phi}$, and is also related to the performances of many signal recovery algorithms [65]. It is therefore recommended as a figure of merit that should be made as small as possible to guarantee that a generic $\mathbf{\Phi}$ allow for the recovery of a sparse vector $\boldsymbol{x}$.

The next question therefore is, which matrices satisfy the RIP and/or the coherence conditions to ensure informative sensing. Such matrices should be non-adaptive, i.e., independent of the sparse dictionary $\mathbf{\Psi}$. In 2006 though, the groundbreaking work of Candés, Romberg and Tao [31, 32] and Donoho [30] came to the rescue. By using the concept of randomness, they were able to define a class of matrices that, with very high probability, will satisfy the RIP and enjoy low coherence properties. Since then, many such classes of matrices have been identified and proven to satisfy the required conditions [67, 68].

For example, consider Gaussian random matrices, i.e. matrices where the entries are identically and independently distributed Gaussian random variables with mean 0 and variance $1/M$, or Bernoulli random matrices, where the entries take the value $+1/\sqrt{(}M)$ or $-1/\sqrt{(}M)$ with equal probability. It can be shown that such matrices satisfy the RIP of some order K with small RIC σ_K with very high probability if the number of rows is chosen large enough [67]. In many of the theory-building work in

CS, Gaussian or Bernoulli random matrices are used. In practice, though, they are of limited use for several reasons. For example, in some applications, the design of the measurement matrix is constrained by physical or other conditions. Also, these matrices do not allow a fast matrix multiplication, which typically has to be performed quite often in practical applications. Therefore, structured random matrices are often preferred [44, 69]. In the following subsection, we review state-of-the-art measurement matrix design for compressive sensing.

2.1.3.1 Measurement Matrix Design

So far many of the CS schemes employ the Gaussian or Bernoulli matrix for their measurement matrix design or optimization. However, as proposed in [70], the Gaussian random matrix, typically used in the CS problems, is not necessarily the best choice for a given basis matrix in terms of the coherence of column pairs in the sensing matrix. Furthermore, in many applications, it is difficult for designers to generate and control a perfect Gaussian random matrix in physical electric circuit with its randomness being well guaranteed. Moreover, there is no efficient algorithm testing the RIP of a random matrix, even though it does satisfy the RIP with overwhelming probability. The question to be asked next, therefore, is whether we can do better than random. Do there exist principled and mathematically founded ways to find matrices that are 'optimal', in some sense, for recovery using compressive sensing methods?

Compared with random sensing matrices, deterministic ones can get rid of these drawbacks. They can be generated on the fly to save storage space and the RIP is often easy to verify. In addition, by exploiting specific structures of deterministic matrices, fast algorithms can be designed to enhance the efficiency of recovery. Many efforts indeed have been excelled to model the way the samples are acquired in practice, which leads to sensing matrices that inherit their structure from the real world.

Early efforts were trying to implement such random measurement ensembles practically. An early trial to implement random compressive measurements is the so called random filter [71]. The approach captures a signal by convolving it with a random-tap FIR filter and then downsampling the filtered signal to obtain a compressed representation. The random filter is generic enough to summarize many types of compressible signals. At the same time, the random filter has enough structure to accelerate measurement and reconstruction algorithms.

One of the earliest works to address the matrix design question is the work of Elad [72] attempting to iteratively decrease the average mutual coherence using a shrinkage operation followed by a singular value decomposition (SVD) step. Another method [73]

involved a design of sensing matrix entries by minimizing the Frobenius norm of the departure of the Gram matrix of the effective dictionary from the identity matrix. There have been many efforts for compressive sensing design since, all using the coherence as a goodness criterion for sensing matrices. In [74], the authors apply non-uniform sampling, by segmenting the input signal and taking samples with different rates from each segment. In a following work [75], they propose a gradient based method to optimize a randomly selected measurement matrix to decrease the coherence. The proposed algorithm aims at minimizing a cost function in an alternating scheme. Overall, the results of these methods show enhancement in terms of both reconstruction accuracy and the maximum allowable sparsity that CS can recovery.

In [76], DeVore uses polynomials over finite fields to construct binary sensing matrices with a prime power that satisfy the RIP. Connection to coding theory has been similarly exploited in [77] proposing a deterministic compressive sensing matrix that comes by design with a very fast reconstruction algorithm, in the sense that its complexity depends only on the number of measurements and not on the signal dimension. The matrix construction is based on the second order Reed-Muller codes and associated functions. This matrix does not have RIP uniformly with respect to all K-sparse vectors, but it acts as a near isometry on K-sparse vectors with very high probability. It was shown in [78] that such constructions satisfy the statistical RIP. The statistical RIP is weaker than the RIP and guarantees recovery of all but an exponentially small fraction of sparse signals. In [79], binary matrices are constructed by exploiting hash functions and extractor graphs. In [80–82], it was shown how random dense matrices could be replaced by the adjacency matrices of an optimized family of expander graphs, thereby reducing the space complexity of matrix storage and, more important, the time complexity of recovery to a few very simple iterations. In [83], a new connection between orthogonal optical codes and the RIP have been introduced, towards the construction of binary sampling matrices. A design for bipolar matrices has been proposed using linear binary correction codes, especially BHC codes. Another work proposed chirp sensing codes towards obtaining a deterministic CS measurement matrix with recovery guarantees and fast decoding [84].

In [35], which is an application to magnetic resonance imaging (MRI), the authors define an incoherence criterion based on point spread functions (PSF) and propose a Monte Carlo scheme for random incoherent sampling of this type of data. In [85], they propose a variable density sampling strategy by exploiting the prior information about the statistical distributions of natural images in the wavelet domain. Their proposed method is computationally efficient and can be applied to several transform domains. [86]

applies coherence minimization to design structured matrices for the Coded Aperture Snapshot Spectral Imaging (CASSI) system [87,88]. [89] and [90] apply coherence based design to environmental sounds and electromagnetic compressive sensing applications respectively.

In [91–93], the use of Toeplitz and circulant structures as CS matrices was proposed inspired by applications in communications where a sparse prior is placed on the signal to be estimated, such as a channel response or a multiuser activity pattern. When compared with generic CS matrices, subsampled circulant matrices have a significantly smaller number of degrees of freedom due to the repetition of the matrix entries along the rows and columns. However, it is was shown that it is possible to employ different probabilistic tools to provide guarantees for subsampled circulant matrices. The results still require randomness in the selection of the entries of the circulant matrix.

In the context of Radar and MIMO Radar, an adaptive computational framework for optimizing the transmission waveform and Gaussian random measurement matrix separately and simultaneously was introduced in [94], incorporating the target scene information for optimization. The framework leads to smaller cross-correlations between different target responses but has to bear great computation load when the scene is varying fast. The work in [70] proposed two approaches: the first one minimizes a performance penalty which is a linear combination of the coherence of the sensing matrix (CSM) and the inverse signal-to-interference ratio (SIR). It aims at improving the SIR and reducing the coherence of the sensing matrix at the same time. The second one, aiming at improving SIR only, imposes a structure on the measurement matrix and determines the parameters involved. It requires carefully chosen waveforms to guarantee the desired CS performance. Their simulation showed that the two measurement matrices with the proper waveform could improve detection accuracy as compared to the Gaussian random measurement matrix (GRMM).

In this thesis, we are interested in deterministic as opposed to random sampling (sensing) matrices. Practically, deterministic sampling matrices are useful because the sampler has to be a deterministic matrix; although random matrices perform quite well on the average, there is no guarantee that a specific realization works. Moreover, by proper choice of the matrix, we might be able to improve some features such as computational complexity, compression ratio and estimation quality. We propose design methodologies for constructing measurement matrices and compare them to random ones.

2.1.4 Non-Linear Recovery

Restricting ourselves to the case of sparse signals, and using the proposed informative, incoherent measurement ensembles, there are still infinitely many solutions to our acquisition problem $\boldsymbol{y} = \boldsymbol{\Phi} \cdot \boldsymbol{x}$. Classically one solves this type of inverse problem by finding the least squares solution to this equation, i.e., solving the problem

$$\min \|\boldsymbol{x}\|_2 \quad \text{subject to} \quad \boldsymbol{\Phi} \cdot \boldsymbol{x} = \boldsymbol{y}, \tag{2.6}$$

which has a convenient closed form solution given by $\hat{\boldsymbol{x}} = (\boldsymbol{\Phi} \cdot \boldsymbol{\Phi}^H)^{-1} \cdot \boldsymbol{\Phi}^H \cdot \boldsymbol{y}$. However, the solution is always wrong as it is almost never sparse.

Alternatively, an intuitive strategy would be to simply choose the sparsest vector that is consistent with the measurements, i.e., to solve the ℓ_0-norm minimization [1] problem

$$\min \|\boldsymbol{x}\|_0 \quad \text{subject to} \quad \boldsymbol{\Phi} \cdot \boldsymbol{x} = \boldsymbol{y}. \tag{2.7}$$

Unfortunately, the ℓ_0-norm is not convex and the problem is NP hard [95] and cannot be solved in a tractable amount of time. The CS way of getting around is to study the convex relaxation of that problem, i.e., solve the ℓ_1-norm minimization problem (the closest convex p-norm) [96]

$$\min \|\boldsymbol{x}\|_1 \quad \text{subject to} \quad \boldsymbol{\Phi} \cdot \boldsymbol{x} = \boldsymbol{y}, \tag{2.8}$$

which is a convex problem that is widely used and computationally tractable. It is widely known as the basis pursuit (BP) [97, 98].

The incentive for using this norm, rather than e.g., the ℓ_2-norm is because it is also sparsity enforcing. BP utilizes the geometry of the octahedron to recover the sparse signal. It is clear in Figure 2.3 that the ℓ_1 constraint, which corresponds to the diamond shape, is more likely to produce an intersection with the solution space (i.e., the black line in our case) that has one component of the solution is zero (i.e., the sparse model). This is not the case for the circular ℓ_2 ball.

In the more practical case, the measurements are subject to noise sources and so the measurement vector can be written as $\boldsymbol{y} = \boldsymbol{\Phi} \cdot \boldsymbol{x} + \boldsymbol{n}$, where $\boldsymbol{n}$ represents an additive noise vector. This suggests relaxing the equality condition $\boldsymbol{y} = \boldsymbol{\Phi} \cdot \boldsymbol{x}$ to an inequality constraint admitting some uncertainty between the measurements and the actual solution. This

[1] Although this is known as the ℓ_0-norm, it is not a real norm.

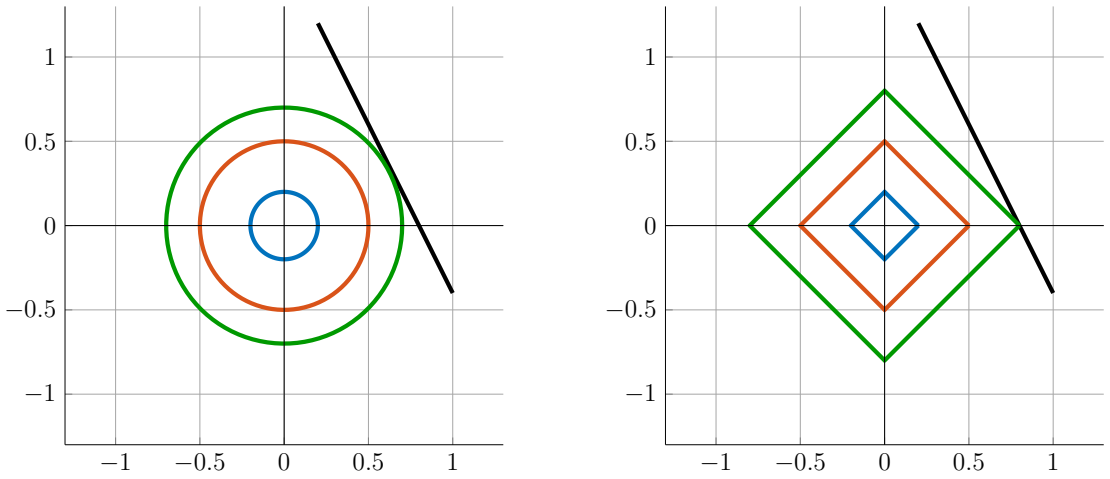

(a) ℓ_2-norm recovery **(b)** ℓ_1-norm recovery

Figure 2.3: Geometric Comparison of ℓ_2 and ℓ_1- minimization for a 2 dimensional sparse signal recovery.

strategy is usually called basis pursuit denoising (BPDN) defined as

$$\min \|\boldsymbol{x}\|_1 \quad \text{subject to} \quad \|\boldsymbol{\Phi} \cdot \boldsymbol{x} - \boldsymbol{y}\|_2 \leq \epsilon, \tag{2.9}$$

where ϵ is an upper bound on the noise level. It can also be further relaxed and formulated as a least absolute shrinkage and selection operator (LASSO) [99]

$$\min \|\boldsymbol{\Phi} \cdot \boldsymbol{x} - \boldsymbol{y}\|_2 \quad \text{subject to} \quad \|\boldsymbol{x}\|_1 \leq \epsilon. \tag{2.10}$$

The recoverability of a signal from incomplete and incoherent (i.e., random) measurements using the aforementioned recovery algorithms, i.e., (2.8) and (2.9), has been discussed thoroughly in literature and many recovery guarantees in terms of the coherence [100] and RIP [101, 102] have been provided.

By now there are many different algorithms solving (2.8) and (2.9) at a feasible computational complexity and acceptable runtime [103,104]. In general, the ℓ_1-minimization approach provides uniform guarantees over all sparse signals and also stability and robustness under measurement noises and approximately sparse signals, but relies on optimization which has relatively high complexity. For example, with standard linear programming, the complexity of grows cubic in the problem dimension N. In many applications which involve very large dimension processing, these approaches are not optimally fast.

Another family of algorithms is the greedy types which have obtained a lot of attention for sparse recovery and compressive sensing. Here, the support of the unknown

signal is recovered iteratively. One calculates the support of the signal and it makes the locally optimal choice at each time to build up an approximation. This is repeated until the criterion is fulfilled. Once the support of the signal is computed correctly, the pseudo-inverse of the measurement matrix restricted to the corresponding columns can be used to reconstruct the actual signal [105]. The clear advantage of such approaches are speed and ease of implementation. The most prominent examples are the matching pursuit (MP) [65], the orthogonal matching pursuit (OMP) [106, 107], the stagewise orthogonal matching pursuit (SOMP) [108] and the compressive sampling matching pursuit (CoSaMP) [109]. A special class of greedy algorithms is the one with iterative thresholding performing some thresholding function on each iteration [110, 111].

The drawback of greedy algorithms is that they are not as easy to derive general performance bounds for. However, they are most often significantly faster and may rival the recovery performance of ℓ_1-norm minimization algorithms in many cases. Furthermore, it is fairly easy to incorporate further structure, beyond dictionary-based sparsity, into the reconstruction with greedy algorithms than it is to do so with convex optimization algorithms [112]. Another significant difference is that greedy algorithms often assume known sparsity K. The sparsity may be estimated or assumed known, but this is nonetheless a drawback.

In this thesis, both families are used and explicitly specified (and sometimes compared) where needed.

2.1.4.1 Recovery off the Grid

In a standard CS framework, signal recovery is often performed on a discrete sampling grid. Thus, to apply the CS framework we need to construct a finite dictionary by sampling the required domain with a predefined sampling grid. That also implies that the target signal under investigation is assumed to have entries only on the grid points. In reality, the positions can never be exactly at the computational grid points. No matter how large the size of the grid is, the actual field will not place its sources on the center of the grid points. This means the signal is actually not sparse in the basis defined by the grid. This leads to a model mismatch causing a degradation of the performance. That is one of the main challenges towards applying sparse signal recovery for compressive sensing.

In [113, 114] the effect of the basis mismatch problem on the reconstruction performance of CS has been analyzed and the resultant performance degradation levels and analytical norm error bounds due to the basis mismatch have been investigated. The work of [114] describes the grid mismatch problem and proposes a model for it. The

authors also illustrate the effect for the discrete Fourier transform (DFT) matrix and discuss the bounds on the errors for the basis pursuit (BP) solution. In [113], the authors propose the errors in variables (EIV) model for modeling the error in the model matrix and also give error bounds for the BP solution.

One natural solution to such a problem is to improve the sampling to provide a sufficiently "dense" grid and so reducing the offgrid error as much as possible. However, relative to the gained accuracy, the additional computational burden is high and the classical convex methods are frequently reported to run into numerical problems. On the other hand, aiming for an increasingly dense sampling of the parameter space introduces performance issues in sparsity-leveraging algorithms. In particular, increasing the resolution of the parameter sampling worsens the coherence of the dictionary that provides sparsity for relevant signals [115]. This both prevents certain algorithms from finding the sparse representation successfully and introduces ambiguity on the choice of representations available for a signal in the dictionary.

Many grid-based methods have been proposed to alleviate the drawbacks of the finite discretization with affordable computational workloads. In [116], the dictionary is extended to several dictionaries and solution is pursued not in a single orthogonal basis, but in a set of bases using a tree structure, assuming that the given signal is sparse in at least one of the basis. In the Continuous Basis Pursuit approach [117], perturbations are assumed to be continuously shifted features of the functions on which the sparse solution is searched for, and ℓ_1 based minimization is proposed. Also in this method, perturbations are assumed to have structures that are modeled with a first order Taylor approximation or polar interpolators. In [118], ℓ_1-minimization based algorithms are proposed for linear structured perturbations on the sensing matrix. In [119], a total least square (TLS) solution is proposed for the problem, in which an optimization over all signals $\boldsymbol{x}$, perturbation matrix $\boldsymbol{P}$ and error vector spaces should be solved. To reduce complexity, suboptimal optimization techniques have been proposed. In [120], the perturbed orthogonal matching pursuit (POMP) algorithm is presented where controlled perturbation mechanism is applied on the selected columns of each OMP iteration. The selected column vectors are perturbed in directions that decrease the orthogonal residual at each iteration. Proven limits on perturbations are obtained. In [121], an algorithm based on the off-grid model from a Bayesian perspective for CS based DOA estimation is proposed with a reduced computational complexity of the signal recovery process and a lower sensitivity to noise.

Since the gridding introduces significant complications and has no proper physical justification, it would be highly desirable to eliminate it and work with a grid-free

continuous representation. In fact, recent developments in the mathematical literature have addressed sparse recovery in the continuous domain without introducing a grid [122]. The first gridless sparse method for frequency estimation is introduced in [123] where the authors sidestep the issues arising from discretization by working directly on the continuous parameter space. They propose estimating the continuous frequencies and amplitudes of a mixture of complex sinusoids from partially observed time samples based upon atomic norm minimization [124]. They show how the atomic norm for moment sequences can be derived either from the perspective of sparse approximation or rank minimization and prove that atomic norm minimization achieves nearly optimal recovery bounds. The noiseless complete data case is studied where it is shown that the frequencies can be exactly recovered provided that they are appropriately separate. The bounded energy-noise case is then studied in [125]. An atomic norm soft thresholding (AST) method is presented in [126] in the presence of stochastic noise which is then generalized in [127] where also a gridless version of sparse iterative covariance-based estimation SPICE [128] is proposed.

2.2 Direction of Arrival Estimation

Direction of arrival (DOA) estimation has been an active field of research for many decades [19]. Estimated DOAs are used in various applications like localization of transmitting sources, for direction finding [20, 21], massive MIMO and 5G Networks [21, 22], channel sounding and modeling [23–26], tracking and surveillance in radar [27], and many others.

The main objective of the DOA estimation or source localization problem is to estimate the spatial energy spectrum and therefore determine the location of the sources of energy. To do this, temporal and spatial information is first obtained by sampling the wave field with sensor arrays and then processed with the aim to reveal the directions of the emitting sources that form this wave field. Its origins date back to the 1940s when the first attempt on spectral analysis using spatio-temporally sampled data was conducted [15]. From then onwards, there has been ongoing research in the field of source localization with the goal of developing methods that do not only yield accurate estimates under ideal conditions, but more importantly are robust to non ideal conditions such as noisy measurements, limitations on the number of measurements, the aperture size of the array or the number of sensors.

What follows serves as a brief introduction to the problem of DOA estimation of sources that impinge on a linear array of sensors. After the formal description of the

conventional array signal model in Section 2.2.1, an overview of the most popular DOA parameter estimation methods from the field of array processing is given in Section 2.2.2.

2.2.1 The Array Signal Model

In the section, we develop the model used to describe the signals received at an array of sensors with distinct spatial locations, due to the emission or reflection of signal energy from certain sources.

Consider an arbitrary array (i.e., arbitrary locations and arbitrary directional characteristics) of M sensors with inter-element spacing d. The sensors sample spatially the wave field, which is assumed to be generated by a finite number of emitting sources. The sources are assumed to have negligible extent relative to the aperture size of the array so that they can be modeled as point sources. The medium is considered homogeneous and therefore the propagating speed is constant. The propagating waves corresponding to the emitters are considered either spherical or planar waves, depending on the distance between the array and the location of the emitting sources [19]. In the former case, which is known as the near-field case, the sources are located relatively close to the array; while in the latter case, known as the far-field propagation model, the location of the sources is far with regards to the aperture size of the array.

We start with one plane wave propagating from the far-field impinging on the array from an unknown direction. It is also assumed that the signal is narrowband. That is, the carrier frequency is fairly large compared to the bandwidth of the signal and so the signal can be treated as quasi-static during time intervals of order τ. A narrowband source is modeled as a complex envelope (or complex bandpass signal)

$$\hat{x}(t) = x(t)e^{jw_c t}, \tag{2.11}$$

where $w_c = 2\pi f_c$ is the carrier frequency and $x(t)$ is the baseband signal [28]. Each sensor captures the incoming signal with a time delay. In the noiseless case, the signal received by the m-th sensor is given by

$$y_m(t) = x(t - \tau_m)e^{jw_c(t-\tau_m)}. \tag{2.12}$$

The narrowband assumption implies that the spectrum of the narrowband signal is band-limited to the region

$$\|w_L\| \leq \pi B_s, \tag{2.13}$$

where $w_L := w - w_c$ and πB_s specifies the maximum signal bandwidth. If it happens

that the bandwidth of the signal is much less than $1/\pi_m (B_s \tau_m \ll 1)$, then one can make use of the narrowband approximation, which allows ignoring the delay τ_m from the baseband signal $x(t - \tau_m) \approx x(t)$. This is because in that case, the signal changes very slowly relative to the travel time across the aperture of the array. Taking this approximation into account, (2.12) becomes

$$y_m(t) \approx x(t) e^{jw_c t} e^{-jw_c \tau_m}, \text{ for m = 1, 2, ..., M.} \tag{2.14}$$

In practice, the dependence on the term $e^{jw_c t}$ is usually dropped (i.e., the signal is usually down-converted to baseband before sampling). It follows that the sensors will capture

$$\begin{aligned} y_1(t) &= \hat{x}(t - \tau_1) \approx x(t) e^{-j2\pi f_c \tau_1} \\ y_2(t) &= \hat{x}(t - \tau_2) \approx x(t) e^{-j2\pi f_c \tau_2} \\ &\vdots \\ y_M(t) &= \hat{x}(t - \tau_M) \approx x(t) e^{-j2\pi f_c \tau_M}, \end{aligned} \tag{2.15}$$

where $\tau_m = (m-1) d \cos(\theta)/c$ if the first sensor of the array is the phase reference, c is the propagation speed and m represents the sensor index.

Therefore the sensor array output can be modeled as

$$y(t) = \begin{bmatrix} e^{-j2\pi f_c \tau_1} \\ e^{-j2\pi f_c \tau_2} \\ \vdots \\ e^{-j2\pi f_c \tau_M} \end{bmatrix} x(t) + \boldsymbol{n}(t) = \boldsymbol{a}(\theta) x(t) + \boldsymbol{n}(t), \tag{2.16}$$

where $\boldsymbol{n}(t) = [n_1(t), n_2(t), \cdots, n_M(t)]^T$ is the $M \times 1$ vector corresponding to the additive noise at the sensors and $\boldsymbol{a}(\theta)$ is the linear array response (usually called the array steering vector) to the impinging plane wave that can be expressed as

$$\boldsymbol{a}(\theta) = \left[e^{-j2\pi f_c \tau_1}, \quad e^{-j2\pi f_c \tau_2}, \quad \cdots, \quad e^{-j2\pi f_c \tau_M} \right]^T. \tag{2.17}$$

Equation (2.16) can be then generalized for K multiple directions of arrival corre-

sponding to multiple propagating plane waves

$$\boldsymbol{y}(t) = \sum_{j=1}^{K} \boldsymbol{a}(\theta_j) x_j(t) + \boldsymbol{n}(t) = \boldsymbol{A}(\boldsymbol{\theta}) x(t) + \boldsymbol{n}(t), \tag{2.18}$$

where

$$\boldsymbol{A}(\boldsymbol{\theta}) = \Big[\boldsymbol{a}(\theta_1), \quad \boldsymbol{a}(\theta_2), \quad \cdots, \quad \boldsymbol{a}(\theta_K)\Big]^T. \tag{2.19}$$

is the $M \times K$ array steering matrix (also called array manifold) containing the array responses to all impinging plane waves,

$$\boldsymbol{x}(t) = \Big[x_1(t), \quad x_2(t), \quad \cdots, \quad x_K(t)\Big]^T \tag{2.20}$$

is the $K \times 1$ vector that contains the K plane waves impinging on the array and

$$\boldsymbol{\theta} = \Big[\theta_1, \quad \theta_2, \quad \cdots, \quad \theta_K\Big]^T \tag{2.21}$$

is the $K \times 1$ vector that contains the DOAs of the incoming signals.

A very important design parameter is the inter-sensor spacing d. It should be chosen properly to avoid the undesirable effects of spatial aliasing. This type of aliasing is identical to the problem of aliasing in time series analysis and can introduce ambiguities to the non-trivial task of DOA estimation, which may make localization impossible [28]. More specifically, the spatial sampling theory suggests that the phase difference should be restricted to π

$$2\pi f_c \Delta\tau \leq \pi, \tag{2.22}$$

where $\delta\tau = d\cos(\theta)/c$. This yields

$$d \leq \frac{1}{2}\frac{c}{f_c}\frac{1}{\cos(\theta)}. \tag{2.23}$$

The denominator of the right hand side of the above inequality takes its maximum value at $\theta = 2k\pi$, where $k = 0, 1, 2, \cdots$. Therefore, substituting $cos(\theta) = 1$ and the wavelength $\lambda = c/f_c$, (2.23) reduces to the following inequality

$$d \leq \lambda/2, \tag{2.24}$$

which means that the inter-sensor spacing should not exceed half the wavelength of the narrowband signal in order to avoid spatial aliasing.

2.2.2 Array Processing DOA Estimation Methods

Sensor array signal processing emerged as an active area of research and was centered on the ability to fuse data collected at several sensors in order to carry out a given estimation task (space-time processing) [19].

Array processing DOA estimation methods can be classified into two main categories, namely spectral-based and parametric approaches. In the former, one forms some spectrum-like function of the parameter(s) of interest, e.g., the DOA. The locations of the highest (separated) peaks of the function in question are recorded as the DOA estimates. Parametric techniques, on the other hand, require a simultaneous search for all parameters of interest.

Parametric approaches include deterministic maximum likelihood (DML) and stochastic maximum likelihood (SML), where the signal waveforms are treated as deterministic and stochastic processes respectively. After the likelihood function has been obtained, the unknown parameters corresponding to the unknown DOAs are estimated so that the likelihood function is maximized. The parametric approaches result in accurate estimates at the price of high computational complexity [129–133].

On the other hand, non-parametric methods are computationally attractive and can be divided into two main subcategories; the beamforming techniques and the subspace based methods. The beamforming techniques attempt to steer the array in one direction at a time and measure its output power at the specific direction. Therefore, the locations that yield the maximum power are the DOA estimates. In contrast, spectral based methods employ subspace analysis and exploit the fact that the noise subspace is orthogonal to the signal subspace. These methods basically make use of the eigen-structure of the covariance matrix of observed signals from the sensor array. Subspace methods are very well known for their high performance and relatively low computational cost.

All DOA estimation methods (to be presented) require that $K < M$, which is therefore assumed throughout the development. It is interesting to note that in the noiseless case, the array output is then confined to an M-dimensional subspace of the complex M-space, which is spanned by the steering vectors. This is the signal subspace, and this observation forms the basis of subspace-based methods.

In this section, we briefly review the most popular DOA estimation methods. We first introduce spectral-based subspace algorithmic solutions to the signal parameter estimation problem. We then contrast these suboptimal solutions to parametric methods.

2.2.2.1 Spectral Estimation

Spectral-based methods which are discussed in this section can be classified into beamforming techniques and subspace-based methods.

Beamforming

Initial trials of signal source localization using arrays were through beamforming techniques. The idea is to form a beam in the direction of waves coming from only one particular direction. The steering directions which result in maximum signal power yields the DOA estimates [134]. The conventional beamforming technique is the simplest one which relays on the Fourier-based spectral analysis to antenna array output. The task of DOA estimation is accomplished by steering the array at different locations through the appropriate weighting (or shifting) of the waveforms captured by each sensor of the array. The purpose is to maximize the output power of the beamformer from a certain signal propagation direction. Conventional beamformers show poor performance when resolving power of two sources spaced closer than a beamwidth. They suffer from the Rayleigh resolution limit, as they cannot resolve two closely spaced sources and its performance is limited by the aperture size of the ULA.

However, a well-known method called Capon's beamforming proposed in [135] (also known as the Minimum Variance Distortionless (MVDR) beamformer), attempts to alleviate this limitation offering the ability of better focusing in the directions where there are multiple sources. In contrast to the conventional beamformer, which attempts to maximize the output power in the look direction θ, the MVDR beamformer attempts to minimize the noise power and the power contributed by signals impinging on the array from other directions than θ with the constraint of unit gain in the look direction θ. In other words, it uses every available degree of freedom to concentrate the received energy in one direction, namely the bearing of interest. Capon's beamformer reduces the spectral leakage caused by closely spaced sources that limits the resolution capability of the conventional beamformer. It can be viewed as an optimal beamformer and this is why it has found extensive use in practical applications [19]. Despite that, its performance is still dependent on the aperture size and the noise level.

Subspace-Based Methods

The introduction of subspace-based estimation techniques [136, 137] marked the beginning of a new era in the sensor array signal processing literature. The subspace based approach relies on certain geometrical properties of the assumed data model, resulting in

a resolution capability which (in theory) is not limited by the array aperture, provided the data collection time and/or SNR are sufficiently large and assuming the data model accurately reflects the experimental scenario.

The most commonly used technique in this family is the MUSIC (MUltiple SIgnal Classification) technique [137]. MUSIC initially obtains an estimate of the covariance matrix of the observations. This is followed by a subspace analysis, in which the covariance matrix is firstly decomposed and the space spanned by the received data is then partitioned into the signal and the noise subspace.

Similar to the beamforming methods, the algorithm requires a one dimensional search. However, there is an additional computational cost associated with the eigenvalue decomposition of the data covariance matrix. MUSIC provides a significant improvement in terms of estimation accuracy over the beamforming methods and when the time samples captured by each sensor of the array are sufficiently long, the algorithm provides statistically consistent estimates.

However, the main limitation of MUSIC appears in the so-called coherent source scenario. When some of the incoming signals happen to be highly correlated, then the algorithm's performance degrades dramatically. This is to be expected, as in that case, the eigenvalue decomposition tends to underestimate the number of sources resulting in signal subspace estimate of reduced dimension. Similar issues can arise when the number of time snapshots is not sufficient enough. This problem is usually referred to as the rank-deficient case [138]. Spatial smoothing [139, 140] was then proposed to solve the correlation problem. The main idea is to split the array into a number of overlapping subarrays with identical steering vectors. The subarray covariance matrices can therefore be averaged after the spatial smoothing induces a random phase modulation which in turn tends to decorrelate the signals that caused the rank deficiency. The drawback with spatial smoothing is that the effective aperture of the array is reduced, since the subarrays are smaller than the original array. However, despite this loss of aperture, the spatial smoothing transformation mitigates the limitation of all subspace-based estimation techniques while retaining the computational efficiency of the one-dimensional spectral searches.

Other subspace-based DOA estimation methods have been proposed, which provide a significantly improved performance as compared to the traditional spectral MUSIC algorithm. Among the most popular algorithms are root-MUSIC [141, 142] and ESPRIT (estimation of signal parameters via rotational invariance technique) [143]. Since these methods avoid any spectral search, their computational complexity is often lower than that of the spectral MUSIC algorithm. However, root-MUSIC and ESPRIT can be

applied only in the case of specific array geometries. In particular, root-MUSIC is applicable only if the sensors are located on a uniform grid, whereas ESPRIT requires that the array consists of two identical and identically oriented subarrays. Several extensions of root-MUSIC and ESPRIT to circular and rectangular arrays can be found in [144–146]. However, the array geometries considered are still rather specific. In particular, these methods cannot be applied in the case of arbitrary array configurations.

One important observation of subspace based methods is that the number of sources K needs to satisfy $K < M$. Beamforming algorithms also have this assumption implicitly. This indicates that the number of sources K that can be resolved is upper bounded by the number of sensors M.

2.2.2.2 Parametric Estimation

While the spectral-based methods presented in the previous section are computationally attractive, they do not always yield sufficient accuracy. In particular, for scenarios involving highly correlated (or even coherent) signals, the performance of spectral-based methods may be insufficient. An alternative is to fully exploit the underlying data model, leading to so-called parametric array processing methods. As we shall see, coherent signals impose no conceptual difficulties for such methods. The price to pay for this increased efficiency and robustness is that the algorithms typically require a multidimensional search to find the estimates.

The parametric approach assumes a probabilistic model for the underlying signal and applies Maximum Likelihood (ML) estimation to extract the unknown parameters of the distribution. Two different assumptions about the source signals $x(t)$ lead to different ML approaches. They are known as deterministic ML (DML) and stochastic ML (SML) algorithms.

For the deterministic model, the source signals are modeled as unknown deterministic quantities and the randomness of $y(t)$ in (2.16) is entirely due to the noise with unknown variance σ_n^2. It therefore appears natural to model the noise as a stationary Gaussian white random process whereas the signal waveforms are deterministic (arbitrary) and unknown.

The other stochastic ML technique models the signal waveforms as Gaussian random processes. This model is reasonable, for instance, if the measurements are obtained by filtering wideband signals using a narrow bandpass filter. Indeed, the SML signal parameter estimates have been shown to have a better large sample accuracy than the corresponding DML estimates [132, 133], with the difference being significant only for small numbers of sensors, low SNR and highly correlated signals. The SML algorithm

also attains the Stochastic Cramér-Rao lower bound (CRB) for Gaussian signals whereas the DML cannot consistently estimate the source parameters and they do not attain the deterministic CRB [147].

Many parametric subspace based methods that have the same statistical performance (both theoretically and practically) as the ML methods have been developed [131, 132, 148, 149]. Such techniques achieve comparable performance to the ML based ones at a much lower complexity.

Chapter 3

Compressive Sensing Based DOA Estimation off the Grid

This chapter studies the problem of offgrid sources in compressive sensing (CS) based direction of arrival (DOA) estimation. A polarimetric extension is also presented for the proposed approach.

After the motivation and the problem formulation in Section 3.1, Section 3.2 describes an analytical approach to investigate the effect of recovering the spectrum of offgrid sources based on examining the specific shape of the resulting spectrum. Section 3.3 suggests that the spectrum of the offgrid source can be well approximated by the closest two dictionary atoms on the grid and their coefficients can be exploited to estimate the grid offset.

In Section 3.3.1 we propose a simple scheme to estimate the grid offset for a single source and then extend our model to consider multiple sources in Section 3.3.2.

In Section 3.4, we extend our CS based DOA estimation model to its full polarimetric description for arbitrary antenna arrays. We show that our CS based model can estimate both the DOA and the polarization state of each individual path on the grid (Section 3.4.2) and off the grid (Section 3.4.3).

Section 3.5 evaluates the proposed approaches via numerical simulations followed by a summary in Section 3.6.

3.1 Motivation

Consider K narrow-band planar waves impinging on an array of M elements from sources lying in the far-field. At the array side, the observations are given by

$$\boldsymbol{y}(t) = \sum_{k=1}^{K} \boldsymbol{a}(\theta_k) \cdot s_k(t) + \boldsymbol{n}(t), \tag{3.1}$$

where $\boldsymbol{a}(\theta) \in \mathbb{C}^M$ is the array manifold, θ_k is the DOA vector, $\boldsymbol{s}_k(t)$ are the amplitudes of the impinging waves at time t, and $\boldsymbol{n}(t)$ is the additive white Gaussian noise (AWGN) contaminating the observations.

One way to interpret the scenario in (3.1) is that the power received at the array sensors concentrates at few locations θ_k from all possible DOAs θ, which means that the received power is "sparse" in the angular domain. This sparsity motivates the use of compressed sensing for DOA estimation. It was shown by the authors of [29] that if the field is modeled as a superposition of a few planar wave-fronts, the DOA estimation problem can be expressed as a sparse recovery problem and the Compressed Sensing (CS) framework can be applied.

The CS based DOA estimation problem is formulated as

$$\boldsymbol{y}(t) = \boldsymbol{A} \cdot \boldsymbol{s}(t) + \boldsymbol{n}(t), \tag{3.2}$$

where $\boldsymbol{A} \in \mathbb{C}^{M \times N}$ is the sampled array manifold (dictionary). The number of grid points is given as $N = M \cdot P$, $P > 1$ where P is the oversampling factor representing how fine the grid is. Note that P is sometimes also referred as the "super resolution factor" [122]. We consider this term misleading since increasing P does not actually improve the resolution (which is limited by M, as also shown in [122]).

We first assume a uniform linear array (ULA) of isotropic sensors. We will show an extension to a practical scenario with a circular array under a polarimetric setting later on. Moreover, in order to achieve a uniform mutual coherence between columns of $\boldsymbol{A}$, we sample the manifold uniformly in the spatial frequency domain instead of the angular domain. For a ULA with half-wavelength inter-element spacing, the spatial frequency μ is defined as $\mu = \pi \cdot \sin\theta$. The dictionary is then sampled at the points $\mu_n = \Delta \cdot (n-1)$, $n = 1, 2, \ldots, N$, where $\Delta = \frac{2\pi}{N}$.

Many powerful CS-based DOA estimation algorithms have been proposed in recent years [150–152] showing tremendous advantages with respect to the hardware complexity of the receiving arrays and the complexity of the numerical solution (compared to Maximum Likelihood algorithms) while being insensitive to source correlation and allowing arbitrary array geometries (as opposed to most subspace-based estimators). However, they all face one common problem. Although the model is sparse in a continuous angular domain, to apply the CS framework we need to construct a finite dictionary by sampling this domain with a predefined sampling grid i.e., the angle space is divided into a large number of grids where the source directions of interest are assumed to exactly lie on some of the grids. However, the target locations in practice are almost surely not located exactly on a subset of these grid points. This leads to a model mismatch that results in a degradation of the performance.

It may seem that the solution is to make the grid as fine as possible. However, this increases the correlation between the adjacent steering vectors and deteriorates the CS recovery process. Early approaches for CS based DOA estimation suggest tackling this off-grid problem by simply refining the grid adaptively around the candidate targets found with an initial, mismatched grid [29] or taking centroids of the dominant coefficients as the exact location [153]. One type of more sophisticated solutions models the mismatch error explicitly and fits it to the observed data statistically [119, 121]. Other approaches deal with the continuous problem directly and propose some modifications to the recovery algorithm to deal with such scenario, i.e., interpolating between grid points [117], atomic norm minimization [123], or perturbed OMP [120]. Note that this typically increases the computational complexity significantly.

In this chapter, we take an analytical approach to investigate the effect of recovering the spectrum of sources not contained in the dictionary. Unlike earlier works that have provided a quantitative analysis of the approximation error [113, 114], we examine the specific shape of the resulting spectrum. We show that for one off-grid source the recovered spectrum is not sparse but it can be well approximated by the closest two dictionary atoms on the grid and their coefficients can be exploited to estimate the grid offset. We then extend our model to consider multiple sources. When they are sufficiently separated, the offset estimation strategy can be applied separately. For closely spaced sources we propose an efficient joint estimation strategy and demonstrate its performance in numerical simulations.

3.2 Analytical Study of the Problem

As mentioned earlier, no matter how fine the grid is, there will always be sources that do not lie exactly on one of the grid points. In this section, we analyze this problem both qualitatively and quantitatively. For simplicity, let us start by one source off the grid. In the absence of noise, this simplifies (3.1) into $\boldsymbol{y} = \tilde{\boldsymbol{a}} \cdot \boldsymbol{s}$, where $\tilde{\boldsymbol{a}} = \boldsymbol{a}(\mu_L + \epsilon \cdot \Delta)$. Here, $L \in \mathbb{N}$, i.e., μ_L represents the next "left" grid point. Moreover, $0 \leq \epsilon < 1$ is the grid offset, expressed as a fraction of Δ.

In general, $\boldsymbol{y}$ is not 1-sparse in $\boldsymbol{A}$. In fact, an exact representation of $\boldsymbol{y}$ in $\boldsymbol{A}$ requires M non-zero coefficients. Moreover, an arbitrary subset of M out of N coefficients could be used to find such a representation.

In the CS framework, we often employ an ℓ_1-type regularization to find a sparse solution. For instance, the Basis Pursuit method [97] solves the following problem

$$\min \|\boldsymbol{\alpha}\|_1 \quad \text{s.t.} \quad \boldsymbol{y} = \boldsymbol{A} \cdot \boldsymbol{\alpha}. \tag{3.3}$$

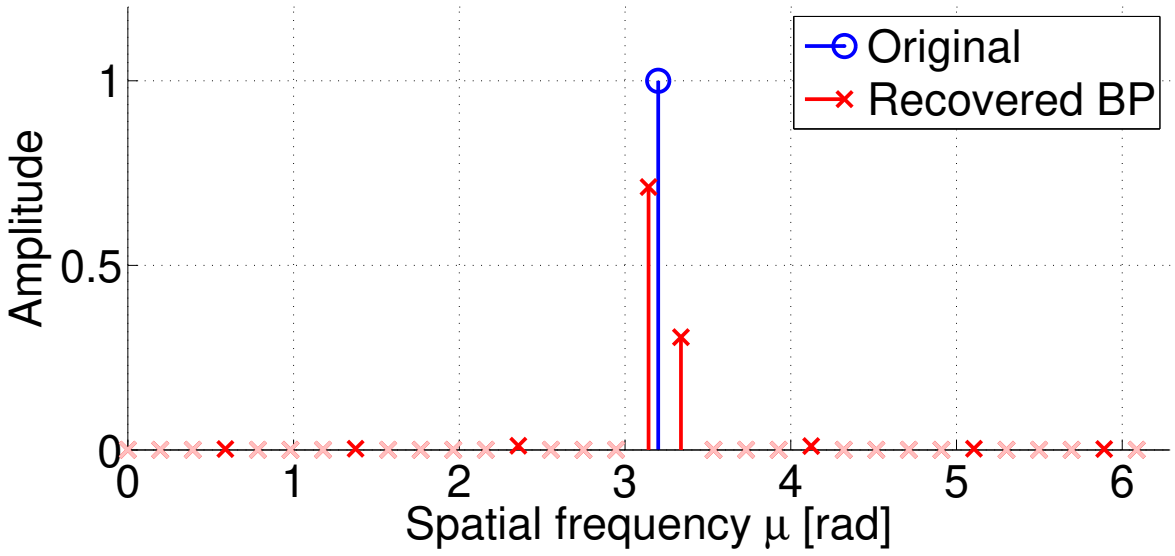

Figure 3.1: Recovered spectrum for one source off the grid ($M = 8, P = 4, \epsilon = 0.3$) using BP

The purpose of this regularization is to concentrate the energy on as few coefficients as possible. This suggests that the solution to (3.3) chooses the closest neighboring atoms on the grid to represent the off-grid source. To support this intuition, Figure 3.1 demonstrates the resulting spectrum when solving (3.3) using BP [97] for $M = 8$, $P = 4$ (i.e., $N = 32$), and $\epsilon = 0.3$. We observe that, as expected, most of the energy is concentrated on the two closest grid points.

3.3 An Approximation Scheme for offgrid Sources

3.3.1 Single Source

Motivated by this finding, we investigate the approximation of $\tilde{\boldsymbol{a}}$ using the two neighboring atoms on the grid, i.e.,

$$\boldsymbol{a}(\mu_L + \epsilon \cdot \Delta) = \Big[\boldsymbol{a}(\mu_L), \boldsymbol{a}(\mu_{L+1})\Big] \cdot \begin{bmatrix} \alpha_1 \\ \alpha_2 \end{bmatrix} + \boldsymbol{a}_{\text{Res}}, \tag{3.4}$$

where $\boldsymbol{a}_{\text{Res}}$ is the residual that is not representable by the neighbors. The coefficients α_1 and α_2 are found by solving

$$\min_{\alpha_1 \alpha_2} \left\| \tilde{\boldsymbol{a}} - \Big[\boldsymbol{a}(\mu_L), \boldsymbol{a}(\mu_{L+1})\Big] \cdot \begin{bmatrix} \alpha_1 \\ \alpha_2 \end{bmatrix} \right\|_2^2. \tag{3.5}$$

The least squares (LS) solution was found to be

$$\alpha_1(\epsilon) = \frac{1}{M^2 - \frac{\sin^2(\frac{M\Delta}{2})}{\sin^2(\frac{\Delta}{2})}} \cdot \left(M \cdot \frac{\sin(\frac{M\Delta}{2} \cdot \epsilon)}{\sin(\frac{\Delta}{2} \cdot \epsilon)} - \frac{\sin(\frac{M\Delta}{2})}{\sin(\frac{\Delta}{2})} \cdot \frac{\sin(\frac{M\Delta}{2} \cdot (\epsilon - 1))}{\sin(\frac{\Delta}{2} \cdot (\epsilon - 1))} \right), \tag{3.6}$$

$$\alpha_2(\epsilon) = \frac{1}{M^2 - \frac{\sin^2(\frac{M\Delta}{2})}{\sin^2(\frac{\Delta}{2})}} \cdot \left(M \cdot \frac{\sin(\frac{M\Delta}{2} \cdot (\epsilon - 1))}{\sin(\frac{\Delta}{2} \cdot (\epsilon - 1))} - \frac{\sin(\frac{M\Delta}{2})}{\sin(\frac{\Delta}{2})} \cdot \frac{\sin(\frac{M\Delta}{2} \cdot \epsilon)}{\sin(\frac{\Delta}{2} \cdot \epsilon)} \right), \tag{3.7}$$

which can then be expressed in terms of ϵ and P as

$$\alpha_1(\epsilon) = \frac{1}{M^2 - \frac{\sin^2(\frac{\pi}{P})}{\sin^2(\frac{\pi}{M \cdot P})}} \cdot \left(M \cdot \frac{\sin(\frac{\pi}{P} \cdot \epsilon)}{\sin(\frac{\pi}{M \cdot P} \cdot \epsilon)} - \frac{\sin(\frac{\pi}{P})}{\sin(\frac{\pi}{M \cdot P})} \cdot \frac{\sin(\frac{\pi}{P} \cdot (\epsilon - 1))}{\sin(\frac{\pi}{M \cdot P} \cdot (\epsilon - 1))} \right), \tag{3.8}$$

$$\alpha_2(\epsilon) = \frac{1}{M^2 - \frac{\sin^2(\frac{\pi}{P})}{\sin^2(\frac{\pi}{M \cdot P})}} \cdot \left(M \cdot \frac{\sin(\frac{\pi}{P} \cdot (\epsilon - 1))}{\sin(\frac{\pi}{M \cdot P} \cdot (\epsilon - 1))} - \frac{\sin(\frac{\pi}{P})}{\sin(\frac{\pi}{M \cdot P})} \cdot \frac{\sin(\frac{\pi}{P} \cdot \epsilon)}{\sin(\frac{\pi}{M \cdot P} \cdot \epsilon)} \right). \tag{3.9}$$

This can be expressed in a more compact form as

$$\alpha_1(\epsilon) = \frac{D(0) \cdot D(\epsilon) - D(1) \cdot D(1 - \epsilon)}{D(0)^2 - D(1)^2} \cdot \mathrm{e}^{\jmath \cdot \epsilon \cdot \pi \frac{(M-1)}{M \cdot P}}, \tag{3.10}$$

$$\alpha_2(\epsilon) = \frac{D(0) \cdot D(1 - \epsilon) - D(1) \cdot D(\epsilon)}{D(0)^2 - D(1)^2} \cdot \mathrm{e}^{-\jmath \cdot (1-\epsilon) \cdot \pi \frac{(M-1)}{M \cdot P}}, \tag{3.11}$$

$$\text{where} \quad D(x) = \frac{\sin\left(\frac{\pi \cdot x}{P}\right)}{\sin\left(\frac{\pi \cdot x}{M \cdot P}\right)}. \tag{3.12}$$

Figure 3.2 shows the behavior of the calculated coefficients with varying the offset ϵ for $P = 2$ and 4. It can be shown that

$$\lim_{P\to\infty} \alpha_1(\epsilon) = 1 - \epsilon, \tag{3.13}$$

$$\lim_{P\to\infty} \alpha_2(\epsilon) = \epsilon, \tag{3.14}$$

i.e., as P increases (and so N), α_1 and α_2 becomes more linear with ϵ.

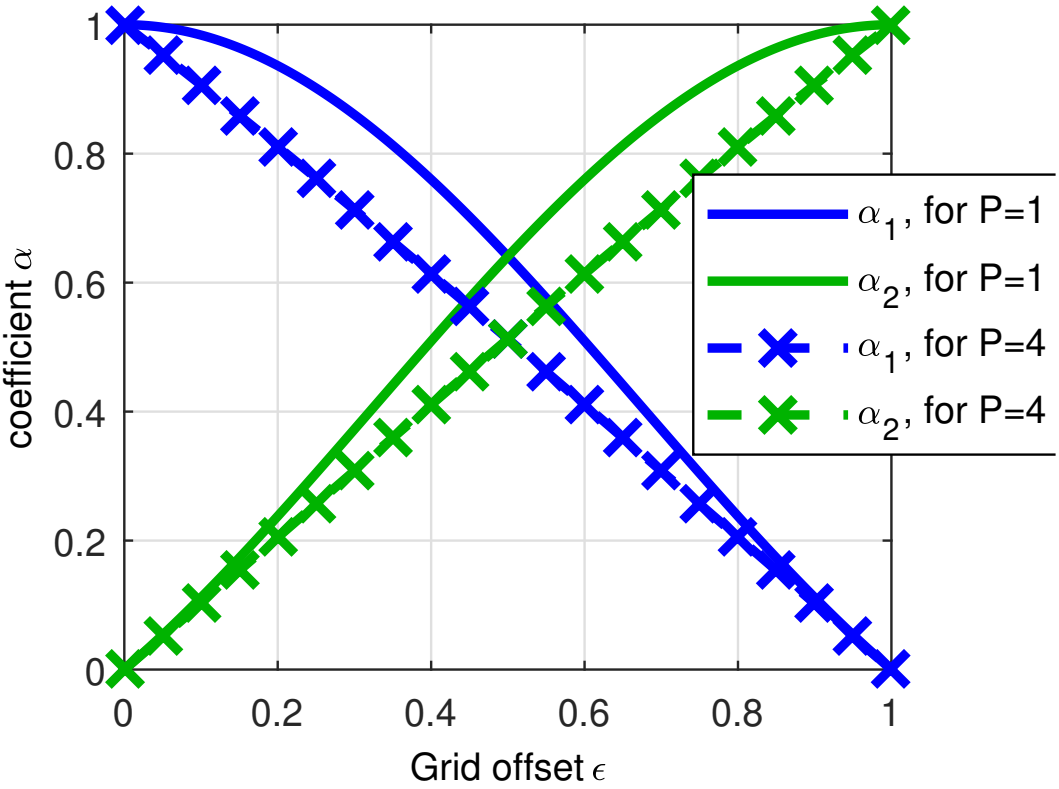

Figure 3.2: Behavior of the approximation coefficients α_1 and α_2 for $M = 8$.

To assess the accuracy of our two term approximation, the relative approximation error (AE) has been examined. We define

$$\mathrm{AE}(\epsilon, M, P) \doteq \frac{\|\boldsymbol{a}_{\mathrm{Res}}\|_2^2}{\|\tilde{\boldsymbol{a}}\|_2^2}. \tag{3.15}$$

Figure 3.3 shows the approximation error as a function of ϵ. The AE is convex and symmetric in ϵ and that $\mathrm{AE}(\epsilon, M, P) \leq \mathrm{AE}(1/2, M, P)$, i.e., as expected, the worst case error is at $\epsilon = 0.5$.

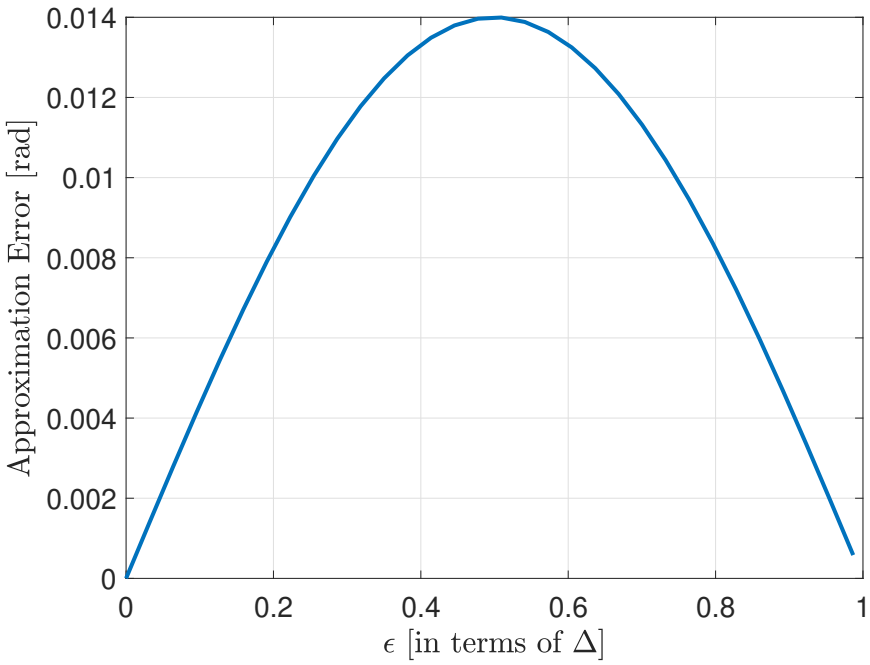

Figure 3.3: Behavior of the approximation error as a function of ϵ for $M = 8$.

Moreover, a closed form expression for this worst case error is given by

$$\mathrm{AE}(1/2, M, P) = 1 - \frac{4\sin^2\left(\frac{\pi}{2P}\right)\cot\left(\frac{\pi}{2MP}\right)}{M^2\sin\left(\frac{\pi}{MP}\right) + M\sin\left(\frac{\pi}{P}\right)}, \tag{3.16}$$

which we depict in Figure 3.4. In fact, Figure 3.4 shows that (3.16) increases mildly with M and decreases rapidly with increasing P (0.01 at $P = 2$ and 0.001 at $P = 3$).

In the limits we have

$$\lim_{P\to\infty} \mathrm{AE}(1/2, M, P) = 0, \tag{3.17}$$

$$\lim_{M\to\infty} \mathrm{AE}(1/2, M, P) = 1 - \frac{4\left(1-\cos\left(\frac{\pi}{P}\right)\right)P^2}{\pi\left(P\sin\left(\frac{\pi}{P}\right)+\pi\right)}. \tag{3.18}$$

From the results of (3.10) and (3.11), we were inspired [1] to define a simple estimator for ϵ given by

$$\hat{\epsilon} = \frac{\alpha_2}{\alpha_1 + \alpha_2}. \tag{3.19}$$

[1] Note that similar estimators are used in the literature for frequency interpolation [154, 155]. However, they have been derived in a completely different context and it was not expected that such techniques are applicable to a spectrum recovered by ℓ_1-minimization.

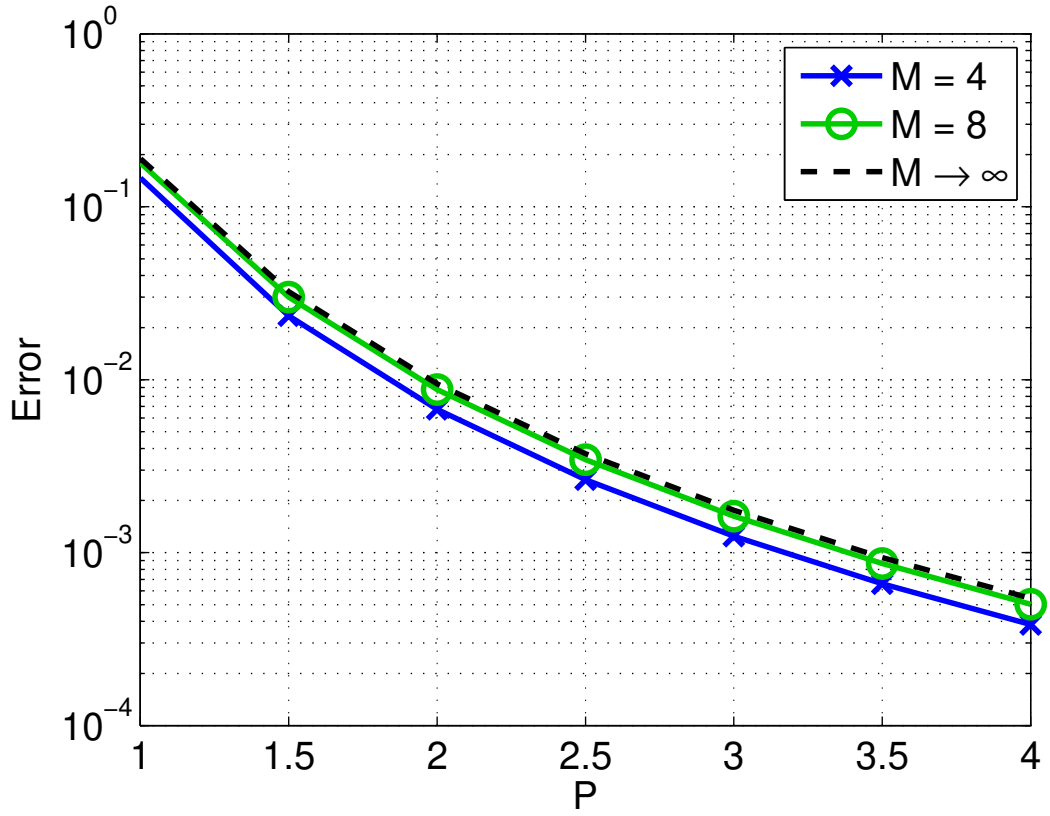

Figure 3.4: Worst-case approximation error $\mathrm{AE}(1/2, M, P)$ vs. M and P.

Note that in the absence of noise we have from (3.13) and (3.14)

$$\lim_{P\to\infty} \hat{\epsilon} = \epsilon. \tag{3.20}$$

To use such scheme in practice, we solve (3.3) to get the coefficients at the neighboring grid points that are close to the α_1 and α_2 we got from the LS fit. This means that we take the estimated amplitudes after solving (3.3) and use them directly in (3.19). If we choose another sparse recovery scheme (e.g., OMP), then we have to compute the LS fit manually before being able to apply the estimator.

3.3.2 Multiple Sources

So far, we have discussed a single source only. When multiple sources are present, their mutual influence depends on the correlation between the array steering vectors. As long as the distance between the sources is $\gg P$ grid points, they are almost orthogonal and hence the mutual influence is very low. In this case, they can be treated independently and the estimator (3.19) can be applied separately. This is exemplified in Figure 3.5

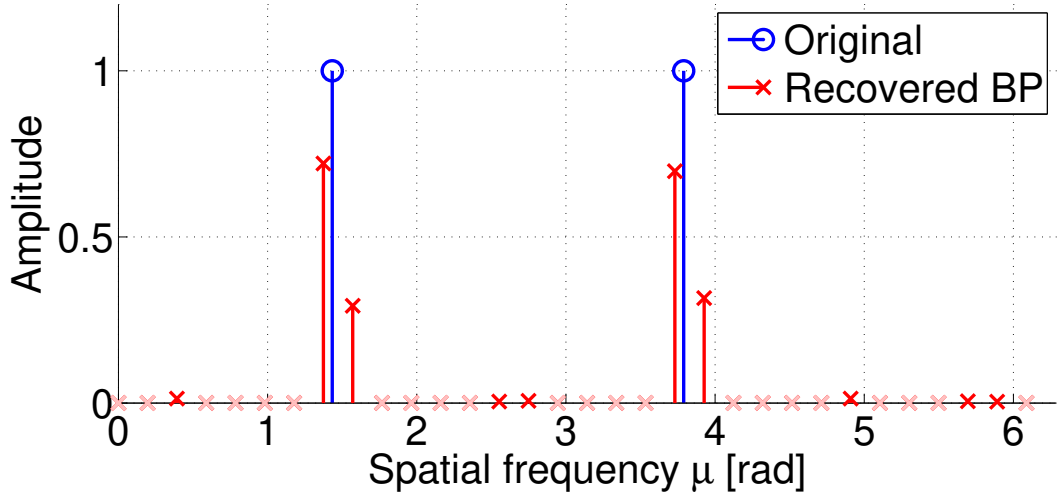

Figure 3.5: Recovered spectrum for two far sources ($M = 8, P = 4, \epsilon_1 = \epsilon_2 = 0.3$).

which depicts such a case ($M = 8$, $P = 4$, $\mu_1 = 6.3\Delta$, $\mu_2 = 15.3\Delta$).

This strategy fails for any pair of sources that has a distance which is close to (or even below) P grid points. Note that it has been shown that the CS-based recovery of the correct support can only be guaranteed when the sources have a spacing that is $\geq P$ grid points [122][2]. Let us assume that the support has been estimated correctly, i.e., for two sources located at $\mu_k = (L_k - 1 + \epsilon_k) \cdot \Delta$, $k = 1, 2$ we have found the left neighboring grid points L_1 and L_2. Then, the best two-term approximation for one source shown in (3.5) can be extended to the joint estimation of the grid offsets for two sources by considering the four neighboring grid points $L_1, L_1 + 1, L_2$, and $L_2 + 1$. These provide four coefficients $\boldsymbol{\alpha} = [\alpha_1, \alpha_2, \alpha_3, \alpha_4]^{\mathrm{T}} \in \mathbb{C}^{4\times 1}$ which depend on both offsets ϵ_1 and ϵ_2. Although we have not found a closed-form solution like (3.19), we propose a simple numerical procedure to estimate ϵ_1 and ϵ_2 from $\boldsymbol{\alpha}$.

The noiseless DOA estimation problem in case of two sources can be written as

$$\boldsymbol{y} = \Big[\boldsymbol{a}\Big((L_1 + \epsilon_1) \cdot \Delta\Big) \quad \boldsymbol{a}\Big((L_2 + \epsilon_2) \cdot \Delta\Big)\Big] \cdot \begin{bmatrix} s_1 \\ s_2 \end{bmatrix} = \tilde{\boldsymbol{A}} \cdot \boldsymbol{s}. \tag{3.21}$$

A four-term approximation using the neighboring on-grid points $L_1, L_1 + 1, L_2$, and

[2]In fact, a spacing of P grid points corresponds to a distance in spatial frequency of $2\pi/M$ radians, which is referred to as the "Rayleigh resolution limit" [19].

$L_2 + 1$ can be written as

$$\boldsymbol{y} \approx \Big[\boldsymbol{a}\Big(L_1 \cdot \Delta\Big) \quad \boldsymbol{a}\Big((L_1+1) \cdot \Delta\Big) \quad \boldsymbol{a}\Big(L_2 \cdot \Delta\Big) \quad \boldsymbol{a}\Big((L_2+1\Big) \cdot \Delta)\Big] \cdot \begin{bmatrix} \alpha_1 \\ \alpha_2 \\ \alpha_3 \\ \alpha_4 \end{bmatrix} = \boldsymbol{A}^{(S)} \cdot \boldsymbol{\alpha}. \tag{3.22}$$

Solving for $\boldsymbol{\alpha}$ that minimizes the approximation error, a least-square solution is given as

$$\boldsymbol{\alpha}_{\mathrm{LS}}(\epsilon_1, \epsilon_2, s_1, s_2) = \boldsymbol{A}^{(S)^+} \cdot \tilde{\boldsymbol{A}} \cdot \boldsymbol{s} = \Big(\boldsymbol{A}^{(S)^{\mathrm{H}}} \cdot \boldsymbol{A}^{(S)}\Big)^{-1} \cdot \boldsymbol{A}^{(S)^{\mathrm{H}}} \cdot \tilde{\boldsymbol{A}} \cdot \boldsymbol{s}, \tag{3.23}$$

where

$$\Big(\boldsymbol{A}^{(S)^{\mathrm{H}}} \cdot \boldsymbol{A}^{(S)}\Big)^{-1} = \begin{bmatrix} \Gamma(0) & \Gamma(1) & \Gamma(d) & \Gamma(d+1) \\ \Gamma(-1) & \Gamma(0) & \Gamma(d-1) & \Gamma(d) \\ \Gamma(-d) & \Gamma(-d+1) & \Gamma(0) & \Gamma(1) \\ \Gamma(-d-1) & \Gamma(-d) & \Gamma(-1) & \Gamma(0) \end{bmatrix}^{-1}, \tag{3.24}$$

$$\boldsymbol{A}^{(S)^{\mathrm{H}}} \cdot \tilde{\boldsymbol{A}} = \begin{bmatrix} \Gamma(\epsilon_1) & \Gamma(d+\epsilon_2) \\ \Gamma(\epsilon_1 - 1) & \Gamma(d-1+\epsilon_2) \\ \Gamma(-d+\epsilon_1) & \Gamma(\epsilon_2) \\ \Gamma(-d-1+\epsilon_1) & \Gamma(\epsilon_2 - 1) \end{bmatrix}, \tag{3.25}$$

with $\Gamma(x) = \frac{\sin(\frac{\pi \cdot x}{P})}{\sin(\frac{\pi \cdot x}{M \cdot P})} \cdot \mathrm{e}^{\jmath \cdot \pi \cdot x \frac{M-1}{M \cdot P}}$ and $d = L_2 - L_1$.

This means that

$$\boldsymbol{\alpha}_{\mathrm{LS}} = \begin{bmatrix} \Gamma(0) & \Gamma(1) & \Gamma(d) & \Gamma(d+1) \\ \Gamma(-1) & \Gamma(0) & \Gamma(d-1) & \Gamma(d) \\ \Gamma(-d) & \Gamma(-d+1) & \Gamma(0) & \Gamma(1) \\ \Gamma(-d-1) & \Gamma(-d) & \Gamma(-1) & \Gamma(0) \end{bmatrix}^{-1} \cdot \begin{bmatrix} \Gamma(\epsilon_1) & \Gamma(d+\epsilon_2) \\ \Gamma(\epsilon_1 - 1) & \Gamma(d-1+\epsilon_2) \\ \Gamma(-d+\epsilon_1) & \Gamma(\epsilon_2) \\ \Gamma(-d-1+\epsilon_1) & \Gamma(\epsilon_2 - 1) \end{bmatrix} \cdot \begin{bmatrix} s_1 \\ s_2 \end{bmatrix}. \tag{3.26}$$

Recalling $D(x) = \frac{\sin(\frac{\pi \cdot x}{P})}{\sin(\frac{\pi \cdot x}{M \cdot P})}$ and using it to simplify (3.26)

$$\boldsymbol{\alpha}_{\mathrm{LS}} = \boldsymbol{\Phi}^{\mathrm{H}} \cdot \boldsymbol{D}_0^{-1} \cdot \boldsymbol{D}_1(\epsilon_1, \epsilon_2) \cdot \begin{bmatrix} \mathrm{e}^{\jmath \epsilon_1 \pi \frac{M-1}{M \cdot P}} \cdot s_1 \\ \mathrm{e}^{\jmath (\epsilon_2 + d) \pi \frac{M-1}{M \cdot P}} \cdot s_2 \end{bmatrix}. \tag{3.27}$$

To this end, let $\boldsymbol{d}(x) = [D(x), D(x-1), D(x-d), D(x-d-1)]^{\mathrm{T}} \in \mathbb{R}^{4 \times 1}$, $\boldsymbol{D}_0 = [\boldsymbol{d}(0), \boldsymbol{d}(1), \boldsymbol{d}(d), \boldsymbol{d}(d+1)] \in \mathbb{R}^{4 \times 4}$, and $\boldsymbol{D}_1 = [\boldsymbol{d}(\epsilon_1), \boldsymbol{d}(\epsilon_2 + d)] \in \mathbb{R}^{4 \times 2}$, where $d = L_2 - L_1$. Moreover, we define $\bar{\boldsymbol{\alpha}} = \boldsymbol{D}_0 \cdot \boldsymbol{\Phi} \cdot \boldsymbol{\alpha}$, where $\boldsymbol{\Phi} = \mathrm{diag}\left\{ \begin{bmatrix} 1 & \mathrm{e}^{\jmath \pi \frac{M-1}{M \cdot P}} & \mathrm{e}^{\jmath \pi d \frac{M-1}{M \cdot P}} & \mathrm{e}^{\jmath \pi (d+1) \frac{M-1}{M \cdot P}} \end{bmatrix} \right\}$. Then it can be shown that in the absence of noise, $\bar{\boldsymbol{\alpha}}$ is a linear combination of $\boldsymbol{d}(\epsilon_1)$ and $\boldsymbol{d}(\epsilon_2 + d)$. Therefore, we can obtain ϵ_1 and ϵ_2 by minimizing the cost function

$$\left\| \hat{\boldsymbol{\alpha}} - \boldsymbol{\alpha}_{\mathrm{LS}} \right\|_2^2 = \left\| \hat{\boldsymbol{\alpha}} - \boldsymbol{\Phi}^{\mathrm{H}} \cdot \boldsymbol{D}_0^{-1} \cdot \boldsymbol{D}_1(\epsilon_1, \epsilon_2) \cdot \begin{bmatrix} \mathrm{e}^{\jmath \epsilon_1 \pi \frac{M-1}{M \cdot P}} \cdot s_1 \\ \mathrm{e}^{\jmath (\epsilon_2 + d) \pi \frac{M-1}{M \cdot P}} \cdot s_2 \end{bmatrix} \right\|_2^2, \tag{3.28}$$

$$= \left\| \boldsymbol{\Phi}^{\mathrm{H}} \cdot \boldsymbol{D}_0^{-1} \cdot \left(\boldsymbol{D}_0 \cdot \boldsymbol{\Phi} \cdot \hat{\boldsymbol{\alpha}} - \boldsymbol{D}_1(\epsilon_1, \epsilon_2) \cdot \begin{bmatrix} \mathrm{e}^{\jmath \epsilon_1 \pi \frac{M-1}{M \cdot P}} \cdot s_1 \\ \mathrm{e}^{\jmath (\epsilon_2 + d) \pi \frac{M-1}{M \cdot P}} \cdot s_2 \end{bmatrix} \right) \right\|_2^2. \tag{3.29}$$

This can be simplified to

$$J(\epsilon_1, \epsilon_2) = \left\| \bar{\boldsymbol{\alpha}} - \boldsymbol{D}_1 \cdot \boldsymbol{D}_1^{+} \cdot \bar{\boldsymbol{\alpha}} \right\|_2^2, \tag{3.30}$$

i.e., tuning ϵ_1, ϵ_2 such that the overlap of $\bar{\boldsymbol{\alpha}}$ with the column space of $\boldsymbol{D}_1$ is maximized.

For more than two sources, the extension is straightforward. From a first CS-based recovery with N grid points, we obtain an initial coarse estimate of the sources' locations. Based on it we identify clusters of sources that are closely spaced where the different clusters are sufficiently far apart so that they can be treated independently. For each cluster, we apply a joint estimation of the grid offsets using the single-source strategy shown in (3.19), the two-source strategy from (3.30), or an appropriately extended K-source strategy, depending on the number of sources per cluster.

3.4 Polarimetric Extension

The actual polarimetric model of DOA estimation takes into account the sensitivity of the receiving antenna array to the polarization state of the incoming wave, i.e., the relative strength and the phase offset between the vertical and horizontal electromagnetic wave components. Nevertheless, in the DOA estimation literature, it is still very common

to consider a non-polarimetric model since this simplifies the mathematical model and the estimation problem. However, it ignores the physics of practical antennas which are always to some degree sensitive to both polarizations. In fact, it has been shown that ignoring the polarization can lead to entirely useless estimation results [156]. Therefore, a full polarimetric data model consisting of the two radiation patterns should always be used [26]. Almost all CS based DOA estimation techniques consider a non-polarimetric model. An exception is given by [157]. However, [157] is specific to vector-sensor arrays and the authors assume on-grid sources only and do not consider the off-grid problem which makes it unrealistic. In this section, we extend our CS based DOA estimation model to its full polarimetric description for arbitrary antenna arrays. For efficient storage and fast interpolation of arbitrary array manifolds, we leverage the Effective Aperture Distribution Function (EADF) [158]. We show that our CS based model can estimate both the DOA and the polarization state of each individual path and that we achieve an accuracy close to the Cramér-Rao Bound.

3.4.1 Polarimetric CS based DOA Estimation

Consider K narrow-band planar waves impinging on an array of M antennas. At the array side, the observations are given by

$$\begin{aligned}\boldsymbol{y}(t) &= \sum_{k=1}^{K} \begin{bmatrix}\boldsymbol{a}_{\mathrm{V}}(\theta_k) & \boldsymbol{a}_{\mathrm{H}}(\theta_k)\end{bmatrix} \cdot \boldsymbol{p}_k \cdot s_k(t) + \boldsymbol{n}(t), \\ &= \sum_{k=1}^{K} \boldsymbol{A}(\theta_k) \cdot \boldsymbol{p}_k \cdot s_k(t) + \boldsymbol{n}(t), \end{aligned} \tag{3.31}$$

where $\boldsymbol{A}(\theta_k) = \begin{bmatrix}\boldsymbol{a}_{\mathrm{V}}(\theta_k) & \boldsymbol{a}_{\mathrm{H}}(\theta_k)\end{bmatrix} \in \mathbb{C}^{M\times 2}$ is the polarimetric array manifold as a function of the azimuth angle θ, consisting of the array manifold for vertical and horizontal excitation $\boldsymbol{a}_{\mathrm{V}}(\theta)$ and $\boldsymbol{a}_{\mathrm{H}}(\theta)$, respectively. Moreover, θ_k and $s_k(t)$ denote the direction of arrival angle and the amplitude for the k-th source, and $\boldsymbol{p}_k = [p_{k,1},\ p_{k,2}]^{\mathrm{T}} \in \mathbb{C}^{2\times 1}$ is the Jones vector [159], describing the state of the polarization. Finally, $\boldsymbol{n}(t)$ represents the additive white Gaussian noise (AWGN) contaminating the observations.

The CS based DOA estimation model can be extended to the polarimetric model using the same model of (3.2)

$$\boldsymbol{y}(t) = \boldsymbol{A} \cdot \boldsymbol{s}(t) + \boldsymbol{n}, \tag{3.32}$$

where $\boldsymbol{A} = \left[\boldsymbol{A}(\theta_1^{(\mathrm{G})}) \quad \boldsymbol{A}(\theta_2^{(\mathrm{G})}) \quad \dots \quad \boldsymbol{A}(\theta_N^{(\mathrm{G})})\right] \in \mathbb{C}^{M\times(2N)}$ contains the polarimetric array manifold $\boldsymbol{A}(\theta)$ sampled at a pre-defined N-point sampling grid $\theta_n^{(\mathrm{G})}, n = 1, 2, \dots, N$. Again we consider uniform sampling such that $\theta_n^{(\mathrm{G})} = (n-1)\cdot\Delta$, where $\Delta = \frac{2\pi}{N}$ is the width of the grid. Moreover, $\boldsymbol{s} \in \mathbb{C}^{2N\times 1}$ is a block-sparse vector: it contains the vectors $\boldsymbol{p}_k \cdot s_k(t)$ at the indices $2n-1$ and $2n$ if $\theta_k = \theta_n^{(\mathrm{G})}$, i.e., the k-th source falls exactly onto the n-th grid point. Therefore, if all sources are "on-grid", $\boldsymbol{s}$ has up to $2K$ non-zero entries corresponding to the K impinging wavefronts and zeros elsewhere.

3.4.2 Polarimetric CS based DOA Estimation on the Grid

If all sources are exactly on the grid, the model in (3.32) is fulfilled exactly. Therefore, we can use an arbitrary sparse recovery algorithm, e.g., the Basis Pursuit (BP) method [97] or the Orthogonal Matching Pursuit (OMP) method [106] to find the estimated sparse vector $\hat{\boldsymbol{s}}$ from the observations $\boldsymbol{y}$. Note that the odd entries of $\boldsymbol{s}$ correspond to the vertical polarization state and the even entries of $\boldsymbol{s}$ to the horizontal polarization state, respectively. Since the polarization is unknown, we propose to compute a reduced-size vector $\tilde{\boldsymbol{s}} \in \mathbb{R}^N$, where the n-th entry of $\tilde{\boldsymbol{s}}$ is given by $\tilde{s}_n = |\hat{s}_{2n-1}|^2 + |\hat{s}_{2n}|^2$. Under ideal conditions, $\tilde{\boldsymbol{s}}$ is K-sparse and its K non-zeros correspond to the DOAs θ_k.

Not only is our signal sparse in nature, but also it exhibits a structure in its sparsity. From (2), the signal $\boldsymbol{s}(t)$ has 2 successive non zero entries at each direction of arrival θ_k. Such signals are referred to as block sparse signals [160]. There exist sparse recovery algorithms that take such a block-sparse structure into account to achieve a superior recovery performance. For instance, for ℓ_1-type algorithms like BP, a structured-sparsity extension called "Group BP" was proposed in [161]. Moreover, for greedy algorithms like the OMP, a "Block OMP" (BOMP) algorithm is introduced in [162]. We compare the performance of ℓ_1 and greedy recovery algorithms in the numerical results shown in Section 3.5.

3.4.3 Polarimetric CS based DOA Estimation off the Grid

As mentioned earlier throughout this chapter, the assumption that all DOAs are on the predefined sampling grid is not realistic. A more realistic model for an off-grid source as described in Section 3.3 can be written as

$$\theta_k = \theta_{L_k}^{(G)} + \epsilon_k \cdot (\theta_{L_{k+1}}^{(G)} - \theta_{L_k}^{(G)}), \tag{3.33}$$

where $L_k \in \mathbb{Z}^+$ is the index of the "left" neighboring grid point and $\epsilon_k \in [0, 1)$ models the grid offset. For the special case of the $N-$point uniformly sampling grid, (3.33) simplifies to

$$\theta_k = (L_k - 1 + \epsilon_k) \cdot \Delta. \tag{3.34}$$

Alternatively, we can define the off-grid model via

$$\theta_k = (C_k + \bar{\epsilon}_k) \cdot \Delta, \tag{3.35}$$

where $C_k \in \mathbb{Z}^+$ is the closest grid point for the $k-$th source and $\bar{\epsilon}_k \in [-0.5, 0.5)$.

As mentioned earlier, CS-based recovery algorithms aim at concentrating the energy in $\hat{\boldsymbol{s}}$ at as few coefficients as possible. It is therefore reasonable to assume that most of the energy will be found in the two adjacent grid points L_k and L_{k+1} for the k-th source. In Section 3.3.1, we have computed the best representation of one off-grid source in terms of the closest two grid points explicitly and exploited the resulting amplitudes to obtain a simple and yet efficient estimator for the grid offset given by

$$\hat{\epsilon}_k = \frac{\alpha_k}{\alpha_k + \alpha_{k+1}}, \tag{3.36}$$

where α_k and α_{k+1} are the coefficients of the recovered amplitude vector belonging to the grid points L_k and L_{k+1}.

For the polarimetric model, we could apply (3.36) to $\tilde{\boldsymbol{s}}$ defined in Section 3.4.2. However, since this estimator was derived assuming a uniform linear array composed of isotropic elements, it is expected that it does not work well when the array is more irregular. Also, the OMP spectrum does not return the two neighboring coefficients but rather one coefficient which is the nearest on the grid.

We therefore propose an alternative strategy to find $\bar{\epsilon_k}$ from equation (3.35) similar to the one proposed in Section 3.3.2 in case of multiple sources. First, we obtain an estimate for the closest grid point $\hat{C}$, e.g., as the index of the largest element in $\tilde{\boldsymbol{s}}$. We then choose a set $\mathcal{S} = \{S_1, \cdots, S_{N_S}\}$ which consists of $N_S \geq 2$ indices in the vicinity of $\hat{C}$, e.g., $\mathcal{S} = \{\hat{C} - 1, \hat{C}, \hat{C} + 1\}$ for $N_S = 3$. Next, we find a representation of $\boldsymbol{y}$ in the subspace spanned by the dictionary atoms in $\mathcal{S}$ and compare it to the representation of a wavefront from the azimuth angle $(\hat{C} + \bar{\epsilon}) \cdot \Delta$ in the same subspace. The grid offset $\bar{\epsilon}$ which provides the best match is chosen as the final estimate.

More precisely, let $\boldsymbol{U}^{(S)} \in \mathbb{C}^{M \times 2N_S}$ be an orthonormal basis for the subspace spanned

by the dictionary atoms in $\mathcal{S}$, i.e., $\boldsymbol{U}^{(S)} = \boldsymbol{A}^{(S)} \cdot \left(\boldsymbol{A}^{(S)^H} \cdot \boldsymbol{A}^{(S)}\right)^{-\frac{1}{2}}$.

$$\boldsymbol{A}^{(S)} = [\boldsymbol{A}(S_1 \cdot \Delta), \cdots, \boldsymbol{A}(S_{N_S} \cdot \Delta)] \in \mathbb{C}^{M \times 2N_S}. \tag{3.37}$$

Then, a representation of $\boldsymbol{y}$ in the subspace spanned by the dictionary atoms in $\mathcal{S}$ is given by $\boldsymbol{\alpha} = \boldsymbol{U}^{(S)^H} \cdot \boldsymbol{y} \in \mathbb{C}^{2N_S \times 1}$. A wavefront with the azimuth angle $\theta = (C + \bar{\epsilon} \cdot \Delta$, the polarization state $\boldsymbol{p}$ and the amplitude $\boldsymbol{s}$ is expanded in $\boldsymbol{U}^{(S)}$ via

$$\hat{\boldsymbol{\alpha}}(\bar{\epsilon}) = \boldsymbol{U}^{(S)^H} \cdot \boldsymbol{A}((C + \bar{\epsilon}) \cdot \Delta) \cdot \boldsymbol{p} \cdot \boldsymbol{s} = \boldsymbol{D}(\bar{\epsilon}) \cdot \boldsymbol{p} \cdot \boldsymbol{s}, \tag{3.38}$$

where $\boldsymbol{D}(\bar{\epsilon}) = \boldsymbol{U}^{(S)^H} \cdot \boldsymbol{A}((C + \bar{\epsilon}) \cdot \Delta) \in \mathbb{C}^{2N_S \times 2}$.

To compare $\hat{\alpha}(\bar{\epsilon})$ with α, we need to eliminate the unknown polarization state $\boldsymbol{p}$ and amplitude $\boldsymbol{s}$. To this end, note that $\hat{\alpha}(\bar{\epsilon})$ is a linear combination of the columns of the matrix $\boldsymbol{D}(\bar{\epsilon})$. Therefore, we can find $\bar{\epsilon}$ by maximizing the overlap between α and the column space of $\boldsymbol{D}(\bar{\epsilon})$, which eliminates the unknown polarization state and amplitude. We therefore propose the following cost function for finding the grid offset

$$\begin{aligned} \hat{\bar{\epsilon}} &= \arg\min J_1(\bar{\epsilon}), \\ \text{where} \quad J_1(\bar{\epsilon}) &= \|\alpha - \boldsymbol{D}(\bar{\epsilon}) \cdot \boldsymbol{D}(\bar{\epsilon})^+ \cdot \alpha\|_2^2. \end{aligned} \tag{3.39}$$

Multiple Sources

For deriving (3.39), we have assumed that there is a single source only. In the presence of multiple sources, the search strategy depends on their angular distance. Similar to Section 3.3.2, if the sources are sufficiently far apart (i.e., more than the spatial bandwidth of the array), the estimator (3.39) can be applied to each source independently. If they are closer, then we should switch to a joint estimation strategy. For instance, for two sources located at $\theta_1 = (C_1 + \bar{\epsilon}_1) \cdot \Delta$ and $\theta_2 = (C_2 + \bar{\epsilon}_2) \cdot \Delta$ we form the set $\mathcal{S}$ to contain $N_S \geq 3$ indices in the vicinity of the estimated $\hat{C}_1$ and $\hat{C}_2$. As in the single source case, let $\boldsymbol{U}^{(S)} \in \mathbb{C}^{M \times 2N_S}$ be an orthonormal basis for the space spanned by the dictionary atoms contained in $\mathcal{S}$. Then the cost function (3.39) becomes

$$\epsilon_1, \epsilon_2 = arg\min \|\tilde{\boldsymbol{\alpha}} - \boldsymbol{D}(\epsilon_1, \epsilon_2) \cdot \boldsymbol{D}(\epsilon_1, \epsilon_2)^+ \cdot \tilde{\boldsymbol{\alpha}}\|_2^2, \tag{3.40}$$

where $\tilde{\boldsymbol{\alpha}} = \boldsymbol{U}^{(S)^H} \cdot \boldsymbol{y} \in \mathbb{C}^{2N_S \times 1}$ and $\boldsymbol{D}(\epsilon_1, \epsilon_2) \in \mathbb{C}^{2N_S \times 4}$ is given by

$$\boldsymbol{D}(\epsilon_1, \epsilon_2) = \boldsymbol{U}^{(S)^H} \cdot [\boldsymbol{A}((\hat{C}_1 + \bar{\epsilon_1}) \cdot \Delta), \boldsymbol{A}((\hat{C}_1 + \bar{\epsilon_1}) \cdot \Delta)].$$

For more than two sources, the extension is straightforward (similar to Section 3.3.2). From a first CS-based recovery with N grid points, we obtain an initial coarse estimate of the sources' locations. Based on it we identify clusters of sources that are closely spaced where the different clusters are sufficiently far apart so that they can be treated independently. For each cluster, we apply a joint estimation of the grid offsets using the single source strategy shown in (3.39), the two-source strategy from (3.40), or an appropriately extended K-source strategy, depending on the number of sources per cluster. Note that for the joint estimation of K sources in one cluster, we need a set $\mathcal{S}$ with at least $N_S \geq K + 1$ indices.

3.4.4 The Cost Function and its Implementation

To solve the cost function presented throughout the chapter (e.g., (3.39)) we resort to iterative methods, such as gradient-descent algorithms. According to our experience, the cost function is well-behaved around its minimum, i.e., it is a smooth and locally convex surface.

A typical realization of the cost function $J_1(\bar{\epsilon})$ is shown in Figure 3.6. We observe that it is a smooth and convex function, which is comparably simple to minimize, e.g., via a gradient descent algorithm. In fact, we have observed that it can often be very well approximated by a quadratic function, which then permits a closed-form solution for finding the minimum. For such a solution, it is already sufficient to sample three points, i.e., the cost function $J_1(\bar{\epsilon})$ needs to be evaluated only three times.

Depending on the type of solver that is used, it has to be evaluated a number of times, where the largest fraction of the computational complexity is spent in computing $\boldsymbol{D}(\epsilon_1, \epsilon_2)$. We therefore discuss now how to obtain this matrix efficiently and how many multiplications this step requires.

Computing the matrix $\boldsymbol{D}(\epsilon_1, \epsilon_2)$ requires evaluating the array manifold $\boldsymbol{A}(\theta)$ at the points $(\hat{C}_k + \bar{\epsilon}_k) \cdot \Delta$ for $k = 1, 2$. In practice, the array manifold is usually obtained by performing measurements in an anechoic chamber. As a result, we have the array manifold at the sampling points that are chosen for the measurement. To find $\boldsymbol{A}(\theta)$ for an arbitrary angle θ, we need to perform interpolation. It has been shown in [163] that the Effective Aperture Distribution Function (EADF) provides an accurate and efficient description of the polarimetric beam pattern and allows for a computationally efficient interpolation based on the DFT. In essence, the polarimetric array response $\boldsymbol{A}(\theta)$ is

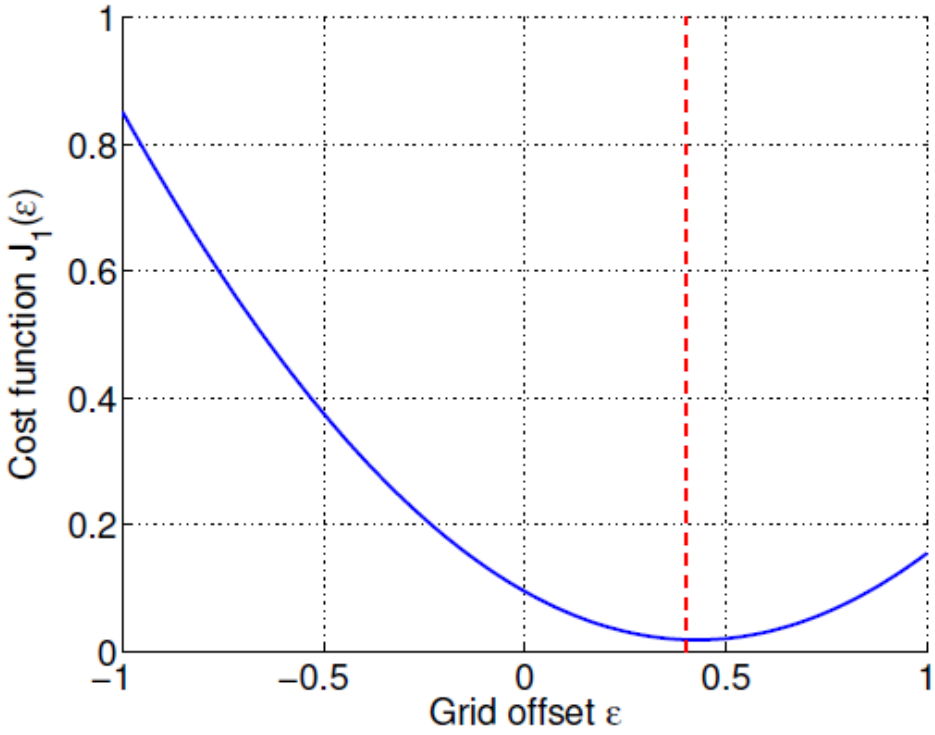

Figure 3.6: A typical realization of the cost function $J_1(\bar{\epsilon})$

computed as

$$\boldsymbol{A}(\theta) = [\boldsymbol{G}_V \cdot \boldsymbol{d}(\theta), \boldsymbol{G}_H \cdot \boldsymbol{d}(\theta) \in \mathbb{C}^{M\times 2}], \tag{3.41}$$

where $\boldsymbol{G}_V \in \mathbb{C}^{M\times N_C}$ and $\boldsymbol{G}_H \in \mathbb{C}^{M\times N_C}$ contain the N_C coefficients for the interpolation of the vertical and the horizontal beam patterns of each port (which are obtained from the measurement of the antenna array) and $\boldsymbol{d}(\theta) = \exp^{-j\theta\mu^T} \in \mathbb{C}^{N_C\times 1}$ with $\mu = \left[-\frac{N_C-1}{2}, \cdots, \frac{N_C-1}{2}\right]$ represents the interpolating DFT vector.

Based on (3.41), we find $\boldsymbol{D}(\epsilon_1, \epsilon_2)$ via

$$\begin{aligned}\boldsymbol{D}(\epsilon_1, \epsilon_2) = [&\tilde{\boldsymbol{G}}_V \cdot \boldsymbol{d}\left((\hat{C}_1 + \bar{\epsilon}_1)\cdot\Delta\right), \tilde{\boldsymbol{G}}_H \cdot \boldsymbol{d}\left((\hat{C}_1 + \bar{\epsilon}_1)\cdot\Delta\right), \\ &\tilde{\boldsymbol{G}}_V \cdot \boldsymbol{d}\left((\hat{C}_2 + \bar{\epsilon}_2)\cdot\Delta\right), \tilde{\boldsymbol{G}}_H \cdot \boldsymbol{d}\left((\hat{C}_2 + \bar{\epsilon}_2)\cdot\Delta\right)],\end{aligned} \tag{3.42}$$

where $\tilde{\boldsymbol{G}}_V = \boldsymbol{U}^{(S)^H} \cdot \boldsymbol{G}_V \in \mathbb{C}^{2N_S\times N_C}$ and $\tilde{\boldsymbol{G}}_H = \boldsymbol{U}^{(S)^H} \cdot \boldsymbol{G}_H \in \mathbb{C}^{2N_S\times N_C}$. Based on (3.42), the matrix $\boldsymbol{D}(\epsilon_1, \epsilon_2)$ can be computed via $8N_S \times N_C$ complex multiplications[3].

[3]The computational complexity required for this step can be additionally reduced by exploiting the symmetry of the complex exponentials as in [163]

The subsequent calculations that are necessary to compute the cost function (3.39) are significantly less complex since they are independent of N_C (and M) and only depend on the (much smaller) N_S. Overall this demonstrates that our proposed cost function can be calculated very efficiently based on the EADF which leads to an estimator with an overall low computational complexity.

3.5 Numerical Results

3.5.1 CS based DOA Estimation off the Grid

In this section, we evaluate our algorithm for CS-based DOA estimation off the grid without considering the polarization. We consider $M = 8$ sensors and a single snapshot t. The noise samples are drawn from a zero mean circularly symmetric complex Gaussian distribution with variance P_{N}. The symbols s_k are generated according to $s_k = \mathrm{e}^{\jmath\varphi_k}$, where φ_k are i.i.d. uniformly distributed random variables in $[0, 2\pi]$. We depict the mean square estimation error of the spatial frequencies vs. the SNR $= 1/P_{\mathrm{N}}$.

We compare the following strategies: "Nearest", "2-term single" and "2-term joint" refer to choosing the nearest grid point, applying (3.19), and solving (3.30), respectively, where the support has been estimated using the BP algorithm [97]. For reference, we depict the performance of the OGSBI algorithm [121] and the ℓ1-SVD [29] using three refinement steps. Note that the computational complexity of both reference schemes is higher than our proposed solutions. We also show the deterministic Cramér-Rao Bound (CRB).

Figure 3.7 shows the performance for a single source at $7.1 \cdot \Delta$ and $P = 6$. We observe that the estimator (3.19) successfully finds the grid offset and the resulting estimator achieves the CRB.

In the case of two sources, Figure 3.8 shows the MSE vs. SNR for a case where the spatial separation $\mu_2 - \mu_1 = 2 \cdot P \cdot \Delta$, i.e., the sources are relatively far from each other. In this case, applying the estimator (3.19) separately provides accurate estimates with a small bias becoming visible only at very high SNRs. Moreover, the solution of (3.30) achieves the CRB.

Figure 3.9 depicts the MSE vs. the spatial separation $\Delta\mu$ where the SNR is fixed to 30 dB and we have $\mu_1 = 0.75 \cdot \Delta$, $\mu_2 = \mu_1 + \Delta\mu$. We observe that the single-source approximation scheme works reasonably well until a separation of $P \cdot \Delta$ which is the lower limit derived in [122]. Below it, the mutual influence becomes too strong. On the other hand, the joint estimator still works very well for distances below this limit and outperforms the more complex ℓ1-SVD and the OGSBI algorithm.

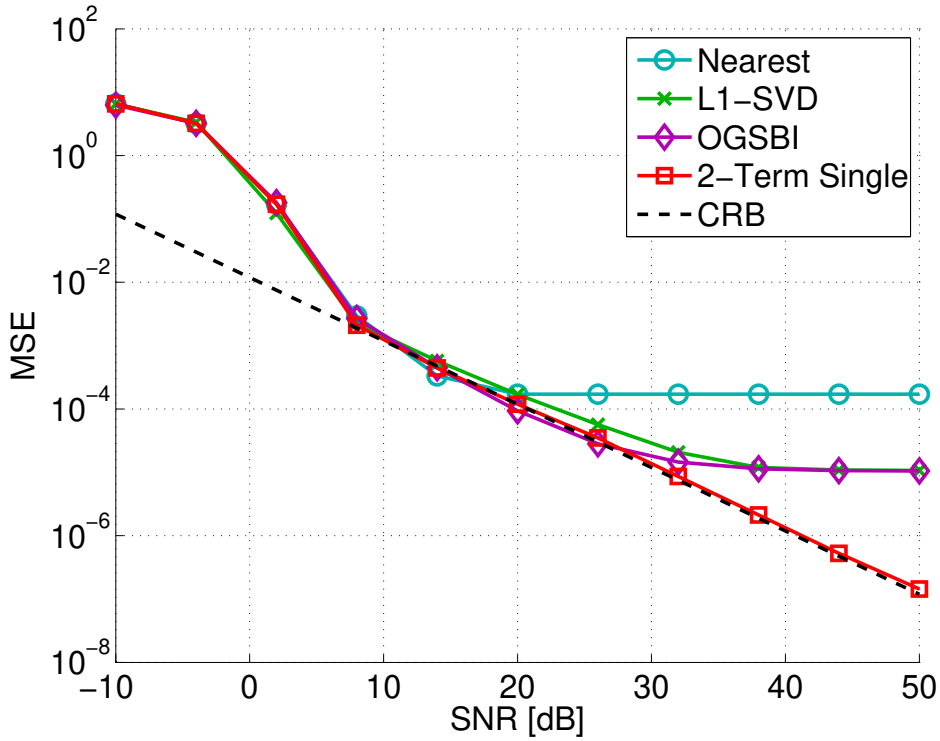

Figure 3.7: MSE vs. SNR for $P = 6$, one source at $\mu = 7.1 \cdot \Delta$

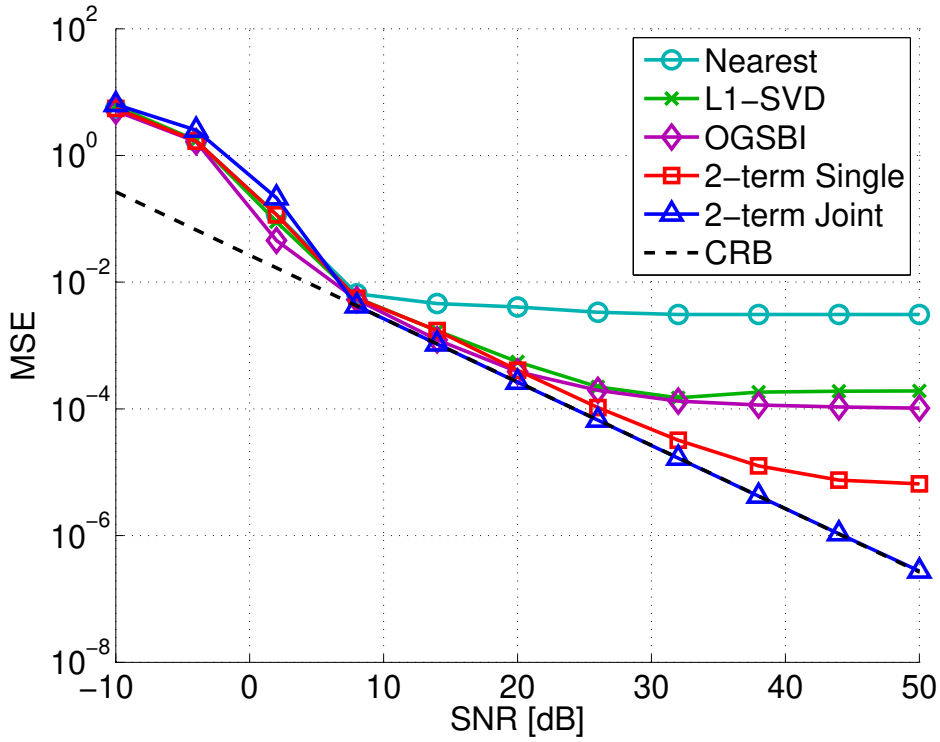

Figure 3.8: MSE vs. SNR for $P = 8$, two sources at $\mu_1 = 12.4 \cdot \Delta$, $\mu_2 = 28.4 \cdot \Delta$, i.e., $\mu_2 - \mu_1 = 2 \cdot P \cdot \Delta$

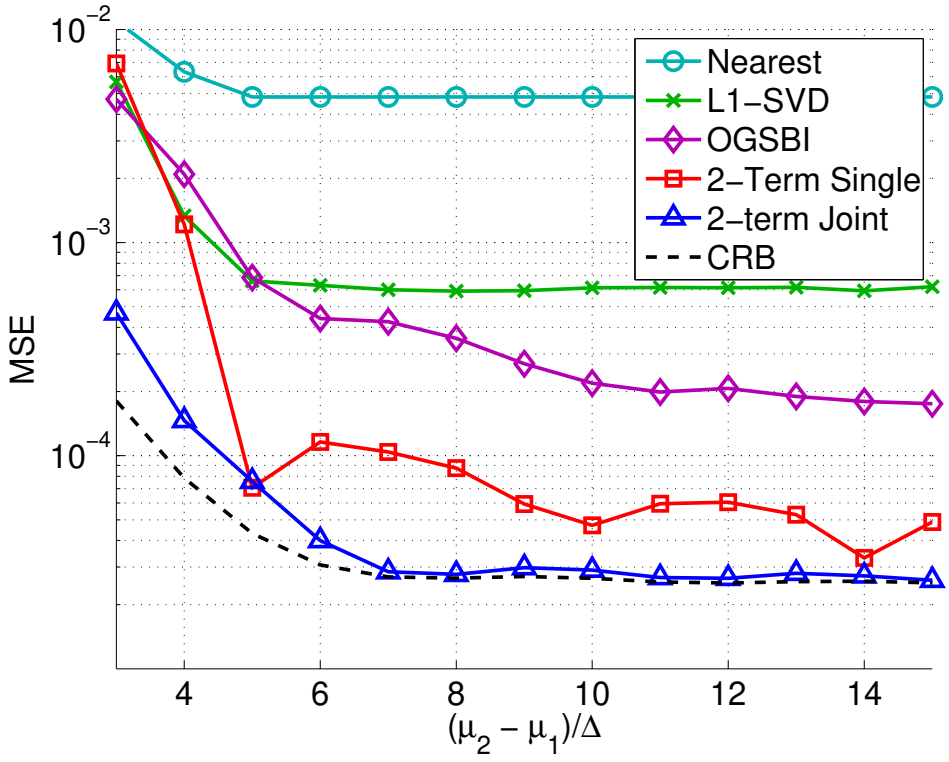

Figure 3.9: MSE vs. $\Delta\mu$ for $P = 4$, $\mu_1 = 0.75 \cdot \Delta$, $\mu_2 = \mu_1 + \Delta\mu$

3.5.2 Polarimetric CS DOA Estimation off the Grid

We now turn our attention to assess the performance of the CS-based *polarimetric* DOA estimation approach. We employ an 8-element (16-port) Polarimetric Uniform Linear Patch Array (PULPA) and a 48-element (96- port) Stacked Polarimetric Uniform Circular Patch Array (SPUCPA) which consists of four rings of 12-element uniform circular arrays. The polarimetric array manifold $\boldsymbol{A}(\theta)$ was measured in an anechoic chamber for both antenna arrays by our Electronic Measurement Lab in Ilmenau. Based on the measured manifolds, we create synthetical measurement data according to (3.31), where θ_k, $\boldsymbol{p}_k$ and $\boldsymbol{s}_k$ are chosen manually and the noise samples $\boldsymbol{n}(t)$ are drawn from an i.i.d. circularly symmetric complex Gaussian random process with zero mean and variance σ_n^2.

Impact of the Sparse Recovery Algorithm

We first study the impact of the sparse recovery scheme used in the first step of our proposed estimator. To this end, we compare four different approaches: the ℓ_1-type BP algorithm [97], its group sparsity extension "Group BP" (GBP) [161], the greedy OMP algorithm [106] and its structured sparsity version "Block OMP" (BOMP) [162].

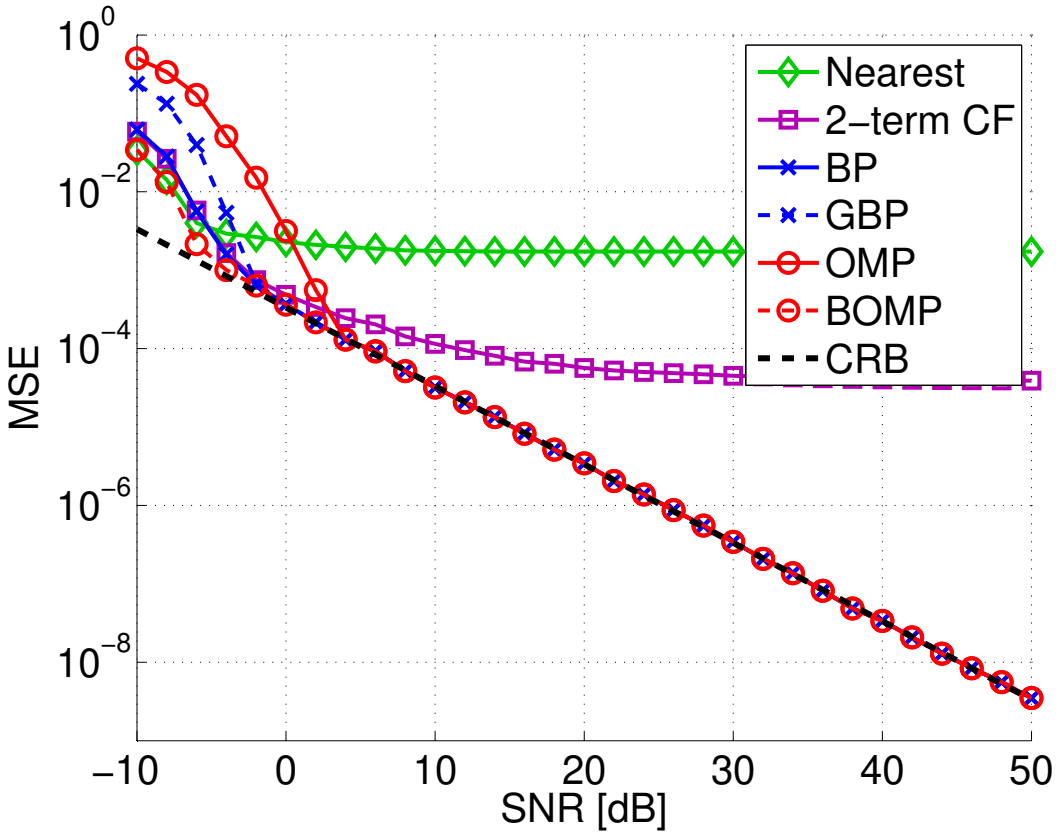

Figure 3.10: MSE vs. the SNR for two sources

For reference, we also show the MSE resulting from an estimator that selects the DOA corresponding to the grid point with the largest amplitude ("Nearest") as well as the single-source closed-form estimator shown in (3.36) ("2-term CF") and the Deterministic Cramér-Rao Bound (CRB).

We start by using the PULPA and consider two wavefronts at $\theta_1 = 3.94°$ and $\theta_2 = 24.19°$, both diagonally polarized ($\boldsymbol{p1} = \boldsymbol{p2} = [1,1]^T/\sqrt{2}$). The amplitudes are chosen according to $s_1 = 1$ and $s_2 = j$. Moreover, we set $P = 4$, i.e., we discretize the manifold using $N = 64$ grid points. Therefore, the grid offsets are given by $\epsilon_1 = 0.3$ and $\epsilon_2 = 0.7$. The MSE vs. the Signal to Noise Ratio[4](SNR $= \sigma_n^{-2}$) is shown in Figure 3.10.

The results show that all versions of our proposed estimator achieve the CRB in the high SNR regime. They also demonstrate an enhanced behavior of the BOMP compared to OMP for low SNRs. The difference between BP and GBP is not very significant. We observe that the BOMP algorithm performs almost identically well as the ℓ_1-type algorithms. Taking into account that the computational complexity of BOMP is very low, we use it for all the subsequent simulation results. We additionally observe that,

[4]This is the SNR before the antenna array, i.e., it does not include the gain of the antenna elements.

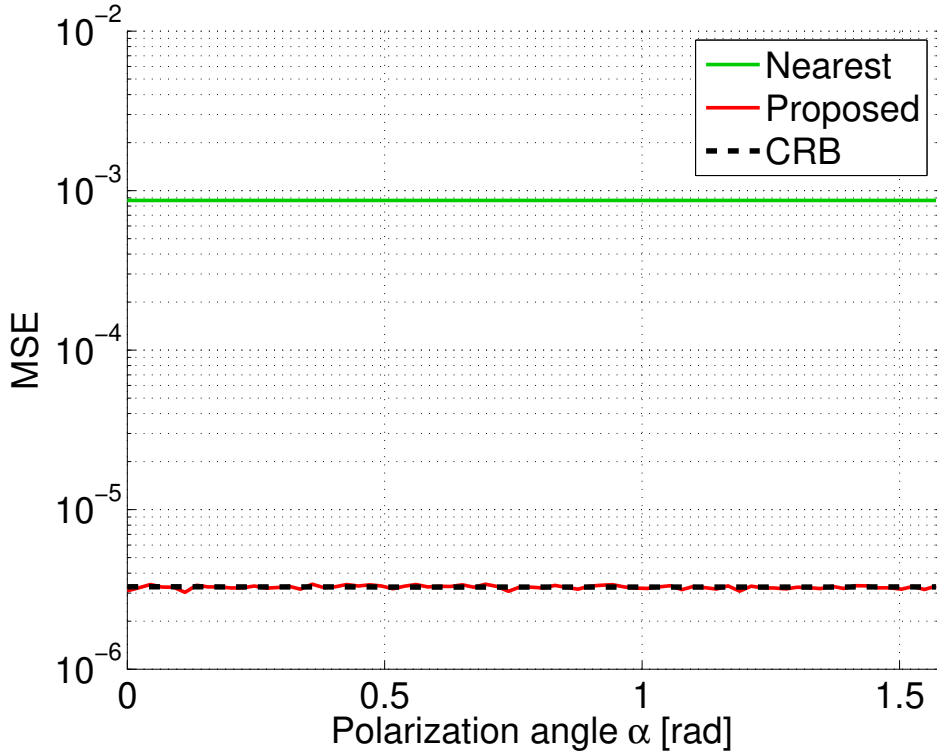

Figure 3.11: MSE vs. the polarization angle α for one source

while the two-term CF strategy still achieves a significant improvement over the initial grid-based estimate ("Nearest"), it does not provide an efficient estimate. Therefore, we do not consider it in the subsequent simulations.

Performance of the Proposed Estimator

For the following simulation results, the set of curves labeled "Proposed" refers to the solution of the cost functions (3.39) and (3.42) combined with the BOMP for the sparse recovery step. We choose $N_S = K + 1$. For the first set of simulation results we use the 8-element PULPA and set $P = 4$. For the scenario shown in Figure 3.11, we consider one wavefront at $\theta_1 = 3.94°$ with an amplitude of $s_1 = 1$. We fix the noise variance to $\sigma_n^2 = 0.1$. To demonstrate that our estimator is capable of handling arbitrary polarization states, we choose the Jones vector according to $\boldsymbol{p}_1 = [cos(\alpha), sin(\alpha)]^T$ and vary α from 0 to $\pi/2$. Figure 3.11 shows the mean square estimation error (MSE) vs. the polarization angle α. We observe that the "Proposed" estimator significantly improves over the initial grid ("Nearest") and attains the CRB for all polarization states.

To investigate the effect of the phase offset between two coherent wavefronts, in the next experiment we choose the amplitudes of $K = 2$ sources as $s_1 = 1$ and $s_2 = e^{j\phi}$

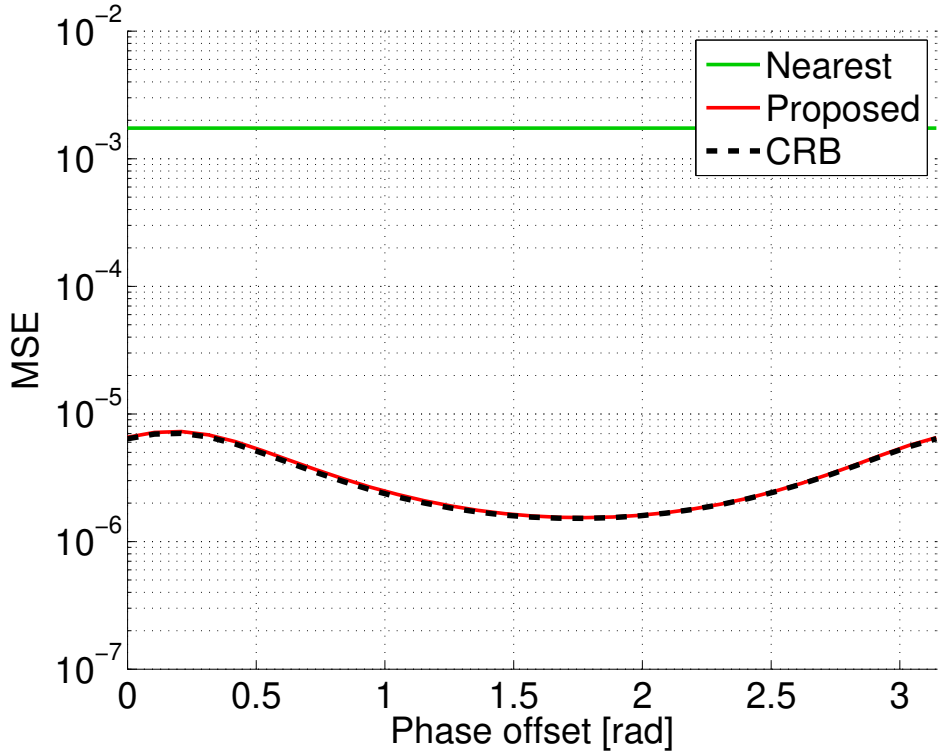

Figure 3.12: MSE vs. the polarization angle α for two sources

and vary ϕ between 0 and π. The azimuth angles are fixed to $\theta_1 = 3.94°$ and $\theta_2 = 7.88°$. Figure 3.12 shows that our proposed algorithm still follows the CRB. Moreover, it demonstrates that the phase offset affects the performance, since it leads to either constructive or destructive interference for coherent sources.

To demonstrate that our proposed algorithm finds the grid offset for any value of ϵ, we consider a single-source case with amplitude one, diagonal polarization, and a fixed SNR of 10 dB and vary the grid offset ϵ by choosing $\theta = \epsilon \cdot \Delta$ for ϵ from 0.1 to 0.9. Figure 3.13 shows that our proposed algorithm always achieves the CRB independent of the grid offset.

Another important aspect is the resolution capability of our proposed algorithm which we investigate by considering two closely spaced sources. We fix one source at $\theta_1 = 3.94°$ and vary the distance of the second source by choosing $\theta_2 = \theta_1 + \Delta\theta$ for $\Delta\theta$ between 1 deg to 30°. Note that the spatial bandwidth of the array is approximately equal to 30°. Figure 3.14 shows that our algorithm follows the CRB even for very close sources.

We now switch to the 48-element (96-port) Stacked Polarimetric Uniform Circular Patch Array (SPUCPA) and set $P = 2$, i.e., we discretize the manifold using $N = 192$ grid points. We consider a scenario with two wavefronts at $\theta_1 = 1.087°$ and $\theta_2 = 6.672°$,

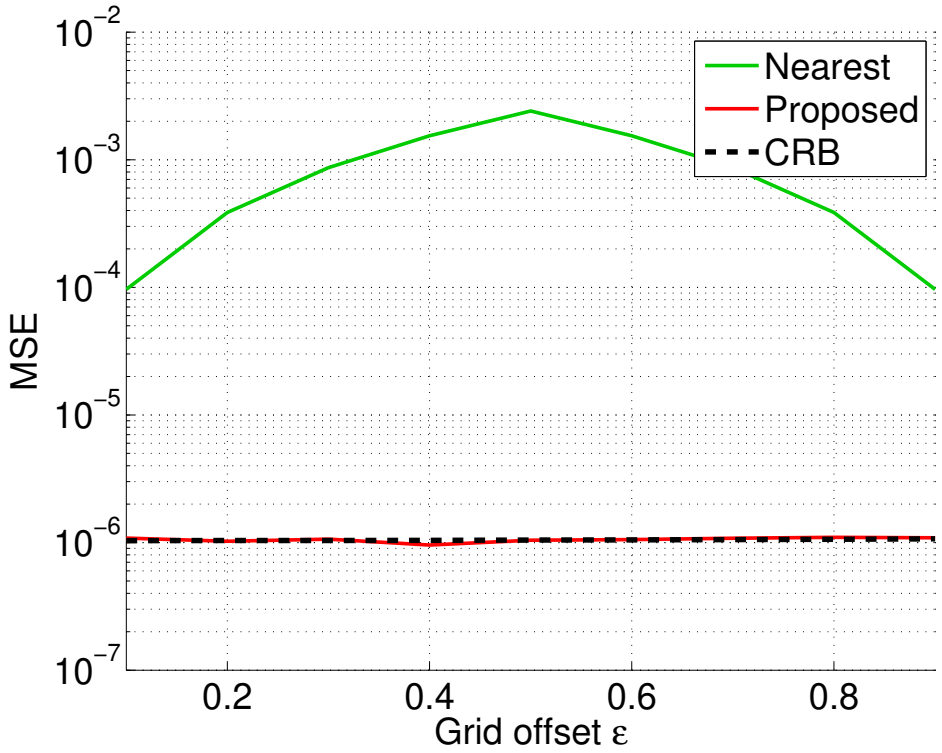

Figure 3.13: MSE vs. the grid offset ϵ for one source

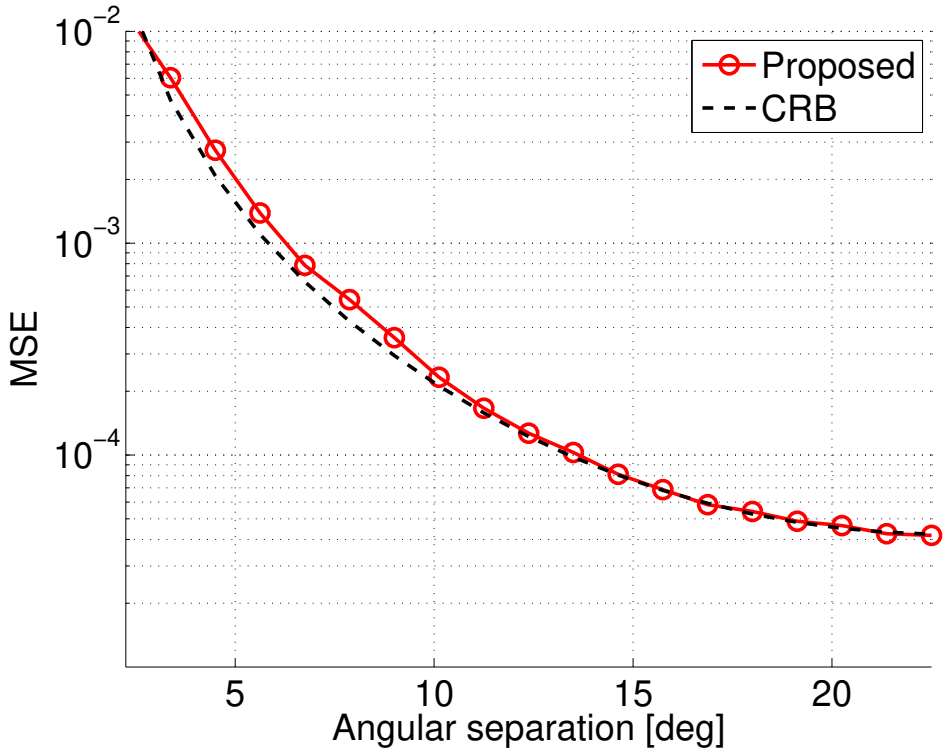

Figure 3.14: MSE vs. the angular separation for two sources

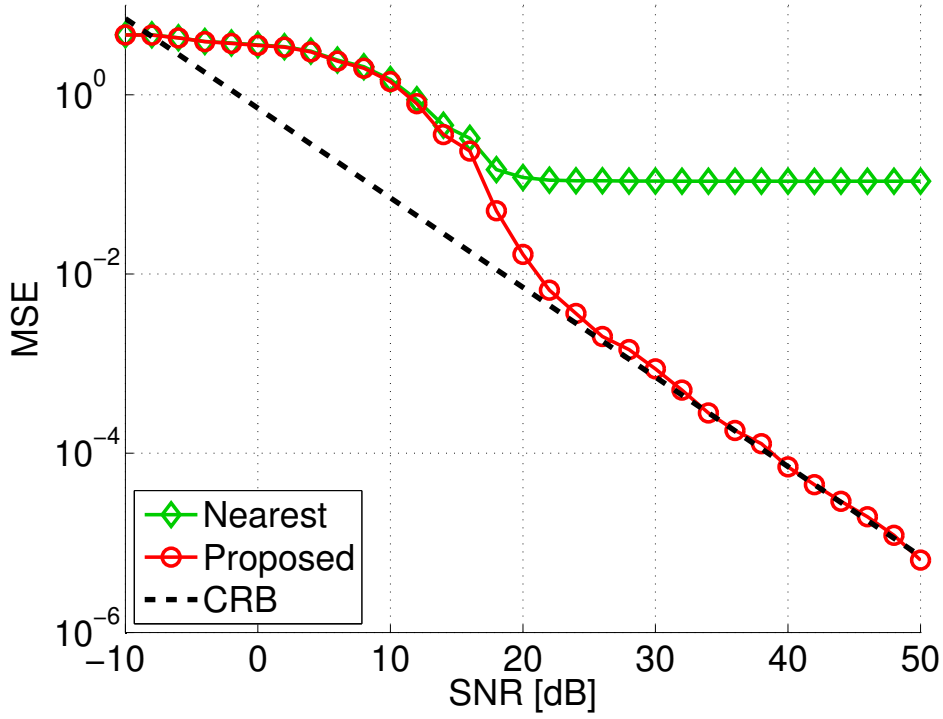

Figure 3.15: MSE vs. the SNR for two sources for the SPUCPA

both diagonally polarized ($\boldsymbol{p}_1 = \boldsymbol{p}_2 = [1,1]^T/\sqrt{2}$). The amplitudes are chosen according to $s_1 = 1$ and $s_2 = j$. Again, the grid offsets are given by $\epsilon_1 = 0.3$ and $\epsilon_2 = 0.7$. The MSE vs. the SNR $= \sigma_n^{-2}$ is shown in Figure 3.15. Our proposed algorithm attains the CRB in the high SNR regime.

3.6 Summary

In this chapter, we address the problem of CS-based DOA estimation for off-grid sources. We study the spectrum in the case of off-grid sources qualitatively and find that most of the energy of the off-grid source after reconstruction is concentrated in the two neighboring grid points. Based on this observation, we derive the best two-term approximation coefficients explicitly and show that the approximation error is very small for $N > M$.

Moreover, based on the asymptotically linear behavior of the coefficients with the grid offset, we propose a very simple scheme to estimate the grid offset based on the observed coefficients. For multiple sources, we show that this simple scheme still works well when they are sufficiently spaced. For closely spaced sources, we propose a numerical procedure for the joint estimation of their offsets from the recovered spectra at their neighboring grid points. Numerical simulations demonstrate the effectiveness of the proposed schemes.

We show that the CS-based formulation of the DOA estimation problem can be extended to the polarimetric model, which gives rise to an amplitude vector that possesses a structured sparsity (with non-zero blocks of size $\times 1$ for each source). We discuss the off-grid problem in the polarimetric setting and propose an estimator for the grid offset of one source (or an isolated source) as well as a joint estimator for the grid offsets of two closely-spaced sources. We show that its cost function can be efficiently calculated based on the EADF, leading to an overall low computational complexity. Numerical results demonstrate that the estimators can recover the DOA regardless of the polarization state of the incoming wave and is applicable to arbitrary arrays. Moreover, it is capable of resolving even very closely-spaced sources and it achieves the Cramér-Rao Bound.

Chapter 4

Compressive Antenna Arrays for Direction of Arrival Estimation

This chapter deals with the analysis and design of compressive arrays for DOA estimation. Section 4.1 motivates the concept of compressive array and reviews the state of the art. In Section 4.2 we present a basic receiver architecture for compressive arrays and introduce a generic system model that includes different options for the hardware implementation. Based on the generic system model, Section 4.3 deals with the design of the combining matrix, with the goal to obtain an array that is suitable for DOA estimation. In Section 4.4, we extend the design approach and propose a design methodology that focuses the array towards a specific area of interest. The optimized design approaches proposed are all in 1D DOA estimation (i.e., azimuth). Section 4.5 provides an analysis of the achievable performance of the proposed compressive arrays for DOA estimation based on two estimation quality measures: the achievable estimation accuracy, and the resolution capabilities. Section 4.6 evaluates the proposed approaches via numerical simulations followed by a summary in Section 4.7.

4.1 Motivation

In general, DOA estimation addresses the problem of locating sources which are radiating energy that is received by an array of sensors with known spatial positions [28]. A major goal in research on DOA estimation is to develop approaches that allow minimizing hardware complexity in terms of receiver costs and power consumption while providing a desired level of estimation accuracy and robustness in the presence of multiple sources and/or multiple paths. Furthermore, the developed methods shall be appropriate for realistic antenna arrays whose characteristics often significantly vary from

commonly considered ideal models [156].

In the last few decades, research on narrow-band DOA estimation using array processing has largely focused on uniform arrays (e.g., linear and circular) [28] for which many efficient parameter estimation algorithms have been developed. Some well-known examples are ESPRIT [164], MUSIC [137] and Maximum Likelihood (ML)-based methods [25, 165]. Note that ML-based methods are particularly suitable for realistic, non-ideal antenna arrays since they can easily account for the full set of parameters of the antenna array (e.g., antenna polarization, non-ideal antennas and array geometries, etc.). However, to perform well, the algorithms require to fulfill certain conditions on the sampling of the wavefront of the incident waves in the spatial domain.

Namely, the distance between adjacent sensors should be less than or equal to half a wavelength of the impinging planar wavefronts, otherwise it leads to grating lobes (sidelobes) in the spatial correlation function which correspond to near ambiguities in the array manifold. At the same time, to achieve DOA estimation with a high resolution, the receiving arrays should have a relatively large aperture [28]. This implies that arrays with a large number of antennas are needed to obtain a high resolution, which is not always feasible.

This limitation has triggered the development of arrays with inter-element spacing larger than half the impinging wave's wavelength combined with specific constraints to control the ambiguity problem in DOA estimation. Such arrays are usually called sparse arrays. In [166], it was proposed to constitute a non-uniform sparse array with elements spaced at random positions. However, using such random arrays will often result in unpredictable behavior of the sidelobes in the array's spatial correlation function. As a result, it is necessary to optimize the positions of the antenna elements in order to achieve a desired performance. An early approach towards that goal was the Minimum Redundancy Linear Array (MRLA) [167], where it is proposed to place the antenna elements such that the number of pairs of antennas which have the same spatial correlation properties are as small as possible. However, it is very difficult to construct an MRLA when the number of elements is relatively large [168]. Some non-linear optimization methods like genetic algorithms [169] and simulated annealing [170] have been regularly used to find optimum configurations for these sparse arrays. Moreover, it is shown in [171] that the optimization of the array aperture with respect to the Cramér-Rao Bound leads to V-shaped arrays. Recently, it was shown that with co-prime arrays [172], and nested arrays [173] it is possible to resolve $\mathcal{O}(N^2)$ of uncorrelated sources with $\mathcal{O}(N)$ sensors, when observed over a large window in time.

Recently, compressive sensing (CS) has been widely suggested for applications that

exhibit sparsity in time, frequency or space to reduce the sampling efforts. The usage of sparse recovery in narrow-band DOA estimation has been considered for applications like localization of transmitting sources [174], channel modeling [153], tracking and surveillance in radar [40], and many others. As mentioned earlier in the previous chapter, if the electromagnetic field is modeled as a superposition of a few plane waves, the DOA estimation problem can be expressed as a sparse recovery problem. The main focus there was to use the sparse recovery algorithms that became popular in the CS field for the DOA estimation problem as an alternative to existing parameter estimation algorithms [151, 175–177].

Compressed sensing has also been suggested to be applied in the spatial domain (e.g., array processing and radar) with the main goal to reduce the complexity of the measurement process by using fewer RF chains and storing less measured data without the loss of any significant information. Hence, the idea of sparse random arrays with increased aperture size has been revisited recently and proposed to perform spatial compressed sensing [178–181].

An alternative approach that attempts to apply CS to the acquisition of the RF signals that are used for DOA estimation has recently been proposed in [45, 150]. In particular, the CS paradigm can be applied in the spatial domain by employing N antenna elements that are combined using an analog combining network to obtain a smaller number of $M < N$ receiver channels. Since only M channels need to be sampled and digitized, the hardware complexity[1] remains comparably low (e.g., consuming less energy and storing less data) while a larger aperture is covered which yields a better selectivity than a traditional, Nyquist ($\lambda/2$) spaced M-channel antenna array.

Note that equipping every antenna with an RF chain may imply a prohibitive hardware complexity (in terms of cost as well as power consumption) in certain applications where reconfigurable arrays with a high gain call for hundreds [182] or even several thousands of antenna elements [183]. Moreover, using a tunable analog combining network, CS-arrays allow to reconfigure the array on the fly without any change in receiver hardware. This advantage in flexibility can be crucial in many applications. A recent example is millimeter wave radio, where one of the major challenges is to solve the gain-resolution dilemma. In order to account for the high pass loss, a high gain is needed while at the same time the full angular domain needs to be scanned [184]. A similar

[1]The hardware complexity (as well as the power consumption) depends on the frequency range, sampling rate/bandwidth, array application, exact realization of the antenna array and its elements, realization of the phase-shifter network, used RF amplifiers and ADC/DAC components, TX/RX switches, filters, etc. As an exact quantization of the hardware cost savings depends on so many factors and our approach is applicable to a wide range of scenarios, we avoid to give concrete numbers in this work.

problem occurs during the target acquisition and high resolution target tracking phases in radar [185]. Because of its flexibility, the compressive hardware architecture is particularly suitable for these applications (see for example [186] for more precise details on the practical implementation of such architectures).

In baseband, the operation of the combining network can be described by complex weights applied to the antenna outputs with a subsequent combination of the received signals from the antennas. The combining (measurement) matrix that contains the complex weights and the antenna array form an effective "compressive" array whose properties define the DOA estimation performance.

In the field of "CS-DOA" it is usually advocated to draw the coefficients of the measurement matrix from a random distribution (e.g., Gaussian, Bernoulli) [45, 150]. Random matrices have certain guarantees for signal recovery in the noise-free case and provide some stability guarantees in the noisy case [66, 67, 187]. However, since no criterion is used to design them, it is likely that they provide sub-optimal performance [4].

In this chapter, we discuss the design and the performance of *compressive* arrays employing linear combinations in the analog domain by means of a network of power splitters, phase shifters, and power combiners. We present a basic receiver architecture of such a compressive array and introduce a generic system model that includes different options for the hardware implementation. Importantly, the model reflects the implications for the noise sources.

Particularly, a well-known source of the receiver noise is the low noise amplifier (LNA) that is usually placed at the antenna outputs to account for the power losses of the following distribution/combining network. Depending on the frequency range, the components of the analog combining network (power combiners, power splitters, phase shifters) will induce additional losses which also have to be compensated by the LNAs. To name an example, some typical commercially available phase shifters for phased array radar applications can induce insertion losses between 5 to 10 dB depending on the frequency range [188] while architectures based on waveguides promise a loss as low as 3 dB [183]. This motivates the need for the signal amplification prior to the combining network.

Based on the generic system model we then discuss the design of the combining matrix, with the goal to obtain an array that is suitable for DOA estimation (i.e., minimum variance of DoA estimates and robustness in terms of low side lobe levels or low probability of false detections). We consider two design approaches. The first is based on the spatial correlation function which is a low-complexity scheme that in certain cases even admits a closed-form solution. The second is based on the minimization of the Cramér-Rao Bound (CRB). Our numerical simulations demonstrate that both proposed design approaches have a significant performance improvement compared to the state of the art, namely an array with a randomly chosen combining matrix and a sparse array with optimized sensor positions.

Furthermore, the compressive array is not only superior to the random and sparse arrays with respect to its estimation capabilities but also in terms of its ability to alter its weights on demand and thus facilitate signal-adaptive measurements. The comparison between the proposed designs demonstrates a trade-off between the minimization of the CRB and the increase in the sidelobe level. In the proposed design, the trade-off "CRB vs. sidelobe level" can be controlled by varying the parameters during the optimization. This provides an additional degree of freedom for the system design that is unavailable in case of random and sparse arrays.

It is worth mentioning that similar efforts in spatial domain processing exist in the context of beam space array processing [189–196] and hybrid beamforming [197–199]. In contrast to the element space processing, where signals derived from each element are weighted and summed to produce the array output, the beam space processing is a two-stage scheme. The first stage takes the array signals as an input and produces a set of multiple outputs, which are then weighted and combined to form the array output. These multiple outputs may be thought of as the output of multiple beams. The weights applied to different beam outputs are finally optimized according to a specific optimization criterion [200].

In hybrid beamforming, the main idea is to apply beamforming techniques in both, the analog and the digital domain [201]. This technique has attracted significant research attention in millimeter wave (mmWave) applications [202] for the next-generation indoor and mobile wireless networks [22, 203].

While the overall goal in these areas is similar (reducing the number of digitally processed receiver channels), the actual design criterion for the antenna is entirely different from the one we consider in this work. We aim to obtain an array that is ideally suited for DOA estimation in the sense that it achieves an accurate estimate (by minimizing the CRB) while controlling the sidelobe characteristics.

4.2 Compressive Arrays

Consider K narrowband plane waves impinging on an array of N antenna elements. At the antenna output, the received (baseband) signal can be expressed as

$$\boldsymbol{y}(t) = \sum_{k=1}^{K} \boldsymbol{a}(\boldsymbol{\gamma}_k) \cdot s_k(t) + \boldsymbol{n}(t), \tag{4.1}$$

where $\boldsymbol{y}(t) \in \mathbb{C}^{N\times 1}$ is a vector of antenna outputs, $\boldsymbol{n}(t) \in \mathbb{C}^{N\times 1}$ is an additive noise vector, t indicates the continuous time, and $\boldsymbol{a}(\boldsymbol{\gamma})$ denotes the antenna response as a function of the parameter vector $\boldsymbol{\gamma}$ with $\boldsymbol{\gamma}^{\mathrm{T}} = [\theta, \psi, \boldsymbol{p}^{\mathrm{T}}]$ where θ and ψ are the azimuth and elevation angles and $\boldsymbol{p} \in \mathbb{C}^{2\times 1}$ represents the Jones vector that describes the polarization state of the incident plain wave at the receiver. Additionally, $s_k(t)$ in (4.1) denotes the amplitude of the kth source, whereas $\boldsymbol{\gamma}_k^{\mathrm{T}} = [\theta_k, \psi_k, \boldsymbol{p}_k^{\mathrm{T}}]$ is the vector containing its azimuth (θ_k) and elevation (ψ_k) angles of arrival along with its Jones vector $\boldsymbol{p}_k^{\mathrm{T}} = [p_{k,1}, p_{k,2}]$. Similar to the previous chapter, it is often useful to write (4.1) in a matrix form as

$$\boldsymbol{y}(t) = \boldsymbol{A} \cdot \boldsymbol{s}(t) + \boldsymbol{n}(t). \tag{4.2}$$

Here, $\boldsymbol{A} = [\boldsymbol{a}(\boldsymbol{\gamma}_1), \boldsymbol{a}(\boldsymbol{\gamma}_2), \cdots, \boldsymbol{a}(\boldsymbol{\gamma}_K)] \in \mathbb{C}^{N\times K}$ is the array steering matrix and $\boldsymbol{s}(t) = [s_1(t), s_2(t), \cdots, s_K(t)]^{\mathrm{T}} \in \mathbb{C}^{K\times 1}$ is a vector containing the complex amplitudes of the K sources.

The model in (4.2) presumes a dedicated radio frequency (RF) receiver chain for each individual antenna element including a low-noise amplifier (LNA), filters, down-conversion, analog-to-digital (ADC) conversion, etc. For specific applications, however, such separate RF chains for each antenna element may come at a high cost in terms of the overall receiver complexity, the amount of data to be processed in the digital domain (e.g., FPGA) and power consumption.

To further illustrate our point, we show an example from [186] with some realistic design parameters for a phased antenna array for aeronautical applications at Ka-band (Rx-direction) in Table 4.1. Considering a typical array gain of 40 to 45 dBi, the number of required elements of the array is larger than 20,000. Considering the practical implementation of the RF chain including the low noise amplifier and ADC associated with each antenna element and all the baseband connections, it turns out that a fully digital realization of the beamforming network for such an array would not be possible. In order to reduce the hardware complexity, analog or hybrid combining/beamforming networks like the one we investigate here are typically considered for such arrays.

Antenna Size	0.75 m (edge size of squared phased array)
Frequency	19.7 GHz (Ka band)
Antenna Efficiency	0.7
Antenna Elements	21609 (assuming $\lambda/2$ spacing)
Element gain	2.5 dB (per radiating element, e.g., patch) (assuming $\lambda/2$ spacing)
Antenna Gain	44.3 dBi (as a function of effective area)

Table 4.1: Realistic design parameters for a phased antenna array for aeronautical applications at Ka-band [186].

In order to reduce the number of RF channels without a loss in the array aperture, we apply the *compressive* approach, where the antenna outputs are first linearly combined in the analog domain and then passed through a lower number of RF chains to obtain the digital baseband signals as illustrated in Figure 4.1. In this way, M RF receiver channels (fewer than the N antenna elements) are used for signal processing in the digital domain. Such a compressive architecture allows reconfiguring the array on the fly without any change in the receiver hardware which can be very advantageous in many applications.

The signal combining can be done at different stages within the receiver, e.g., on the RF (Radio Frequency) signal or at the IF (Intermediate Frequency) stage. The particular choice on where to place the combining network highly depends on the application, especially the considered frequency. In any case, additional signal losses will be introduced by the power splitters and combiners as well as the phase shifters inside the combining network. The actual losses' value will depend on multiple parameters including frequency, bandwidth and adaptability of the phase shifters. However, these losses need to be compensated by LNAs placed in each receiver chain as shown in Figure 4.1.

To this end, let $\boldsymbol{\Phi} \in \mathbb{C}^{M \times N}$ denote the analog combining matrix of a compressive array which compresses the output of N antenna elements to M active RF channels. Then, the complex (baseband) antenna output (4.2) after combining can be expressed as

$$\tilde{\boldsymbol{y}}(t) = \boldsymbol{\Phi}\left(\boldsymbol{A} \cdot \boldsymbol{s}(t) + \boldsymbol{v}(t)\right) + \boldsymbol{w}(t), \tag{4.3}$$

where $[\boldsymbol{\Phi}]_{m,n} = \alpha_{m,n} e^{\jmath\varphi_{m,n}}, \alpha_{m,n} \in [0,1], \varphi_{m,n} \in [0, 2\pi], m = 1, 2, \cdots M, n = 1, 2, \cdots, N$, whereas $\boldsymbol{v}(t) \in \mathbb{C}^{N \times 1}$ and $\boldsymbol{w}(t) \in \mathbb{C}^{M \times 1}$ are noise vectors with covariance matrices $\boldsymbol{R}_{\text{vv}}$ and $\boldsymbol{R}_{\text{ww}}$ that represent additive noise sources which act before and after the combining network, respectively.

For example, LNAs placed ahead the combining network contribute to $\boldsymbol{v}(t)$ (signal noise), whereas the ones placed behind the combining network contribute to $\boldsymbol{w}(t)$ (measurement noise).

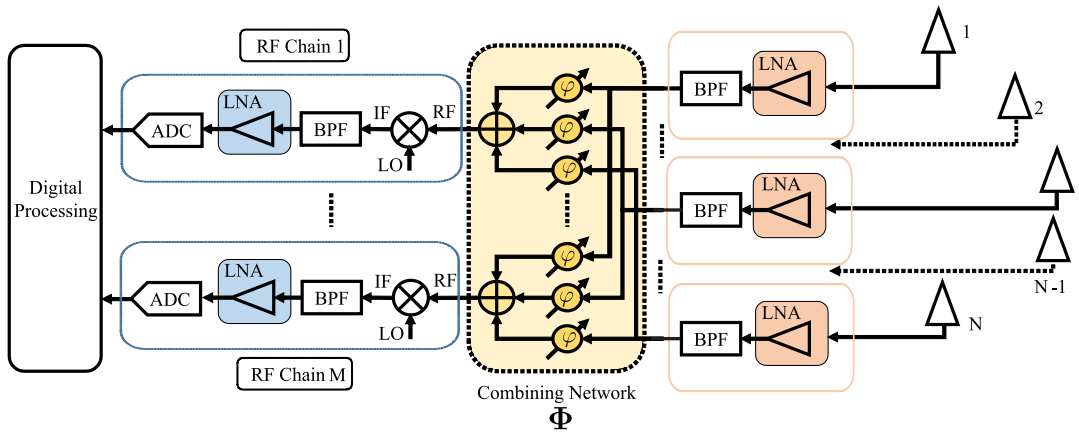

Figure 4.1: Compressive array hardware architecture [8]

Let $\tilde{\boldsymbol{A}} = \boldsymbol{\Phi} \cdot \boldsymbol{A}$ be the effective array steering matrix after combining, then (4.3) becomes

$$\tilde{\boldsymbol{y}}(t) = \tilde{\boldsymbol{A}} \cdot \boldsymbol{s}(t) + \tilde{\boldsymbol{n}}(t), \tag{4.4}$$

where

$$\tilde{\boldsymbol{n}}(t) = \boldsymbol{\Phi} \cdot \boldsymbol{v}(t) + \boldsymbol{w}(t) \tag{4.5}$$

is the effective noise vector with covariance $\boldsymbol{R}_{\mathrm{nn}} = \boldsymbol{\Phi}\boldsymbol{R}_{\mathrm{vv}}\boldsymbol{\Phi}^{\mathrm{H}} + \boldsymbol{R}_{\mathrm{ww}}$. Assuming that $\boldsymbol{v}(t)$ and $\boldsymbol{w}(t)$ are white with elements that have variance σ_1^2 and σ_2^2, respectively, the covariance of $\tilde{\boldsymbol{n}}(t)$ becomes $\boldsymbol{R}_{\mathrm{nn}} = \sigma_1^2\boldsymbol{\Phi}\boldsymbol{\Phi}^{\mathrm{H}} + \sigma_2^2\mathbf{I}_M$. Finally, we define the input SNR as

$$\rho = \frac{P_{\mathrm{s}}}{\mathbb{E}\left\{\|\boldsymbol{R}_{\mathrm{nn}}\|_2^2\right\}} = \frac{P_{\mathrm{s}}}{\sigma_1^2\|\boldsymbol{\Phi}\boldsymbol{\Phi}^{\mathrm{H}}\|_{\mathrm{F}} + M\sigma_2^2}, \tag{4.6}$$

where $P_{\mathrm{s}} = \mathbb{E}\left\{\|\boldsymbol{s}(t)\|_2^2\right\}$ and $\|\cdot\|_{\mathrm{F}}$ denotes the Frobenius norm.

Given (4.4), we aim to design $\boldsymbol{\Phi}$ in a way that allows for robust and efficient estimation of the DOAs of the K sources $s_k(t)$ from the set of measurements $\tilde{\boldsymbol{y}}(t)$. Hence, our main design goal includes the minimization of the number of the receiver chains while providing a minimum variance of the DOA estimates and a reduced probability of spurious and/or ghost path estimates (i.e., lower sidelobes in the spatial correlation function).

4.3 Design of the Combining Matrix

4.3.1 Generic Design Approach

Consider the receiver architecture from Figure 4.1 where the combining network is realized by: (i) splitting the analog RF signal of each of the N antennas into $L \leq M$ branches; (ii) applying phase shifts in each of the branches; (iii) adding the branches to form each of the M outputs, which are then passed to the M RF chains. Mathematically, we model this structure by a matrix $\mathbf{\Phi}$ with elements given by

$$[\mathbf{\Phi}]_{m,n} = \begin{cases} \frac{1}{\sqrt{L}} \cdot \eta \cdot \mathrm{e}^{\jmath\varphi_{m,n}} & \text{if } (m,n) \text{ are connected} \\ 0 & \text{otherwise,} \end{cases} \tag{4.7}$$

where the connections between antennas and ports are such that $\mathbf{\Phi}$ has L nonzero elements per column. In (4.7), the factor $\frac{1}{\sqrt{L}}$ represents the power splitting of each antenna's signal to L branches and $\eta \in (0, 1]$ is a scalar parameter that attributes for the fact that each analog branch (consisting of a power splitter, a phase shifter, and a combiner) is non-ideal and incorporates losses. A lossless combining network would correspond to the special case $\eta = 1$.

From (4.7), the combining matrix $\mathbf{\Phi}$ has MN elements that provide MN degrees of freedom for its design. In the CS literature, a typical approach for choosing $\mathbf{\Phi}$ would be to draw $\varphi_{m,n}$ randomly. This, however, only gives little control over the array characteristics. Furthermore, it might result in unwanted effects as high sidelobes and blind spots [4].

Here, we aim at a design of $\mathbf{\Phi}$ that results in an effective array that has desired properties depending on the application scenario, e.g., uniform sensitivity and low cross-correlation for direction finding, adaptive spatial selectivity for parameter estimation during beam tracking, etc. Generally, the design task can be formulated as the following constrained optimization problem

$$\mathbf{\Phi}_{\text{opt}} = \arg\min_{\mathbf{\Phi}} \; J(\mathbf{\Phi}) \quad \text{s.t. } c(\mathbf{\Phi}, \alpha, \beta, \cdots), \tag{4.8}$$

where $J(\mathbf{\Phi})$ is some objective function defined by the scenario and $c(\mathbf{\Phi}, \alpha, \beta, \cdots)$ represents the set of optimization constraints. In the following, we propose two particular formulations of (4.8) for direction finding applications: based on the spatial correlation function (SCF) and the Cramér-Rao Lower Bound (CRB).

For the SCF-based approach, we build our design on the spatial correlation function defined as

$$\rho_\gamma(\boldsymbol{\gamma}_1, \boldsymbol{\gamma}_2) = \tilde{\boldsymbol{a}}(\boldsymbol{\gamma_1})^{\mathrm{H}} \cdot \tilde{\boldsymbol{a}}(\boldsymbol{\gamma}_2), \tag{4.9}$$

where $\tilde{\boldsymbol{a}}(\boldsymbol{\gamma}) = \boldsymbol{\Phi} \cdot \boldsymbol{a}(\boldsymbol{\gamma})$ represents the effective array manifold after combining. The main idea is to design $\boldsymbol{\Phi}$ such that the spatial correlation function $\rho_\gamma(\boldsymbol{\gamma}_1, \boldsymbol{\gamma}_2)$ follows as close as possible some pre-specified target $T(\boldsymbol{\gamma}_1, \boldsymbol{\gamma}_2)$. By defining an appropriate target function, we can provide the desired properties in the spatial correlation function as discussed in the following.

We then compare the SCF based approach to another optimization approach that is based on the specific requirements on the estimation accuracy. More specifically, it aims at improving the accuracy of DOA estimation by designing $\boldsymbol{\Phi}$ such that it minimizes the CRB while keeping the probability of detecting a false direction at a certain (desired) level.

4.3.2 Design Based on the SCF

For the sake of simplicity, we start by assuming that the sources are located in the azimuthal plane of the antenna array. Furthermore, the impinging waves are co-polarized with the antenna array which is assumed to have perfectly matched antennas. Hence, the effective array manifold depends on the azimuth angle θ only, i.e., $\tilde{\boldsymbol{a}}(\boldsymbol{\gamma}_1) = \tilde{\boldsymbol{a}}(\theta_1)$.

Under these assumptions, an ideal generic array for direction finding would satisfy the conditions

$$\rho_\gamma(\theta_1, \theta_2) = \tilde{\boldsymbol{a}}(\theta_1)^{\mathrm{H}} \cdot \tilde{\boldsymbol{a}}(\theta_2) = \begin{cases} \text{const} & \theta_1 = \theta_2 \\ 0 & \theta_1 \neq \theta_2 \end{cases}. \tag{4.10}$$

The first condition guarantees that the array gain is constant over all azimuth angles and makes the array uniformly sensitive, whereas the second condition forces optimal cross-correlation properties to tell signals from different directions apart. However, this is an example for a generic direction finder. For particular applications, the design goal may differ, i.e., constraining on a certain sector of angles only or allowing certain values for the residual cross-correlation. We denote the target function as $T(\theta_1, \theta_2)$, where $T(\theta_1, \theta_2) = \text{const} \cdot \delta(\theta_1 - \theta_2)$ represents the ideal generic array (4.10).

Due to the finite aperture of an N-element array, the target in (4.10) can only be achieved approximately. This allows us to define a criterion for the optimization of $\boldsymbol{\Phi}$

according to the cost function

$$\begin{aligned} e(\boldsymbol{\Phi}, \theta_1, \theta_2) &= \left| \tilde{\boldsymbol{a}}(\theta_1)^{\mathrm{H}} \cdot \tilde{\boldsymbol{a}}(\theta_2) - T(\theta_1, \theta_2) \right| \\ &= \left| \boldsymbol{a}(\theta_1)^{\mathrm{H}} \cdot \boldsymbol{\Phi}^{\mathrm{H}} \cdot \boldsymbol{\Phi} \cdot \boldsymbol{a}(\theta_2) - T(\theta_1, \theta_2) \right| . \end{aligned} \tag{4.11}$$

We can approximate the continuous variables θ_1 and θ_2 by considering the P-point sampling grid $\theta_p^{(\mathrm{G})}, p = 1, 2, \ldots, P$ and define the $P \times P$ matrices $\boldsymbol{E}$ and $\boldsymbol{T}$ according to $\boldsymbol{E}_{(i,j)} = e(\boldsymbol{\Phi}, \theta_i^{(\mathrm{G})}, \theta_j^{(\mathrm{G})})$ and $\boldsymbol{T}_{(i,j)} = T(\theta_i^{(\mathrm{G})}, \theta_j^{(\mathrm{G})})$. Note that since the array manifolds are smooth functions, it is sufficient to choose the sampling grid slightly above Nyquist, i.e., $P = c \cdot N$ where $c > 1$. We typically choose c between 2 and 4 in our experiments. After insertion into (4.11), we obtain

$$\boldsymbol{E} = \left| \boldsymbol{A}^{\mathrm{H}} \cdot \boldsymbol{\Phi}^{\mathrm{H}} \cdot \boldsymbol{\Phi} \cdot \boldsymbol{A} - \boldsymbol{T} \right| . \tag{4.12}$$

Based on (4.12), the quality of $\boldsymbol{\Phi}$ can be assessed by a suitable norm of $\boldsymbol{E}$. As a first step, let us consider the Frobenius norm, i.e., we optimize $\boldsymbol{\Phi}$ according to

$$\boldsymbol{\Phi}_{\mathrm{opt}} = \arg\min_{\boldsymbol{\Phi}} \|\boldsymbol{E}\|_{\mathrm{F}}^2 . \tag{4.13}$$

In the special case[2] where $\boldsymbol{A} \cdot \boldsymbol{A}^{\mathrm{H}} = C \cdot \mathbf{I}_N$, with C being a constant, the optimization problem in (4.13) admits a closed-form solution as shown in the following theorem.

Theorem 1. *Let $\boldsymbol{S} = \boldsymbol{A} \cdot \boldsymbol{T} \cdot \boldsymbol{A}^{\mathrm{H}}$ and let $\boldsymbol{S}_M$ be a rank-M-truncated version of $\boldsymbol{S}$ obtained by setting its $P - M$ smallest eigenvalues to zero. Then the set of optimal solutions to* (4.13) *is given by the set of matrices $\boldsymbol{\Phi}$ that satisfy $\boldsymbol{\Phi}^{\mathrm{H}} \boldsymbol{\Phi} = \boldsymbol{S}_M$.*

Proof. To prove the theorem, we use the fact that for a unitary matrix $\boldsymbol{U}$ and an arbitrary square matrix $\boldsymbol{X}$ we have $\|\boldsymbol{X} \cdot \boldsymbol{U}\|_{\mathrm{F}} = \|\boldsymbol{U} \cdot \boldsymbol{X}\|_{\mathrm{F}} = \|\boldsymbol{X}\|_{\mathrm{F}}$. Since $\boldsymbol{A}$ satisfies $\boldsymbol{A} \cdot \boldsymbol{A}^{\mathrm{H}} = N \cdot \boldsymbol{I}_M$ we can find a matrix $\bar{\boldsymbol{A}} \in \mathbb{C}^{(M-N) \times N}$ such that $\boldsymbol{V} \doteq 1/\sqrt{N} \cdot [\boldsymbol{A}^{\mathrm{T}}, \bar{\boldsymbol{A}}^{\mathrm{T}}]^{\mathrm{T}} \in \mathbb{C}^{N \times N}$ is a unitary matrix. Therefore, we have $\boldsymbol{V} \cdot \boldsymbol{A}^{\mathrm{H}} = \left[\sqrt{N} \cdot \boldsymbol{I}_M, \mathbf{0}_{M \times N-M} \right]^{\mathrm{T}}$.

[2] This condition is, e.g., fulfilled for an ULA if the sampling grid is chosen to be uniform in the spatial frequencies (direction cosines). Moreover, for many arrays the condition is approximately fulfilled (e.g., for UCAs). In this case, the closed-form solution can still be applied as a heuristic method.

The cost function (4.13) can then be rewritten as

$$\begin{aligned}
\|\boldsymbol{E}\|_{\mathrm{F}}^2 &= \left\|\boldsymbol{V}\cdot\boldsymbol{E}\cdot\boldsymbol{V}^{\mathrm{H}}\right\|_{\mathrm{F}}^2 \\
&= \left\| \begin{bmatrix} \sqrt{N}\boldsymbol{I}_M \\ \boldsymbol{0}_{N-M\times M} \end{bmatrix} \boldsymbol{\Phi}^{\mathrm{H}}\boldsymbol{\Phi} \left[\sqrt{N}\boldsymbol{I}_M, \boldsymbol{0}_{M\times N-M}\right] - \boldsymbol{V}\boldsymbol{T}\boldsymbol{V}^{\mathrm{H}} \right\|_{\mathrm{F}}^2 \\
&= \left\| \begin{bmatrix} N\boldsymbol{\Phi}^{\mathrm{H}}\cdot\boldsymbol{\Phi} & \boldsymbol{0}_{M\times N-M} \\ \boldsymbol{0}_{N-M\times M} & \boldsymbol{0}_{N-M\times N-M} \end{bmatrix} - N\cdot \begin{bmatrix} \boldsymbol{A} \\ \bar{\boldsymbol{A}} \end{bmatrix} \boldsymbol{T} \left[\boldsymbol{A}^{\mathrm{H}}, \bar{\boldsymbol{A}}^{\mathrm{H}}\right] \right\|_{\mathrm{F}}^2 \\
&= \left\| N\cdot \begin{bmatrix} \boldsymbol{\Phi}^{\mathrm{H}}\cdot\boldsymbol{\Phi} - \boldsymbol{A}\cdot\boldsymbol{T}\cdot\boldsymbol{A}^{\mathrm{H}} & -\boldsymbol{A}\cdot\boldsymbol{T}\cdot\bar{\boldsymbol{A}}^{\mathrm{H}} \\ -\bar{\boldsymbol{A}}\cdot\boldsymbol{T}\cdot\boldsymbol{A}^{\mathrm{H}} & -\bar{\boldsymbol{A}}\cdot\boldsymbol{T}\cdot\bar{\boldsymbol{A}}^{\mathrm{H}} \end{bmatrix} \right\|_{\mathrm{F}}^2 \\
&= N^2\cdot\left\|\boldsymbol{\Phi}^{\mathrm{H}}\cdot\boldsymbol{\Phi} - \boldsymbol{S}\right\|_{\mathrm{F}}^2 + \text{const},
\end{aligned} \tag{4.14}$$

using the short-hand notation $\boldsymbol{S} = \boldsymbol{A}\cdot\boldsymbol{T}\cdot\boldsymbol{A}^{\mathrm{H}}$. Equation (4.14) demonstrates that the optimization problem is equivalent to finding the best approximation of the matrix $\boldsymbol{S}$ by the matrix $\boldsymbol{\Phi}^{\mathrm{H}}\cdot\boldsymbol{\Phi}$. Since $\boldsymbol{\Phi}$ is an $m\times M$ matrix, the rank of the $M\times M$ matrix $\boldsymbol{\Phi}^{\mathrm{H}}\cdot\boldsymbol{\Phi}$ is less than or equal to $m < M$. Therefore, (4.14) represents a low-rank approximation problem. According to the Eckart-Young theorem, its optimal solution is given by truncating the $M-m$ smallest eigenvalues of $\boldsymbol{S}$. □

In other words, Theorem 1 states that we can find an optimal $\boldsymbol{\Phi}$ by computing a square-root factor of the best rank-M approximation of $\boldsymbol{S}$. Moreover, the following corollary can be found from Theorem 1:

Corollary 1. *Under the conditions of Theorem 1, any matrix $\boldsymbol{\Phi}$ is optimal in terms of the "ideal" target from* (4.10) *if and only if the rows of $\boldsymbol{\Phi}$ have equal norm and are mutually orthogonal.*

Proof. The sampled version of (4.10) is given by a scaled identity matrix, i.e., $\boldsymbol{T} = C\cdot\boldsymbol{I}_N$. Since $\boldsymbol{A}$ is row-orthogonal, it follows that $\boldsymbol{S} = \boldsymbol{A}\cdot\boldsymbol{T}\cdot\boldsymbol{A}^{\mathrm{H}} = C\cdot N\cdot\boldsymbol{I}_M$. As all eigenvalues of $\boldsymbol{S}$ are equal to $C\cdot N$, its eigenvalue decomposition can be written as $\boldsymbol{S} = \boldsymbol{U}\cdot(C\cdot N\cdot\boldsymbol{I}_M)\cdot\boldsymbol{U}^{\mathrm{H}}$, where $\boldsymbol{U}\in\mathbb{C}^{M\times M}$ is an arbitrary unitary matrix. Truncating the $M-m$ "smallest" eigenvalues, we obtain $\boldsymbol{S}_m = C\cdot N\cdot\boldsymbol{U}_m\cdot\boldsymbol{U}_m^{\mathrm{H}}$, where $\boldsymbol{U}_m\in\mathbb{C}^{M\times m}$ contains the first m columns of $\boldsymbol{U}$. Invoking Theorem 1, we have $\boldsymbol{\Phi}_{\mathrm{opt}}^{\mathrm{H}}\boldsymbol{\Phi}_{\mathrm{opt}} = C\cdot N\cdot\boldsymbol{U}_m\cdot\boldsymbol{U}_m^{\mathrm{H}}$ and therefore $\boldsymbol{\Phi}_{\mathrm{opt}}$ is a scaled version of $\boldsymbol{U}_m^{\mathrm{H}}$, which proves the claim. □

Corollary 1 agrees with the intuition that the measurements (i.e., the rows of $\boldsymbol{\Phi}$) should be chosen such that they are orthogonal in order to make every observation as

informative as possible. In addition, the corollary shows that this choice also minimizes $\left\|\boldsymbol{\Phi}^{\mathrm{H}}\boldsymbol{\Phi} - C \cdot P \cdot \mathbf{I}_M\right\|_{\mathrm{F}}$ which contains the correlations between all pairs of columns in $\boldsymbol{\Phi}$ as well as the deviation of the columns' norms (therefore, in a sense, this choice minimizes the "average" mutual correlation). On the other hand, this also demonstrates that the optimization in (4.13) is not sufficiently selective since all row-orthogonal matrices achieve the same minimum of the cost function.

The cost function (4.13) assigns equal weight to the error for all pairs of grid points $\theta_1^{(\mathrm{G})}, \theta_2^{(\mathrm{G})}$, i.e., it tries to maintain the resemblance to the target spatial correlation function $\boldsymbol{T}$ in the mainlobe area with the same weight as in the certain off-diagonal regions that contain the sidelobes. In practice, however, it is often desirable to have more control over the shape of the spatial correlation function. There are many ways additional constraints could be incorporated in the optimization, e.g., maximum constraints on the magnitude of cross-correlation in some region and interval constraints on the autocorrelation inside the mainlobe. For numerical tractability, we follow a simpler approach by introducing a weighting matrix $\boldsymbol{W} \in \mathbb{R}^{P \times P}$ into (4.13). The modified optimization problem is given by

$$\boldsymbol{\Phi}_{\mathrm{opt}} = \arg\min_{\boldsymbol{\Phi}} \|\boldsymbol{E} \odot \boldsymbol{W}\|_{\mathrm{F}}^2 , \tag{4.15}$$

where $\odot$ represents the Schur (element-wise) product. The weighting matrix allows to put more or less weight on the main diagonal certain off-diagonal regions, or even placing zeros for regions that remain arbitrary. Thereby, more flexibility is gained and the solution can be tuned to more specific requirements.

The drawback of (4.15) is that it does not admit a closed-form solution in general. However, it can be solved by numerical optimization routines that are available in modern technical computing languages.

4.3.3 Design Based on the CRB

For the case of a single source, a correlation-based DOA estimator amounts to find the DOA that corresponds to the global maximum in the beamformer spectrum $D(\theta)$

$$D(\theta) = |\tilde{\boldsymbol{a}}^{\mathrm{H}}(\theta)\tilde{\boldsymbol{y}}(t)|^2, \tag{4.16}$$

with $\tilde{\boldsymbol{a}}(\theta) \equiv \boldsymbol{\Phi} \cdot \boldsymbol{a}(\theta)$. Note that in this case, (4.16) is equivalent to the maximum likelihood (ML) cost function, and therefore, the correlation-based DOA estimator is equivalent to the ML estimator. We define then the false detection as the event where

the global maximum in the beamformer spectrum $D(\theta)$ is outside the mainlobe area (either 3-dB or null-to-null beamwidth). The error probability P_d is hence given by

$$P_d \equiv \text{Prob}\big(\exists\theta \in \mathcal{U} : D(\theta_0) < D(\theta)\big), \tag{4.17}$$

where $\mathcal{U}$ denotes the set of DOAs corresponding to the directions in the beamformer spectrum outside the mainlobe area while $\theta_0 \notin \mathcal{U}$ is the true DOA that corresponds to the mainlobe peak.

A direct evaluation of (4.17) is analytically intractable. In [204], an analytic expression for the false detection probability has been derived and given as

$$P_d \leq \frac{1}{2G}\sum_{q=1}^{L}\sum_{g=1}^{G}\hat{\Psi}_q\left(\frac{(2g-1)\pi}{2G}\right) \tag{4.18}$$

The analytic expression for the false detection probability can now be used to optimize the combining matrix $\boldsymbol{\Phi}$ with the objective to improve the CRB while keeping the probability of false detection below some desired level ϵ_0 for a given input SNR ρ_0.

This said, for detection of a single source, we can formulate it as

$$\begin{aligned}\boldsymbol{\Phi}_{\text{opt}} = &\arg\min_{\boldsymbol{\Phi}}\max_{\theta_0}\ \text{CRB}(\boldsymbol{\Phi},\theta_0)\\ &\text{s. t. } P_d(\boldsymbol{\Phi},\theta_0,\rho_0) < \epsilon_0.\end{aligned} \tag{4.19}$$

To derive $\text{CRB}(\boldsymbol{\Phi},\theta_0)$, we use the expression in [28] for the receiver model shown in Figure 4.1 where the noise vectors $\boldsymbol{v}(t)$ and $\boldsymbol{w}(t)$ are assumed to be white with covariances $\boldsymbol{R}_{\text{vv}} = \sigma_1^2\mathbf{I}_N$ and $\boldsymbol{R}_{\text{ww}} = \sigma_2^2\mathbf{I}_M$, respectively. The associated CRB matrix is then found to be

$$\text{CRB}(\boldsymbol{\Phi},\boldsymbol{\theta}) = \sigma_1^2\big(2\text{Re}\left\{\boldsymbol{F}\odot\boldsymbol{R}_s^{\text{T}}\right\}\big)^{-1}, \tag{4.20}$$

where $\odot$ denotes Schur (element-wise) matrix product, $\boldsymbol{R}_s = \boldsymbol{s}(t)\boldsymbol{s}^{\text{H}}(t)$ is the signal covariance matrix, and $\boldsymbol{F}$ is a matrix that depends on the array beam pattern and the combining matrix $\boldsymbol{\Phi}$ as

$$\boldsymbol{F} = \boldsymbol{D}^{\text{H}}\boldsymbol{\Phi}^{\text{H}}\boldsymbol{Z}\boldsymbol{\Phi}\boldsymbol{D}. \tag{4.21}$$

Substituting in (4.21),

$$\begin{aligned}\boldsymbol{Z} &= \boldsymbol{Q}\Big(\mathbf{I}_N - \tilde{\boldsymbol{A}}\Big(\tilde{\boldsymbol{A}}^{\text{H}}\boldsymbol{Q}\tilde{\boldsymbol{A}}\Big)^{-1}\tilde{\boldsymbol{A}}^{\text{H}}\boldsymbol{Q}\Big),\\ \boldsymbol{D} &= \big[\partial\boldsymbol{a}(\theta_0)/\partial\theta_0, \partial\boldsymbol{a}(\theta_1)/\partial\theta_1, ..., \partial\boldsymbol{a}(\theta_{K-1})/\partial\theta_{K-1}\big],\end{aligned}$$

and $\boldsymbol{Q} = (\boldsymbol{\Phi}\boldsymbol{\Phi}^{\mathrm{H}} + \beta \mathbf{I}_N)^{-1}$ where $\beta = \frac{\sigma_2^2}{\sigma_1^2}$. Since we consider only a single source for solving the optimization problem in (4.19), $\boldsymbol{F}$ reduces to a scalar F and $\boldsymbol{R}_s$ to $R_{ss} = \|s(t)\|^2$. Therefore, for a single source (4.20) becomes

$$\mathrm{CRB}(\boldsymbol{\Phi}, \theta_0) = \sigma_1^2 \Big(2F R_{ss}\Big)^{-1} = \frac{1}{2F\zeta}, \tag{4.22}$$

where $\zeta = \frac{R_{ss}}{\sigma_1^2}$ is the input SNR.

Both the constraint and the objective in (4.19) are non-convex functions with respect to $(\boldsymbol{\Phi}, \theta_0)$. The optimization problem is thereby a non-convex problem exhibiting a multi-modal cost function, where the optimal (global) solution can only be found by an exhaustive search strategy. Therefore, we apply a local minimizer to the above problem using an algorithm based on the interior-reflective Newton method [205], [206]. However, by using this algorithm the obtained solution strongly depends on the initialization of the parameters $(\boldsymbol{\Phi}, \theta_0)$. Moreover, there is no guarantee that the global optimum is found.

One way of addressing this issue is to apply the algorithm several times, where for each run the initialization of the parameters $(\boldsymbol{\Phi}, \theta_0)$ is different. In doing so, the obtained solution to (4.19) is likely to be sufficiently close to the optimal solution. However, it might be time consuming due to the complexity of the optimization problem at hand. Another way of tackling this problem is to first obtain a solution for $\boldsymbol{\Phi}$ by the SCF approach described above and then use it for the initialization in (4.19).

So far, we have discussed the case of a single source's wave impinging on the antenna array. However, we can easily extend the CRB design approach to account for the presence of multiple signal sources by applying the full CRB given by (4.20) in (4.19) and modifying the false detection probability expression in (4.18). Particularly, assuming a correlation-based DOA estimator, we need to compute the false detection probability of the strongest source being falsely detected in the presence of $K-1$ weaker ones (see [8] for more details).

4.4 Adaptive Focusing Design

In (4.8), our target is a static combining matrix that yields an array with certain properties, such as uniform sensitivity and low sidelobe level, which is a good choice if no prior knowledge of the targeted sources is available. However, we can extend this approach towards an adaptive design that makes use of the fact that for a slowly changing scene, the estimates from the previous snapshots provide prior information about the

source locations in the next snapshots. This fact can be utilized for adaptive focusing of the array's sensitivity towards regions of interest where the targets are expected [7]. In doing so, the SNR and the effective resolution in these directions of interest can be further improved, resulting in a superior DOA estimation performance. To achieve this, we adopt a sequential measurement strategy which starts with a combining matrix designed for uniform sensitivity and then gradually refine it towards the directions of interest that have been identified in the observations collected so far [7].

The main idea is to design $\mathbf{\Phi}$ such that the spatial correlation function $r(\theta_1, \theta_2) \doteq \tilde{\boldsymbol{a}}(\theta_1)^{\mathrm{H}} \cdot \tilde{\boldsymbol{a}}(\theta_2)$ follows as close as possible to a prespecified target $T(\theta_1, \theta_2)$, i.e., a matrix $\mathbf{\Phi}$ that minimizes

$$e(\mathbf{\Phi}, \theta_1, \theta_2) = |r(\theta_1, \theta_2) - T(\theta_1, \theta_2)| \tag{4.23}$$

The target $T(\theta_1, \theta_2)$ is adapted to the current knowledge of the scene. A uniform target function is used when no prior knowledge is available. When regions of interest have been specified (e.g., via an estimate of the angular power spectrum or a previous reconstructed scene), the target can be adapted to focus on these regions in order to provide a superior estimate (e.g., improved SNR and/or resolution).

To this end, an ideal uniform target function can be described by

$$T_{\mathrm{uni}}(\theta_1, \theta_2) = \begin{cases} \text{const} & \theta_1 = \theta_2 \\ 0 & \theta_1 \neq \theta_2 \end{cases}, \tag{4.24}$$

where the first condition guarantees that the array gain is constant for all angles (to make the array uniformly sensitive in all directions) and the second condition asks for good cross-correlation properties to tell signals from different directions apart.

On the other hand, a target function that focuses in an interval Θ is given by

$$T_{\Theta}(\theta_1, \theta_2) = \begin{cases} \text{const} & \theta_1 = \theta_2 \in \Theta \\ 0 & \theta_1 \neq \theta_2 \end{cases}, \tag{4.25}$$

where the interval Θ can for instance be describe by a center c_θ and a width w_θ via $\Theta = \left[c_\theta - \frac{w_\theta}{2}, c_\theta + \frac{w_\theta}{2}\right]$.

In order to find a matrix $\mathbf{\Phi}$ that minimizes (4.23), we utilize the mechanism introduced earlier in Section 4.3.2 which we restate here for convenience. It is based on the following steps: First, to eliminate the continuous variables θ_1 and θ_2, we consider the N-point sampling grid $\theta_n^{(\mathrm{G})}, n = 1, 2, \ldots, N$ used for CS and define the $N \times N$ matrices

$\boldsymbol{R}$ and $\boldsymbol{T}$ according to $\boldsymbol{R}_{(i,j)} = r(\theta_i^{(\mathrm{G})}, \theta_j^{(\mathrm{G})})$ and $\boldsymbol{T}_{(i,j)} = T(\theta_i^{(\mathrm{G})}, \theta_j^{(\mathrm{G})})$. Note that $\boldsymbol{R}$ can be written as $\boldsymbol{R} = \boldsymbol{A}^{\mathrm{H}} \cdot \boldsymbol{\Phi}^{\mathrm{H}} \cdot \boldsymbol{\Phi} \cdot \boldsymbol{A}$. The deviation between the sampled spatial correlation function $\boldsymbol{R}$ and its target $\boldsymbol{T}$ can then be measured via a suitable norm of the error matrix $\boldsymbol{E} \doteq \boldsymbol{R} - \boldsymbol{T}$. A closed-form solution for $\boldsymbol{\Phi}$ can be obtained if we choose the Frobenius norm of $\boldsymbol{E}$. In particular, if we let

$$\boldsymbol{\Phi}_{\mathrm{opt}} = \arg\min_{\boldsymbol{\Phi}} \|\boldsymbol{E}\|_{\mathrm{F}}^2 . \tag{4.26}$$

we can obtain $\boldsymbol{\Phi}_{\mathrm{opt}}$ via the following procedure: Let $\boldsymbol{S} = \boldsymbol{A} \cdot \boldsymbol{T} \cdot \boldsymbol{A}^{\mathrm{H}}$ and let $\boldsymbol{S}_m$ be a rank-m-truncated version of $\boldsymbol{S}$ obtained by setting its $N - m$ smallest eigenvalues to zero. Then every square-root factor of $\boldsymbol{S}_m$ (i.e., any $\boldsymbol{\Phi}$ satisfying $\boldsymbol{\Phi}^{\mathrm{H}}\boldsymbol{\Phi} = \boldsymbol{S}_m$) is an optimal solution to (4.26) [4].

Since $\boldsymbol{\Phi}_{\mathrm{opt}}$ can be obtained in closed form with a very low computational complexity, it is feasible to adapt it during the observations, i.e., the target can be refined to the current knowledge of the scene.

The adaptation mechanism proceeds as follows:

1. We begin by scanning the scene with a matrix $\boldsymbol{\Phi}$ designed according to (4.13) or (4.15), designed for a uniform target T or according to (4.19) for the full angular range $\theta_0 \in (0, 2\pi]$.

2. Identify regions of interest based on an estimate of the angular power spectrum obtained from the initial observation(s).

3. Define a focusing region Θ as the union of all regions of interest.

4. Modify $\boldsymbol{\Phi}$ by solving (4.26) for a target designed for the focusing region Θ in the SCF-based approach or solving (4.19) with a restricted angular range.

5. As the sources are assumed to change their position gradually, track sources by repeating steps (2) to (4) sequentially, moving the regions of interest along with the currently identified source locations.

6. Every S snapshots, rescan the scene with a matrix $\boldsymbol{\Phi}$ designed for a uniform sensitivity in order to detect newly appearing sources. If new sources are found, incorporate their location into the set Θ.

The parameter S represents a design parameter that determines how quickly the system reacts to sources appearing outside the current direction of interest.

4.5 Estimation Quality

In this section, we provide an analysis of the achievable performance of the proposed compressive arrays for DOA estimation. In the noisy case, there are two main estimation quality measures: the achievable estimation accuracy, and the resolution capabilities.

Estimation Accuracy

For a fixed aperture, the achievable accuracy is mainly determined by the effective SNR at the antenna output. For this reason, we compare the SNR of a compressive array and a sparse array[3] at the same number of active channels M.

We express the output signal for a single source via (4.3) as

$$\tilde{\boldsymbol{y}}(t) = \boldsymbol{\Phi} \cdot \boldsymbol{a}(\boldsymbol{\gamma}_1) \cdot s_1(t) + \tilde{\boldsymbol{n}}(t), \tag{4.27}$$

where the elements of $\boldsymbol{\Phi}$ are given by (4.7) and the covariance of $\tilde{\boldsymbol{n}}(t)$ is given by $\boldsymbol{R}_{\mathrm{nn}} = \sigma_1^2 \boldsymbol{\Phi}\boldsymbol{\Phi}^{\mathrm{H}} + \sigma_2^2 \mathbf{I}_M$. The SNR of the compressed array can then be computed as

$$\begin{aligned} \rho_{\mathrm{c}} &= \frac{\mathbb{E}\left\{\left\|\boldsymbol{\Phi} \cdot \boldsymbol{a}(\boldsymbol{\gamma}_1) \cdot s_1(t)\right\|^2\right\}}{\operatorname{trace}\left\{\boldsymbol{R}_{\mathrm{nn}}\right\}} \\ &= \frac{\left\|\boldsymbol{\Phi} \cdot \boldsymbol{a}(\boldsymbol{\gamma}_1)\right\|^2 \cdot P_{\mathrm{s}}}{\operatorname{trace}\left\{\boldsymbol{\Phi}^{\mathrm{H}}\boldsymbol{\Phi}\right\}\sigma_1^2 + M\sigma_2^2} \\ &= \frac{\operatorname{trace}\left\{\boldsymbol{\Phi} \cdot \boldsymbol{a}(\boldsymbol{\gamma}_1) \cdot \boldsymbol{a}^{\mathrm{H}}(\boldsymbol{\gamma}_1) \cdot \boldsymbol{\Phi}^{\mathrm{H}}\right\} \cdot P_{\mathrm{s}}}{\operatorname{trace}\left\{\boldsymbol{\Phi}^{\mathrm{H}}\boldsymbol{\Phi}\right\}\sigma_1^2 + M\sigma_2^2}, \end{aligned} \tag{4.28}$$

where $P_{\mathrm{s}} = \mathbb{E}\left\{|s_1(t)|^2\right\}$ is the source power.

As evident from (4.28), the SNR is dependent on the parameter vector $\boldsymbol{\gamma}$, i.e., on the DOA. It is therefore meaningful to consider the average SNR over all possible source directions. This requires to compute the average of $g(\boldsymbol{\gamma}) = \left\|\boldsymbol{\Phi} \cdot \boldsymbol{a}(\boldsymbol{\gamma})\right\|^2$ over $\boldsymbol{\gamma}$ which is not possible without further assumptions either about the array or about $\boldsymbol{\Phi}$. Let $\bar{g}$ be the average of $g(\boldsymbol{\gamma})$ over $\boldsymbol{\gamma}$, i.e., $\bar{g} = \Gamma^{-1} \int g(\boldsymbol{\gamma}) \mathrm{d}\boldsymbol{\gamma}$ with $\Gamma = \int 1 \mathrm{d}\boldsymbol{\gamma}$. Moreover, let us define the matrix $\boldsymbol{J} = \Gamma^{-1} \int \boldsymbol{a}(\boldsymbol{\gamma}) \cdot \boldsymbol{a}(\boldsymbol{\gamma})^{\mathrm{H}} \mathrm{d}\boldsymbol{\gamma}$ so that $\bar{g} = \operatorname{trace}\left\{\boldsymbol{\Phi} \cdot \boldsymbol{J} \cdot \boldsymbol{\Phi}^{\mathrm{H}}\right\}$. To proceed, we would like to replace $\bar{g}$ by $\operatorname{trace}\left\{\boldsymbol{\Phi}\boldsymbol{\Phi}^{\mathrm{H}}\right\}$. We can always do so when $\boldsymbol{J} = \mathbf{I}_N$ which implies that the beam patterns of all antennas are orthogonal over the entire parameter space. This is, e.g., fulfilled for an ULA if it is parametrized by spatial frequencies

[3] By sparse arrays we mean here any array that is capable of providing a larger aperture than a "traditional" array with $\lambda/2$-spaced elements, while having a dedicated receiver channel for each antenna element. Examples of sparse arrays include arrays with randomly positioned elements [178–181] as well as nested and co-prime arrays [172, 173].

$\mu = \cos(\theta)$. Furthermore, for $\boldsymbol{J} \neq \mathbf{I}_N$ one can show that $\mathbb{E}_{\boldsymbol{\Phi}}\{\bar{g}\} = \mathbb{E}_{\boldsymbol{\Phi}}\left\{\text{trace}\left\{\boldsymbol{\Phi}\boldsymbol{\Phi}^{\text{H}}\right\}\right\}$ for any random ensemble of $\boldsymbol{\Phi}$ where its elements are i.i.d. Note that in our case, due to (4.7), $\text{trace}\left\{\boldsymbol{\Phi}\boldsymbol{\Phi}^{\text{H}}\right\}$ is not random but deterministic. Hence, the expectation on the right-hand side is not needed. In light of this assumption, we can express the average SNR $\bar{\rho}_{\text{c}}$ (averaged over $\boldsymbol{\gamma}$) as

$$\bar{\rho}_{\text{c}} = \frac{\text{trace}\left\{\boldsymbol{\Phi}\boldsymbol{\Phi}^{\text{H}}\right\} \cdot P_{\text{s}}}{\text{trace}\left\{\boldsymbol{\Phi}^{\text{H}}\boldsymbol{\Phi}\right\}\sigma_1^2 + M\sigma_2^2} = \frac{\|\boldsymbol{\Phi}\|_{\text{F}}^2 \cdot P_{\text{s}}}{\|\boldsymbol{\Phi}\|_{\text{F}}^2\,\sigma_1^2 + M\sigma_2^2} \tag{4.29}$$

Using (4.7) it is easy to see that $\|\boldsymbol{\Phi}\|_{\text{F}}^2 = \left(\frac{\eta}{\sqrt{L}}\right)^2 \cdot N \cdot L = \eta^2 \cdot N$. Therefore, the average SNR becomes

$$\bar{\rho}_{\text{c}} = \frac{\eta^2 \cdot N \cdot P_{\text{s}}}{\eta^2 \cdot N\sigma_1^2 + M\sigma_2^2} = \frac{P_{\text{S}}}{\sigma_2^2} \cdot \frac{\eta^2 \cdot N}{\eta^2 \cdot N \cdot \frac{\sigma_1^2}{\sigma_2^2} + M} \tag{4.30}$$

To compare this SNR to the one that can be achieved with a sparse array we model the observed signal as $\boldsymbol{a}_{\text{s}}(\boldsymbol{\gamma}_1) \cdot s_1(t) + \boldsymbol{w}_{\text{s}}(t)$, where the elements of $\boldsymbol{w}_{\text{s}}(t)$ are i.i.d. with variance σ_2^2.

We then obtain for the SNR of a sparse array

$$\bar{\rho}_{\text{s}} = \frac{M \cdot P_{\text{s}}}{M\sigma_2^2} = \frac{P_{\text{s}}}{\sigma_2^2}. \tag{4.31}$$

Therefore, the ratio of the SNRs becomes

$$\frac{\rho_{\text{c}}}{\rho_{\text{s}}} = \frac{\eta^2 \cdot N}{\eta^2 \cdot N \cdot \frac{\sigma_1^2}{\sigma_2^2} + M} \tag{4.32}$$

Overall, this shows that if there is significant signal noise (i.e., $\sigma_1^2 \gg \sigma_2^2$) in the compressed arrays, their achieved SNR degrades linearly with the ratio of signal to measurement noise power compared to sparse arrays. On the other hand, for dominating measurement noise (i.e., $\sigma_1^2 \ll \sigma_2^2$), the SNR ratio approaches $\eta^2\frac{N}{M}$ which means an SNR improvement if the efficiency of the lossy components satisfies $\eta > \sqrt{\frac{M}{N}}$. In practice, the compression ratio $\frac{N}{M}$ can be quite high and therefore, the SNR improvement of the compressive arrays can be very significant.

Note that another particular advantage of the proposed compressive arrays is their reconfigurability, as discussed in Section 4.4. If we follow this idea, the array performs beamforming towards the already detected targets. In this case, the SNR is further improved by the beamforming gain which is a factor on the order of N.

Resolution

The ability to distinguish closely spaced sources is an important characteristic of an antenna array. The achievable resolution of the array mainly depends on its aperture, i.e., the largest distance between pairs of antenna elements. For ULAs, the aperture is equal to $(N-1)\lambda/2$ since the elements are spaced in half-wavelength distance from each other. For compressive arrays as well as sparse arrays, this distance can be increased further. As a result, the array's correlation function becomes sharper, at the price of an increase in sidelobes (grating lobes). We can control the height of the grating lobes by proper design of the antenna placement (in the case of sparse arrays) as well as the analog combining network (in the case of compressive arrays). In general, we expect that at the same covered aperture and the same number of active RF chains, the compressive arrays will have lower sidelobes (since the many degrees of freedom in the analog combining network allow to suppress the sidelobes significantly). As it is difficult to quantify the achievable sidelobe suppression analytically, we will focus on this aspect in the numerical results in Section 4.6.

4.6 Numerical Results

In this section, we evaluate the performance of the compressive array with an optimized combining network and compare it to its closest counterparts in terms of the aperture and hardware complexity, namely random and sparse arrays. We also evaluate the performance of the adaptive focusing design showing its advantages over the uniform one.

4.6.1 Performance Analysis of the SCF Based Design

We start first by examining the SCF- based design. To this end, we consider an $M = 12$ element ULA that is reduced to $m = 8, 6, 4$ channels via an $m \times 12$ combining matrix $\mathbf{\Phi}$. This matrix is chosen according to $[\mathbf{\Phi}]_{(m,n)} = \mathrm{e}^{\jmath\varphi_{m,n}}$, where $\varphi_{m,n}$ are the optimization variables in the proposed approach and drawn from a uniform distribution for the random approach.

It is certainly possible to include the amplitude in the design process as well. Of course, this requires additional analog components, since in addition to phase shifters we will also need attenuators to adjust the amplitudes. These do not only increase the complexity of the combining network but also introduce additional losses and noise. For this reason, it is very common to consider only phase shifters in these networks,

which already provide a lot of flexibility. This is one of the baseline assumptions in the mmWave hybrid beamforming community (see e.g., [203] and references therein) and in SatCom applications (see e.g., [184]).

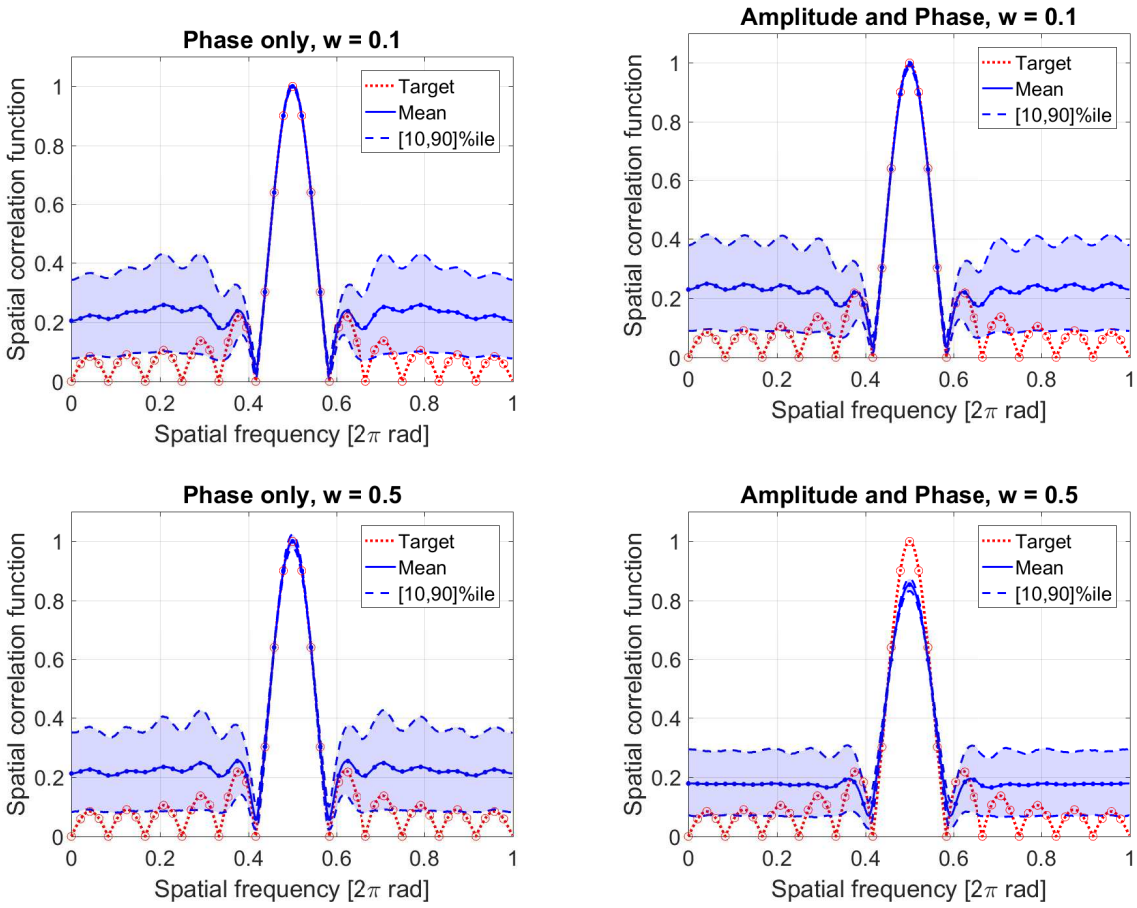

Figure 4.2: SCF-approach: phase-only optimization (left) vs. optimization of amplitude and phase (right) for two different weight matrices.

Nevertheless, to give an example of performance loses due to considering the phase only instead of amplitudes and phases we have conducted an experiment which is shown in Figure 4.2. Here we compare the SCF-based optimization for $M = 12, m = 8, P = 48$, using the SCF of the uncompressed 12-ULA as a target $\boldsymbol{T}$. The weight matrix is chosen such that it is equal to one for the mean beam (i.e., four points to the left and the right of the main diagonal) and w for all other points, such that higher values of w put more emphasis on the side lobes. For $w = 0.1$ (top two plots) and $w = 0.5$ (bottom two plots), we compare optimizing only the phase of $\boldsymbol{\Phi}$ (left) with optimizing magnitude and phase of $\boldsymbol{\Phi}$) (right). Each graph displays the mean of the average SCF (solid blue line) as well as the 10/90 percentiles (shaded area) over 1000 random initializations of the SCF-based optimization method. We observe that for $w = 0.1$ there is barely any

visible change, whereas for $w = 0.5$ the side lobes are suppressed slightly stronger, at the expense of a reduction of the main lobe peak. In general, the difference between optimizing only phase or magnitude and phase is not very pronounced since satisfactory results can be already achieved by optimizing the phase.

To find an optimized design $\boldsymbol{\Phi}_{\text{opt}}$, we solve the weighted optimization problem (4.15) via MATLAB's numerical optimization features. We run `fmincon` with 100 random initializations and pick the solution with the smallest value of the cost function. As a target we set $\boldsymbol{T} = \boldsymbol{A}^{\text{H}} \cdot \boldsymbol{A}$ which is the correlation function we would achieve with an M-ULA. The weighting matrix is chosen according to $[\boldsymbol{W}]_{(n_1,n_2)} = \rho^{|n_1-n_2|}$ where $\rho \in (0, 1]$ is a parameter that controls the decay of the weights. Essentially, smaller values of ρ put significantly more weight at the main lobe and its quick decay and less weight on the side-lobes that are far from the main lobe. The limiting value $\rho = 1$ represents the unweighted case.

Figure 4.3 demonstrates the advantage of using a measurement matrix $\boldsymbol{\Phi}$ that is optimized according to our proposed methodology as compared to choosing $\boldsymbol{\Phi}$ randomly. The SCF of the random design (Figure 4.3a) suffers many blind spots and high side lobes whereas the optimized design enjoys a smooth main lobe and relatively low side lobe level.

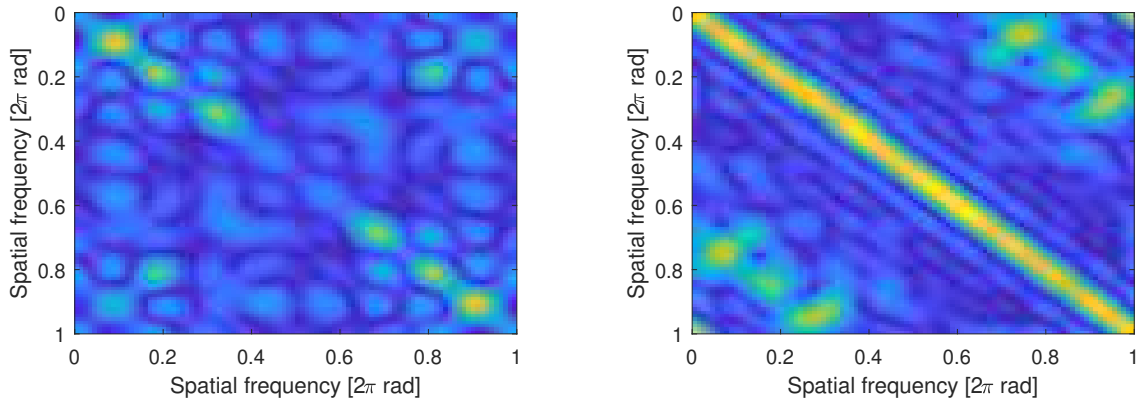

(a) Random **(b)** Optimized SCF

Figure 4.3: SCF comparison for an SCF optimized design versus random ones for $M = 12$ and $m = 8$.

Figure 4.4 depicts the normalized spatial correlation function (SCF) defined as

$$\varphi(\mu_1, \mu_1 + \Delta\mu) = \frac{\tilde{\boldsymbol{a}}(\mu_1)^{\text{H}} \tilde{\boldsymbol{a}}(\mu_1 + \Delta\mu)}{\tilde{\boldsymbol{a}}(\mu_1)^{\text{H}} \tilde{\boldsymbol{a}}(\mu_1)} \tag{4.33}$$

for $\mu_1 = \pi$. For reference, the black line indicates the 12-ULA whereas the blue line

represents the result of the optimization for $\rho = 0.95$. We observe that the optimized design comes close to the M-ULA except for slightly higher sidelobes. Figure 4.4 also shows the SCFs that are obtained when we draw $\mathbf{\Phi}$ randomly without any optimization. We depict the average SCF (solid line), the 5-th and the 95-th percentile (shaded area) and one example realization (dash-dotted line). As evident from the figure, randomly chosen measurement matrices lead to significantly higher spatial correlations. In particular, every realization shows sidelobes that are sometimes even higher than the main lobe.

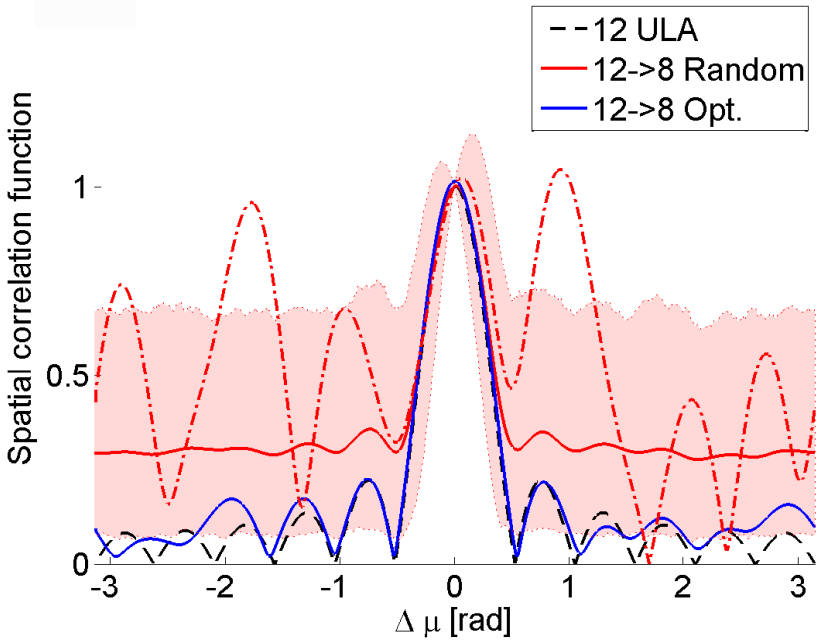

Figure 4.4: Spatial correlation function $\varphi(\mu_1, \mu_1 + \Delta\mu)$ for $\mu_1 = \pi$. We compare the $M = 12$ element ULA with an 8×12 CS array. To show the variability of choosing $\mathbf{\Phi}$ randomly, we depict the average correlation (solid line), the 5-th and 95-th percentile (shaded area) and one example realization (dash-dotted line).

Figure 4.5 demonstrates the DOA estimation performance if we use the OMP algorithm for the sparse recovery stage. We consider a noise-free scenario with two sources that are located on the $N = 48$ point uniform sampling grid, i.e., $\mu_{1,2} = (n_0 \pm d/2) \cdot \Delta$ where $n_0 \in [1, N]$ and d is the inter-source spacing in grid points. For each value of d, the mean square error $\text{MSE} = \frac{1}{2}\sum_{k=1}^{2}(\mu_k - \hat{\mu}_k)^2$ is averaged over all values of n_0. An estimate of the Complementary Cumulative Distribution Function (CCDF) of this average MSE obtained from 1000 realizations of $\mathbf{\Phi}$ is shown. As evident from the figure, the average MSE exceeds the source spacing d with a probability of 95 % for $d = 2$, 80 % for $d = 4$, and 30 % for $d = 8$. For the same scenario, our optimized design (choosing $w = 0.7$) achieves an MSE very close to zero (shown with the dashed lines), i.e., 0.72Δ for $d = 2$, 0.13Δ for $d = 4$, and 0.03Δ for $d = 8$.

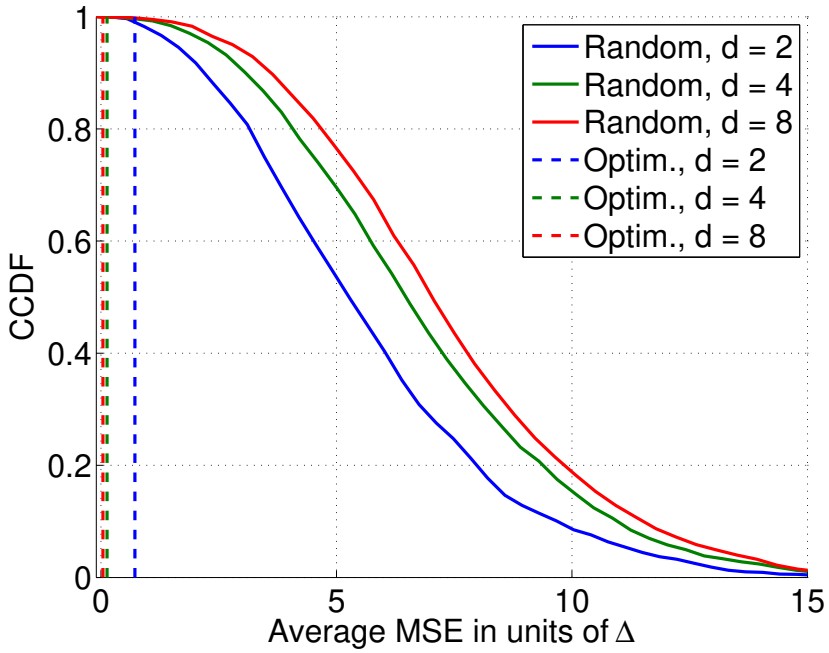

Figure 4.5: Mean square estimation error for randomly drawn $\mathbf{\Phi}$, using OMP for the sparse recovery step. We consider two sources positioned at $\mu_{1,2} = (n_0 \pm d/2) \cdot \Delta$. The MSE is averaged over all values $n_0 \in [1, N]$ and a histogram over this average MSE is estimated for three values of the source distance $d = 2, 4, 8$. MSE and source distance are shown in units of the grid spacing Δ to facilitate their comparison. The average MSE of our optimized design is indicated with the dashed lines.

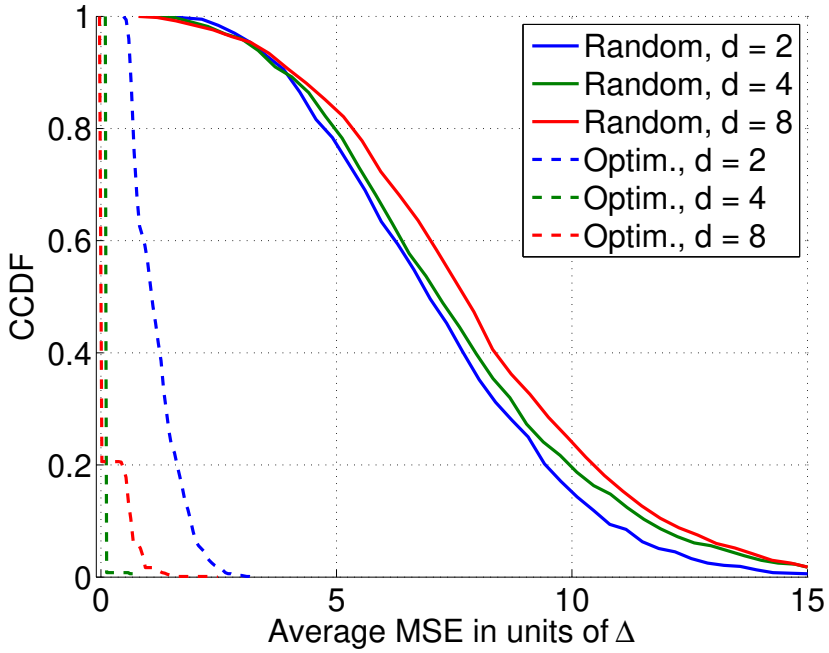

Figure 4.6: The same scenario as shown in Figure 4.5 but this time including noise at an SNR of 10 dB.

To investigate the effect of additive noise, we have repeated the experiment from Figure 4.5 with additive noise. In particular, we have drawn the noise vector $\boldsymbol{w}$ (cf. (5.12)) from a zero mean circularly symmetric complex Gaussian distribution with a variance of 0.1, which corresponds to an SNR of 10 dB. The result is shown in Figure 4.6. Once more, the optimized design achieves a significantly lower average MSE compared to the randomly chosen measurement matrices.

Though the main concern for optimizing $\boldsymbol{\Phi}$ has been put on correlation-based recovery algorithms such as the OMP, we have tested it on the Basis Pursuit (BP) algorithm [97] as well and found that it also offers some advantages there. To this end, we have repeated the previous simulation with the same parameters, using BP instead of OMP for the recovery stage. The result is shown in Figure 4.7. The figure shows the CCDF of the average MSE over 1000 random realizations of $\boldsymbol{\Phi}$. Our proposed design is not shown since it achieves an exact reconstruction result (MSE=0) for all values of d. As expected, BP is more reliable and less sensitive to sidelobes compared to OMP. In fact, for each value of d there is a non-zero chance to draw a matrix $\boldsymbol{\Phi}$ randomly that achieves an exact reconstruction as well. However, these "lucky" choices are not very stable in the sense that changing the grid size N or the source spacing d results in estimation errors to occur.

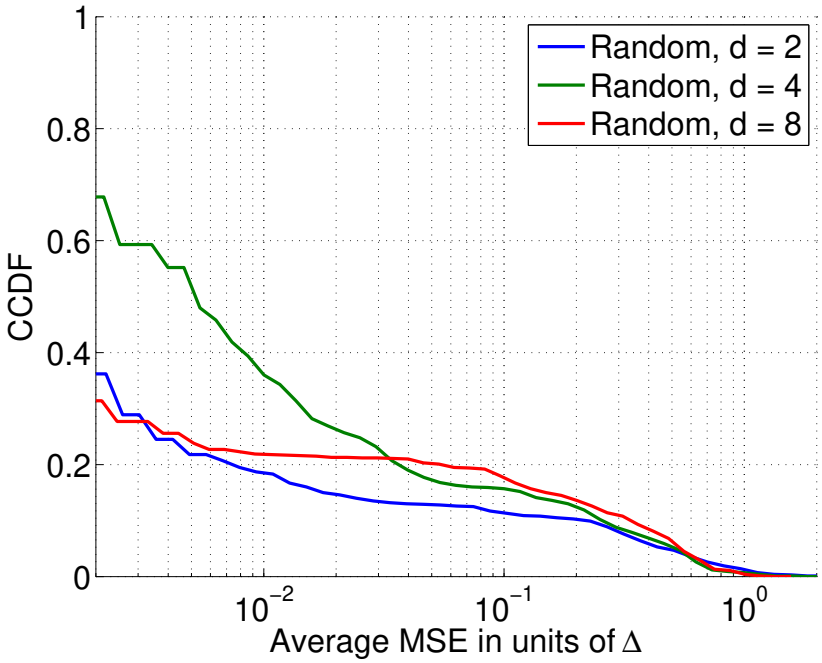

Figure 4.7: The same scenario as shown in Figure 4.5, this time using Basis Pursuit (BP) for the recovery stage. Our proposed design achieves an average MSE of zero for $d = 2$, 4, and 8.

4.6.2 Comparison to the CRB Based Design and Sparse Arrays

We now compare the SCF based design to the CRB based one and also to sparse arrays. The latter can be obtained by varying the element positions of a "traditional" antenna array to achieve a high resolution (low CRB). Via a careful design of the element positions, the level of the resulting grating lobes can be controlled (cf., e.g., [171]). Note that we do not compare our design to nested or co-prime arrays [172, 173]. While these approaches in theory allow to construct $\mathcal{O}(M^2)$ virtual sensors from $\mathcal{O}(M)$ antennas, this is only possible if we observe the scene over a large number of snapshots in time (during which it must remain static) and all sources are mutually uncorrelated. Since the proposed array as well as optimized sparse arrays can operate on an arbitrary number of snapshots (down to the single snapshot case) and have no restrictions in terms of the source correlation, a comparison of the achievable accuracy and resolution with nested or co-prime arrays would not be fair.

We change our scenario to reduce the optimization complexity for the CRB based design and use UCAs instead of ULAs. We perform the numerical study based on a uniform circular array (UCA) with $N = 9$ elements that are compressed to $M = 5$ receiver channels (this amounts to ≈ 1.8 times reduction in the number of receiver channels). Note that for a UCA with isotropic elements the response of the n^{th} antenna element as a function of the azimuth angle θ can be written as

$$a_n(\theta) = e^{\jmath 2\pi \tilde{R} \cos(\theta - \vartheta_n)}, \tag{4.34}$$

where $\vartheta_n = 2\pi(n-1)/N$ with $n = 1, 2, \cdots, N$ and $\tilde{R} = \frac{R}{\lambda}$ is the array radius normalized to the wavelength. For both proposed designs, the radius $\tilde{R}$ was fixed and set to 0.65.

The combining matrix $\mathbf{\Phi}$ is chosen according to $[\mathbf{\Phi}]_{(m,n)} = \mathrm{e}^{\jmath\varphi_{m,n}}$, where $\varphi_{m,n}$ are the optimization variables in the proposed approaches. This implies that the role of the efficiency η is not considered, implicitly assuming $\eta = 1$. Note that this is not uncommon in the related literature [203, 207]. Moreover, for $\eta < 1$, the sidelobe level (and thus the false detection probability) are unaffected while the CRB scales linearly with η^2. Therefore, for low values of η, sparse arrays may outperform the proposed compressive arrays. On the other hand, the latter are reconfigurable and can hence perform beamforming in the directions of interest, to partially compensate the analog combining losses.

To find an optimized design $\mathbf{\Phi}_{\text{opt}}$, we solve the weighted optimization problems (4.15) and (4.19) via MATLAB's numerical optimization features. Since run-time is not a

concern for an off-line design, and in order to avoid local minima, we run `fmincon` and `fminimax` to solve (4.15) and (4.19), respectively, with 100 random initializations and pick the solution with the smallest value of the cost function. In the following, we refer to the design obtained by the SCF optimization approach from (4.15) as Opt SCF, whereas the design obtained as a result of the CRB minimization from (4.19) is referred to as Opt CRB. For the Opt SCF approach, we set $\boldsymbol{T} = \boldsymbol{A}^{\mathrm{H}} \cdot \boldsymbol{A}$ as a target which is the correlation function we would achieve with an M-element (uncompressed) UCA. The weighting matrix is chosen according to $[\boldsymbol{W}]_{(n_1,n_2)} = w^{|n_1-n_2|}$ where $w \in (0,1]$ is a parameter that controls the decay of the weights. Essentially, smaller values of w put significantly more weight at the main lobe and its quick decay and less weight on the side-lobes that are far from the main lobe. The limiting value $w = 1$ represents the unweighted case. For the Opt CRB approach, the threshold false detection probability ϵ_0 is set to 0.05 to be achieved at an input SNR of $\rho_0 = 0$dB.

We begin by examining the performance of the optimized compressive arrays with respect to the attainable CRB and the sidelobe level in the case of a single source as discussed in Sections 4.3.2 and 4.3.3.

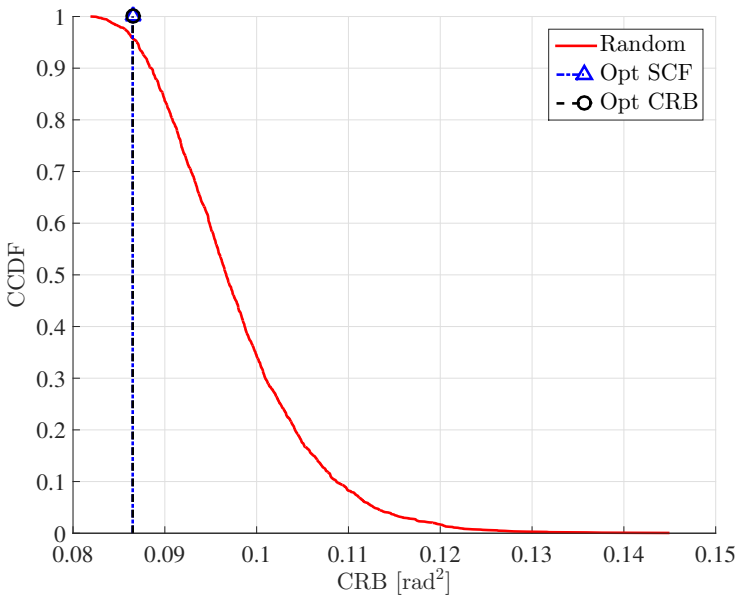

Figure 4.8: Comparison of the CRBs of the optimized compressive arrays versus the random ones. The CCDF of the CRB for 5000 random realizations are shown together with that of the optimized kernel.

Figure 4.8 shows the achievable CRB of the compressive arrays with the optimized combining network and the random ones that have the same number of antennas and sampling channels while $\varphi_{m,n}$ are drawn uniformly at random from $(0, 2\pi]$. At a fixed

SNR level of 0 dB, an estimate of the Complementary Cumulative Distribution Function (CCDF) of the CRB obtained from 5000 random realizations of $\mathbf{\Phi}$ is shown. The optimized networks for both approaches have been designed to achieve the same CRB. This has been done by varying w of the Opt SCF approach such that the resulting optimized $\mathbf{\Phi}$ achieves a similar CRB as the one obtained from the Opt CRB approach. As evident from the figure, the CRB of the optimized compressive arrays is almost in every case lower than that of the random ones. In other words, the random kernel can potentially provide a performance comparable to the optimized ones but with a very low probability. The CCDFs of the average sidelobe levels for the same scenario are shown in Figure 4.9. We observe that the random compressive arrays provide significantly higher sidelobe levels compared to both the SCF and the CRB-optimized ones. This supports the intuition that designing the combining matrix randomly results in sub-optimal performance.

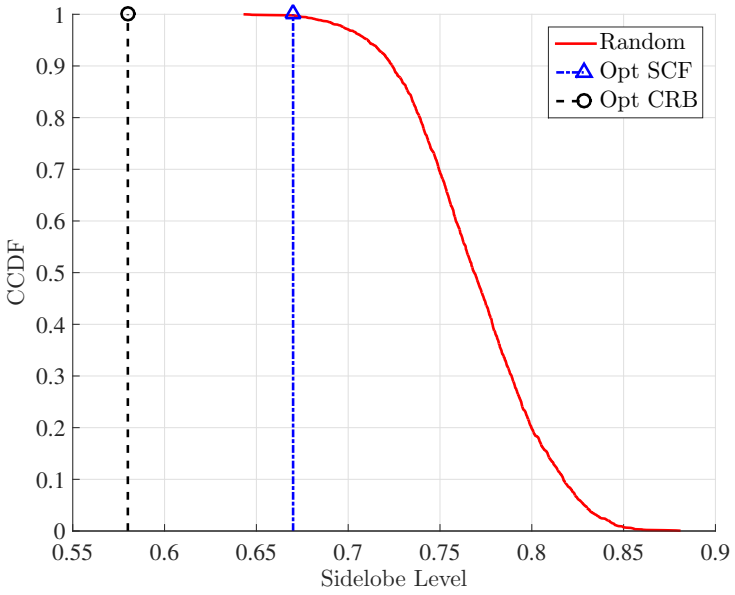

Figure 4.9: Comparison of the sidelobe levels of the optimized linear combining network versus the random ones. The CCDF of the mean sidelobe levels for 5000 random realizations are shown together with that of the optimized kernel.

Comparing the sidelobe level of the SCF and CRB-optimized compressive arrays, we can notice that the latter has a lower sidelobe level at a specific CRB. This is confirmed by the corresponding (analytic) probabilities of false detection depicted in Figure 4.10. For comparison Figure 4.10 also presents the results for the uncompressed UCAs with $N = 9$ and $N = 5$ (i.e., with smaller aperture size) as well as the average P_d for the random arrays. As can be seen, both proposed approaches achieve lower probability of false detection P_d than the uncompressed UCA with a lower number of antennas,

whereas the sparse arrays on average are significantly inferior to all the rest. It is worth noting that for both proposed optimization approaches, the CRB and the sidelobe level (and hence the probability of false detection) can be controlled: explicitly in the case of the CRB-based approach via setting a threshold ϵ_0 on P_d, and indirectly in the case of the SCF-based approach via a proper choice of the weighting matrix $\boldsymbol{W}$ in (4.15).

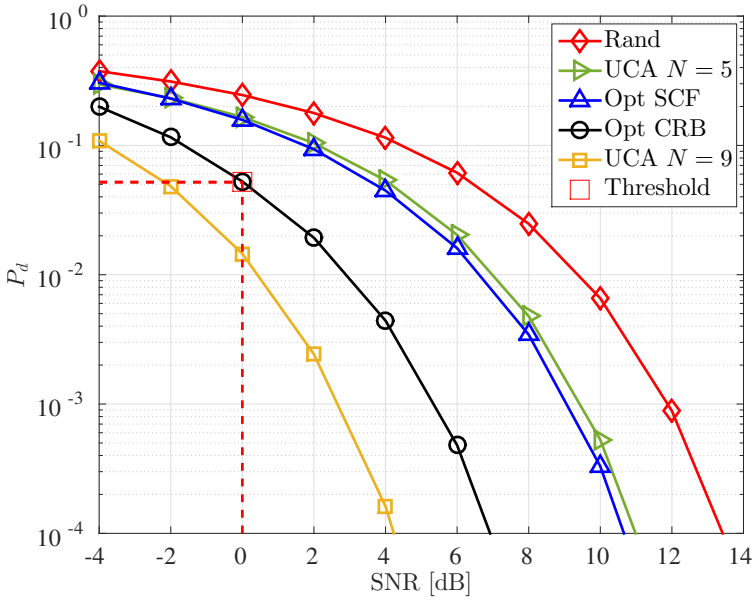

Figure 4.10: False detection probability of the uncompressed UCAs, compressive arrays, and the random ones.

Now we compare the compressive array to a sparse array that has the same number of receiver chains, i.e., for the considered scenario it means that for a sparse array $N = M = 5$. According to [171], we design the sparse array such that the positions of its elements are optimized towards obtaining a uniform sensitivity and desired CRB. Note that this results in an array geometry closely resembling that of a V-shaped array [171]. Figure 4.11 shows the spatial correlation functions at a specific DOA for the sparse array and an SCF-optimized compressive array (compression from $N = 9$ elements to $M = 5$ receiver chains) that achieves the same CRB (0.113) at the fixed SNR level of 0 dB. It can be noted that the sidelobe level of the sparse array is relatively high compared to that of the compressive one (especially the Opt CRB design). Particularly, the mean level of the sidelobes for the optimized compressive array is 0.53 compared to 0.68 of the sparse array.

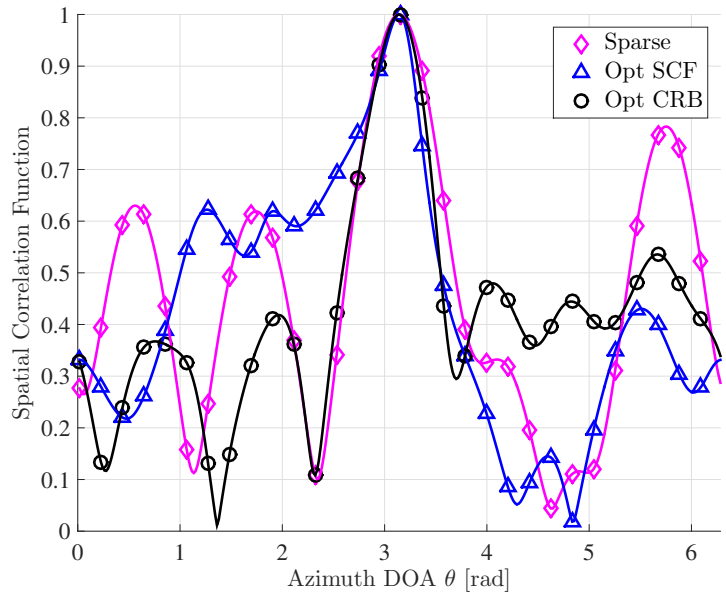

Figure 4.11: The spatial correlation function at a specific DOA of an optimized sparse array and a compressive array with the same number of receiver chains and an optimized combining network

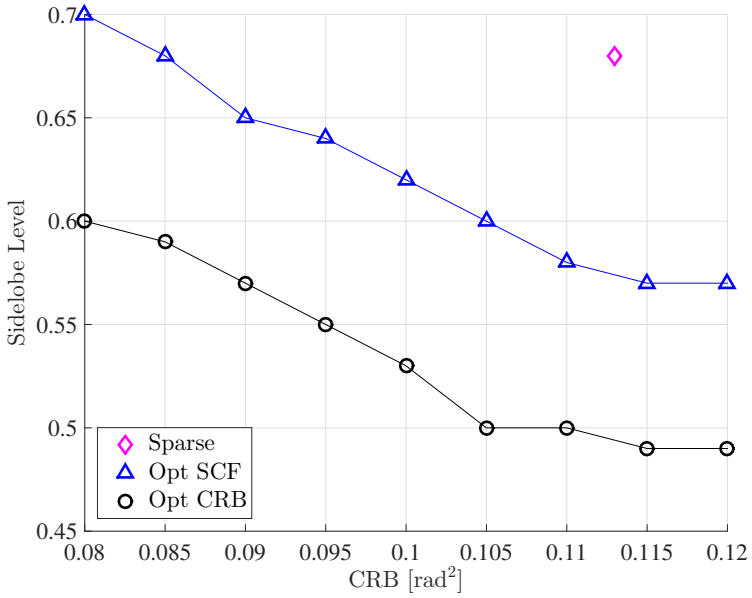

Figure 4.12: The CRB versus the sidelobe level for a compressive array with an optimized combining network and a sparse array (single diamond marker)

Figure 4.12 shows the resulting trade-off between providing a good CRB and maintaining a low sidelobe level. One can see that the compressive array (with either of the optimization schemes) outperforms the sparse one and gives more degrees of freedom

to tune the array design with respect to some desired properties (e.g., targeted CRB or sidelobe level). This figure also confirms once again that the Opt CRB approach outperforms the Opt SCF approach as it gives more control over the sidelobe level for a specific CRB. Note that the comparison to the sparse array is optimistic since it assumes an efficiency of $\eta = 1$. For $\eta < 1$, the sidelobe level is unaffected but the CRB scales linearly with η^2, shifting the Opt SCF and Opt CRB curves to the right. However, one should not forget that in contrast to the sparse array, the proposed arrays are reconfigurable, allowing to carry out beamforming in directions of interest once some targets have been detected. This beamforming can partially compensate the analog combining losses.

The superiority of the compressive arrays over the sparse ones with respect to adaptability is further highlighted in Figure 4.13. It presents the CRB and the sidelobe level of an optimized compressive array as a function of the number of antennas N. It is clear that the compressive arrays not only allow to control the CRB and the sidelobe level via an optimization of the combining network, but also by adding more antenna elements while the number of receiver channels is kept fixed. In Figure 4.13, we can see that the CRB can be improved significantly when the number of antenna elements is increased at the price of higher sidelobe levels. However the network can then be re-optimized for the new scenario (e.g., with the Opt CRB approach), aiming at a better suppression of the sidelobes while a certain level of CRB improvement is maintained.

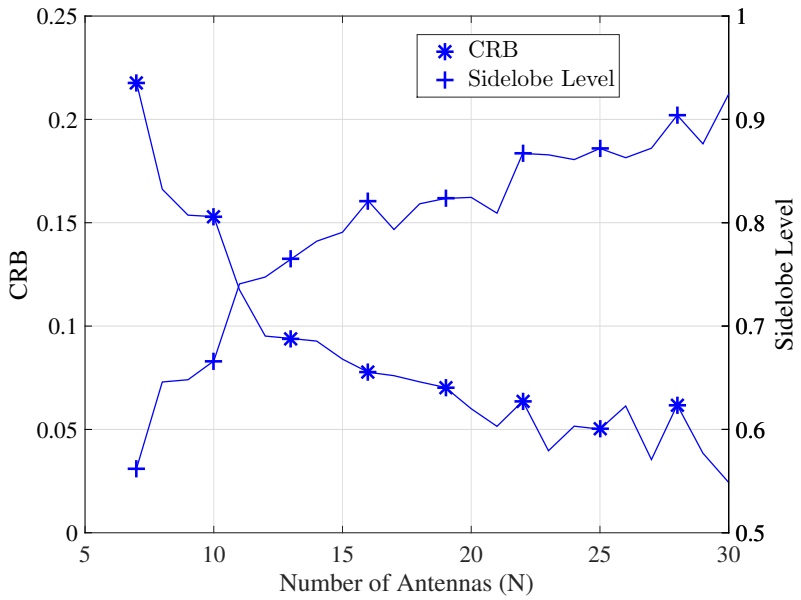

Figure 4.13: The CRB and the sidelobe level for a compressive array with different number of antenna elements and fixed number of channels

Now we examine the performance of the proposed optimized compressive array in the case of two sources impinging on the array from different DOAs. The power ratio between the two sources is set to $\alpha = |s_2/s_1|^2 = -6$ dB, while their DOAs are d radians apart, i.e., $\theta_1 = \theta$, $\theta_2 = \theta + d$ where θ scans the whole angular space. The two sources are inphase.

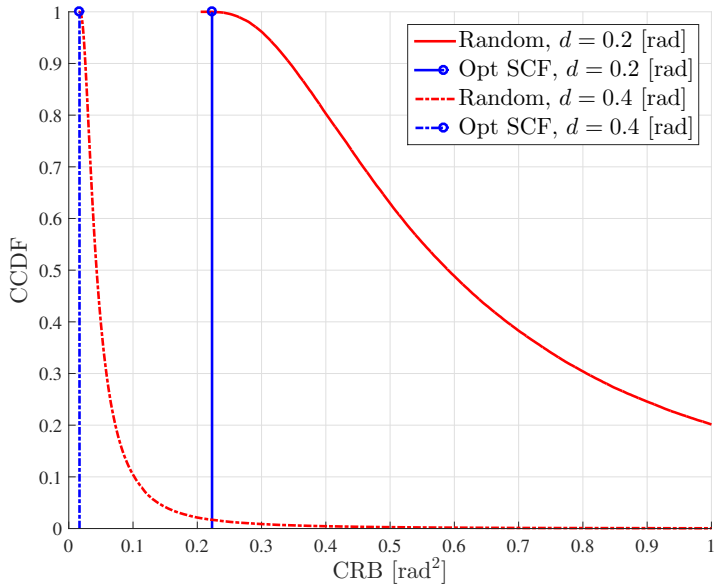

Figure 4.14: Comparison of the CRBs of the optimized compressive arrays versus the random ones for the case of two impinging sources. The CCDF of the CRB for 5000 random realizations are shown together with that of the optimized kernel.

Similar to Figure 4.8, Figure 4.14 shows the achievable CRB of the strongest path using the compressive arrays with the optimized combining network and the random ones that have the same number of antennas and sampling channels for an SNR level (with respect to the strongest source) of 12 dB. The CCDF of the CRB obtained from 5000 random realizations of $\mathbf{\Phi}$ is shown for $d = 0.2$ and $d = 0.4$ radians. As discussed earlier, the Opt SCF and the Opt CRB designs both provide the same CRB and so only the Opt SCF is shown for clarity. The CCDF shows that the CRB of the optimized compressive arrays is again almost in every case lower than that of the random ones. As the sources get closer (e.g., $d = 0.2$), the need for the optimized network increases as the probability to achieve acceptable properties (e.g., low CRB) by the random design gets lower.

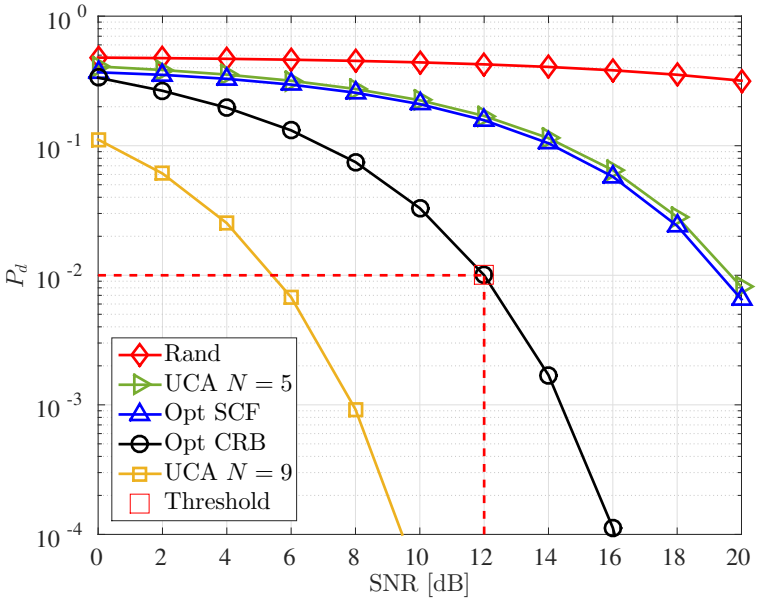

Figure 4.15: False detection probability of the uncompressed UCAs, compressive arrays, and the random ones with two source signals with power ratio $\alpha = -6$dB.

It has been proposed in Section 4.3.3, to extend the design based on CRB for the case of multiple sources. Considering the same set-up with two sources, and for a specific DOA of the first source, to do so the sidelobes in the correlation function have to be searched for all possible DOAs of the second source. This leads to a very high computational complexity. The same search strategy has to be performed for all possible DOAs of the first source. Therefore, for simplicity, we fix the second source DOA and perform the optimization similar to that of the single source case. Figure 4.15 shows the probabilities of false detection P_{d} for two sources. It can be seen that the design based on CRB shows superior performance in terms of lower false detection probability compared to that of the uncompressed $(N = 5)$-element UCA, compressive array with SCF based designed network, and the averaged random ones. Although the SCF based design can not be re-optimized for the multiple source case, it still provides a significantly lower probability of false detection compared to the random arrays and is comparable to a non-compressed $(N = 5)$-element UCA.

4.6.3 Performance Analysis for Adaptive Focusing

In this section, we present some numerical results to demonstrate the advantage of using the focusing measurement matrix design according to our proposed methodology. To this end, we consider a $M = 12$ element ULA that is reduced to $m = 8$ channels via an

8×12 compression/focusing matrix $\boldsymbol{\Phi}$. We sample the spatial space using an $N = 64$ point uniform sampling grid, i.e., $\mu_{1,2} = (n_0 \pm d/2) \cdot \Delta$ where $n_0 \in [1, N]$ and d is the inter-source spacing in grid points.

To construct the uniform matrix ensemble $\boldsymbol{\Phi}_{\text{uni}}$ we solve the optimization problem (4.26) to obtain the closed form solution. As a target we set $\boldsymbol{T}_{\text{uni}} = \boldsymbol{I}_N$ which is the ideal uniform target function described by (4.24). We will only consider it here as an initial estimator of the regions of interest towards which the main beam is focused afterwards.

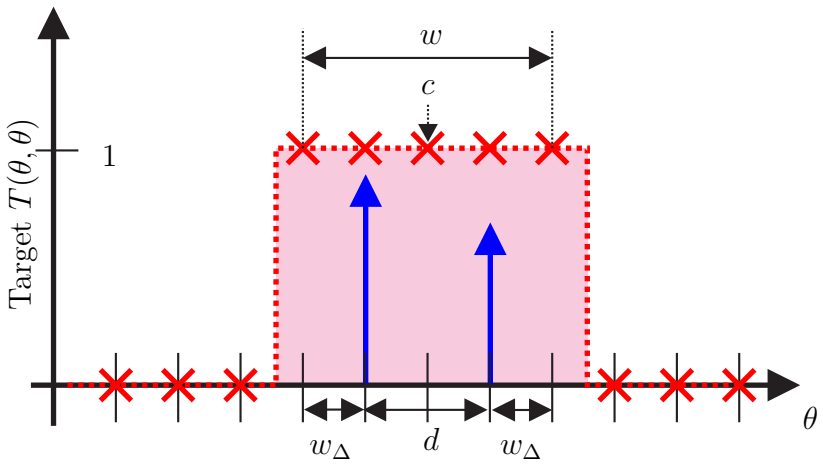

Figure 4.16: Definition of the focusing window: the blue arrows indicate the estimated DOAs with a distance of d grid points. The window is centered at grid point c, located in the middle of the targets, and has a width of w grid points, where $w = d + 2w_\Delta$.

The focusing measurement design $\boldsymbol{\Phi}_{\text{foc}}$ is obtained by modifying the target according to (4.25) where $\boldsymbol{T}_{\text{focus}}$ is an $N \times N$ matrix that contains the identity matrix in the focusing region and nulls otherwise. The focusing region is identified based on an initial estimate of the source locations, e.g., by a reconstruction of the scene based on a first measurement carried out with $\boldsymbol{\Phi}_{\text{uni}}$. Figure 4.16 shows how to define the target for two closely spaced sources, in which case we define one interval containing both as the region of interest. The blue arrows represent the (estimated) source positions. The focusing interval Θ is described as mentioned earlier by a center grid point c which we place in the middle of the two sources and a width w. Naturally, we have $w = d + 2w_\Delta$, where w_Δ is the number of extra grid points we allow to both sides of the identified sources (in Figure 4.16 we have $w_\Delta = 1$) and d is the distance between the sources estimated from the uniform measurement initialization step. In general, the width w represents a design parameter where smaller values indicate a more narrow focus. If the initial estimate of the regions of interest is not very reliable, w should be chosen larger to allow for some

deviations of the source position estimate in the refocused measurements. A concrete strategy for the choice of w is discussed below. Note that if more than two sources are present, the focusing interval Θ can be found by the union of several intervals, each centered around the middle of a cluster of identified sources.

As a first step, we compare the performances of the three measurement designs of $\mathbf{\Phi}$: the random design advocated in the earlier papers [45, 150], the uniform we proposed in [4] and the focusing design proposed in this work. The latter uses the estimate of the uniform design as an initialization, i.e., its first measurement is carried out with $\mathbf{\Phi}_{\text{uni}}$, the scene is reconstructed, and then used to identify the regions of interest to find $\mathbf{\Phi}_{\text{foc}}$ for the second measurement. For this experiment, we choose $w_\Delta = 6$, i.e., a window width of $w = d + 12$ grid points as the focusing region.

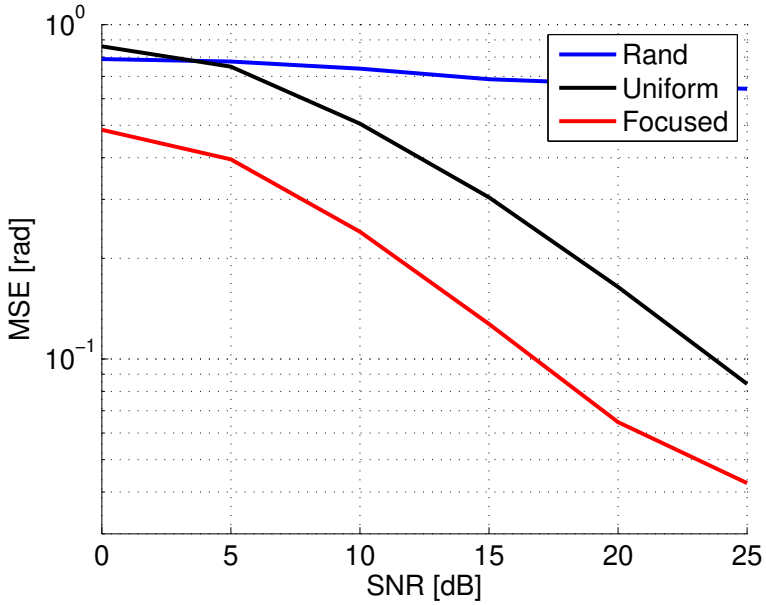

Figure 4.17: MSE versus SNR for two sources using the random, uniform, and focusing design where the source separation d is varied randomly. The focusing interval is defined according to the knowledge about the region of interest obtained from the first uniform measurement with a window width given by $w_\Delta = 6$.

Figure 4.17 shows the mean square error (MSE) versus the signal to noise ratio (SNR) for a scenario with two sources that are located on the grid and d grid points apart. The MSE is averaged over randomly drawn distances d and noise vectors $\boldsymbol{w}$ (cf. (5.12)) drawn from a zero mean circularly symmetric complex Gaussian distribution. For each trial, the fast orthogonal matching pursuit (OMP) [106] is used for the DOA estimation process and then the mean square error MSE $= \frac{1}{2}\sum_{k=1}^{2}(\mu_k - \hat{\mu}_k)^2$ is calculated for the three designs.

As depicted in the figure, the random measurement design shows the worst performance as expected (see [4] for more details). The results show that the focusing design provides a significant improvement in terms of the SNR.

To investigate the effect of the focusing interval width, we have repeated the experiment from Figure 4.17 with different focusing widths while fixing the sources' spacing to $d = 4$ which corresponds to 0.75 Rayleigh distances (i.e., they are closely spaced). Figure 4.18 compares the resulting MSE for a focusing width parameter $w_\Delta = 3$, 5, and 7, respectively. We observe that a more narrow focus leads to significantly reduced MSEs and thus a superior resolution of the two closely spaced sources compared to the unfocused, uniform design.

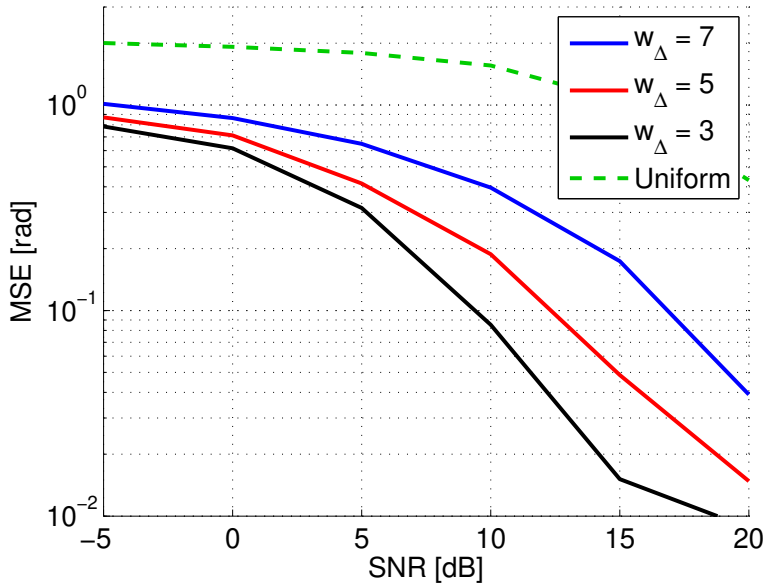

Figure 4.18: MSE versus SNR for two sources separated by four grid points using different focusing interval lengths. A smaller window size leads to a more narrow focus, resulting in an improved resolution.

We now turn our attention towards a concrete example of a possible implementation of our focusing design without any special prior knowledge about the scene. Our idea is to perform the focusing sequentially, starting with an unfocused, uniform design and then gradually narrowing the focus by sequentially reducing the window size w. Each of the sequential measurements provides an improved estimate of the scene (as we have seen in Figure 4.18) which can be used to update the center of the window c and thus make sure that the focus is put in the correct direction.

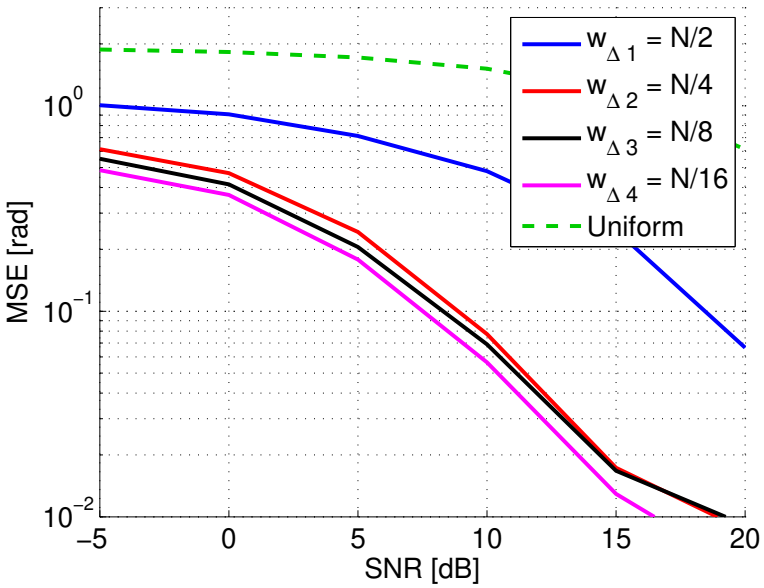

Figure 4.19: Same scenario as shown in Figure 4.18 but this time the focusing is done sequentially with w_Δ being halved at each step.

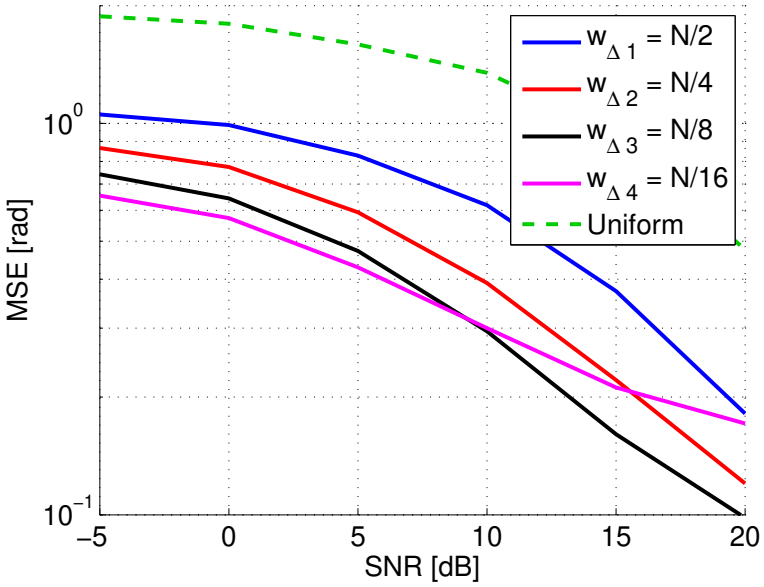

Figure 4.20: Same scenario as shown in Figure 4.19 but this time the sources are only $d = 2$ grid intervals apart.

Figure 4.19 shows such a process where we investigate a scenario with two sources $d = 4$ grid points apart and we keep decreasing the window size parameter w_Δ from $N/2$

to $N/4$ to $N/8$ to $N/16$. The curves labeled $w_{\Delta,i}$ for $i = 1, 2, 3, 4$ correspond to the i-th sequential measurement which positions the target window according to the estimate from the $(i-1)$-th measurement and sets the window size to $N/2^i$, as indicated in the legend of the figure. The results show that each of the sequential measurements provides a more narrow focus which leads to a lower MSE, although the change from $N/8$ to $N/16$ does not improve the MSE significantly anymore.

Figure 4.20 depicts the result for the same scenario with the sources only $d = 2$ grid points apart. Here the fourth measurement $w_{\Delta,i} = N/16$ shows a worse performance than the third measurement using $w_{\Delta,3} = N/8$. This suggests that over-focusing might result in a worse performance, e.g., if the focus center c is not placed exactly in the correct direction.

So far, all the numerical results were based on the OMP algorithm for the sparse recovery step. To demonstrate that our proposed measurement matrix design can be applied to any sparse recovery algorithm, Figure 4.21 shows the same scenario as Figure 4.18, comparing the basis pursuit (BP) [97] with the OMP algorithm. The results show that as expected, the convex optimization based BP algorithm outperforms OMP, however, both algorithms benefit in a similar way from our proposed adaptive measurement matrix design.

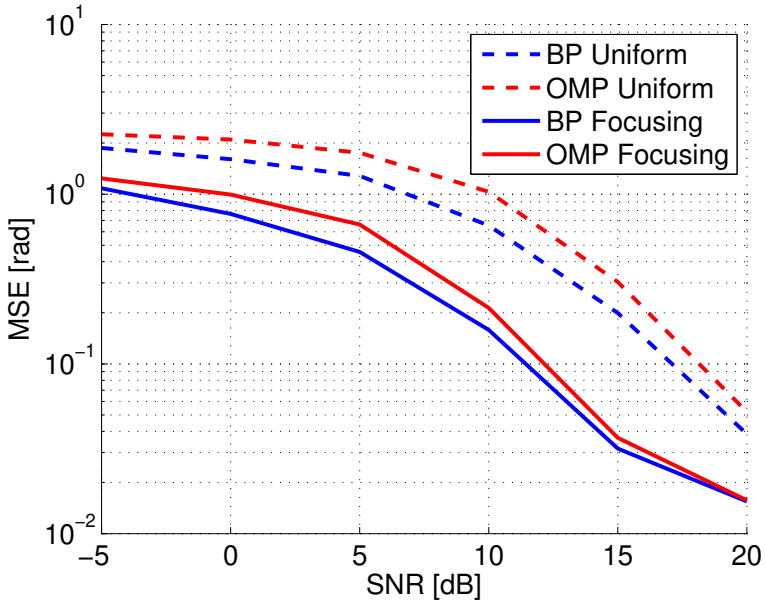

Figure 4.21: Same scenario as before but instead using BP for initialization

4.7 Summary

In this chapter we consider the design of compressive antenna arrays for direction of arrival (DOA) that aim to provide a larger aperture with a reduced hardware complexity and allowing reconfigurability compared to traditional array designs. We present an architecture of such a compressive array and introduce a generic system model that includes different options for the hardware implementation. We then focus on the choice of the coefficients in the analog combining network. We have demonstrated that choosing it randomly may lead to undesirable effects in the effective CS array such as very high sidelobes. These are particularly problematic for correlation-based sparse recovery algorithms such as the Orthogonal Matching Pursuit since they may lead to the detection of spurious peaks.

Instead of choosing them randomly, we propose a generic design approach for the analog combining network with the goal to obtain an array with certain desired properties, e.g., uniform sensitivity, low cross-correlation, or low variance in the DOA estimates. We exemplify the array design via two concrete examples. Our numerical simulations demonstrate the superiority of the proposed optimized compressive arrays to compressive arrays with randomly chosen combining kernels, as the latter result in very high sidelobes (which imply a higher probability of false detection) as well as higher CRBs. We also compare our optimized compressive array to a sparse array of the same complexity (i.e., same number of receiver channels M) and find that sparse arrays suffer from much higher sidelobes at the same CRB level. Also our proposed compressive array enjoys a high degree of adaptability since the combining weights can be altered to adjust the array to the current requirements, which is impossible for sparse arrays due to their static nature.

We have also proposed a focusing design of the compression matrix based on the SCF technique. The main idea is to apply measurements in a sequential fashion: first, we measure with a uniform design that is equally sensitive in all directions and thus allows us to obtain a good estimate for the region(s) of interest in the angular domain. Then, the measurements are iteratively focused towards these regions. We have demonstrated that the focusing design results in a significant performance improvement compared to the uniform design. In particular, our numerical results demonstrated that a narrower focus, leads to an improved SNR and resolution. We have demonstrated that the width of the focusing region is a parameter that can be used to control the degree of focus depending on the reliability of the estimate of the regions of interest and provided a sequential focusing strategy as a concrete example.

Chapter 5

Compressive Time Delay Estimation

This chapter extends the ideas from the previous chapters applying them to time delay estimation (TDE) and synchronization. After the motivation in Section 5.1, we introduce the TDE model in Section 5.2. The compressive sensing (CS) based TDE architecture is then presented in Section 5.3 followed by a description of the TDE procedure in the compressed domain in Section 5.4. In Section 5.5 an optimization based design for the measurement kernels of the CS based TDE architectures is proposed extending the ideas from the previous chapter. Afterwards, we deal with the synchronization of the TDE network in Section 5.6 and propose a CS based reference broadcast synchronization where the reference signal is an opportunistic signal already in the system. Section 5.7 evaluates the proposed approaches via numerical simulations followed by a summary in Section 5.8.

5.1 Motivation

Time delay estimation (TDE) is a fundamental challenge arising in many applications such as wireless communications [208], radar [209], localization [210], sensor networks [211], and many others. A wide range of TDE techniques have been proposed, see, e.g., [212] for a survey for TDE in linear dynamic systems.

In this chapter, we treat the special case of estimating the delay of a signal with a known pulse shape from a noisy superposition of several delayed copies. Such problems occur in synchronization of wireless sensor networks [213], localization [214] or wideband channel estimation [215] due to the multipath channel.

The complexity bottleneck in these systems is the high data rate from the high-speed AD converters that are required to sample the wideband signals which are used to ensure a high resolution in time. However, since the pulse shape is known, the actual rate of

(unknown) information in the received signals is low. Therefore, it has been proposed to apply compressed sensing (CS) to reduce the hardware complexity while maintaining high precision. In [216, 217], a framework for sampling time-delayed signals is presented based on a union of subspaces approach [218]. The authors derive sufficient conditions on the transmitted pulse and the sampling functions in order to ensure perfect recovery of the channel parameters in the absence of noise, which includes conditions on the minimal required sampling rate.

Considering concrete choices of the low rate sampling kernels, it is often suggested in the CS literature to use random kernels which are incoherent with any basis and so achieving informative measurements even at low rates. Though randomly chosen kernels represent a simple and generic approach, it is known that they do not provide the optimal robustness against noise. Only recently, the optimization of the measurement kernels has been investigated [219–221]. In particular, [219] studies the optimization of a discrete measurement matrix in time domain and [220] consider a continuous (sum-of-sincs) kernel in time domain whose output that is sampled at a sub-Nyquist rate. Both use criteria inspired by the Bayesian Cramér-Rao bound to optimize the kernels. In [221], the measurement matrix is optimized such that for a given (overcomplete) basis, the sensing matrix has a small average coherence.

In this chapter, we propose another optimization based design for the measurement kernels of the CS based TDE architectures. We consider an architecture based on a bank of K continuous-time periodic functionals that are sampled once per period. We show that their Fourier-domain representation allows to optimize these functions based on a finite number of coefficients. We demonstrate numerically that the optimized CS kernels outperform a randomly chosen one in terms of the delay estimation accuracy.

It is also worth mentioning that the fully wireless operation for TDE also poses significant synchronization challenges compared to a wired network (i.e., precise time synchronization is essential). A certain degree of synchronization is required in any WSN in order to establish the communication protocols. However, some TDE applications such as using a WSN for wireless distributed localization of a set of targets, require a very accurate synchronization which is even more challenging.

The simplest approach for synchronizing a WSN is given by transmitting a known reference signal from at least one node in the network. Each node can then obtain its timing information by comparing the known signal to its own received copy [213]. However, accurate timing information requires a reference signal with high bandwidth, thus consuming precious resources (when done wirelessly).

A promising alternative approach to the problem is presented in [211, 222] and ex-

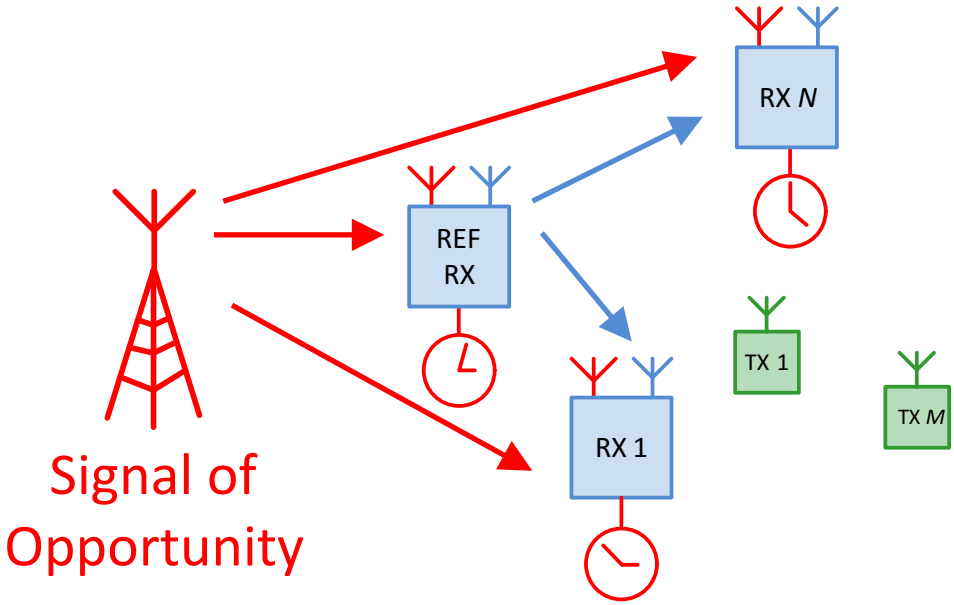

Figure 5.1: Example WSN using signals of opportunity for the wireless synchronization. The blue nodes represent the WSN that shall localize the green tags.

emplified in Figure 5.1. Using so-called signals of opportunity like communication (e.g., LTE) or broadcast (e.g., DVB-T) signals, a precise time synchronization between the RX nodes can be realized. Since it is desirable that the system is able to use arbitrary signals of opportunity, it should operate without having to fully decode these signals (which would be impossible, e.g., for LTE signals). Traditionally, orthogonal frequency division multiplexing (OFDM) receivers synchronize themselves on the received signal [223–225]. Additionally, the own or the remote clock error may be modeled and corrected according to [226]. However, this requires that either the signal is completely demodulated or even decoded [224, 225] or this requires that small pieces of the received signal at the reference RX (REF RX) are distributed to all other RX (Figure 5.1, blue arrows) via a data link. We refer to this as the reference signal. At the RX the received time sampled copy of the reference signal is compared with the originally received signals of opportunity (Figure 5.1, red arrow) and a time difference between the local clocks and the clock of the REF RX can be estimated.

It is clear that retransmitting the wideband reference signal requires significant resources. In [222], it is proposed to extract features from the OFDM symbol stream and compare the features in a centralized unit for timing offset compensation. In this work, we propose to compress the reference signal before transmission to all other nodes. We rely on the basic ideas of CS to design the compression matrix without significantly affecting the properties of the correlation function which determine the synchroniza-

tion precision compared to the original non-compressed scenario. We show that the correlation can be calculated in the compressed domain, yet achieving correlation characteristics comparable to the high bandwidth correlation obtained with opportunistic signals. In particular, we demonstrate that the compression does not affect the width of the main peak in the correlation function, but rather it leads to higher cross-correlation levels. Therefore, the compression ratio allows to control the trade-off between the required bandwidth of the reference node and the effective SNR which can be tolerated.

5.2 Time Delay Estimation

The time delay estimation (TDE) between a reference signal and its delayed version is a fundamental problem arising in many applications such as wireless communications [208], radar [209], localization [210], sensor networks [211], and many others.

In a typical scenario, a pulse with a priori known shape is transmitted through a medium. As a result, the received signal is composed of a delayed and a weighted replica of the transmitted pulse. In various applications, the time delay and the gain coefficient have to be estimated from the received signal.

A typical TDE problem can be described as:

$$y(t) = G(p)u(t - T_d) + n(t), \tag{5.1}$$

where the signal $u(t)$ is the so called reference signal, $y(t)$ is the one measured (i.e., recieved), $n(t)$ is the measurement noise and $G(p)$ is a linear system (without time-delay). The time delay to be determined is T_d. The signal can be either wideband or narrowband. They can also be either real valued or complex valued. Complex (or analytic) signal representation is often used for narrowband signals but can also be used for wideband signals. The impulse response $g(t)$ of $G(p)$ can also be complex valued. Complex signals and impulse responses are commonly used for bandpass systems, e.g., in radar and communications.

A wide range of TDE techniques have been proposed, see, e.g., [212] for a survey for TDE in linear dynamic systems. The conventional method of TDE uses the cross-correlation between the reference and the delayed signal and estimates the time delay by finding the maximum of this cross-correlation [227, 228].

The time delay estimation problem can be formalized as follows. A transmitter sends a signal $s(t)$ to allow a receiver (or multiple receivers) that know $s(t)$ to synchronize themselves. For simplicity, we assume that $s(t)$ is t_p-periodic, i.e., $s(t) = s(t + t_\mathrm{p})$.

Periodic synchronization signals are common, e.g., in GNSS [229] and UWB Radar applications [230]. They allow receivers to keep track of the synchronization over time and to average over multiple periods. For the problem at hand, another advantage is that since these signals are also band-limited to a certain bandwidth B, they can be completely described by a finite number of $M = B \cdot t_p$ coefficients. Therefore, we can write $s(t)$ as

$$s(t) = \sum_{m \in \mathcal{M}} c_s[m] \mathrm{e}^{\jmath 2\pi m \frac{t}{t_\mathrm{p}}} \tag{5.2}$$

where $\mathcal{M}$ is the set of points in frequency where $s(t)$ is non-zero[1] with $|\mathcal{M}| = M$.

Due to the multipath nature of wireless propagation channels, the receiver observes a weighted sum of delayed copies of $s(t)$, i.e., the received signal can be written as

$$x(t) = \sum_{\ell=1}^{L} \alpha_\ell s(t - \tau_\ell) + w(t), \tag{5.3}$$

where α_ℓ and τ_ℓ represent the complex amplitude and delay of the ℓ-th propagation path for $\ell = 1, 2, \ldots, L$, respectively, and $w(t)$ is the additive white Gaussian measurement noise. Note that since $s(t)$ is t_p-periodic so is $x(t)$ (besides for the additive noise).

5.3 Compressive Sampling TDE Architecture

We employ a compressive sampling architecture similar to [216], which is depicted in Figure 5.2. After an initial downconversion stage to remove the carrier frequency[2], instead of sampling the received signal $x(t)$ directly, the receiver performs a bank of analog multiplications with the functions $p_k(t)$, $k = 1, 2, \ldots, K$, followed by sampling with a lower rate to yield the coefficients ψ_k. Since $x(t)$ is periodic, it is convenient to choose $p_k(t)$ such that they are also t_p-periodic.

[1] We employ a complex representation of all signals, which can refer to the complex low-pass domain where $\mathcal{M} = \{-\frac{M}{2} + 1, \ldots, \frac{M}{2}\}$ or analytic signals where only the positive half of the spectrum is considered.

[2] The transmitter sends the bandwidth-B signal by modulating it onto a carrier frequency f_c, which is removed at this stage. The signal model is described entirely in the complex low-pass domain.

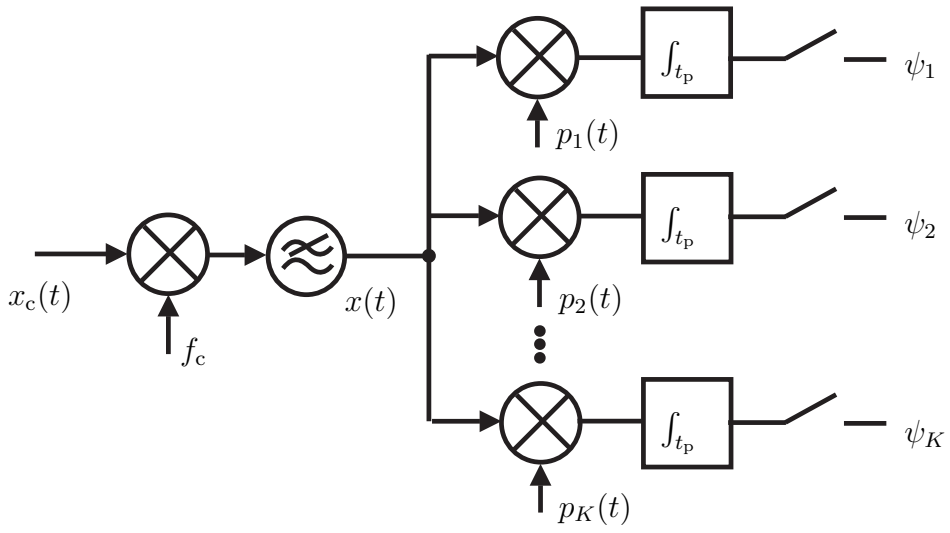

Figure 5.2: Compressive receiver architecture: the signal is multiplied with K periodic waveforms $p_k(t)$ and the result is sampled once per period in each branch.

The overall sampling rate of the receiver is then equal to $\frac{K}{t_\mathrm{p}} = \frac{K}{M} \cdot B$ which means that the compression factor relative to Nyquist sampling is equal to $\frac{K}{M}$. Note that each of the K ADCs operates at a rate $\frac{B}{M}$, i.e., a factor M times lower than in a conventional system.

It is important to note that since our receiver is linear and $x(t)$ is a linear combination of delayed copies of $s(t)$, it is sufficient to describe the sampling of one delayed signal $s(t-\tau)$. Once a mathematical model for this has been obtained, the sampled version of $x(t)$ follows from a trivial linear combination.

Therefore, if we let $x(t) = s(t-\tau)$, the k-th sample ψ_k for $k = 1, 2, \ldots, K$ is given by

$$\psi_k(\tau) = \frac{1}{t_\mathrm{p}} \int_{t_\mathrm{p}} p_k(t)^* \cdot s(t-\tau) \mathrm{d}t. \tag{5.4}$$

As both, $p_k(t)$ and $s(t)$ are periodic, they can be expressed using a discrete representation in the Fourier domain, namely

$$p_k(t) = \sum_{m=-\infty}^{\infty} c_{p,k}[m] \mathrm{e}^{\jmath 2\pi m \frac{t}{t_\mathrm{p}}}. \tag{5.5}$$

With the help of (5.5) and (5.2), we can now rewrite (5.4) in frequency domain [216].

For clarity, let us begin with $\tau = 0$ to obtain

$$\begin{aligned}\psi_k(0) &= \frac{1}{t_\mathrm{p}} \int_{t_\mathrm{p}} \left(\sum_{m_1=-\infty}^{\infty} c^*_{p,k}[m_1] \mathrm{e}^{-\jmath 2\pi m_1 \frac{t}{t_\mathrm{p}}} \right) \\ &\qquad \cdot \left(\sum_{m_2 \in \mathcal{M}} c_s[m_2] \mathrm{e}^{\jmath 2\pi m_2 \frac{t}{t_\mathrm{p}}} \right) \mathrm{d}t \\ &= \sum_{m_1=-\infty}^{\infty} \sum_{m_2 \in \mathcal{M}} c^*_{p,k}[m_1] c_s[m_2] \frac{1}{t_\mathrm{p}} \underbrace{\int \mathrm{e}^{-\jmath 2\pi m_1 \frac{t}{t_\mathrm{p}}} \mathrm{e}^{\jmath 2\pi m_2 \frac{t}{t_\mathrm{p}}} \mathrm{d}t}_{t_p \cdot \delta[m_1 - m_2]} \\ &= \sum_{m \in \mathcal{M}} c^*_{p,k}[m] c_s[m]. \end{aligned} \tag{5.6}$$

Equation (5.6) shows, not surprisingly, that only the M coefficients of $p_k(t)$ that coincide with the spectral support of $s(t)$ contribute to the coefficients ψ_k. Therefore, if the hardware realization allows it, they should be chosen such that they are bandlimited to B as well[3].

Introducing the short hand notations $\boldsymbol{c}_s \in \mathbb{C}^{M\times 1}$ and $\boldsymbol{c}_{p,k} \in \mathbb{C}^{M\times 1}$ for the M coefficients that $c_s[m]$ and $c_{p,k}[m]$ in (5.6) we then have $\psi_k(0) = \boldsymbol{c}^\mathrm{H}_{p,k} \cdot \boldsymbol{c}_s$. Moreover, it is now easy to carry out the same computation for $\tau \neq 0$. We obtain

$$\begin{aligned}\psi_k(\tau) &= \sum_{m \in \mathcal{M}} c^*_{p,k}[m] \mathrm{e}^{-\jmath 2\pi m \frac{\tau}{t_\mathrm{p}}} c_s[m] \\ &= \boldsymbol{c}^\mathrm{H}_{p,k} \cdot \mathrm{diag}\{\boldsymbol{d}(\tau)\} \cdot \boldsymbol{c}_s, \qquad (5.7) \\ &= \boldsymbol{c}^\mathrm{H}_{p,k} \cdot \mathrm{diag}\{\boldsymbol{c}_s\} \cdot \boldsymbol{d}(\tau), \qquad (5.8)\end{aligned}$$

where we have defined the vector $\boldsymbol{d}(\tau) = \left[\mathrm{e}^{-\jmath 2\pi m \frac{\tau}{t_\mathrm{p}}}\right]_{m\in\mathcal{M}}$.

Based on (5.8), the entire vector of observations $\boldsymbol{\psi}(\tau) \in \mathbb{C}^{K\times 1}$ can be described as

$$\boldsymbol{\psi}(\tau) = [\psi_1(\tau),\ \ldots,\ \psi_K(\tau)]^\mathrm{T} = \boldsymbol{C}^\mathrm{H}_p \cdot \mathrm{diag}\{\boldsymbol{c}_s\} \cdot \boldsymbol{d}(\tau), \tag{5.9}$$

where $\boldsymbol{C}_p = [\boldsymbol{c}_{p,1}, \ldots, \boldsymbol{c}_{p,K}] \in \mathbb{C}^{M\times K}$ contains the coefficients of all the K sequences $p_k(t)$. Equation (5.9) describes the observed output vector for a single delayed copy of $s(t)$. Since our receiver is linear, the observed vector $\boldsymbol{y} \in \mathbb{C}^{K\times 1}$ for the input signal $x(t)$

[3]Compressive sampling architectures that use PN-sequences for the $p_k(t)$ have been proposed, e.g., the modulated wideband converter [216]. Although these are not strictly bandlimited to B, their practical advantage is that they can be realized in hardware up to very high switching speeds.

according to (5.3) is given by

$$\boldsymbol{y} = \sum_{\ell=1}^{L} \alpha_\ell \boldsymbol{\psi}(\tau_\ell) + \tilde{\boldsymbol{w}}, \tag{5.10}$$

where $\tilde{\boldsymbol{w}} \in \mathbb{C}^{K\times 1}$ is the effective noise vector.

5.4 Delay Estimation Procedure

5.4.1 Gridded Sparse Recovery Based Estimator

Equation (5.10) shows that our observation vector can be modeled as a weighted sum of L terms $\boldsymbol{\psi}(\tau_\ell)$ under additive noise. Since $\boldsymbol{\psi}(\tau)$ is known to the receiver, this suggests that the delays can be recovered from $\boldsymbol{y}$ if $L < K$. The difficulty in estimating the delays lies in the fact that they can take any value from a continuous domain. A common and very simple approach to tackle such problems is to discretize the parameter space into an N-point sampling grid in τ referred to as $\tau_n^{(\mathrm{G})}$, $n = 1, 2, \ldots, N$. In the special case of a uniform sampling grid, we have $\tau_n^{(\mathrm{G})} = (n-1)\cdot\Delta\tau$, $n = 1, 2, \ldots, N$ where $\Delta\tau = \frac{t_\mathrm{p}}{N}$. Based on the sampled delays, we can define a basis $\boldsymbol{\Psi} \in \mathbb{C}^{K\times N}$ according to

$$\boldsymbol{\Psi} = \left[\boldsymbol{\psi}\left(\tau_1^{(\mathrm{G})}\right),\ \ \boldsymbol{\psi}\left(\tau_2^{(\mathrm{G})}\right),\ \ \ldots,\ \ \boldsymbol{\psi}\left(\tau_N^{(\mathrm{G})}\right)\right]. \tag{5.11}$$

Since the delays τ_ℓ can take any value, they will not be on any predefined sampling grid almost surely. However, it has been shown that if the sampling of the grid is not too coarse, one can still use the fact that $\boldsymbol{y}$ is approximately sparse in $\boldsymbol{\Psi}$ and apply suitable grid offset estimation procedures to correct for the mismatch between the grid points and the actual delays, cf. e.g., [231] for a comparison of interpolation strategies in this setting. Therefore, to facilitate the further explanations we now assume that all the delays τ_ℓ were exactly on the sampling grid, i.e., $\tau_\ell = \tau_{d_\ell}^{(\mathrm{G})}$ for some $d_\ell \in \{1, 2, \ldots, N\}$.

This allows us to write $\boldsymbol{y}$ as

$$\boldsymbol{y} = \boldsymbol{\Psi}\cdot\boldsymbol{\alpha} + \tilde{\boldsymbol{w}}, \tag{5.12}$$

where $\boldsymbol{\alpha} \in \mathbb{C}^{N\times 1}$ contains α_ℓ at the indices d_ℓ for $\ell = 1, 2, \ldots, L$ and zeros otherwise. In other words, besides for the noise, $\boldsymbol{y}$ is L-sparse in $\boldsymbol{\Psi}$. The delay estimation problem

can then be cast as a sparse recovery problem, e.g.,

$$\min \|\boldsymbol{\alpha}\|_1 \quad \text{s.t.} \quad \|\boldsymbol{y} - \boldsymbol{\Psi} \cdot \boldsymbol{\alpha}\|_2^2 \leq \sigma^2, \tag{5.13}$$

where σ^2 is an estimate of the noise power. Note that it has been shown in [216] that $K \geq 2L$ is sufficient to recover all the delays from $\boldsymbol{y}$ in the noise-free case.

5.4.2 Correlation Based Estimator

A simpler estimator is inspired by traditional, Nyquist-sampling based systems which simply correlate the observed signal with the known waveform and then estimate the location of the peak. Note that if there is only one path ($L = 1$) or if paths are very well separated (by more than the width of the correlation peak), this method is in fact optimal. Along these lines, the correlation based estimator in our setting is defined as

$$\hat{\tau} = \arg\max_{\tau} \left| \frac{\boldsymbol{\psi}(\tau)^{\mathrm{H}} \cdot \boldsymbol{y}}{\boldsymbol{\psi}(\tau)^{\mathrm{H}} \cdot \boldsymbol{\psi}(\tau)} \right|, \tag{5.14}$$

where the peak search is not limited to a prespecified grid. It is instructive to expand (5.14) for the special case $L = 1$ where we obtain

$$\hat{\tau} = \arg\max_{\tau} \; \alpha_1 \cdot \underbrace{\frac{\boldsymbol{\psi}(\tau)^{\mathrm{H}} \cdot \boldsymbol{\psi}(\tau_1)}{\boldsymbol{\psi}(\tau)^{\mathrm{H}} \cdot \boldsymbol{\psi}(\tau)}}_{\rho^{(\mathrm{c})}(\tau)} + \frac{\boldsymbol{\psi}(\tau)^{\mathrm{H}} \cdot \tilde{\boldsymbol{w}}}{\boldsymbol{\psi}(\tau)^{\mathrm{H}} \cdot \boldsymbol{\psi}(\tau)}. \tag{5.15}$$

Equation (5.15) shows that we are essentially finding the peak in the "compressed" correlation function $\rho^{(\mathrm{c})}(\tau)$.

5.5 Measurement Design

The previous sections have shown how the CS based receiver can be employed for delay estimation. As we have seen, it provides a sparsifying basis $\boldsymbol{\psi}(\tau)$ for the signal and the atoms $\boldsymbol{\psi}(\tau)$ depend on the choice of the signal $s(t)$ (through the vector $\boldsymbol{c}_s$) and the sampling functions $p_k(t)$ (through the matrix $\boldsymbol{C}_p$). In this section, we shed some light on their proper choice to obtain a good synchronization performance.

An "ideal" choice of $\boldsymbol{\psi}(\tau)$ would satisfy the conditions

$$\boldsymbol{\psi}(\tau_1)^{\mathrm{H}} \cdot \boldsymbol{\psi}(\tau_2) \approx \begin{cases} 0 & \tau_1 \neq \tau_2 \\ \text{const} & \tau_1 = \tau_2, \end{cases} \tag{5.16}$$

where the first condition asks for good cross-correlation properties between different delays and the second condition guarantees that the measurement is equally sensitive to all possible delays. This choice will ensure that the compressed correlation function $\rho^{(\mathrm{c})}(\tau)$ introduced in (5.15) is close to the ideal delta function. At the same time, it is also beneficial for the gridded sparse recovery based estimator since the first condition asks for low correlation between the columns of the sensing matrix $\boldsymbol{\Psi}$ (i.e., a low coherence) and the second condition guarantees that all columns have similar norms (to achieve a uniform sensitivity for all possible delays).

To measure how well a given matrix $\boldsymbol{\Phi}$ satisfies (5.16), we can formulate an error measure of the form $e(\boldsymbol{\Phi}, \tau_1, \tau_2) = (\boldsymbol{\psi}(\tau_1)^{\mathrm{H}} \cdot \boldsymbol{\psi}(\tau_2) - C \cdot \delta[\tau_1 - \tau_2]) \cdot \omega_{\tau_1,\tau_2}$ where $\omega_{\tau_1,\tau_2} \in \mathbb{R}_{\geq 0}$ is a weight function which allows to trade the weight between certain (τ_1, τ_2) regions, e.g., between uniform sensitivity ($\tau_1 = \tau_2$) and low cross-correlation ($\tau_1 \neq \tau_2$).

However, since it is difficult to minimize the error over the continuous variables τ_1 and τ_2 we consider it only on the N-point sampling grid introduced earlier. This leads to an error matrix $\boldsymbol{E}(\boldsymbol{\Phi}) \in \mathbb{R}^{N \times N}$ given by

$$\begin{aligned} \boldsymbol{E}(\boldsymbol{\Phi}) &= \left[e(\boldsymbol{\Phi}, \tau_{n_1}^{(\mathrm{G})}, \tau_{n_2}^{(\mathrm{G})}) \right]_{(n_1,n_2=1,2,\ldots,N)} \\ &= \left(\boldsymbol{\Psi}^{\mathrm{H}} \cdot \boldsymbol{\Psi} - C \cdot \boldsymbol{I}_N \right) \odot \boldsymbol{\Omega}, \\ &= \left(\boldsymbol{D}^{\mathrm{H}} \cdot \mathrm{diag}\{\boldsymbol{c}_s^*\} \cdot \boldsymbol{C}_p \cdot \boldsymbol{C}_p^{\mathrm{H}} \cdot \mathrm{diag}\{\boldsymbol{c}_s\} \cdot \boldsymbol{D} - C \cdot \boldsymbol{I}_N \right) \odot \boldsymbol{\Omega}, \\ &= \left(\boldsymbol{D}^{\mathrm{H}} \cdot \left(\left[\boldsymbol{C}_p \cdot \boldsymbol{C}_p^{\mathrm{H}} \right] \odot \left[\boldsymbol{c}_s^* \cdot \boldsymbol{c}_s^{\mathrm{T}} \right] \right) \cdot \boldsymbol{D} - C \cdot \boldsymbol{I}_N \right) \odot \boldsymbol{\Omega}, \end{aligned} \tag{5.17}$$

where we have used (5.9) to rewrite $\boldsymbol{\Psi}$ and defined $\boldsymbol{D} = [\boldsymbol{d}(\tau_1^{(\mathrm{G})}), \ldots, \boldsymbol{d}(\tau_N^{(\mathrm{G})})] \in \mathbb{C}^{M \times N}$. Moreover, $\odot$ in (5.17) denotes the Hadamard-Schur (elementwise) product and $\boldsymbol{\Omega}$ contains the weights ω_{τ_1,τ_2}. Based on (5.17), the quality of $\boldsymbol{\Psi}$ can be measured via an appropriate norm of $\boldsymbol{E}$. For instance, minimizing the (weighted) average squared error corresponds to minimizing the squared Frobenius norm of $\boldsymbol{E}$, whereas minimizing the maximal error is achieved by minimizing $\|\mathrm{vec}\{\boldsymbol{E}\}\|_\infty$. For simplicity, let us consider a Frobenius norm, leading to the following criterion for $\boldsymbol{C}_p$

$$\min_{\boldsymbol{C}_p} \left\| \left[\boldsymbol{D}^{\mathrm{H}} \cdot \left(\left[\boldsymbol{C}_p \cdot \boldsymbol{C}_p^{\mathrm{H}} \right] \odot \left[\boldsymbol{c}_s^* \cdot \boldsymbol{c}_s^{\mathrm{T}} \right] \right) \cdot \boldsymbol{D} - C \cdot \boldsymbol{I}_N \right] \odot \boldsymbol{\Omega} \right\|_{\mathrm{F}}. \tag{5.18}$$

Note that the problem (5.18) belongs to the class of weighted low-rank approximation problems which have been shown to be NP-hard [232] and do not admit a closed-form solution in general. However, iterative methods with some performance guarantees exist [233].

Note that in the special case $\boldsymbol{\Omega} = \mathbf{1}_{N\times N}$, problem (5.18) is equivalent to coherence minimization which has been studied, e.g., in [221]. Moreover, due to its structure we can actually solve it in closed form. From [4], we have the following theorem:

Theorem 2. *For a row-orthogonal matrix $\boldsymbol{A} \in \mathbb{C}^{M\times N}$ and a square Hermitian matrix $\boldsymbol{T} \in \mathbb{C}^{N\times N}$, consider the following optimization problem over matrices $\boldsymbol{\Phi} \in \mathbb{C}^{m\times M}$ with $m < M$*

$$\arg\max_{\boldsymbol{\Phi}} \left\| \boldsymbol{A}^{\mathrm{H}} \cdot \boldsymbol{\Phi}^{\mathrm{H}} \cdot \boldsymbol{\Phi} \cdot \boldsymbol{A} - \boldsymbol{T} \right\|_{\mathrm{F}}^{2}. \tag{5.19}$$

Then, a matrix $\boldsymbol{\Phi}$ maximizes (5.19) *if and only if $\boldsymbol{\Phi}^{\mathrm{H}} \cdot \boldsymbol{\Phi} = \boldsymbol{S}_m$, where $\boldsymbol{S}_m$ is a rank-m approximation of the matrix $\boldsymbol{S} = \boldsymbol{A} \cdot \boldsymbol{T} \cdot \boldsymbol{A}^{\mathrm{H}}$, obtained by setting all but the dominant m eigenvalues of $\boldsymbol{S}$ to zero.*

Applying Theorem 2 to (5.18) shows that $\boldsymbol{C}_p$ is optimal with respect to (5.18) if and only if it can be written as

$$\boldsymbol{C}_p = \sqrt{C} \cdot \mathrm{diag}\{\boldsymbol{c}_s^*\}^{-1} \cdot \boldsymbol{Q}, \tag{5.20}$$

where $\boldsymbol{Q} \in \mathbb{C}^{M\times K}$ is an arbitrary unitary matrix. However, this result is not very useful since it leaves a large space of possible solutions (any properly scaled row-orthogonal matrix) that achieve the same minimum in the cost function.

Therefore, instead of using (5.20), we choose to solve (5.18) using numerical optimization methods. Note that since the measurement matrix design is performed off-line once only, the computational complexity of solving this problem is not a critical issue.

5.6 Compressive RBS Synchronization

We now consider the challenge of synchronizing the WSN for accurate TDE performance. Now instead of transmitting a synchronization signal throughout the network, we consider reference broadcast synchronization (RBS), where the reference signal is an opportunistic signal already in the system (e.g., FM or TV signals).

The opportunistic signal, denoted as $s(t)$, is generally a non-periodic signal. The

received signal at node k with a delay τ_k is given by

$$y_k(t) = \alpha_k \cdot s(t - \tau_k) + w_k(t), \tag{5.21}$$

where $w_k(t)$ denotes the additive white Gaussian noise (AWGN) contaminating the received signal, α_k is the attenuation factor and τ_k is the true delay at the k-th node. Note that (5.21) ignores the effect of multipath propagation for simplicity, which we discuss later.

For each synchronization attempt, a reference transmitter informs all nodes to start recording an L point sampled version of $y_k(t)$. Let $\boldsymbol{y}_k = [y_k[0], y_k[1], \ldots, y_k[L-1]]^{\mathrm{T}} \in \mathbb{C}^L$ be the windowed sampled version of the recorded signal $y_k(t)$ at sampling times $t_0 \cdot \ell$, $\ell = 0, 1, \ldots, L-1$. For simplicity, we assume that the delays τ_k are integer multiples of the sampling times t_0, i.e., $\tau_k = d_k \cdot t_0$ for $d_k \in \mathbb{N}$.

The reference node records an N-sample version of its own observed signal $y_{\mathrm{ref}}(t)$, denoted by $\boldsymbol{y}_{\mathrm{ref}} \in \mathbb{C}^N$, which is then broadcasted to all other nodes as the synchronization template. By comparing this reference signal to its own observed signal $\boldsymbol{y}_k$, each node can estimate its relative delay to the reference node. Due to the aperiodicity of the SOO one has to ensure that the window of $s(t)$ contained in $\boldsymbol{y}_{\mathrm{ref}}$ falls completely within the window of $s(t)$ captured in $\boldsymbol{y}_k$ for all nodes. However, since it is unknown in advance whether $\tau_k < \tau_{\mathrm{ref}}$ or $\tau_k > \tau_{\mathrm{ref}}$ the reference node needs to start recording $\boldsymbol{y}_{\mathrm{ref}}$ a certain number of samples D_0 after the other nodes have started recording $\boldsymbol{y}_k$ and finishes D_1 samples before the other nodes stop. Thereby, we have $L = D_0 + N + D_1 > N$. The relative delay between $\boldsymbol{y}_k$ and $\boldsymbol{y}_{\mathrm{ref}}$ that the k-th node observes, referred to as Δd_k, is then related to the delays d_k and d_{ref} via $\Delta d_k = D_0 + d_k - d_{\mathrm{ref}}$. Consequently, D_0 must be chosen such that Δd_k is always non-negative, i.e., according to the highest expected delay offset between the reference node and any other node. Since D_0 is a fixed system design parameter, it is known to all nodes so that the relevant timing information can be extracted once Δd_k is estimated.

Now, since $\boldsymbol{y}_{\mathrm{ref}}$ represents a piece of the signal $s(t)$ completely inside the L-point sampling window chosen for $\boldsymbol{y}_k$ with a relative delay of Δd_k samples, we can write

$$\begin{aligned} &\boldsymbol{y}_{\mathrm{ref}} = \alpha_{\mathrm{ref}} \cdot \boldsymbol{s}_{\mathrm{ref}} + \boldsymbol{w}_{\mathrm{ref}} \quad \text{and} \quad \boldsymbol{y}_k = \alpha_k \cdot \boldsymbol{s}_k + \boldsymbol{w}_k, \quad \text{where} \\ &\boldsymbol{s}_{\mathrm{ref}} = \begin{bmatrix} \boldsymbol{0}_{N \times \Delta d_k} & \boldsymbol{I}_N & \boldsymbol{0}_{N \times L-N-\Delta d_k} \end{bmatrix} \cdot \boldsymbol{s}_k. \end{aligned} \tag{5.22}$$

By correlating $\boldsymbol{y}_{\mathrm{ref}}$ with all N-point subvectors of $\boldsymbol{y}_k$, each terminal can determine its relative delay from the location of the peak of the correlation function. Note that the

accuracy of the synchronization depends on the width of the auto correlation function (ACF) of $\boldsymbol{y}_{\text{ref}}$, i.e., for accurate localization, it should be a wideband signal.

The cross correlation function between $\boldsymbol{y}_{\text{ref}}$ and all N-point subvectors of $\boldsymbol{y}_k$ can be defined as

$$\rho_k[\Delta d] = \frac{1}{L}\boldsymbol{y}_{\text{ref}}^{\text{H}} \cdot \boldsymbol{y}_k[\Delta d], \tag{5.23}$$

where $\boldsymbol{y}_k[\Delta d] = \begin{bmatrix}\boldsymbol{0}_{N\times\Delta d} & \boldsymbol{I}_N & \boldsymbol{0}_{N\times L-N-\Delta d}\end{bmatrix} \cdot \boldsymbol{y}_k \in \mathbb{C}^N$ is the N-point subvector of $\boldsymbol{y}_k$ with relative offset $\Delta d = 0, 1, \ldots, L-N$.

The estimated relative delay $\Delta\hat{d}_k$ at node k is then given as

$$\Delta\hat{d}_k = \arg\max_{\Delta d} |\rho_k[\Delta d]|. \tag{5.24}$$

In the ideal noise-free case, we obviously have $\Delta\hat{d}_k = \Delta d_k$ (i.e., $\rho_k[\Delta d]$ has a peak at $\Delta d = \Delta d_k$).

The main drawback of this wireless synchronization approach is that the reference signal $\boldsymbol{y}_{\text{ref}}$ has to be broadcast by the reference node to all the other nodes. Since accurate localization requires the signals to be wideband, this transmission requires a significant amount of bandwidth which is highly undesirable. Therefore, we propose the following remedy, which is based on Compressed Sensing (CS) theory: Instead of $\boldsymbol{y}_{\text{ref}}$, the reference node broadcasts a compressed vector $\boldsymbol{z}_{\text{ref}} = \boldsymbol{\Phi} \cdot \boldsymbol{y}_{\text{ref}} \in \mathbb{C}^{M\times 1}$ where $\boldsymbol{\Phi} \in \mathbb{C}^{M\times N}$. With $M < N$, transmitting $\boldsymbol{z}_{\text{ref}}$ requires less bandwidth than transmitting $\boldsymbol{y}_{\text{ref}}$.

This approach may look strange since $\boldsymbol{y}_{\text{ref}}$ cannot be assumed to be a compressible signal and therefore, $\boldsymbol{y}_{\text{ref}}$ cannot be recovered from $\boldsymbol{z}_{\text{ref}}$ in general (i.e., there is a loss of information). However, note that the goal is not to recover the opportunistic signal but instead to recover (the peak of) its autocorrelation function. Since the latter is in fact quite sparse, it can be well compressed which is achieved by the proposed method, as we show below.

After the nodes have received $\boldsymbol{z}_{\text{ref}}$, the *compressed* correlation function $\rho_k^{(\text{c})}[\Delta d]$ is estimated via

$$\rho_k^{(\text{c})}[\Delta d] = \frac{1}{L}\boldsymbol{z}_{\text{ref}}^{H} \cdot \boldsymbol{z}_k[\Delta d], \tag{5.25}$$

where $\boldsymbol{z}_k[\Delta d] = \boldsymbol{\Phi} \cdot \boldsymbol{y}_k[\Delta d]$ is the compressed version of $\boldsymbol{y}_k[\Delta d]$ and $\boldsymbol{y}_k[\Delta d]$ is an L-point subvector of $\boldsymbol{y}_k$ according to (5.23). Then, the k-th node obtains its estimate $\Delta\hat{d}_k$ from the peak of $\rho_k^{(\text{c})}[\Delta d]$ according to (5.24).

To see why this procedure works, we can express the correlation function in the compressed domain in terms of$\boldsymbol{y}_k$ and $\boldsymbol{y}_{\text{ref}}$ via

$$\rho_k^{(\text{c})}[\Delta d] = \frac{1}{L}\boldsymbol{y}_{\text{ref}}^H \cdot \boldsymbol{\Phi}^H \cdot \boldsymbol{\Phi} \cdot \boldsymbol{y}_k[\Delta d]. \tag{5.26}$$

Now, comparing (5.23) and (5.26), we see that the only difference between the original correlation function $\rho_k[d]$ and the correlation function $\rho_k^{(\text{c})}[d]$ based on the compressed reference signal is in the term $\boldsymbol{\Phi}^H\boldsymbol{\Phi}$ which is the Gram matrix of the compression matrix. However, CS theory has shown that one can find matrices $\boldsymbol{\Phi}$ such that $\boldsymbol{\Phi}^H\boldsymbol{\Phi}$ is close to an identity matrix. Often, $\boldsymbol{\Phi}$ is drawn randomly [31] which is a good strategy if the problem dimensions are not too small. Therefore, (5.26) is expected to have its main correlation peak at $\Delta d = \Delta d_k$ as long as the compression rate is not too high. At the same time, a degradation of the cross-correlation level is expected, which we show via numerical results in Section 5.7.

Note that some simplifying assumptions have been made in this work that need to be lifted before it can be applied in real systems. Firstly, we have not considered the multipath nature of the wireless propagation channel. We consider an extension to the multipath case feasible, e.g., by considering approaches based on signal cross-correlations [234] or by estimating more than one dominant peak in the ACF [217].

Secondly, we have limited our attention to relative delays that are integer multiples of the sampling time. The entire analysis can be extended to the case of fractional delays by applying oversampling to the opportunistic signals before applying the compression. For instance, to evaluate the correlation function at sample 0.25, oversample the received signal by a factor of 4, shift by one subsample, downsample; then compress and compare to the compressed reference signal (which remains the same). The amount of oversampling applied represents a tradeoff between the computational complexity and the final synchronization accuracy that shall be achieved.

5.7 Numerical Results

In this section we present some numerical results to show the performance of the proposed CS-based architecture for delay estimation and to demonstrate the advantage of using the compressed synchronization design according to our proposed methodology.

5.7.1 Compressive Time Delay Estimation

The observed signal is generated according to (5.10). The transmit signal is chosen according to $c_s[m] = \mathrm{e}^{\jmath\varphi_m}$ where φ_m is drawn from a uniform distribution in $[0, 2\pi)$. In other words, the transmitter distributes its power evenly across frequency, which corresponds to a sinc-like pulse in the time domain. The noise samples in the noise vector $\boldsymbol{w}$ are drawn from a zero-mean circularly symmetric complex Gaussian distribution with $N_0 = \frac{1}{\mathrm{SNR}}$.

The coefficients $\boldsymbol{C}_p$ are modeled as $\mathrm{e}^{\jmath\varphi_{m,k}}$ where $\varphi_{m,k}$ are drawn from a uniform distribution in $[0, 2\pi)$ for the random approach and used as optimization variables in the proposed optimized choice of $\boldsymbol{C}_p$. The latter is found by solving (5.18) via Matlabs numerical optimization toolbox. The weight matrix is chosen according to $\boldsymbol{\Omega} = (1-\rho) \cdot \boldsymbol{I}_N + \rho \cdot \boldsymbol{1}_N$, where $\rho \in \mathbb{R}_{[0,1]}$ allows to adjust this trade-off: values close to zero put more weight on the main diagonal (for uniform sensitivity) whereas values closer to one shift the weight to the off-diagonal elements (for low cross-correlation). The results shown here are obtained for $\rho = 0.5$. Finally, the constant C is set to $K \cdot M$.

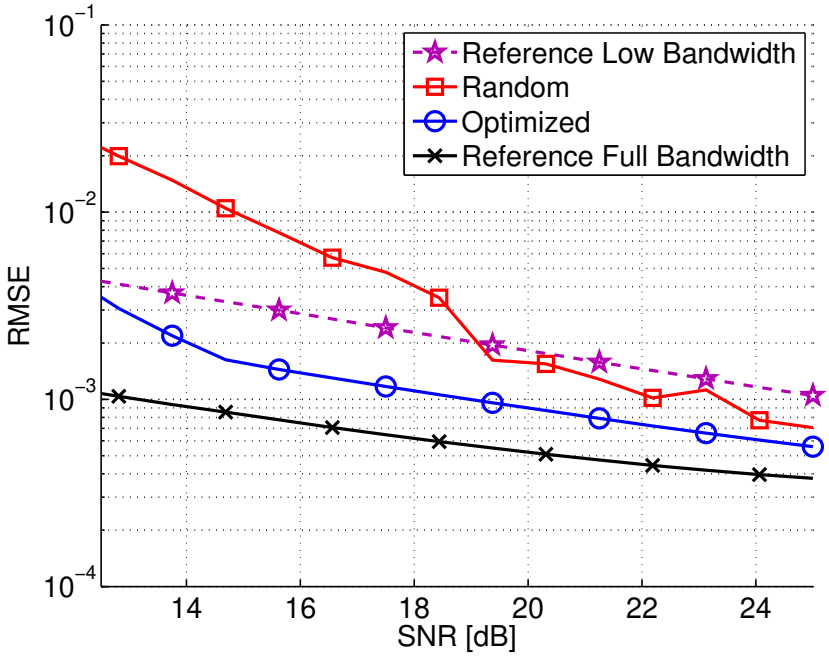

Figure 5.3: Relative RMSE of the delay τ_1 (in units of t_p) vs. SNR for $K = 5$ branches and $M = 20$ spectral lines.

Figure 5.3 depicts the result for a system with $K = 5$ branches that uses $M = 20$ spectral lines (i.e., the compression rate is 4). The relative root mean square delay estimation error of the estimator (5.15) (in units of t_p) is estimated over 100'000 Monte

Carlo trials. A single path scenario is chosen where $\alpha_1 = 1$ and τ_1 is drawn randomly from $[0, t_\mathrm{p})$. Since we have a single path, the correlation-based estimator according to (5.14) is used to estimate the delays.

For comparison, the achievable accuracy of a traditional system that uses no compression but a full-rate ADC is also shown ("Reference Full Bandwidth") as well as the performance of a system that uses 1/4 of the bandwidth ("Reference Low Bandwidth"). The results demonstrate that the optimized measurement kernel outperforms the randomly chosen one, in particular for lower SNRs. This behavior is mainly due to the outliers that occur due to the sidelobes in the compressed correlation function. Moreover, the CS-based system achieves an accuracy better than a Nyquist system operating with a reduced bandwidth / sampling rate.

To shed further light on this aspect, Figure 5.4 depicts the estimated complementary cumulative distribution function (CCDF) of the RMSE for the same simulation at an SNR of 13 dB. We can see that the random choice of the measurement kernels is more prone to outliers. This behavior becomes even more pronounced for lower SNRs.

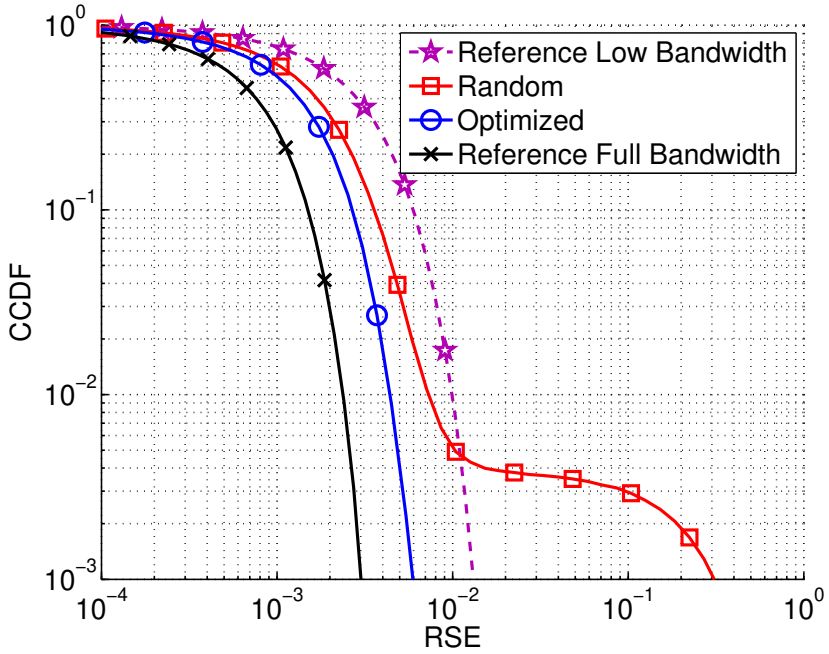

Figure 5.4: Histogram of the relative root squared error of τ_1 for $K = 5$, $M = 20$, and an SNR of 13 dB.

Figure 5.5 shows the estimation result for a $L = 6$ path channel for $K = 10$, $M = 20$, and an SNR of 30 dB, using the estimator from (5.13). The true value of delays and amplitudes are indicated by the markers labeled "True" and compared to the proposed

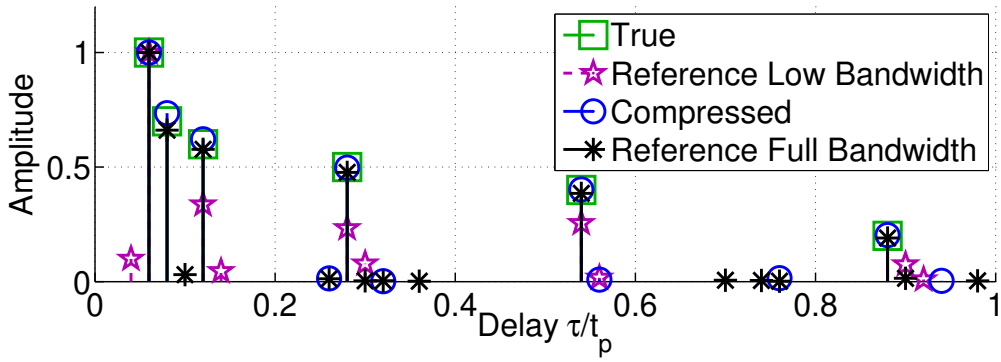

Figure 5.5: Estimation of a multipath channel with $L = 6$ paths for $K = 10$, $M = 20$, SNR = 30 dB

compressed approach (using an optimized matrix for $\rho = 0.5$) and the low/full bandwidth reference.

The result shows that the compressed approach finds all the taps while the low bandwidth version misses some peaks (and finds comparably strong spurious ones).

5.7.2 Compressive RBS Synchronization

We consider an OFDM signal as the opportunistic signal to be used for synchronization. An $L = 2048$ sample window is recorded at each node. The reference signal is chosen to be the first $N = L/2$ samples with $D_0 = L/4$. The received signals at the k^{th} node and the reference node have a delay of $d_k = 36$, and $d_{\text{ref}} = 65$ samples, respectively. Therefore, the correlation peak is expected at the sample index $\Delta d_k = D_0 + d_k - d_{\text{ref}} = 483$. The additive noise vectors are drawn from a zero mean circularly symmetric complex Gaussian distribution with variance P_{N}, corresponding to a (pre-correlation) signal to noise ratio (SNR) of $1/P_{\text{N}}$.

To implement our compressed correlation technique, we use a random compression matrix $\mathbf{\Phi} \in \mathbb{C}^{M \times N}$, where M is the length of the compressed signal to be communicated throughout the network, i.e., the compressed signal has a bandwidth of $\frac{M}{N} \cdot B = \frac{B}{R}$, where $R = N/M$ denotes the compression rate. The coefficients of $\mathbf{\Phi}$ are drawn from a zero mean circularly symmetric complex Gaussian distribution as well where each element has variance $\frac{1}{N}$.

Figure 5.6 shows the correlation functions computed using the proposed compressed design for an SNR of 0 dB (for clarity, only the region around the correlation peak is shown).

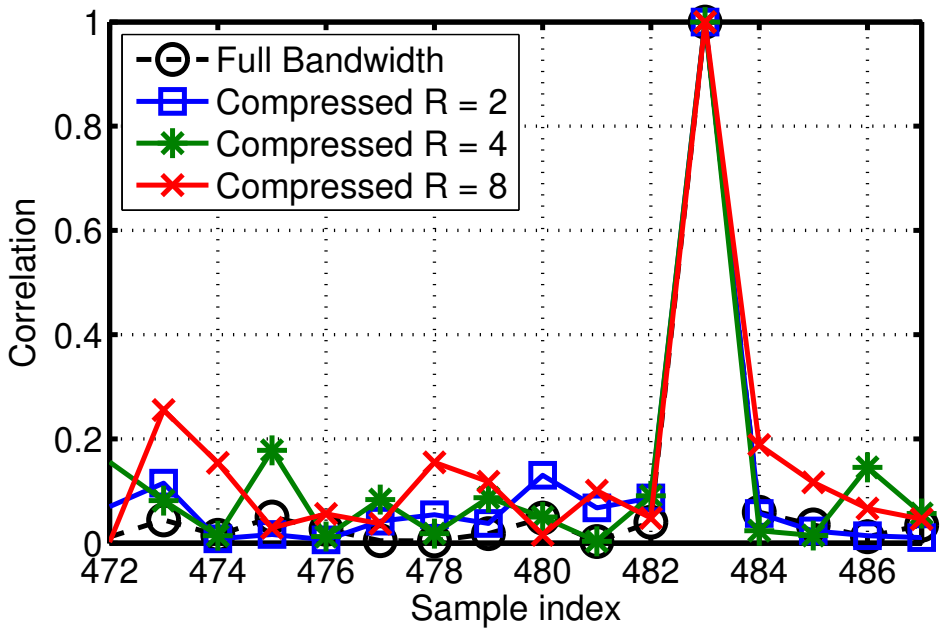

Figure 5.6: Comparison of the correlation function $\rho_k^{(c)}[\Delta d]$ at a node k with $\Delta d_k = 483$ for different compression rates R.

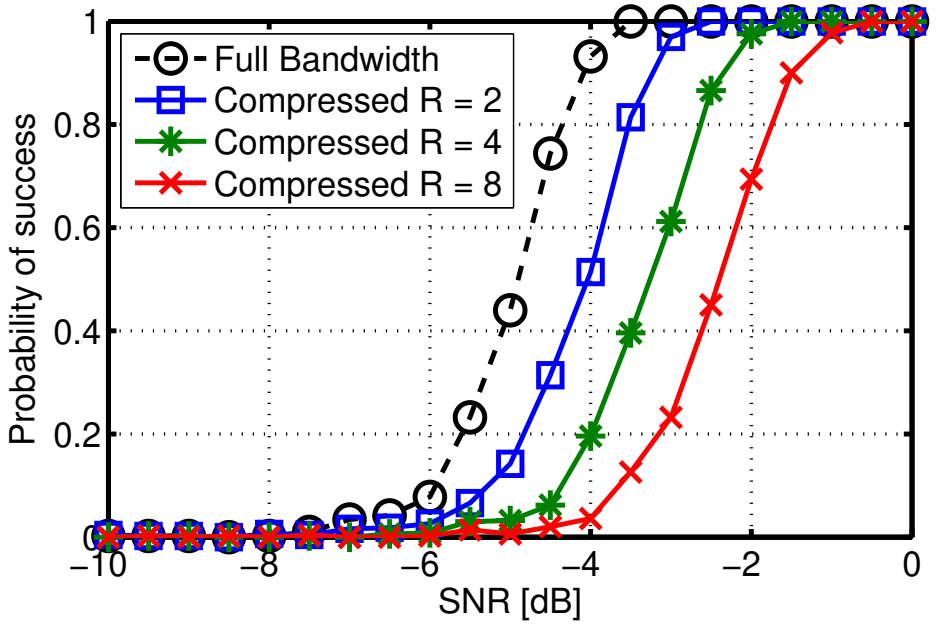

Figure 5.7: Empirical probability of correctly detecting the main correlation peak vs. the SNR for different compression rates R.

For comparison, the graph labeled "Full Bandwidth" shows the result when the reference node sends an uncompressed (high bandwidth) copy of the opportunistic signal to all nodes and they use that to obtain the correlation. As expected, the compressed designs achieve almost the same accuracy as the high bandwidth system (i.e., they all have a peak at the correct delay $\Delta d_k = 483$) at a much lower bandwidth. Figure 5.6 also shows that higher compression leads to higher side lobes.

To further analyze this behavior, we have conducted an additional experiment shown in Figure 5.7. Here, we vary the SNR by scaling all the noise samples to variance 1/SNR. We compute the empirical probability that the main correlation peak is identified at the correct location, i.e., $\Pr[\Delta\hat{d}_k = \Delta d_k]$. The empirical probabilities are averaged over 500 trials where each trial represents a new realization of the noise samples as well as the compression matrix $\mathbf{\Phi}$. Higher compressions move the curve to higher SNRs. This means that to achieve the same success rate a larger SNR is required when compared to the uncompressed approach. This can be explained according to (5.26) where the correlation between the columns of the compression matrix rises and hence $\mathbf{\Phi}^{\mathrm{H}}\mathbf{\Phi}$ deviates stronger from the identity matrix, distorting the shape of the correlation function.

5.8 Summary

In this chapter, we have investigated a system architecture for delay estimation via Compressed Sensing (CS). We propose to use a bank of K periodic functions $p_k(t)$ that multiply the received signal and are sampled once per period. Thereby, the effective sampling rate is reduced by a factor which depends on the period, the bandwidth, and the number of channels K.

We then discuss the design of the functions $p_k(t)$ based on their frequency domain representation. We propose an approach that directly optimizes the shape of the auto-correlation function in terms of the choice of $p_k(t)$ and demonstrate that it outperforms a random choice in terms of the delay estimation accuracy.

We have also discussed a compressed technique for temporal synchronization with high bandwidth opportunistic signals. The main idea is to let the reference node transmit a compressed form of the reference signal for synchronization and thus reducing the data rate needed for communication between the nodes.

We proposed a random design of the compression matrix inspired by the compressed sensing findings about designing measurement ensembles that preserve the information rate of the original system. We have shown that the compression does not significantly affect the correlation function obtained at the receiving nodes compared to the high

bandwidth correlation functions obtained from the original non-compressed reference

However, the expense for the reduction in bandwidth is an increased sidelobe level of the correlation function. This effect mirrors a degradation in the effective SNR which means that there is a tradeoff between the bandwidth reduction and the SNR that can be controlled by the compression ratio.

Chapter 6

Compressive Spatial Channel Sounding

This chapter deals with the application of compressive arrays discussed in Chapter 4 to channel sounding. After the motivation in Section 6.1, the main channel sounding principles are summarized in Section 6.2. In Section 6.3, the usage of compressive arrays for spatial channel sounding is investigated and then evaluated by numerical simulations based on a real scenario in Section 6.4. The chapter is then summarized in Section 6.5.

6.1 Motivation

Electromagnetic (EM) wave propagation between transmitter (TX) and receiver (RX) antennas undergoes a variety of interactions with the objects of the environment leading to multiple propagation paths that are spread in directions of departure (DoD) and arrival (DoA), time delay and Doppler. Proper handling of this multipath diversity is the key enabler to achieve high data rate, robust operation and ubiquitous coverage in mobile radio. Therefore, the multidimensional structure of electromagnetic wave propagation has to be studied, analyzed, and identified.

Multidimensional channel sounding is the key technology for experimental analysis of electromagnetic wave propagation in mobile radio channels [235]. A channel sounder is a multidimensional data recording system, which measures and identifies the multipath propagation structure in mobile radio. These measurement results are required for experimental studies of multipath propagation, channel modeling and mobile radio system performance prediction. If conventional Nyquist schemes are applied, the recorded data volume is determined by the number of antenna array elements at TX and the RX, the length of the channel impulse response and the number of the observed snapshots

over slow time. A wide variety of high resolution parameter estimation (HRPE) is available [19] to estimate these structural parameters by fitting an appropriate data model to the recorded data.

The number of measurements is orders of magnitude larger than the number of parameters. This suggests that there is a significant amount of redundancy (sparsity) in the recorded signals. In this chapter, it is our goal to take advantage of compressive sensing (CS) [30, 31, 101] to reduce the amount of data stored and the hardware complexity without losing any relevant information but saving a huge part of resources. Moreover, snapshot recording time (and thus repetition time) can be considerably reduced (e.g., by minimizing the number of recorded Tx/Rx MIMO links). This allows better handling of dynamic scenarios (i.e., increasing the Doppler range) which is still the highest challenge in MIMO channel sounding.

The application of CS to channel sounding is hardly described in literature. A Channel Sounding Xampler was proposed in [236] based on the sub-Nyquist Xampling architecture [237] reducing the measurement acquisition time while simultaneously estimating time delays, multipath amplitudes, and angles of arrival. However, the main focus was to reduce the sampling effort in the time-frequency domain by exploiting the sparsity of the channel there. Otherwise, related ideas can be found in the application of compressed sensing to MIMO radar [238] and compressive channel sensing [46].

In this chapter, we exploit the application of CS to the double-directional channel sounder in the spatial domain that includes joint DoA/DoD estimation. In particular, the CS paradigm can be implemented in the spatial domain by employing M antenna elements that are combined into a smaller number of $m < M$ active RF chains using an analog combining network (at the transmitter, the receiver or both). Since only m channels need to be sampled and digitized, the hardware complexity remains comparably low while allowing us to cover a larger aperture (and thus be more selective) than a traditional, Nyquist ($\lambda/2$) spaced m-channel antenna array. Based on the fact that the underlying signal is sparse in the angular domain, CS theory suggests that it can be recovered from $m < M$ measurements, provided that the measurement kernel is appropriately chosen.

A compressive spatial channel sounder is proposed and evaluated based on real scenarios showing superior advantages in terms of time, hardware complexity and resolution. In particular, the proposed approach reduces the total number of switching periods, which implies a reduced channel acquisition time and thus an improved Doppler bandwidth. On the other hand, the compressive approach reduces the number of RF chains, which is a very relevant advantage in terms of the overall receiver complexity,

the amount of data to be processed in the digital domain (e.g., FPGA), power consumption, as well as RF hardware calibration. Alternatively, for the same measurement time and/or hardware complexity, one can increase the number of array elements to cover a larger aperture and so achieving better performance in terms of resolution.

6.2 Channel Sounding

The definition of the channel sounding data model is crucial for parameter estimation. It has to represent the reality of wave propagation and the influence of the measurement device. We prefer a data model comprising two components which can be handled separately throughout the estimation procedure. The first part is deterministic and results from specular-like reflections. The second part represents distributed diffuse scattering which typically occurs in a complicated, multipath rich environment. We focus on the first part and leave the second for future works (see e.g., [239] for more details about handling diffuse scattering).

Consider measuring the channel transfer function between two points in space (n_{TX} for the n-th antenna array element at the transmitter and m_{RX} for the m-th receiver element) inside a certain bandwidth. A simplified model for the channel in the multidimensional aperture domain is given by a superposition of a discrete number of S propagation paths [240].

Expressed in the frequency domain, we can write

$$h(f, m_{\mathrm{RX}}, n_{\mathrm{TX}}) = \sum_{s=1}^{S} \gamma_s \cdot \mathrm{e}^{-\jmath 2\pi f \tau_s} \cdot g_{m,\mathrm{RX}}(\mathbf{\Omega}_{s,\mathrm{RX}}) \cdot g_{n,\mathrm{TX}}(\mathbf{\Omega}_{s,\mathrm{TX}}), \tag{6.1}$$

where f denotes the frequency, $\gamma_s \in \mathbb{C}$ and $\tau_s \in \mathbb{R}$ are the amplitude and delay of the s-th path, $\mathbf{\Omega}_{s,\mathrm{RX}}$ and $\mathbf{\Omega}_{s,\mathrm{TX}}$ denote the Direction-of-Arrival (DoA) and Direction-of-Departure (DoD), in general in both azimuth and elevation domain, of the s-th path at the receiving and the transmitting side. Moreover, $g_{m,\mathrm{RX}}$ and $g_{n,\mathrm{TX}}$ denote the complex radiation pattern of the m-th receiver and n-th transmitter element, respectively[1]. The complex patterns describe the gain of the antenna itself as well as the phase shift caused by the geometrical arrangement within the antenna array.

The temporal and frequency characteristics are measured by exciting the channel with a well defined transmit signal. The channel impulse response is obtained by post-processing the recorded data, depending on the type of transmit signal. Common types of signals are pseudo-noise sequences with subsequent correlation of the measured data

[1] In general they will depend on frequency f as well but we assume here that the bandwidth is not too high.

with the transmit sequence as well as specially designed periodic multi-tone signals. The benefit of multi-tone signals is the easier control of the occupied bandwidth (theoretically, it is rectangularly shaped). Furthermore, the transmit signal can be removed from the recorded data (deconvolution of the transmit signal) by a simple division in the frequency domain. This step can be combined with the calibration of the RF equipment resulting in very little additional effort.

For measuring the spatial properties of the channel, MIMO channel sounders are used. They feature antenna arrays at both the transmitter and receiver side. Specifically, double-directional measurements that include joint DoA/DoD estimation allow the separation of the directional dependent influence of the measurement antennas from the channel measurements which is a prerequisite of antenna-independent channel characterization [235].

In theory, all combinations of transmitter and receiver array elements can be measured at the same time and frequency. While this can be achieved with parallel RF chains at the receiver, it is not meaningful to excite all transmitter elements with the same signal at the same time, due to the inability to distinguish the different transmitters at the receiver. To be able to separate TX antennas, one has to choose transmit sequences that are at least linearly independent over the antennas (or better yet, orthogonal). These can be Code, Frequency, or Time Division Multiplexing (CDM or FDM or TDM) or combinations thereof. The most established technique is Time Division Multiplex (TDM). TDM based sounders measure the response from each TX antenna element separately by switching. During a specific time frame, only a single transmitter antenna element is active. For this reason, TDM only needs one TX RF chain followed by a switch, which makes it very attractive from the hardware complexity point of view. We therefore focus on TX TDM exclusively in this paper.

For the measurement at the receiver, we have two main options. The first is to let all M RX antennas listen jointly which then requires M RF chains. The other option is to apply receive switching as well. The advantage of the latter is the use of a single RF-chain and ADC/DAC which relaxes the requirements of the RF calibration dramatically. However, the price we pay is an M times longer measurement time. Intermediate options between the two extremes are possible as well, which allows us to control the trade-off between the hardware complexity and the measurement rate (which controls the Doppler bandwidth we can cover).

At TU Ilmenau, a MIMO channel sounder is available which is designed following the TDM principle [241, 242] at TX and RX. The RUSK-HyEff-Sounder was used throughout numerous channel sounding campaigns where a variety of different antenna arrays

suitable for high resolution parameter estimation were employed. The obtained data was used to directly evaluate the performance of different MIMO systems [243], as well as an input for calculating parameters of the channel model [244].

6.3 Compressive Spatial Channel Sounding

The number of array elements and the choice of the antenna array geometry heavily determines the performance of any subsequent high resolution parameter estimation algorithm. According to the spatial sampling theory, the distance between adjacent sensors should be less than or equal to half a wavelength of the impinging planar wavefronts, otherwise it leads to grating lobes (sidelobes) in the spatial correlation function which correspond to near ambiguities in the array manifold. At the same time, to achieve DoA/DoD estimation with a high resolution, the receiving arrays should have a relatively large aperture [28]. This implies that arrays with a large number of antennas are needed to obtain a high resolution, which then requires complex hardware processors and/or long measurement times. The main goal of this work is to exploit the sparsity of the channel in the spatial domain considering only the specular-like components of the channel towards reducing that measurement complexity (i.e., hardware and time).

Recently, compressed sensing (CS) has been widely suggested for applications that exhibit sparsity in space to reduce the measurement efforts and/or improve the estimation performance (i.e., spatial resolution). It is highlighted in [29] that if the electromagnetic field is modeled as a superposition of a few plane waves, the DoA/DoD estimation problem can be expressed as a sparse recovery problem. Since then, many sparse recovery algorithms became popular in the CS field for the DoA/DoD estimation problem as an alternative to existing parameter estimation algorithms [175, 176]. On the other hand, there has been comparably little research towards applying the CS paradigm spatially to antenna arrays. Yet, this is an attractive idea since the sampling of RF signals is a costly task as each receiver chain requires hardware components such as low-noise amplifiers, filters, mixers, and A/D converters. Therefore, reducing the number of channels that have to be sampled could significantly lower the hardware complexity and the measurement time [8, 45, 150]. In this work, we extend this idea to the double directional MIMO scenario with antenna arrays at both the transmitter and the receiver. We focus on the spatial domain where the ultimate goal is to estimate the DoAs and the DoDs.

Consider a multipath channel scenario with S paths. A MIMO channel sounder is used with N transmit antennas and M receive antennas. For a single snapshot and

assuming only a narrowband scenario, the channel can be written as:

$$h(m_{\mathrm{RX}}, n_{\mathrm{TX}}) = \sum_{s=1}^{S} \gamma_s \cdot a_{m,\mathrm{RX}}(\boldsymbol{\Theta}_{s,\mathrm{RX}}) \cdot a_{n,\mathrm{TX}}(\boldsymbol{\Theta}_{s,\mathrm{TX}}), \tag{6.2}$$

where $\gamma_s \in \mathbb{C}$ and $\tau_s \in \mathbb{R}$ are the amplitude and delay of the s-th path, $\boldsymbol{\Omega}_{s,\mathrm{RX}}$ and $\boldsymbol{\Theta}_{s,\mathrm{TX}}$ denote the Direction-of-Arrival (DoA) and Direction-of-Departure (DoD) in the azimuth domain, of the s-th path at the receiving and the transmitting side. Moreover, $a_{m,\mathrm{RX}}$ and $a_{n,\mathrm{TX}}$ denote the array response of the m-th receiver and n-th transmitter element, respectively.

In matrix notation, one can write

$$\boldsymbol{H} = \boldsymbol{A}_{\mathrm{RX}}^{T} \cdot \boldsymbol{\Gamma} \cdot \boldsymbol{A}_{\mathrm{TX}}, \tag{6.3}$$

where $\boldsymbol{H} \in \mathbb{C}^{M \times N}$ represents the channel transfer function in the spatial domain, $\boldsymbol{\Gamma}$ is a diagonal matrix with the paths' power on the main diagonal, $\boldsymbol{A}_{\mathrm{RX}}$ and $\boldsymbol{A}_{\mathrm{TX}}$ are the array steering matrices for the receive and transmit arrays respectively.

The main idea of spatial CS is that instead of measuring each antenna separately, we sample only a linear combination of the signals from all the antennas. Such linear combinations can be implemented in the analog domain, e.g., via networks of power dividers and phase shifters (see [8] for more details).

For channel sounding, we apply this idea at both the TX and the RX. For the TX, this means that instead of transmitting from one antenna at a time and cycling through all antennas, we transmit via a set of beams, where each beam represents a complex weight vector applied to the TX antennas. We can write this as a sequence of transmit signals $\boldsymbol{\varphi}_{\mathrm{TX},k} \cdot s_k$, $k = 1, 2, \ldots, n$, where $\boldsymbol{\varphi}_{\mathrm{TX},k} \in \mathbb{C}^N$ and s_k are the weight vector and the transmit symbol in the k-th TX switching period, respectively.

At the receiver, instead of measuring the antenna signals directly, we form linear combinations via receive weight vectors denoted as $\boldsymbol{\varphi}_{\mathrm{RX},\ell} \in \mathbb{C}^M$, which can again be implemented as an analog beamforming network. Here, $\ell = 1, 2, \ldots, m$ represents the receive measurement index. After cycling through all n TX beams and all m RX weight vectors, we have collected a total number of $n \cdot m$ compressive observations which we can write as

$$\boldsymbol{H_c} = \boldsymbol{\Phi}_{\mathrm{RX}}^{T} \cdot \boldsymbol{A}_{\mathrm{RX}}^{T} \cdot \boldsymbol{\Gamma} \cdot \boldsymbol{A}_{\mathrm{TX}} \cdot \boldsymbol{\Phi}_{\mathrm{TX}}, \tag{6.4}$$

where $\boldsymbol{H_c} \in \mathbb{C}^{m \times n}$ denotes the compressive spatial channel transfer function and $\boldsymbol{\Phi}_{\mathrm{RX}} \in$

$\mathbb{C}^{m\times M}$ and $\mathbf{\Phi}_{\mathrm{TX}} \in \mathbb{C}^{n\times N}$ represent the RX and TX combining matrices which contain the vectors $\boldsymbol{\varphi}_{\mathrm{RX},\ell}$ and $\boldsymbol{\varphi}_{\mathrm{TX},k}$, respectively.

Compared to the Nyquist approach, this reduces the total number of observations from $M \cdot N$ to $m \cdot n$ where $n < N$ and $m < M$. This implies some relevant practical benefits. First of all, the proposed approach reduces the total number of TX switching periods to $n < N$, which implies a reduced channel acquisition time and thus an improved Doppler bandwidth. For the receiver, the concrete advantage depends on the implementation choice which was discussed in Section 6.2. If we choose to employ M RX RF chains, the compressed approach reduces the number of RF chains to $m < M$, which is a very relevant advantage in terms of the overall receiver complexity, the amount of data to be processed in the digital domain (e.g., FPGA), power consumption, as well as RF hardware calibration. If we choose to measure the RX chains sequentially and employ receive switching, the compressive approach reduces the number of measurement cycles further compared to Nyquist since instead of $M \cdot N$ we then only require $m \cdot n$ cycles.

Note that another advantage of such a compressive architecture is that it allows us to reconfigure the array on the fly without any change in the receiver hardware which can be very advantageous in many applications. In [45] and its follow-up papers, it has been suggested to consider measurement kernels $\mathbf{\Phi}$ drawn from random distributions such as Gaussian or Bernoulli distributions. Such a choice is popular due to its simplicity and certain mathematical guarantees on the uniform support recovery, i.e., recovering arbitrary subsets of K non-zero entries in $\boldsymbol{s}(t)$. In our recent works [4,8], we have shown that optimizing $\mathbf{\Phi}$ can improve the performance significantly. We will compare different constructions of $\mathbf{\Phi}$ via simulations and discuss their implementation.

After having the compressive measurements, the same ML-based estimators (e.g., The RIMAX [245]) could be applied to multidimensional channel parameter estimation from field experiments. In this paper, our goal is to evaluate the performance of recovering the channel parameters from noisy observations. To this end, the performance metrics we consider are the conditional (deterministic) Cramér-Rao Bounds (CRBs) as a proxy to the performance of ML-type estimators. This is done since ML estimators are known to (asymptotically) achieve the CRB and therefore it provides an abstraction over the concrete ML implementation. Moreover, the computation of the CRBs is much simpler allowing for larger ensembles to be considered. In addition, since the compression is a linear operation, it is very easy to find the CRB for the compressed model (6.4), cf. [8]. Future works would feature direct application of an ML-based estimator to the compressive measurements from realistic scenarios towards obtaining the

channel parameters.

6.4 Numerical Simulations

In this section, we present some numerical results to demonstrate the compressive spatial channel sounding concept and evaluate its advantages compared to conventional sounding. At TU Ilmenau, a MIMO channel sounder is available which is designed following the TDM principle at the TX and the RX. The sounder was used throughout numerous channel sounding campaigns where a variety of different antenna arrays suitable for high resolution parameter estimation were employed. We consider a realistic scenario based on a sounding campaign of the RESCUE project [246] at the campus of TU Ilmenau. Here, a V2V-type setup was considered at the campus of the TU Ilmenau at 2.35 GHz carrier frequency and 36 dBm transmit power. The antenna arrays used at both the transmitter and receiver are two 16-element Stacked Polarimetric Uniform Circular Array (SPUCA) placed on two trolleys. The main purpose is to investigate the impact of a moving transmitter on the channel observed by the receiver. Therefore, a grid of transmitter locations was selected where the grid points are separated by 10m on each lane (two adjacent grid points on the same lane are 10m apart). The transmitter was located on each of the grid points and the receiver was slowly moved on the opposite lane. Figure 6.1 shows the grid positions of the TX and the RX where the black circle highlights the positions we use for our simulations.

After the measurement campaign, we have ran the recorded data through the ML-based high-resolution parameter estimation scheme RIMAX [245] to extract the parameters of the individual propagation paths. In particular, for each path, its DoA, DoD (azimuth and elevation), delay, and polarimetric path weights were estimated. This allows to remove (de-embed) the effect of the antenna array that was used to measure the channel. It also allows to resynthesize the channel with a reduced number of relevant paths to simplify its complexity.

Since this paper presents a first study on the possibility of applying spatial CS to the sounding problem without considering all the dimensions (e.g., frequency), the main goal of the numerical evaluation is to provide a proof of concept. We therefore simplify the complexity of the channel significantly by considering only the four dominant paths for a specific TX/RX position and for a single snapshot. Focusing only on the spatial domain, we aim at estimating the DoAs and the DoDs shown in Figure 6.2. Note how there are two paths that are very closely spaced in terms of their DoA, which makes it challenging to resolve them.

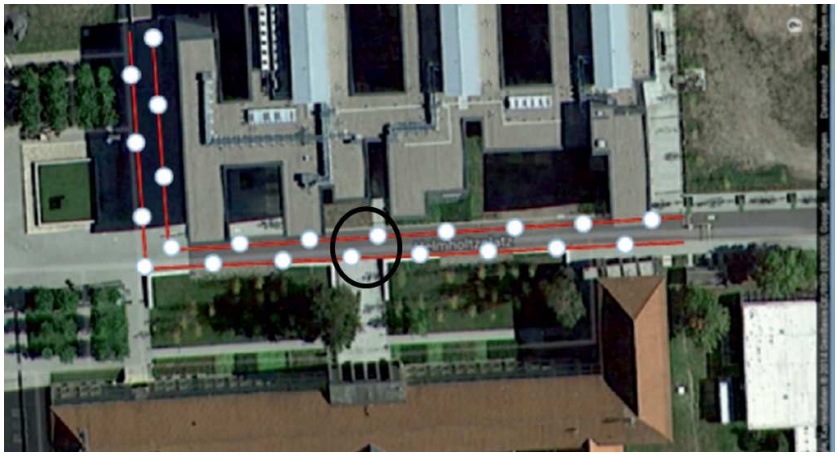

Figure 6.1: Top view of the locations of the transmitter and the receiver during the measurement campaign considered.

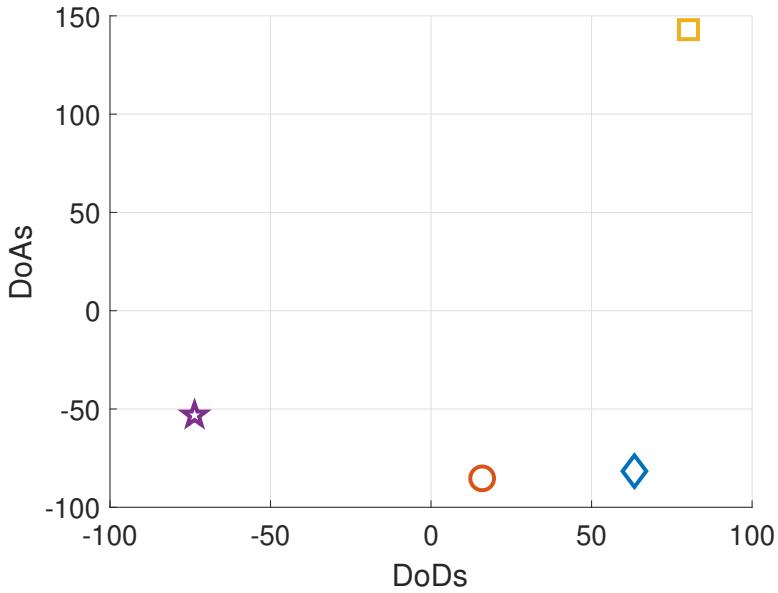

Figure 6.2: The DoAs and the DoDs of the 4 most dominant paths for the considered scenario.

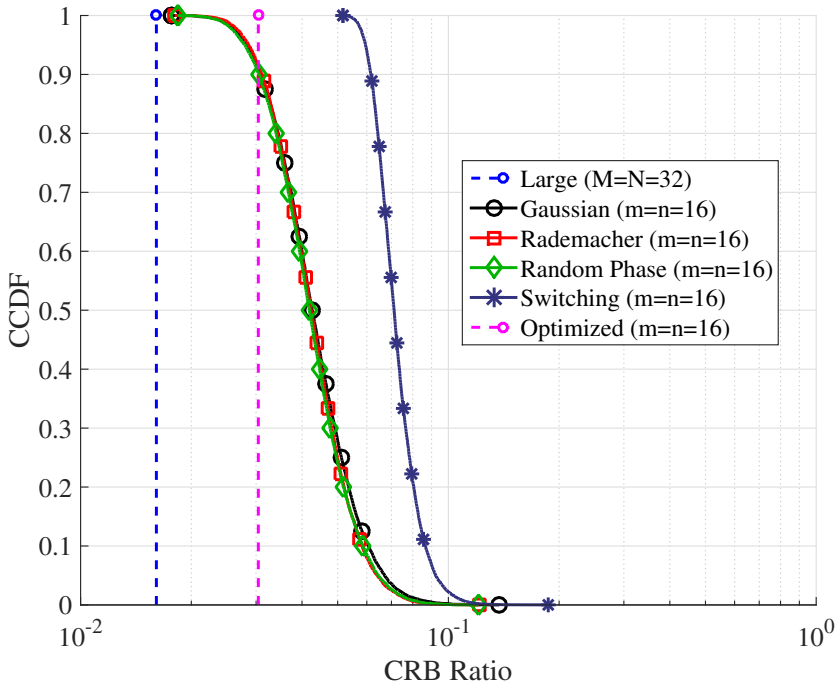

Figure 6.3: The CCDF of the mean CRB of the DoAs and DoDs for 10000 random realizations of $\mathbf{\Phi}_{\text{Tx}}$ and $\mathbf{\Phi}_{\text{Rx}}$ with 4 different designs.

As mentioned earlier, the performance of the compressive sounder will be evaluated based on the CRBs of the DoA/DoD estimation as a proxy to the performance of ML-type estimators. Figure 6.3 studies the performance of the compressive spatial channel sounder for DoD/DoA estimation and compare it to the uncompressed cases. For the case where we have a full array (i.e., fully meshed with no combining network) with 16 TX array elements and 16 RX array elements, the mean CRB of the DoAs and the DoDs is calculated and then used as a reference onward. Let's call this $\text{CRB}_{\text{small}}$. The large array is the one where we have 32 elements instead of 16 which we then call $\text{CRB}_{\text{large}}$. The compressed case is the one where we have 32 antenna elements but only 16 measurements (and/or 16 RF channels) and this we call $\text{CRB}_{\text{compressed}}$. The mean CRB values are calculated for both cases (i.e., the large array and the compressed one) and then normalized to the mean CRB of the small array for comparison. We call this the CRB Ratio where the $\text{CRB}_{\text{large}}$ and the $\text{CRB}_{\text{compressed}}$ shown are normalized to $\text{CRB}_{\text{small}}$ (e.g., CRB Ratio $= \frac{\text{CRB}_{\text{large}}}{\text{CRB}_{\text{small}}}$). The main advantage of this ratio is that it is independent of the SNR. No matter what's the SNR, we will always have this factor in variance reduction in the CRBs.

The coefficients of the combining networks $\mathbf{\Phi}_{\text{Tx}}$ and $\mathbf{\Phi}_{\text{Rx}}$ are then selected according to 5 different criteria which we name Gaussian, Rademacher, Random Phase, Switching

and Optimized. The complementary cumulative distribution function (CCDF) for 10000 realizations of the random combining networks is shown (i.e., the Gaussian; the Random Phase, the Rademacher, and the Switching). In the Gaussian case, the coefficients are drawn from a from a zero mean circularly symmetric complex Gaussian distribution. In the Random Phase case, a unit norm is chosen while the phases are drawn uniformly at random from $(0, 2\pi]$. The Rademacher setup is the one where the coefficients are drawn randomly from a Rademacher distribution with only ± 1s as possible outcomes at a 50% chance. The switching design is the one where for each measurement, one TX and one RX antenna/port is selected at random. The optimized design is the one we recently proposed based on optimizing the spatial correlation functions for DoD/DoA estimation [4].

The results show that the optimized design is the best 90% of the cases while the switching case is the worst. The Gaussian, the Random Phase and the Rademacher constructions achieve similar performance. However, from an implementation point of view, the switching design is the most appealing and realizable one where only a switch is needed to construct the network (one at the TX and one at the RX). The Rademacher design with only ± 1s requires only adders and inverters (180° phase shifters) to realize, which make them the second choice to implement. Both the Random Phase and the Optimized cases require phase shifters with an almost continuous phase range which make them very challenging to realize. The Gaussian case with a varying amplitude would make the implementation even more challenging and so that is why it is better to avoid it. We are currently investigating the optimization of the combining network with regard to the implementation challenges as well as the estimation performance.

The figure shows that the CRB of the compressive array is not as good as that of the full large array of 32 elements but still much better (more than 10 times better) than that of the uncompressed, conventional 16-element array. In case of a TDM TX/RX architecture, this means lower measurement time compared to the full 32 array case. Instead of taking $32 \times 32 = 1024$ measurement cycles, only $16 \times 16 = 256$ (i.e., only 1/4 the number of measurements compared to the full array) would suffice and so increasing the Doppler range without degrading the performance drastically. This can be of great importance when considering fast varying channels with a large Doppler spread. In case of a TDM TX and a linear combining compressive RX, we do $16 \times 32 = 512$ measurements and reduce the hardware complexity to $16 < 32$ RX RF chains.

Alternatively, for the same measurement time and/or hardware complexity, one can increase the number of array elements to cover a larger apperture and so achieve better performance in terms of resolution. Figure 6.4 shows the improvement in the CRBs

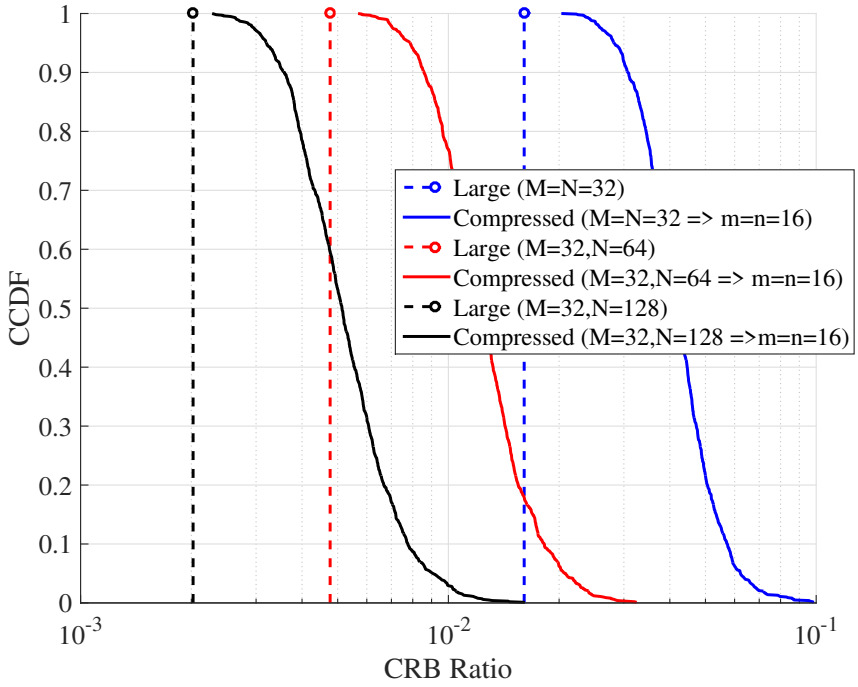

Figure 6.4: The improvement in the CRBs using larger number of array elements at the RX with a fixed number of 32 elements at the TX.

proportional to increasing the number of array elements (the Rademacher design is used to obtain $\mathbf{\Phi}_{\mathrm{Tx}}$ and $\mathbf{\Phi}_{\mathrm{Rx}}$). The TX has 32 elements with a combining network of only 16 measurements. The RX takes only 16 compressive measurements but the number of elements is varied from 32 to 64 to 128 elements. The CRBs of the DoA/DoD estimation improves (i.e., reduces) significantly while keeping the measurement complexity the same (i.e., 16 measurements). This can be interpreted as increasing the array aperture by using more antenna elements at the RX and so achieving a better resolution.

6.5 Summary

In this chapter, we consider the application of compressive sensing (CS) to channel sounding in the spatial domain. We proposed a compressive spatial channel sounding architecture where the antenna elements at the transmitter, the receiver or both are combined into a smaller number of channels using an analog combining network. The proposed approach reduces the total number of switching periods, which implies a reduced channel acquisition time and thus an improved Doppler bandwidth. On the other hand, the number of RF chains can be reduced, which is a very relevant advantage in terms of the overall receiver complexity, the amount of data to be processed in the

digital domain (e.g., FPGA), power consumption, as well as RF hardware calibration. Alternatively, for the same measurement time and/or hardware complexity, one can increase the number of array elements to cover a larger aperture and so achieving better performance in terms of resolution. Based on a realistic scenario, we show by simulations the superiority of the proposed compressive architecture in terms of the measurement complexity (i.e., time and hardware) and/or estimation performance.

Chapter 7

Conclusions

This chapter concludes this thesis and summarizes its main contributions.

Thesis summary

In this thesis, the application of compressive sensing (CS) to the problem of direction of arrival (DOA) estimation has been examined and its applicability to the time delay (TD) estimation and channel sounding has been investigated. The major objective was to develop approaches that allow to minimize the hardware complexity in terms of receiver costs and power consumption, while providing a desired level of estimation accuracy and robustness in the presence of multiple sources and/or multiple paths.

We started in **Chapter 2** by providing the background related to the work in this thesis. We mainly discussed the underlying principles of CS and DOA estimation.

Chapter 3 addressed the problem of CS-based DOA estimation for off-grid sources. We studied the spectrum in the case of off-grid sources qualitatively and found that most of the energy of the off-grid source after reconstruction is concentrated in the two neighboring grid points. Based on this observation, we derived the best two-term approximation coefficients explicitly and showed that the approximation error is very small. Moreover, we proposed a very simple scheme to estimate the grid offset based on the observed coefficients. For multiple sources, we showed that this simple scheme still works well when they are sufficiently spaced. For closely spaced sources, we proposed a numerical procedure for the joint estimation of their offsets from the recovered spectra at their neighboring grid points. Afterwards, the CS-based formulation of the DOA estimation problem has been extended to the polarimetric model. We discussed the off-grid problem in the polarimetric setting and proposed an estimator for the grid offset of one source (or an isolated source) as well as a joint estimator for the grid offsets

of two closely-spaced sources. Our numerical results demonstrated that the estimators could recover the DOA regardless of the polarization state of the incoming wave and is applicable to arbitrary arrays.

In **Chapter 4** we investigated the application of CS in the spatial domain via compressive arrays that aim to provide a larger aperture with a reduced hardware complexity. We presented an architecture of such a compressive array and introduced a generic system model that included different options for the hardware implementation. We then focused on the choice of the coefficients in the analog combining network. We started by demonstrating that choosing it randomly may lead to undesirable effects in the effective CS array such as very high sidelobes. Instead of choosing them randomly, we proposed a generic design approach for the analog combining network with the goal to obtain an array with certain desired properties, e.g., uniform sensitivity, low cross-correlation, or low variance in the DOA estimates. Our numerical simulations demonstrated the superiority of the proposed optimized compressive arrays to compressive arrays with randomly chosen combining kernels and to a sparse array of the same complexity. Also our proposed compressive array enjoys a high degree of adaptability since the combining weights can be altered to adjust the array to the current requirements, which is impossible for sparse arrays due to their static nature. We have also proposed a focusing design of the compression matrix which resulted in a significant performance improvement compared to the uniform design. Moreover, we proposed an extension for the combining matrix design for 2D (elevation and azimuth) DOA estimation with compressive antenna arrays.

Finally, we considered two other applications of the proposed approaches namely, CS based time delay (TD) estimation and compressive channel sounding. In **Chapter 5**, we investigated a CS based system architecture for TD estimation. We proposed to use a bank of K periodic functions $p_k(t)$ that multiply the received signal and are sampled once per period. Thereby, the effective sampling rate is reduced by a factor which depends on the period, the bandwidth, and the number of channels K. We then discussed the design of the functions $p_k(t)$ based on their frequency domain representation. We proposed an approach that directly optimizes the shape of the autocorrelation function in terms of the choice of $p_k(t)$ and demonstrate that it outperforms a random choice in terms of the delay estimation accuracy.

Chapter 6 considered the application of CS to channel sounding in the spatial domain. We proposed a compressive spatial channel sounding architecture where the antenna elements at the transmitter, the receiver or both are combined into a smaller number of channels using an analog combining network. The proposed approach reduces

the total number of switching periods, which implies a reduced channel acquisition time and thus an improved Doppler bandwidth. On the other hand, the number of RF chains can be reduced, which is a very relevant advantage in terms of the overall receiver complexity, the amount of data to be processed in the digital domain (e.g., FPGA), power consumption, as well as RF hardware calibration. Alternatively, for the same measurement time and/or hardware complexity, one can increase the number of array elements to cover a larger aperture and so achieving better performance in terms of resolution. Based on a realistic scenario, we showed by simulations the superiority of the proposed compressive architecture in terms of the measurement complexity (i.e., time and hardware) and/or estimation performance.

Contributions

The main contributions of this thesis are:

- A qualitative analysis of the model mismatch for CS based DOA estimation off the grid based on the shape of the resulting spectrum.
- A simple scheme for CS based DOA estimation off the grid for one source as well as multiple sources based on the aforementioned analysis.
- A novel polarimetric based CS based DOA estimation off the grid while polarization has been almost always ignored by state-of-the-art CS based DOA estimation methods.
- A basic architecture of a compressive array employing linear combinations in the analog domain by means of a network of power splitters, phase shifters, and power combiners with a generic system model that includes different options for the hardware implementation.
- An efficient design of the combining matrix to obtain an array that is suitable for DOA estimation (i.e., minimum variance of DOA estimates and robustness in terms of low side lobe levels or low probability of false detections).
- An extension of the presented ideas to be applied in TD estimation and synchronization. We mainly proposed an optimization based design for the measurement kernels of the CS based TD estimation architectures. We also proposed a CS based reference broadcast synchronization where the reference signal is an opportunistic signal already in the system (e.g., FM or TV signals).

- A compressive spatial channel sounder is proposed and evaluated based on real scenarios showing superior advantages in terms of time, hardware complexity and resolution.

Closing remarks

Compressive sensing and sparse recovery techniques have opened up new horizons for DOA estimation with sensor arrays. For almost a decade now, many CS based DOA estimation approaches have been proposed that allow to minimize the hardware complexity in terms of receiver costs, measurement time and power consumption, while providing a superior estimation accuracy and robustness in the presence of multiple sources and/or multiple paths.

This thesis tackled two main challenges of CS based DOA estimation, namely: the sparse CS based recovery of offgrid sources and the design of the combining network for compressive arrays. We have studied both problems quantitatively and proposed efficient schemes towards solving them. We have also shown the possible extension of these ideas to other applications, mainly: TD estimation and channel sounding.

Bibliography

Own Publications

[1] F. Römer, R. Alieiev, M. Ibrahim, G. Del Galdo, and R. S. Thomä. An analytical study of sparse recovery algorithms in presence of an Off-Grid source. In *International Workshop on Compressed Sensing applied to Radar*, Bonn, Germany, September 2013.

[2] M. Ibrahim, F. Römer, R. Alieiev, G. Del Galdo, and R. S. Thomä. On the estimation of grid offsets in cs-based direction-of-arrival estimation. In *International Conference on Acoustics, Speech and Signal Processing (ICASSP)*, pages 6776–6780, May 2014.

[3] F. Römer, M. Ibrahim, R. Alieiev, M. Landmann, R. S. Thomä, and G. Del Galdo. Polarimetric compressive sensing based DOA estimation. *ITG Workshop on Smart Antennas (WSA)*, March 2014.

[4] M. Ibrahim, F. Römer, and G. Del Galdo. On the design of the measurement matrix for compressed sensing based doa estimation. In *International Conference on Acoustics, Speech and Signal Processing (ICASSP)*, pages 3631–3635, April 2015.

[5] S. Skoblikov, M. Ibrahim, F. Römer, R. S. Thomä, and G. Del Galdo. Doa estimation with reflectarray according to single pixel camera principle. In *International Workshop on Compressed Sensing Theory and its Applications to Radar, Sonar and Remote Sensing (CoSeRa)*, pages 268–272, Jun 2015.

[6] S. Skoblikov, M. Ibrahim, F. Römer, and R. S. Thomä. Numerical assessment of reflectarray applicability to cs-based doa estimation. In *International Radar Symposium (IRS)*, pages 404–409, June 2015.

[7] M. Ibrahim, F. Römer, and G. Del Galdo. An adaptively focusing measurement design for compressed sensing based doa estimation. In *European Signal Processing Conference (EUSIPCO)*, pages 859–863. IEEE, 2015.

[8] M. Ibrahim, V. Ramireddy, A. Lavrenko, J. König, F. Römer, M. Landmann, M. Grossmann, G. Del Galdo, and R. S. Thomä. Design and analysis of compressive antenna arrays for direction of arrival estimation. *Signal Processing*, 138:35 – 47, 2017.

[9] A. Lavrenko, S. Pawar, M. Ibrahim, F. Römer, G. Del Galdo, and R. S. Thomä. Combining matrix design for 2d doa estimation with compressive antenna arrays. *ITG Workshop on Smart Antennas (WSA)*, March 2017.

[10] M. Ibrahim, F. Römer, N. Hadaschik, H. M. Tröger, B. Sackenreuter, N. Franke, J. Robert, and G. Del Galdo. Compressed temporal synchronization with opportunistic signals. *Radio Wireless Week*, Nov 2015.

[11] M. Ibrahim, F. Römer, N. Hadaschik, H. M. Tröger, B. Sackenreuter, N. Franke, J. Robert, and G. Del Galdo. Temporal wireless synchronization with compressed opportunistic signals. *Radio Wireless Week*, Jan 2016.

[12] F. Römer, M. Ibrahim, N. Franke, N. Hadaschik, A. Eidloth, B. Sackenreuter, and G. Del Galdo. Measurement matrix design for compressed sensing based time delay estimation. In *European Signal Processing Conference (EUSIPCO)*, pages 458–462, Aug 2016.

[13] M. Ibrahim, W. Al-Aqqad, F. Römer, M. Käske, S. Semper, R. S. Thomä, and G. Del Galdo. Compressive spatial channel sounding. In *European Conference on Antennas and Propagation*, London, UK, April 2018.

References by Other Authors

[14] Ericsson AB. Ericsson Mobility Report. White paper, 2017.

[15] D. H. Johnson and D. E. Dudgeon. *Array Signal Processing: Concepts and Techniques*. Simon & Schuster, Inc., New York, NY, USA, 1992.

[16] R. A. Monzingo and T. W. Miller. *Introduction to adaptive arrays*. Scitech Publishing, 1980.

[17] M. I. Skolnik. *Introduction to Radar Systems*. McGraw Hill Book Co., New York, 2 edition, 1980.

[18] L. C. Godara. Application of antenna arrays to mobile communications. ii. beam-forming and direction-of-arrival considerations. *Proceedings of the IEEE*, 85(8):1195–1245, Aug 1997.

[19] H. Krim and M. Viberg. Two decades of array signal processing research: the parametric approach. *IEEE Signal Processing Magazine*, 13(4):67–94, Jul 1996.

[20] S. Valaee, B. Champagne, and P. Kabal. Parametric localization of distributed sources. *IEEE Transactions on Signal Processing*, 43(9):2144–2153, Sep 1995.

[21] J. C. Chen, K. Yao, and R. E. Hudson. Source localization and beamforming. *IEEE Signal Processing Magazine*, 19(2):30–39, Mar 2002.

[22] W. Roh, J. Y. Seol, J. Park, B. Lee, J. Lee, Y. Kim, J. Cho, K. Cheun, and F. Aryanfar. Millimeter-wave beamforming as an enabling technology for 5g cellular communications: theoretical feasibility and prototype results. *IEEE Communications Magazine*, 52(2):106–113, February 2014.

[23] R. S. Thomä, D. Hampicke, A. Richter, G. Sommerkorn, A. Schneider, U. Trautwein, and W. Wirnitzer. Identification of time-variant directional mobile radio channels. *IEEE Transactions on Instrumentation and Measurement*, 49(2):357–364, Apr 2000.

[24] A. Richter, D. Hampicke, G. Sommerkorn, and R. S. Thomä. Joint estimation of dod, time-delay, and doa for high-resolution channel sounding. In *IEE Vehicular Technology Conference*, volume 2, pages 1045–1049 vol.2, 2000.

[25] R. S. Thomä, M. Landmann, and A. Richter. Rimax-a maximum likelihood framework channel parameter estimation in multidimensional channel sounding. *International Symposium on Antennas and Propagation*, pages 53–56, 2004.

[26] M. Landmann, M. Kaske, and R. S. Thoma. Impact of incomplete and inaccurate data models on high resolution parameter estimation in multidimensional channel sounding. *IEEE Transactions on Antennas and Propagation*, 60(2):557–573, Feb 2012.

[27] W. D. Blair and M. B. Pearce. Monopulse doa estimation of two unresolved rayleigh targets. *IEEE Transactions on Aerospace and Electronic Systems*, 37(2):452–469, Apr 2001.

[28] H. L. Van Trees. *Detection, estimation, and modulation theory. Part IV., Optimum array processing.* Wiley-Interscience, New York, 2002.

[29] D. Malioutov, M. Cetin, and A. S. Willsky. A sparse signal reconstruction perspective for source localization with sensor arrays. *IEEE Transactions on Signal Processing*, 53(8):3010–3022, Aug 2005.

[30] D. L. Donoho. Compressed sensing. *IEEE Transactions on Information Theory*, 52(4):1289–1306, 2006.

[31] E. J. Candés and T. Tao. Near optimal signal recovery from random projections: universal encoding strategies. *IEEE Transactions on Information Theory*, 52:5406–5425, 2006.

[32] E. J. Candés, J. Romberg, and T. Tao. Robust uncertainty principles: exact signal reconstruction from highly incomplete frequency information. *IEEE Transactions on Information Theory*, 52(2):489–509, Feb 2006.

[33] M. B. Wakin, J. N. Laska, M. F. Duarte, D. Baron, S. Sarvotham, D. Takhar, K. F. Kelly, and R. G. Baraniuk. An architecture for compressive imaging. In *International Conference on Image Processing*, pages 1273–1276, Oct 2006.

[34] M. F. Duarte, M. A. Davenport, D. Takhar, J. N. Laska, T. Sun, K. F. Kelly, and R. G. Baraniuk. Single-pixel imaging via compressive sampling. *IEEE Signal Processing Magazine*, 25(2):83–91, March 2008.

[35] M. Lustig, D. Donoho, and J. M. Pauly. Sparse mri: The application of compressed sensing for rapid mr imaging. *Magnetic Resonance in Medicine*, 58(6):1182–1195, 2007.

[36] H. Jung, K. Sung, K. S. Nayak, E. Y. Kim, and J. C. Ye. k-t focuss: A general compressed sensing framework for high resolution dynamic mri. *Magnetic Resonance in Medicine*, 61(1):103–116, 2009.

[37] T. T. Do, Yi Chen, D. T. Nguyen, N. Nguyen, L. Gan, and T. D. Tran. Distributed compressed video sensing. In *International Conference on Image Processing (ICIP)*, pages 1393–1396, Nov 2009.

[38] J. P. Nebot, Y. Ma, and T. Huang. Distributed video coding using compressive sampling. In *Picture Coding Symposium*, pages 1–4, May 2009.

[39] M. Herman and T. Strohmer. Compressed sensing radar. In *International Conference on Acoustics, Speech and Signal Processing*, pages 1509–1512, Mar 2008.

[40] J. H. G. Ender. On compressive sensing applied to radar. *Signal Processing*, 90(5):1402 – 1414, 2010. Special Section on Statistical Signal Array Processing.

[41] Potter L. C., Ertin E., Parker J. T., and Cetin M. Sparsity and compressed sensing in radar imaging. *Proceedings of the IEEE*, 98(6):1006–1020, 2010.

[42] J. N. Laska, S. Kirolos, M. F. Duarte, T. S. Ragheb, R. G. Baraniuk, and Y. Massoud. Theory and implementation of an analog-to-information converter using random demodulation. In *International Symposium on Circuits and Systems*, pages 1959–1962, May 2007.

[43] M. F. Duarte, S. Sarvotham, D. Baron, M. B. Wakin, and R. G. Baraniuk. Distributed compressed sensing of jointly sparse signals. In *Asilomar Conference onSignals, Systems and Computers, 2005.*, pages 1537–1541, Oct 2005.

[44] J. Haupt, W. U. Bajwa, M. Rabbat, and R. Nowak. Compressed sensing for networked data. *IEEE Signal Processing Magazine*, 25(2):92–101, Mar 2008.

[45] Y. Wang, G. Leus, and A. Pandharipande. Direction estimation using compressive sampling array processing. In *2009 IEEE/SP 15th Workshop on Statistical Signal Processing*, pages 626–629. IEEE, 2009.

[46] W. U. Bajwa, J. Haupt, A. M. Sayeed, and R. Nowak. Compressed channel sensing: A new approach to estimating sparse multipath channels. *Proceedings of the IEEE*, 98(6):1058–1076, June 2010.

[47] C. R. Berger, S. Zhou, J. C. Preisig, and P. Willett. Sparse channel estimation for multicarrier underwater acoustic communication: From subspace methods to compressed sensing. *IEEE Transactions on Signal Processing*, 58(3):1708–1721, March 2010.

[48] J. Bobin, J. L. Starck, and R. Ottensamer. Compressed sensing in astronomy. *IEEE Journal of Selected Topics in Signal Processing*, 2(5):718–726, Oct 2008.

[49] Y. Wiaux, L. Jacques, G. Puy, A. M. M. Scaife, and P. Vandergheynst. Compressed sensing imaging techniques for radio interferometry. *Monthly Notices of the Royal Astronomical Society*, 395(3):1733–1742, 2009.

[50] F. Parvaresh, H. Vikalo, S. Misra, and B. Hassibi. Recovering sparse signals using sparse measurement matrices in compressed dna microarrays. *IEEE Journal of Selected Topics in Signal Processing*, 2(3):275–285, Jun 2008.

[51] M. Hilbert and P. Lopez. The World's Technological Capacity to Store, Communicate, and Compute Information. *Science*, 332(6025):60–65, 2011.

[52] M. D. K. Silver. *Digital Insights 2020: How the Digital Technology Revolution is Changing Business and All Our Lives*. Troubador Publishing, 2014.

[53] R. G. Gallager. *Principles of Digital Communication*. Cambridge University Press, 2008.

[54] H. Nyquist. Certain topics in telegraph transmission theory. *Transactions of the American Institute of Electrical Engineers*, 47(2):617–644, April 1928.

[55] C. E. Shannon. Communication in the presence of noise. *Proceedings of the IRE*, 37(1):10–21, Jan 1949.

[56] R. J. Clarke. Transform coding of images. *Journal of Astrophysics*, 1985.

[57] M. Vetterli, P. Marziliano, and T. Blu. Sampling signals with finite rate of innovation. *IEEE Transactions on Signal Processing*, 50(6):1417–1428, Jun 2002.

[58] W. B. Pennebaker and J. L. Mitchell. *JPEG Still Image Data Compression Standard*. Kluwer Academic Publishers, Norwell, MA, USA, 1st edition, 1992.

[59] D. L. Donoho and J. M. Johnstone. Ideal spatial adaptation by wavelet shrinkage. *Biometrika*, 81(3):425–455, 1994.

[60] S. Mallat. *A Wavelet Tour of Signal Processing*. Academic Press, Boston, third edition edition, 2009.

[61] D. S. Taubman and M. W. Marcellin. *JPEG 2000: Image Compression Fundamentals, Standards and Practice*. Kluwer Academic Publishers, Norwell, MA, USA, 2001.

[62] K. Liu, F. Römer, J. P. C. L. da Costa, J. Xiong, Y. S. Yan, W. Q. Wang, and G. Del Galdo. Tensor-based sparsity order estimation for big data applications. In *European Signal Processing Conference (EUSIPCO)*, pages 648–652, Aug 2017.

[63] M. F. Duarte and Y. C. Eldar. Structured compressed sensing: From theory to applications. *IEEE Transactions on Signal Processing*, 59(9):4053–4085, Sep 2011.

[64] A. M. Tillmann and M. E. Pfetsch. The computational complexity of the restricted isometry property, the nullspace property, and related concepts in compressed sensing. *IEEE Transactions on Information Theory*, 60(2):1248–1259, Feb 2014.

[65] S. G. Mallat and Z. Zhang. Matching pursuits with time-frequency dictionaries. *IEEE Transactions on Signal Processing*, 41(12):3397–3415, Dec 1993.

[66] Y. C Eldar and G. Kutyniok. *Compressed sensing: theory and applications*. Cambridge University Press, 2012.

[67] R. Baraniuk, M. Davenport, R DeVore, and M Wakin. A simple proof of the restricted isometry property for random matrices. *Constructive Approximation*, 28(3):253–263, 2008.

[68] S. Mendelson, A. Pajor, and N. Tomczak-Jaegermann. Uniform uncertainty principle for bernoulli and subgaussian ensembles. *Constructive Approximation*, 28(3):277–289, Dec 2008.

[69] H. Rauhut. Compressive sensing and structured random matrices. *Theoretical foundations and numerical methods for sparse recovery*, 9:1–92, 2010.

[70] Y. Yu, A. P. Petropulu, and H. V. Poor. Measurement matrix design for compressive sensing-based mimo radar. *IEEE Transactions on Signal Processing*, 59(11):5338–5352, Nov 2011.

[71] J. A. Tropp, M. B. Wakin, M. F. Duarte, D. Baron, and R. G. Baraniuk. Random filters for compressive sampling and reconstruction. In *International Conference on Acoustics Speech and Signal Processing Proceedings*, volume 3, May 2006.

[72] M. Elad. Optimized projections for compressed sensing. *IEEE Transactions on Signal Processing*, 55(12):5695–5702, Dec 2007.

[73] J. M. Duarte-Carvajalino and G. Sapiro. Learning to sense sparse signals: Simultaneous sensing matrix and sparsifying dictionary optimization. *IEEE Transactions on Image Processing*, 18(7):1395–1408, July 2009.

[74] V. Abolghasemi, S. Sanei, S. Ferdowsi, F. Ghaderi, and A. Belcher. Segmented compressive sensing. In *IEEE/SP Workshop on Statistical Signal Processing*, pages 630–633, Aug 2009.

[75] V. Abolghasemi, S. Ferdowsi, and S. Sanei. A gradient-based alternating minimization approach for optimization of the measurement matrix in compressive sensing. *Signal Processing*, 92(4):999 – 1009, 2012.

[76] R. A. DeVore. Deterministic constructions of compressed sensing matrices. *Journal of Complexity*, 23(4):918 – 925, 2007.

[77] S. D. Howard, A. R. Calderbank, and S. J. Searle. A fast reconstruction algorithm for deterministic compressive sensing using second order reed-muller codes. In *Annual Conference on Information Sciences and Systems*, pages 11–15, March 2008.

[78] R. Calderbank, S. Howard, and S. Jafarpour. Construction of a large class of deterministic sensing matrices that satisfy a statistical isometry property. *IEEE Journal of Selected Topics in Signal Processing*, 4(2):358–374, April 2010.

[79] P. Indyk. Explicit constructions for compressed sensing of sparse signals. In *Annual ACM-SIAM Symposium on Discrete Algorithms*, SODA '08, pages 30–33, Philadelphia, PA, USA, 2008. Society for Industrial and Applied Mathematics.

[80] W. Xu and B. Hassibi. Efficient compressive sensing with deterministic guarantees using expander graphs. In *2007 IEEE Information Theory Workshop*, pages 414–419, Sept 2007.

[81] R. Berinde, A. C. Gilbert, P. Indyk, H. Karloff, and M. J. Strauss. Combining geometry and combinatorics: A unified approach to sparse signal recovery. In *Annual Allerton Conference on Communication, Control, and Computing*, pages 798–805, Sept 2008.

[82] S. Jafarpour, W. Xu, B. Hassibi, and R. Calderbank. Efficient and robust compressed sensing using optimized expander graphs. *IEEE Transactions on Information Theory*, 55(9):4299–4308, Sept 2009.

[83] A. Amini and F. Marvasti. Deterministic construction of binary, bipolar, and ternary compressed sensing matrices. *IEEE Transactions on Information Theory*, 57(4):2360–2370, April 2011.

[84] L. Applebaum, S. D. Howard, S. Searle, and R. Calderbank. Chirp sensing codes: Deterministic compressed sensing measurements for fast recovery. *Applied and Computational Harmonic Analysis*, 26(2):283 – 290, 2009.

[85] Z. Wang, G. R. Arce, and J. L. Paredes. Variable density compressed image sampling. In *European Signal Processing Conference*, pages 2022–2026, Aug 2009.

[86] A. Parada-Mayorga and G. R. Arce. Colored coded aperture design in compressive spectral imaging via minimum coherence. *IEEE Transactions on Computational Imaging*, 3(2):202–216, June 2017.

[87] M. E. Gehm, R. John, D. J. Brady, R. M. Willett, and T. J. Schulz. Single-shot compressive spectral imaging with a dual-disperser architecture. *Opt. Express*, 15(21):14013–14027, Oct 2007.

[88] A. Wagadarikar, R. John, R. Willett, and D. Brady. Single disperser design for coded aperture snapshot spectral imaging. *Appl. Opt.*, 47(10):B44–B51, Apr 2008.

[89] B. Bouchhima, R. Amara, and M. T. H. Alouane. Design of optimal matrices for compressive sensing: Application to environmental sounds. In *European Signal Processing Conference (EUSIPCO)*, pages 130–134, Aug 2015.

[90] R. Obermeier and J. A. Martinez-Lorenzo. Sensing matrix design via mutual coherence minimization for electromagnetic compressive imaging applications. *IEEE Transactions on Computational Imaging*, 3(2):217–229, June 2017.

[91] W. U. Bajwa, J. D. Haupt, G. M. Raz, S. J. Wright, and R. D. Nowak. Toeplitz-structured compressed sensing matrices. In *IEEE/SP Workshop on Statistical Signal Processing*, pages 294–298, Aug 2007.

[92] J. Romberg. Compressive sensing by random convolution. *SIAM Journal on Imaging Sciences*, 2(4):1098–1128, 2009.

[93] H. Rauhut, J. K. Romberg, and J. A. Tropp. Restricted Isometries for Partial Random Circulant Matrices. *Applied and Computational Harmonic Analysis*, abs/1010.1, 2010.

[94] J. Zhang, D. Zhu, and G. Zhang. Adaptive compressed sensing radar oriented toward cognitive detection in dynamic sparse target scene. *IEEE Transactions on Signal Processing*, 60(4):1718–1729, April 2012.

[95] B. K. Natarajan. Sparse approximate solutions to linear systems. *SIAM Journal on Computing*, 24(2):227–234, 1995.

[96] D. L. Donoho and B. F. Logan. Signal recovery and the large sieve. *SIAM J. Appl. Math.*, 52(2):577–591, April 1992.

[97] S. Chen, D. Donoho, and M. Saunders. Atomic decomposition by basis pursuit. *SIAM Rev.*, 43(1), January 2001.

[98] S. Boyd and L. Vandenberghe. *Convex Optimization*. Cambridge University Press, New York, NY, USA, 2004.

[99] R. Tibshirani. Regression shrinkage and selection via the lasso. *Journal of the Royal Statistical Society, Series B*, 58:267–288, 1994.

[100] R. Gribonval and M. Nielsen. Sparse representations in unions of bases. *IEEE Transactions on Information Theory*, 49(12):3320–3325, Dec 2003.

[101] E. Candés, J. Romberg, and T. Tao. Stable signal recovery from incomplete and inaccurate measurements. *Communications on Pure and Applied Mathematics*, 59(8):1207–1223, 2006.

[102] E. J. Candés. The restricted isometry property and its implications for compressed sensing. *Comptes Rendus Mathematique*, 346(9):589–592, 2008.

[103] M. A. T. Figueiredo, R. D. Nowak, and S. J. Wright. Gradient projection for sparse reconstruction: Application to compressed sensing and other inverse problems. *IEEE Journal of Selected Topics in Signal Processing*, 1(4):586–597, Dec 2007.

[104] S. J. Kim, K. Koh, M. Lustig, S. Boyd, and D. Gorinevsky. An interior-point method for large-scale l1-regularized least squares. *IEEE Journal of Selected Topics in Signal Processing*, 4:606–617, Dec 2007.

[105] D. Needell and R. Vershynin. Signal recovery from incomplete and inaccurate measurements via regularized orthogonal matching pursuit. *IEEE Journal of Selected Topics in Signal Processing*, 4(2):310–316, April 2010.

[106] Y. C. Pati, R. Rezaiifar, and P. S. Krishnaprasad. Orthogonal matching pursuit: recursive function approximation with applications to wavelet decomposition. In *Asilomar Conference on Signals, Systems and Computers*, pages 40–44 vol.1, Nov 1993.

[107] J. A. Tropp. Greed is good: algorithmic results for sparse approximation. *IEEE Transactions on Information Theory*, 50(10):2231–2242, Oct 2004.

[108] D. L. Donoho, Y. Tsaig, I. Drori, and J. L. Starck. Sparse solution of underdetermined systems of linear equations by stagewise orthogonal matching pursuit. *IEEE Transactions on Information Theory*, 58(2):1094–1121, Feb 2012.

[109] D. Needell and J.A. Tropp. Cosamp: Iterative signal recovery from incomplete and inaccurate samples. *Applied and Computational Harmonic Analysis*, 26:301–321, 2009.

[110] T. Blumensath and M. E. Davies. Iterative hard thresholding for compressed sensing. *Applied and Computational Harmonic Analysis*, 27(3):265–274, 2009.

[111] S. Foucart. Hard thresholding pursuit: An algorithm for compressive sensing. *SIAM Journal on Numerical Analysis*, 49(6):2543–2563, 2011.

[112] M. F. Duarte and R. G. Baraniuk. Spectral compressive sensing. *Applied and Computational Harmonic Analysis*, 35(1):111–129, 2013.

[113] M. A. Herman and T. Strohmer. General deviants: An analysis of perturbations in compressed sensing. *IEEE Journal of Selected Topics in Signal Processing*, 4(2):342–349, Apr 2010.

[114] Y. Chi, L. L. Scharf, A. Pezeshki, and A. R. Calderbank. Sensitivity to basis mismatch in compressed sensing. *IEEE Transactions on Signal Processing*, 59(5):2182–2195, May 2011.

[115] K. Fyhn, H. Dadkhahi, and M. F. Duarte. Spectral compressive sensing with polar interpolation. In *International Conference on Acoustics, Speech and Signal Processing*, pages 6225–6229, May 2013.

[116] G. Peyre. Best basis compressed sensing. *IEEE Transactions on Signal Processing*, 58(5):2613–2622, May 2010.

[117] C. Ekanadham, D. Tranchina, and E. P. Simoncelli. Recovery of sparse translation-invariant signals with continuous basis pursuit. *IEEE Transactions on Signal Processing*, 59(10):4735–4744, Oct 2011.

[118] Z. Yang, C. Zhang, and L. Xie. Robustly stable signal recovery in compressed sensing with structured matrix perturbation. *IEEE Transactions on Signal Processing*, 60(9):4658–4671, Sept 2012.

[119] H. Zhu, G. Leus, and G. B. Giannakis. Sparsity-cognizant total least-squares for perturbed compressive sampling. *IEEE Transactions on Signal Processing*, 59(5):2002–2016, May 2011.

[120] O. Teke, A. C. Gurbuz, and O. Arikan. Perturbed orthogonal matching pursuit. *IEEE Transactions on Signal Processing*, 61(24):6220–6231, Dec 2013.

[121] Z. Yang, L. Xie, and C. Zhang. Off-grid direction of arrival estimation using sparse bayesian inference. *IEEE Transactions on Signal Processing*, 61(1):38–43, Jan 2013.

[122] E. J. Candés and C. F. Granda. Towards a mathematical theory of super-resolution. *Communications on Pure and Applied Mathematics*, 67(6):906–956, Jun 2014.

[123] G. Tang, B. N. Bhaskar, P. Shah, and B. Recht. Compressed sensing off the grid. *IEEE Transactions on Information Theory*, 59(11):7465–7490, Nov 2013.

[124] V. Chandrasekaran, B. Recht, P. A. Parrilo, and A. S. Willsky. The convex geometry of linear inverse problems. *Foundations of Computational Mathematics*, 12(6):805–849, Dec 2012.

[125] E. J. Candès and C. F. Granda. Super-resolution from noisy data. *Journal of Fourier Analysis and Applications*, 19(6):1229–1254, Dec 2013.

[126] B. N. Bhaskar, G. Tang, and B. Recht. Atomic norm denoising with applications to line spectral estimation. *IEEE Transactions on Signal Processing*, 61(23):5987–5999, Dec 2013.

[127] Z. Yang and L. Xie. On gridless sparse methods for line spectral estimation from complete and incomplete data. *IEEE Transactions on Signal Processing*, 63(12):3139–3153, June 2015.

[128] P. Stoica and P. Babu. Spice and likes: Two hyperparameter-free methods for sparse-parameter estimation. *Signal Processing*, 92(7):1580 – 1590, 2012.

[129] J. Böhme. Estimation of source parameters by maximum likelihood and nonlinear regression. In *IEEE International Conference on Acoustics, Speech, and Signal Processing (ICASSP)*, volume 9, pages 271–274, Mar 1984.

[130] A. G. Jaffer. Maximum likelihood direction finding of stochastic sources: a separable solution. In *International Conference on Acoustics, Speech, and Signal Processing (ICASSP)*, pages 2893–2896 vol.5, Apr 1988.

[131] P. Stoica and K. C. Sharman. Maximum likelihood methods for direction-of-arrival estimation. *IEEE Transactions on Acoustics, Speech, and Signal Processing*, 38(7):1132–1143, Jul 1990.

[132] P. Stoica and A. Nehorai. Performance study of conditional and unconditional direction-of-arrival estimation. *IEEE Transactions on Acoustics, Speech, and Signal Processing*, 38(10):1783–1795, Oct 1990.

[133] B. Ottersten, M. Viberg, and T. Kailath. Analysis of subspace fitting and ml techniques for parameter estimation from sensor array data. *IEEE Transactions on Signal Processing*, 40(3):590–600, Mar 1992.

[134] B. D. Van Veen and K. M. Buckley. Beamforming: a versatile approach to spatial filtering. *IEEE ASSP Magazine*, 5(2):4–24, April 1988.

[135] J. Capon. High-resolution frequency-wavenumber spectrum analysis. *Proceedings of the IEEE*, 57(8):1408–1418, Aug 1969.

[136] G. Bienvenu and L. Kopp. Adaptivity to background noise spatial coherence for high resolution passive methods. In *IEEE International Conference on Acoustics, Speech, and Signal Processing*, volume 5, pages 307–310, Apr 1980.

[137] R. Schmidt. Multiple emitter location and signal parameter estimation. *IEEE Transactions on Antennas and Propagation*, 34(3):276–280, Mar 1986.

[138] K. Lee and Y. Bresler. Subspace-augmented music for joint sparse recovery with any rank. In *2010 IEEE Sensor Array and Multichannel Signal Processing Workshop*, pages 205–208, Oct 2010.

[139] T. J. Shan, M. Wax, and T. Kailath. On spatial smoothing for direction-of-arrival estimation of coherent signals. *IEEE Transactions on Acoustics, Speech, and Signal Processing*, 33(4):806–811, Aug 1985.

[140] B. Friedlander and A. J. Weiss. Direction finding using spatial smoothing with interpolated arrays. *IEEE Transactions on Aerospace and Electronic Systems*, 28(2):574–587, Apr 1992.

[141] A. Barabell. Improving the resolution performance of eigenstructure-based direction-finding algorithms. In *IEEE International Conference on Acoustics, Speech, and Signal Processing*, volume 8, pages 336–339, Apr 1983.

[142] B. D. Rao and K. V. S. Hari. Performance analysis of root-music. *IEEE Transactions on Acoustics, Speech, and Signal Processing*, 37(12):1939–1949, Dec 1989.

[143] R. Roy, A. Paulraj, and T. Kailath. Estimation of signal parameters via rotational invariance techniques - esprit. In *IEEE Military Communications Conference*, volume 3, pages 41.6.1–41.6.5, Oct 1986.

[144] C. P. Mathews and M. D. Zoltowski. Eigenstructure techniques for 2-d angle estimation with uniform circular arrays. *IEEE Transactions on Signal Processing*, 42(9):2395–2407, Sep 1994.

[145] M. D. Zoltowski, M. Haardt, and C. P. Mathews. Closed-form 2-d angle estimation with rectangular arrays in element space or beamspace via unitary esprit. *IEEE Transactions on Signal Processing*, 44(2):316–328, Feb 1996.

[146] J. Ramos, C. P. Mathews, and M. D. Zoltowski. Fca-esprit: a closed-form 2-d angle estimation algorithm for filled circular arrays with arbitrary sampling lattices. *IEEE Transactions on Signal Processing*, 47(1):213–217, Jan 1999.

[147] P. Stoica and A. Nehorai. Music, maximum likelihood, and cramér-rao bound. *IEEE Transactions on Acoustics, Speech, and Signal Processing*, 37(5):720–741, May 1989.

[148] M. Viberg, B. Ottersten, and T. Kailath. Detection and estimation in sensor arrays using weighted subspace fitting. *IEEE Transactions on Signal Processing*, 39(11):2436–2449, Nov 1991.

[149] M. Viberg and A. L. Swindlehurst. A bayesian approach to auto-calibration for parametric array signal processing. *IEEE Transactions on Signal Processing*, 42(12):3495–3507, Dec 1994.

[150] J. F. Gu, W. P. Zhu, and M. N. S. Swamy. Compressed sensing for doa estimation with fewer receivers than sensors. In *IEEE International Symposium of Circuits and Systems (ISCAS)*, pages 1752–1755, May 2011.

[151] A. C. Gurbuz, V. Cevher, and J. H. Mcclellan. Bearing estimation via spatial sparsity using compressive sensing. *IEEE Transactions on Aerospace and Electronic Systems*, 48(2):1358–1369, APRIL 2012.

[152] C. D. Austin, J. N. Ash, and R. L. Moses. Parameter estimation using sparse reconstruction with dynamic dictionaries. In *IEEE International Conference on Acoustics, Speech and Signal Processing (ICASSP)*, pages 2852–2855, May 2011.

[153] C. Feng, S. Valaee, and Z. Tan. Multiple target localization using compressive sensing. In *Global Telecommunications Conference*, pages 1–6, Nov 2009.

[154] V. K. Jain, W. L. Collins, and D. C. Davis. High-accuracy analog measurements via interpolated fft. *IEEE Transactions on Instrumentation and Measurement*, 28(2):113–122, June 1979.

[155] E. Jacobsen and P. Kootsookos. Fast, accurate frequency estimators [dsp tips tricks]. *IEEE Signal Processing Magazine*, 24(3):123–125, May 2007.

[156] M. Landmann and R. S. Thomä. Common pitfalls in multidimensional high resolution channel parameter estimation. In *IEEE Digital Signal Processing Workshop and 5th IEEE Signal Processing Education Workshop*, pages 314–319, Jan 2009.

[157] H. Chen, Q. Wan, Y. P. Liu, and A. M. Huang. A sparse signal reconstruction perspective for direction-of-arrive estimation with a distributed polarization sensitive array. In *2009 International Conference on Wireless Communications Signal Processing*, pages 1–5, Nov 2009.

[158] M. Landmann, A. Richter, and R. S. Thoma. Doa resolution limits in mimo channel sounding. In *IEEE Antennas and Propagation Society Symposium, 2004.*, volume 2, pages 1708–1711 Vol.2, Jun 2004.

[159] R. Clark Jones. A new calculus for the treatment of optical systemsi. description and discussion of the calculus. *Journal of the Optical Society of America*, 31(7):488–493, Jul 1941.

[160] Y. C. Eldar and M. Mishali. Robust recovery of signals from a structured union of subspaces. *IEEE Transactions on Information Theory*, 55(11):5302–5316, Nov 2009.

[161] E. van den Berg and M. P. Friedlander. SPGL1: A solver for large-scale sparse reconstruction, June 2007. http://www.cs.ubc.ca/labs/scl/spgl1.

[162] J. Fang and H. Li. Recovery of block-sparse representations from noisy observations via orthogonal matching pursuit. *arXiv preprint arXiv:1109.5430*, 2011.

[163] M. Landmann and G. Del Galdo. Efficient antenna description for mimo channel modelling and estimation. In *European Conference on Wireless Technology, 2004.*, pages 217–220, Oct 2004.

[164] R. Roy and T. Kailath. Esprit-estimation of signal parameters via rotational invariance techniques. *IEEE Transactions on Acoustics, Speech, and Signal Processing*, 37(7):984–995, Jul 1989.

[165] P. Stoica, B. Ottersten, M. Viberg, and R. L. Moses. Maximum likelihood array processing for stochastic coherent sources. *IEEE Transactions on Signal Processing*, 44(1):96–105, Jan 1996.

[166] Y. Lo. A mathematical theory of antenna arrays with randomly spaced elements. *IEEE Transactions on Antennas and Propagation*, 12(3):257–268, May 1964.

[167] A. Moffet. Minimum-redundancy linear arrays. *IEEE Transactions on Antennas and Propagation*, 16(2):172–175, Mar 1968.

[168] W. K. Ma, T. H. Hsieh, and C. Y. Chi. Doa estimation of quasi-stationary signals via khatri-rao subspace. In *International Conference on Acoustics, Speech and Signal Processing*, pages 2165–2168, April 2009.

[169] R. L. Haupt. Thinned arrays using genetic algorithms. *IEEE Transactions on Antennas and Propagation*, 42(7):993–999, July 1994.

[170] A. Trucco and V. Murino. Stochastic optimization of linear sparse arrays. *IEEE Journal of Oceanic Engineering*, 24(3):291–299, Jul 1999.

[171] H. Gazzah and K. Abed-Meraim. Optimum ambiguity-free directional and omnidirectional planar antenna arrays for doa estimation. *IEEE Transactions on Signal Processing*, 57(10):3942–3953, Oct 2009.

[172] P. P. Vaidyanathan and P. Pal. Sparse sensing with co-prime samplers and arrays. *IEEE Transactions on Signal Processing*, 59(2):573–586, Feb 2011.

[173] P. Pal and P. P. Vaidyanathan. Nested arrays: A novel approach to array processing with enhanced degrees of freedom. *IEEE Transactions on Signal Processing*, 58(8):4167–4181, Aug 2010.

[174] V. Cevher, A. C. Gurbuz, J. H. McClellan, and R. Chellappa. Compressive wireless arrays for bearing estimation. In *International Conference on Acoustics, Speech and Signal Processing*, pages 2497–2500, March 2008.

[175] A. Gretsistas and M. D. Plumbley. *A Multichannel Spatial Compressed Sensing Approach for Direction of Arrival Estimation*, pages 458–465. Springer Berlin Heidelberg, Berlin, Heidelberg, 2010.

[176] P. Stoica, P. Babu, and J. Li. Spice: A sparse covariance-based estimation method for array processing. *IEEE Transactions on Signal Processing*, 59(2):629–638, Feb 2011.

[177] D. Model and M. Zibulevsky. Signal reconstruction in sensor arrays using sparse representations. *Signal Processing*, 86(3):624 – 638, 2006. Sparse Approximations in Signal and Image ProcessingSparse Approximations in Signal and Image Processing.

[178] K. Han, Y. Wang, B. Kou, and W. Hong. Parameters estimation using a random linear array and compressed sensing. In *International Congress on Image and Signal Processing (CISP)*, volume 8, pages 3950–3954, Oct 2010.

[179] M. Rossi, A. M. Haimovich, and Y. C. Eldar. Spatial compressive sensing in mimo radar with random arrays. In *Annual Conference on Information Sciences and Systems (CISS)*, pages 1–6, March 2012.

[180] S. Shakeri, D. D. Arianandа, and G. Leus. Direction of arrival estimation using sparse ruler array design. In *International Workshop on Signal Processing Advances in Wireless Communications (SPAWC)*, pages 525–529, June 2012.

[181] M. B. Hawes and W. Liu. Compressive sensing-based approach to the design of linear robust sparse antenna arrays with physical size constraint. *IET Microwaves, Antennas Propagation*, 8(10):736–746, July 2014.

[182] A. L. Swindlehurst, E. Ayanoglu, P. Heydari, and F. Capolino. Millimeter-wave massive MIMO: The next wireless revolution. *IEEE Communications Magazine*, 52(9):56–62, 2014.

[183] R. Zetik et al. D3.3 cost-efficient combinations of beamforming networks and antenna apertures. Technical report, H2020-ICT project SANSA (Shared Access Terrestrial-Satellite Backhaul Network enabled by Smart Antennas), 2016.

[184] S. Kutty and D. Sen. Beamforming for millimeter wave communications: An inclusive survey. *IEEE Communications Surveys Tutorials*, 18(2):949–973, Secondquarter 2016.

[185] D. Ramasamy, S. Venkateswaran, and U. Madhow. Compressive tracking with 1000-element arrays: A framework for multi-gbps mm wave cellular downlinks. In *Annual Allerton Conference on Communication, Control, and Computing*, pages 690–697, Oct 2012.

[186] D. Ntaikos et al. D2.4 requirements specification for the key enabling components. Technical report, H2020-ICT project SANSA (Shared Access Terrestrial-Satellite Backhaul Network enabled by Smart Antennas), 2016.

[187] T T. Cai, T. Jiang, et al. Limiting laws of coherence of random matrices with applications to testing covariance structure and construction of compressed sensing matrices. *The Annals of Statistics*, 39(3):1496–1525, 2011.

[188] TriQuint Semiconductor. Phase shifters, August 2016. http://www.triquint.com/products/all/control-products/phase-shifters.

[189] H. B. Lee and M. S. Wengrovitz. Resolution threshold of beamspace music for two closely spaced emitters. *IEEE Transactions on Acoustics, Speech, and Signal Processing*, 38(9):1545–1559, Sep 1990.

[190] S. Anderson. Optimal dimension reduction for sensor array signal processing. In *Asilomar Conference on Signals, Systems and Computers*, pages 918–922 vol.2, Nov 1991.

[191] M. D. Zoltowski, G. M. Kautz, and S. D. Silverstein. Beamspace root-music. *IEEE Transactions on Signal Processing*, 41(1):344–, Jan 1993.

[192] Guanghan Xu, S. D. Silverstein, R. H. Roy, and T. Kailath. Beamspace esprit. *IEEE Transactions on Signal Processing*, 42(2):349–356, Feb 1994.

[193] M. D. Zoltowski, M. Haardt, and C. P. Mathews. Closed-form 2-d angle estimation with rectangular arrays in element space or beamspace via unitary esprit. *IEEE Transactions on Signal Processing*, 44(2):316–328, Feb 1996.

[194] A. B. Gershman. Direction finding using beamspace root estimator banks. *IEEE Transactions on Signal Processing*, 46(11):3131–3135, Nov 1998.

[195] A. Hassanien, S. A. Elkader, A. B. Gershman, and K. M. Wong. Convex optimization based beam-space preprocessing with improved robustness against out-of-sector sources. *IEEE Transactions on Signal Processing*, 54(5):1587–1595, May 2006.

[196] H. Hung and M. Kaveh. Focussing matrices for coherent signal-subspace processing. *IEEE Transactions on Acoustics, Speech, and Signal Processing*, 36(8):1272–1281, Aug 1988.

[197] V. Venkateswaran and A. J. van der Veen. Analog beamforming in mimo communications with phase shift networks and online channel estimation. *IEEE Transactions on Signal Processing*, 58(8):4131–4143, Aug 2010.

[198] X. Huang, Y. J. Guo, and J. D. Bunton. A hybrid adaptive antenna array. *IEEE Transactions on Wireless Communications*, 9(5):1770–1779, May 2010.

[199] J. Nsenga, A. Bourdoux, and F. Horlin. Mixed analog/digital beamforming for 60 ghz mimo frequency selective channels. In *IEEE International Conference on Communications*, pages 1–6, May 2010.

[200] L. C. Godara. *Smart Antennas*. CRC Press LLC, 2004.

[201] T. E. Bogale and L. B. Le. Beamforming for multiuser massive mimo systems: Digital versus hybrid analog-digital. In *IEEE Global Communications Conference*, pages 4066–4071, Dec 2014.

[202] Z. Pi and F. Khan. An introduction to millimeter-wave mobile broadband systems. *IEEE Communications Magazine*, 49(6):101–107, June 2011.

[203] O. E. Ayach, S. Rajagopal, S. Abu-Surra, Z. Pi, and R. W. Heath. Spatially sparse precoding in millimeter wave MIMO systems. *IEEE Transactions on Wireless Communications*, 13(3):1499–1513, March 2014.

[204] M. Grossmann, V. Ramireddy, J. König, M. Landmann, F. Römer, G. Del Galdo, and R. Perthold. Antenna array optimization strategies for robust direction finding. In *European Conference on Antennas and Propagation (EuCAP)*, pages 1–5, April 2016.

[205] T. Coleman and Y. Li. On the convergence of reflective newton methods for large-scale nonlinear minimization subject to bounds. *Mathematical Programming*, 67(2):189–224, 1994.

[206] T. Coleman and Y. Li. An interior trust region approach for nonlinear minimization subject to bounds. *SIAM Journal on optimization*, 6(2):418–445, 1996.

[207] A. Alkhateeb, O. El Ayach, G. Leus, and R. W. Heath. Hybrid precoding for millimeter wave cellular systems with partial channel knowledge. In *Information Theory and Applications Workshop (ITA)*, pages 1–5, Feb 2013.

[208] G. L. Turin. Introduction to spread-spectrum antimultipath techniques and their application to urban digital radio. *Proc. IEEE*, 68(3):328–353, March 1980.

[209] A. Quazi. An overview on the time delay estimate in active and passive systems for target localization. *IEEE Trans. Acoust., Speech, Signal Process.*, 29(3):527–533, 1981.

[210] T. Grün, N. Franke, D. Wolf, N. Witt, and A. Eidloth. A real-time tracking system for football match and training analysis. In A. Heuberger, G. Elst, and R. Hanke, editors, *Microelectronic Systems*, pages 199–212. Springer Berlin Heidelberg, 2011.

[211] Cauligi S. Raghavendra, Krishna M. Sivalingam, and Taieb Znati. *Wireless sensor networks*. Springer Science & Business Media, 2004.

[212] S. Björklund. *A Survey and Comparison of Time-delay Estimation Methods in Linear Systems*. PhD thesis, Linköping University, 2003.

[213] J. Elson, L. Girod, and D. Estrin. Fine-grained network time synchronization using reference broadcasts. *SIGOPS Oper. Syst. Rev.*, 36(SI):147–163, Dec 2002.

[214] G. Mao, B. Fidan, and B. D. O. Anderson. Wireless sensor network localization techniques. *Comput. Netw.*, 51(10):2529–2553, July 2009.

[215] Jose L Paredes, Gonzalo R Arce, and Zhongmin Wang. Ultra-wideband compressed sensing: channel estimation. *IEEE Journal of Selected Topics in Signal Processing*, 1(3):383–395, 2007.

[216] M. Mishali and Y. C. Eldar. From theory to practice: Subnyquist sampling of sparse wideband analog signals. *IEEE Journal of Selected Topics in Signal Processing*, 4(2):375–391, 2010.

[217] K. Gedalyahu and Y. C. Eldar. Time-delay estimation from low-rate samples: A union of subspaces approach. *IEEE Transactions on Signal Processing*, 58(6):3017–3031, June 2010.

[218] Y. M. Lu and M. N. Do. A theory for sampling signals from a union of subspaces. *IEEE Transactions on Signal Processing*, 56(6):2334–2345, June 2008.

[219] Y. Gu and N. A. Goodman. Compressive sensing kernel optimization for time delay estimation. In *IEEE Radar Conference*, pages 1209–1213, May 2014.

[220] S. Bernhardt, R. Boyer, S. Marcos, Y. Eldar, P. Larzabal, and R. Boyer. Sampling FRI Signals with the SoS Kernel: Bounds and Optimal Kernel. In *European Signal Processing Conference (EUSIPCO'15)*, Nice, France, August 2015.

[221] G. Li, Z. Zhu, D. Yang, L. Chang, and H. Bai. On projection matrix optimization for compressive sensing systems. *IEEE Transactions on Signal Processing*, 61(11):2887–2898, June 2013.

[222] R. K. Martin, J. Velotta, and J. Raquet. Multicarrier modulation as a navigation signal of opportunity. In *IEEE Aerospace Conference*, pages 1–8, March 2008.

[223] M. Speth, S. Fechtel, G. Fock, and H. Meyr. Optimum receiver design for ofdm-based broadband transmission .ii. a case study. *IEEE Transactions on Communications*, 49(4):571–578, Apr 2001.

[224] K. Shi, E. Serpedin, and P. Ciblat. Decision-directed fine synchronization in ofdm systems. *IEEE Transactions on Communications*, 53(3):408–412, March 2005.

[225] P. Thevenon, O. Julien, C. Macabiau, D. Serant, S. Corazza, M. Bousquet, L. Ries, and T. Grelier. Pseudo-range measurements using ofdm channel estimation. *International Technical Meeting of The Satellite Division of the Institute of Navigation*, pages 481–493, Sep 2009.

[226] L. Patino-Studencka, A. Eidloth, and J. Thielecke. Modelling of free-running clocks for a virtually synchronized microwave locating system. In *Workshop on Positioning, Navigation and Communication*, pages 151–155, March 2009.

[227] C. Knapp and G. Carter. The generalized correlation method for estimation of time delay. *IEEE Transactions on Acoustics, Speech, and Signal Processing*, 24(4):320–327, Aug 1976.

[228] G. C. Carter. Coherence and time delay estimation. *Proceedings of the IEEE*, 75(2):236–255, Feb 1987.

[229] P. Misra and P. Enge. *Global positioning system: signals, measurements, and performance*. Ganga-Jamuna Press, 2006.

[230] David J Daniels. *Ground penetrating radar*, volume 1. IET, 2004.

[231] K. Fyhn, S. H. Jensen, and M. F. Duarte. Compressive time delay estimation using interpolation. In *IEEE Global Conference on Signal and Information Processing*, pages 624–624, Dec 2013.

[232] Nathan Srebro and Tommi Jaakkola. Weighted low-rank approximations. In *ICML*, volume 3, pages 720–727, 2003.

[233] William Rey. On weighted low-rank approximation. *arXiv preprint arXiv:1302.0360*, 2013.

[234] H. Wang and P. Chu. Voice source localization for automatic camera pointing system in videoconferencing. In *IEEE International Conference on Acoustics, Speech, and Signal Processing*, volume 1, pages 187–190 vol.1, Apr 1997.

[235] R. S. Thomä, M. Landmann, G. Sommerkorn, and A. Richter. Multidimensional high-resolution channel sounding in mobile radio. In *Instrumentation and Measurement Technology Conference*, volume 1, pages 257–262 Vol.1, May 2004.

[236] J. I. Tamir, T. S. Rappaport, Y. C. Eldar, and A. Aziz. Analog compressed sensing for RF propagation channel sounding. In *International Conference on Acoustics, Speech and Signal Processing (ICASSP)*, pages 5317–5320, March 2012.

[237] M. Mishali, Y. C. Eldar, and A. J. Elron. Xampling: Signal acquisition and processing in union of subspaces. *IEEE Transactions on Signal Processing*, 59(10):4719–4734, Oct 2011.

[238] M. Rossi, A. M. Haimovich, and Y. C. Eldar. Spatial compressive sensing for MIMO radar. *IEEE Transactions on Signal Processing*, 62(2):419–430, Jan 2014.

[239] A. Richter and R. S. Thomä. Parametric modeling and estimation of distributed diffuse scattering components of radio channels. In *COST 273, Prague*, volume 198, pages 24–26, Sept 2003.

[240] M. Steinbauer, A. F. Molisch, and E. Bonek. The double-directional radio channel. *IEEE Antennas and Propagation Magazine*, 43(4):51–63, Aug 2001.

[241] R. S. Thomä, D. Hampicke, A Richter, G. Sommerkorn, A.l Schneider, U. Trautwein, and W. Wirnitzer. Identification of time-variant directional mobile radio channels. *IEEE Transactions on Instrumentation and Measurement*, 49(2):357–364, Apr 2000.

[242] R. S. Thomä, D. Hampicke, A. Richter, G. Sommerkorn, and U. Trautwein. MIMO vector channel sounder measurement for smart antenna system evaluation. *European Transactions on Telecommunications*, 12(5):427–438, Sep/Oct 2001.

[243] C. Schneider and R. S. Thomä. Empirical study of higher order MIMO capacity at 2.53 GHz in urban macro cell. In *European Conference on Antennas and Propagation (EuCAP)*, pages 477–481, April 2013.

[244] M. Narandzic, C. Schneider, W. Kotterman, and R. Thomä. Quantification of scenario distance within generic WINNER channel model. *EURASIP Journal of Antennas and Propagation*, 2013, 2013.

[245] R. S. Thomä, M. Landmann, and A. Richter. Rimax: A maximum likelihood framework for parameter estimation in multidimensional channel sounding. In *International Symposium on Antennas and Propagation (ISAP)*, pages 53–56, 2004.

[246] C. Schneider, M. Käske, G. Sommerkorn, R. S. Thomä, A. Roivainen, J. Meinilä, and V. Tervo. Directional analysis of multipath propagation in vehicle-2-vehicle channels. In *European Conference on Antennas and Propagation (EuCAP)*, pages 1–5, April 2016.